ADVANCED PHOTONICS

Theme Issue on

Quantum Technologies

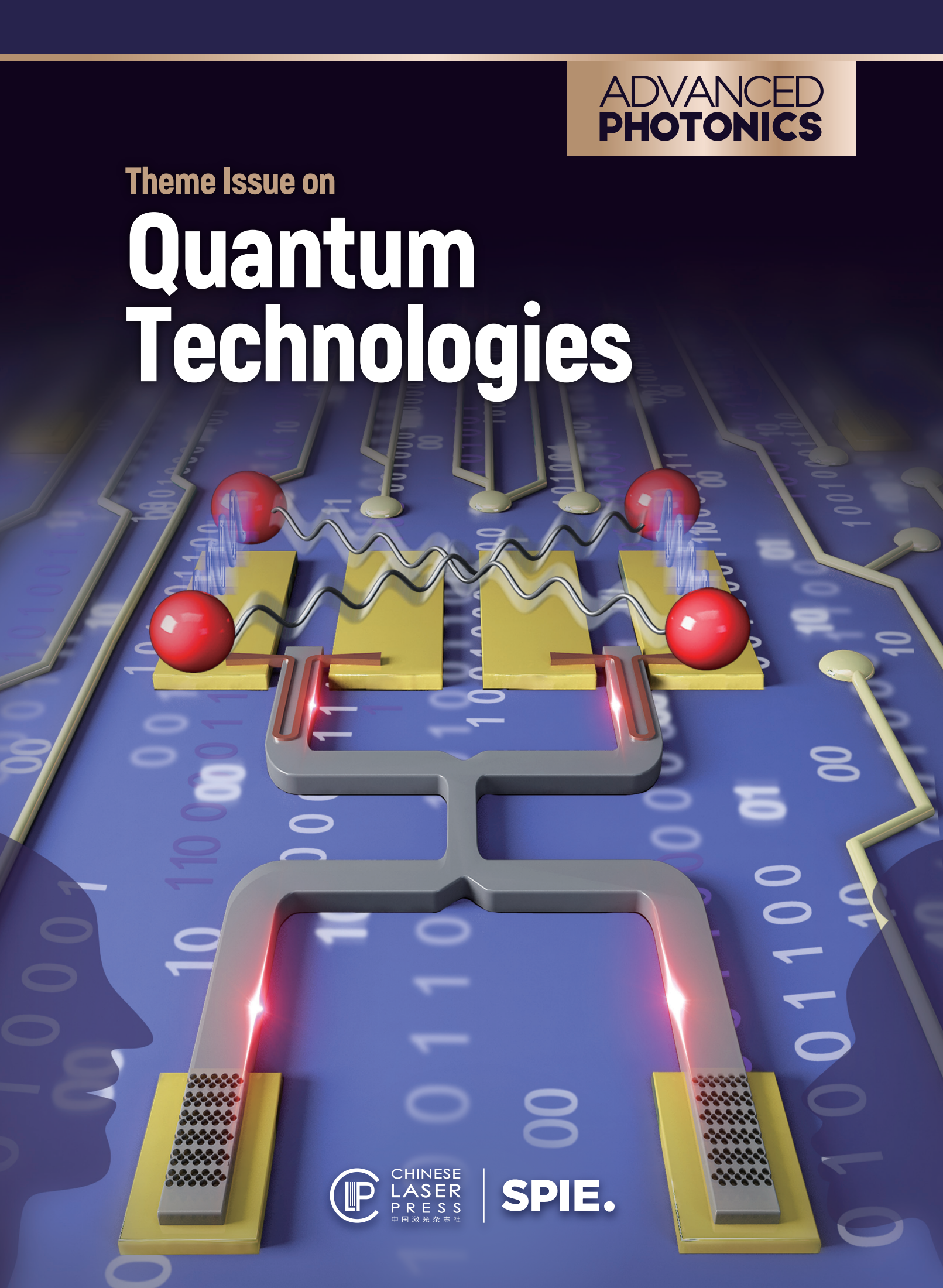

CHINESE LASER PRESS 中国激光杂志社 | SPIE.

GUEST EDITORS

Theme Issue **Quantum Technologies**

Mario Agio

University of Siegen, Laboratory of Nano-Optics

Siegen, Germany

National Research Council, National Inst. of Optics (CNR-INO)

Florence, Italy

Chao-Yang Lu

University of Science and Technology of China (USTC)

Hefei National Laboratory for Physical Sciences at the Microscale

Hefei, China

CONTENTS

ADVANCED PHOTONICS
Quantum Technologies

Photonics Advances Quantum Science and Technologies

Mario Agio
University of Siegen, Laboratory of Nano-Optics
Siegen, Germany
National Research Council, National Inst. of Optics (CNR-INO)
Florence, Italy

Chao-Yang Lu
University of Science and Technology of China (USTC)
Hefei National Laboratory for Physical Sciences at the Microscale
Hefei, China

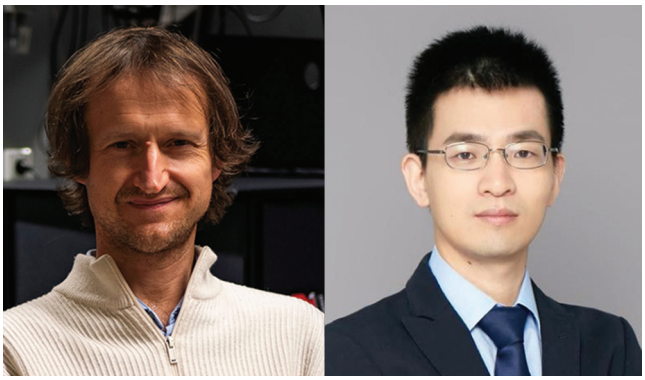

Mario Agio (Univ. of Siegen & CNR-INO; photo credit, S. Nimmrichter) (left); Chao-Yang Lu (USTC) (right).

Quantum science and technology is currently one of the most exciting frontiers in research and innovation. Tremendous effort is being devoted to pushing fundamental science into technology, with support from large, coordinated programs that involve academia, research centers, and industry worldwide. Throughout more than half a century of research, driven by curiosities in fundamental quantum physics, experiments in quantum optics, together with atomic, molecular, and optical physics, have laid the foundation for the development of a second quantum revolution, where fundamental concepts like quantum superposition, entanglement, and indistinguishability are now routinely exploited to realize quantum computing components, secure communications, and quantum-enhanced sensors with unprecedented performances. However, to become practically useful technologies, these ambitious goals still require a great deal of basic research effort, which must be combined with engineering and other disciplines to succeed. This exciting and intriguing perspective can be clearly witnessed in the recent interview of Prof. Xiaosong Ma with Sir Peter Knight in this issue of *Advanced Photonics*.

To spotlight advances in quantum science and technologies, we have invited review articles and original research contributions on this topic, gathered here in a collection. The collection is not intended to be a comprehensive account of photonic advances in quantum, but rather aims at emphasizing the important role of photonics in enabling the development of quantum technologies. We present two review articles and five original contributions from authoritative scientists in the field. S. Castelletto and A. Boretti review the emerging use of color centers in wide-band gap materials for sub-diffraction imaging, pointing out the widening of activities based on solid-state quantum emitters, originally addressed in solid-state quantum optics. Wang et al. discuss the impressive advancements on the implementation of quantum entanglement on a chip, based on progress in different integrated photonics platforms. The original research papers demonstrate how advanced photonics, such as the use of metasurfaces, integrated optics, and quantum dots, represents a unique resource for quantum technologies. They also point out that there is still much room, and need, for improvement in quantum-optical techniques and protocols.

We hope that readers, both established and early career researchers, will find this collection inspiring and, years later, will remember the onset of quantum technologies like Sir Peter Knight did for the onset of quantum optics: "I found it really fascinating!"

For convenience, the collection of articles is listed here:

"From fundamental quantum optics to quantum information technology: the personal journey of Sir Peter Knight" by Xiaosong Ma
DOI: https://doi.org/10.1117/1.AP.3.6.060501

"Color centers in wide-bandgap semiconductors for subdiffraction imaging: a review" by Stefania Castelletto and Alberto Boretti
DOI: https://doi.org/10.1117/1.AP.3.5.054001

"Quantum entanglement on photonic chips: a review" by Xiaojiong Chen, Zhaorong Fu, Qihuang Gong, and Jianwei Wang
DOI: https://doi.org/10.1117/1.AP.3.6.064002

"Heterogeneously integrated, superconducting silicon-photonic platform for measurement-device-independent quantum key distribution" by Xiaodong Zheng, Peiyu Zhang, Renyou Ge, Liangliang Lu, Guanglong He, Qi Chen, Fangchao Qu, Labao Zhang, Xinlun Cai, Yanqing Lu, Shining Zhu, Peiheng Wu, and Xiao-Song Ma
DOI: https://doi.org/10.1117/1.AP.3.5.055002

"Direct characterization of coherence of quantum detectors by sequential measurements" by Liang Xu, Huichao Xu, Jie Xie, Hui Li, Lin Zhou, Feixiang Xu, and Lijian Zhang
DOI: https://doi.org/10.1117/1.AP.3.6.066001

"Enhanced generation of non-degenerate photon-pairs in nonlinear metasurfaces" by Matthew Parry, Andrea Mazzanti, Alexander Poddubny, G. D. Valle, Dragomir Neshev, and Andrey A. Sukhorukov
DOI: https://doi.org/10.1117/1.AP.3.5.055001

"Entanglement-based quantum key distribution with a blinking-free quantum dot operated at a temperature up to 20K" by Christian

Schimpf, Santanu Manna, Saimon F. Covre da Silva, Maximilian Aignera, and Armando Rastelli
DOI: https://doi.org/10.1117/1.AP.3.6.065001

"Dynamical learning of a photonics quantum state-engineering process" by Alessia Suprano, Danilo Zia, Emanuele Polino, Tiara Giordani, Luca Innocenti, Alessandro Ferraro, Mauro Paternostro, Nicolò Spagnolo, and Fabio Scarrino
DOI: https://doi.org/10.1117/1.AP.3.6.066002

Mario Agio studied physics at the University of Pavia and Iowa State University with Prof. Lucio Claudio Andreani and Prof. Costas M. Soukoulis, respectively. He graduated in 2003 with a thesis on the fundamentals and applications of semiconductor-based photonic crystals. In 2004 he joined the Nano-Optics Group of Prof. Vahid Sandoghdar at ETH Zurich, where his research interests have broadened to single-molecule spectroscopy, near-field optics, and quantum optics. He was awarded the Italian Physical Society prize for graduate students (2002) and the Latsis Prize of ETH Zurich (2010) for his accomplishments in nano-optics. In 2011 he received the habilitation in physical chemistry from ETH Zurich. From 2012 to 2015 he was with the National Institute of Optics (CNR-INO) and the European Laboratory for Nonlinear Spectroscopy (LENS) in Florence. Since April 2015 he is responsible for the Laboratory of Nano-Optics at the University of Siegen, Germany, and since April 2021 he also holds a part-time appointment with CNR-INO.

Chao-Yang Lu obtained his PhD in physics from the University of Cambridge in 2011. He is currently a professor of physics at USTC. His research interests include quantum computation, quantum photonics, multiparticle entanglement, quantum teleportation, superconducting circuits, and atomic arrays. His work on quantum teleportation was selected by *Physics World* as "Breakthrough of the Year 2015." He has been recognized as one of *Nature*'s top ten "science stars of China" (2016), elected an OSA fellow (2017), and awarded numerous prizes, including the Fresnel Prize from the European Physical Society (2017), AAAS Newcomb Cleveland Prize (2018), Huangkun Prize from Chinese Physical Society (2019), Nishina Asian Award (2019), Xplorer Prize (2019), IUPAP-ICO Young Scientist Prize in Optics (2019), OSA Adolph Lomb Medal (2020), and Rolf Landauer and Charles H. Bennett Award in Quantum Computing (2021).

From fundamental quantum optics to quantum information technology: the personal journey of Sir Peter Knight

Xiaosong Ma
Nanjing University, School of Physics, Nanjing, China

Professor Sir Peter Knight, Imperial College London, UK

Xiaosong Ma: What inspired you to choose quantum optics as your major when you were a student, and can you share your experience or research journey in this field?

Peter Knight: Quantum optics, as a discipline, was more or less formed during the time I've been active in the area. I started thinking about things that we would now call quantum optics in the middle of the 1960s when I was a student. As a subject, it was really hardly developed at that point, but looking in particular at the way that the quantum nature of light would manifest itself in regular laser type experiments was then beginning to emerge. The field initially was called "quantum electronics" at that point, and "quantum optics" was a term used by very few people who started to worry about what the quantum nature of light would do.

I started in this area as an undergraduate. Like many students, to demonstrate that you can do something original of your own, I had to do a project. The project I chose was to work on optical pumping: making a cesium cell and looking really carefully at ways in which you could monitor coherent transients in optical pumping. In particular, I was measuring the way that Rabi oscillations could be monitored and looking at decoherence—which sounds like the things we worry about now, but this of course was in the radio frequency regime. This was experimental activity that was done with really simple experiments and simple apparatus. Of course, this is before tunable lasers. This experiment was all done with thermal light sources.

Firstly, I found the field really fascinating. And secondly, I was probably deluded in thinking that I could be an experimentalist, because the apparatus was really simple. So, when I started my PhD, my project was to do a kind of mix of theory and experiment, and it very quickly emerged that I was totally incompetent, really useless as an experimentalist. And I think the people in the lab were really delighted when I said, "I think it would be best if I turned pretty much to theory." So my PhD was in theory. But I've always maintained a really close engagement with experimentalists around me. Rather than being a theorist only in a theoretical environment, I have always enjoyed working with colleagues who were doing experiments so we could feed off each other. So that journey was a kind of accident, but it was fascinating and it's something that I've done ever since, so in all of my roles and positions, I've always had people I could talk with who were doing wonderful experiments. I guess that's kind of unusual in many places in the UK, where theoreticians and experimentalists are often in separate departments.

I did my PhD in that area, and then I went off to the United States as a postdoc, working with Joseph Eberly in the United States. And again, you know, a really powerful theoretician but always working with experimentalists. I had a wonderful three years in Eberly's group as a postdoc, working with really great people and really understanding, for the first time, how we could put together a group, how to plan a long-term career.

I came back to the UK in 1974. Around that time, the number of people interested in quantum optics theory in the UK with proper academic jobs was probably about four or five people, in the whole country. It was an extreme minority interest. But it was something that was becoming really exciting. Coming in at the very beginning of a subject area was always a wonderful experience. When I came back to the UK, one of the leaders in the field was Rodney Loudon at the University of Essex. Of those three or four people other than me working in quantum optics, he was someone who was really influential in my career. And again, Rodney had worked very closely with experimentalists.

I had various fellowships, and that gave me my chance to have my first graduate students of my own. I basically co-supervised graduate students in the US. In particular, some of Eberly's students worked primarily with me. Peter Milonni, for example, worked primarily with me. That already gave me the experience of working with really talented people to hit tough problems. Working in isolation, on your own, you could do something; but working with a group of like-minded people, you could do so much more.

In 1979 I moved to Imperial College, and I've basically been at Imperial College ever since. My group expanded, became almost a subdepartment of the department, always with many experimental colleagues involved. And my experience of working in the US and then coming back to the UK really demonstrated to me that this kind of activity was an international endeavor. I really benefited from collaborating with people from around the world, so my group became extremely

international during its most productive time. I do believe that's something that really is a lesson for everybody: working with the best around the world, you can do so much.

Xiaosong Ma: That's fantastic. You mentioned that it's good to be in the beginning of a subject, such as quantum optics in 1970s. To follow up on that, what do you think about, for example, quantum information, which is also an emerging technology nowadays. Which phase do you think we are in now for this technology?

Peter Knight: That's a really good question. Quantum information science was really born out of quantum optics, where there was a lot of basic research done over a very long period. Quantum computing, quantum cryptography, and so on, all came out of really basic research. The implementation to make these things practical has taken quite a while. I think we are pretty close to understanding a lot of the physical phenomena. While rolling this out as technology is a real challenge, we do understand many things. In some areas, we're making tremendous progress, yet underneath it there are still some puzzles that need to be worked out.

One of the questions you were going to ask me and I'm going to jump ahead to it was, what would you do if you were starting out as a student now? There's a tremendous amount of interest all around the world in quantum computing. People are making basic prototypes that are working wonderfully well, and we saw this huge advance in China recently using a superconducting chip, which could demonstrate the scaling as you increase the number of qubits. There was also the squeezed state boson sampling done in China as well. They already begin to demonstrate the idea that you can get a quantum advantage.

Now, maybe I'm alone in worrying about this, but I don't think we really understand the origin of the quantum advantage. Why do we get a speed up? Where's it coming from? We know that there's quantum entanglement, we know there's coherence, we know that there's quite a lot of worry about nonlocality. But, the engine of quantum computing is poorly understood. What is it that gives us the advantage? So, if I were starting out all over again, I would say that's one of the really big problems to address: we know that it's beginning to work, but *why* does it work? And by the way, I very rarely say that sentence to politicians who are funding us.

Xiaosong Ma: We will make sure this will not appear in the interview transcript.

Peter Knight: No, you should keep it in. Because, we have an unknown power. We know it's got power and we know it's going to give us tremendous advantage in information technology, but the origins of the advantage are still to be explored. Now, coming back to the beginning of your question earlier, you talked about starting out in the field. If you have a really established subject and you are a young scientist, it's quite hard to make your mark in the subject, because there's so much already done. This is a feeling often with young students in established fields, that they can only do a little bit of incremental work. But in a new subject, you can be a game changer—you can provide completely new ways of looking at things, which are revolutionary. Now I'm going to give you some examples of people that I worked with in the past. One of my most famous former students was Artur Ekert. He came up with entanglement-based quantum cryptography in the final few months of his PhD. As it happens, we'd been interested in quantum correlations for a long time. He had done a great deal of work on Bell inequalities, so it was a natural thing for him to investigate towards the end of his PhD. So, there you have an example: quite a new researcher in the field can transform the subject. Another example of someone who was not my student, but someone I know quite well is Andrew Steane, in Oxford. He was the co-inventor of quantum error correction as an early career researcher. You can see how young people in an emerging field could be transformative. That's why, in quantum information science, we're getting some of the brightest young people in the world wanting to work on it. It's fascinating and there're huge challenges, but they know they can make a difference personally.

Xiaosong Ma: That's amazing. You've just mentioned Artur Ekert, his research on Bell's inequality, correlations, etc., primarily on the foundations of quantum physics. That's very fundamental research, I would say. Do you envision that this fundamental research could be transformed into application, such as entanglement-based QKD at the very beginning?

Peter Knight: I think some of the advances we're seeing still require quite a lot of engineering investigation. We can see that we can build entanglement-based quantum communications. After all, we can now do long-distance quantum communication along optical fibers and in free space, and even via satellite as the Micius experiment demonstrated. So there is tremendous potential for it. But you know the moving around of information security is only a part of the issue. You've got to be able to work on the entire security of the system, how is it implemented. So we need security proofs of the real apparatus, not the idealized apparatus. And that's still work in progress, because you really wouldn't want to reengineer the entire communications system and find that through the way that the engineering is implemented it becomes faulty.

I think a lot of work is underway on implementation protocols and security of these things. But it is wonderful to see that something as strange as nonlocal Bell correlation is generating a new industry. I did meet John Bell a number of times and I think he would have been astonished by all this. Bell was actually quite a practical person. For most of his career, he was an accelerator scientist, working on designs of accelerators—that was what he was paid for. The fundamental work was a kind of sideline hobby of his. I don't think he would have ever thought that his own work would have been the foundation of a whole new industry, which it is.

We knew that quantum could be transformative. Not just the entanglement-based side of things, but coherence. After all, atomic coherence is a driver of one of the main features of modern technology: it's what under underlies GPS, atomic clocks in satellites, and so on. So, our navigation and timing systems all around the world are wholly dependent on the preservation of coherence amongst atomic spins. People don't realize that. When people say quantum technology is a new thing yet to prove itself, it's always worth reminding them that we've come a long way: GPS contributes enormously to the world economy, and it depends on quantum superpositions.

Xiaosong Ma: We have talked about superposition, coherence, and also entanglement. Those are main features for quantum systems, and they are applied to this new quantum revolution. Do you think there are still undiscovered quantum features that could be potentially useful?

Peter Knight: In terms of usefulness, I think we're beginning to understand where the limitations are, and what the advantages are. In quantum sensors that can detect, for example, electromagnetic fields, or gravitational irregularities, we're already seeing that. And again, it's worth remembering that these things move very fast. For example, I mentioned that when I first started, I was worrying about optical pumping, way back in 1967. It's now possible to build really small optical pumping cells that can detect the electromagnetic signals in the brain. Of course, all of this is used a lot in brain scanners, huge superconducting coils, and so on. But quantum technology is working at ways in which we can now build a really compact sensor that's like a cycle helmet and will monitor brain activity. One of the developments in

that area is that some of our colleagues in quantum technology in Nottingham have built a brain sensor of that kind that's already being used by surgeons looking at epilepsy, so it's being used in hospitals. So, this is a quantum sensor of brain activity that's being used to direct a surgeon's knife. That's amazing, really amazing.

If you work in a built environment, something that's been there for a long time: one of the dangers of any new construction development is what's under your feet—where are the tunnels, where are the voids. And in big cities where there's a lot of redevelopment going on, it's really difficult to work out what's under your feet. We waste an awful lot of money in civil engineering on doing that. A quantum interferometer that can measure gravitational differences can already tell you what's under your feet. There are a number of people around the world who are building basically cold-atom interferometers that measure the ground infrastructure. Firstly, it's fascinating—you can map the underworld—but also there's the practical advantage of not wasting billions digging up the road trying to work out where the pipe work is. These are interesting things because the way the interferometer works is looking at really fundamental aspects of quantum physics. And we're applying it to work out where the drain is—a wonderful combination of the practical and the unknown!

Now we are still thinking about some of the more fundamental things. I mentioned that we don't really know what the power quantum computation derives from, but equally, most of what we're doing in this subject is built on an assumption that our current ideas of quantum mechanics will remain true—in other words, superpositions and linearity. Well, is it true? Or are we going to have evidence from really sensitive experiments that would demonstrate that there's something more out there than what we see already from linear quantum mechanical superpositions? People are beginning to think about that, because we know that gravity changes things. So, there are some really fundamental things to do in the area. And again, around the world, people are starting to look at ways in which this extraordinary sensitivity of quantum technology could be used to detect whether we really do understand all the fundamental laws of nature. Obviously, we promise our taxpayers we're going to be useful. But equally, the sensitivity of the experimentation can enable us to explore new things in fundamental science.

Xiaosong Ma: That's really intriguing. To use quantum mechanics to explore gravitational effects would be very interesting for the fundamental research. I guess you meant that can also be a potential new area for researchers, to use sensitive quantum sensors to explore gravitational effects.

Peter Knight: People are starting to look at whether quantum technology could be a useful vehicle to detect dark matter. Dark matter is one of the things that is a huge failure of modern physics. Most of the universe is made up of a stuff that we don't know about: dark matter, dark energy. We don't know what it is! What can we do in terms of sensitive measurements that will tell us a bit about this strange majority component of the universe? Quantum technology is already beginning to offer clues about how we would do this. The interferometer that could detect the gravitational changes in your built environment—if you can make that work at scale, you can start to detect dark matter, perhaps. That's something already occupying some really clever people around the world.

Xiaosong Ma: To follow up, you've mentioned that we already harness quantum features by using GPS, and also we are starting to use sensors for biomedical applications, as well as metrology tasks. How do you foresee this technology will further change our daily life?

Peter Knight: I've given a lot of thought to this question about how it influences, for example, our neighbors, the people who pay our salaries. One of the obvious things to say is that we can be assured that the internet is resilient and robust through encryption techniques that wholly rest on something being difficult—not impossible, but difficult. Obviously, factoring is what I'm thinking about. But security based on difficulty is only secure if it remains difficult. A classical computer would find tasks like factoring extremely difficult, but a quantum computer can do it so much more easily. That's part of the threat to business. What we must do is we must assume that in about 10 years, pretty much around 10 years everybody agrees, it's quite likely that we will have a large-scale quantum computer somewhere. As soon as you have a large-scale quantum computer, all of our encryption techniques that we use—RSA, the whole basis of HTTPS—become vulnerable. And that means that you no longer have a trusted internet ecosystem. The big change that will affect everybody is that we'll have to roll out quantum-safe encryption in order to do transactions, to pay our bills, to do our banking, and so on. That will affect everybody. So, quantum-safe approaches—they might be classical, a new source of algorithms, they could depend on quantum key distribution or whatever—they will affect everybody. If we're paying for stuff on the internet, we rely on the little padlock that appears on the website we're looking at to say yes, it's encrypted and secure. In ten years, we won't be able to assume that it's secure, because a quantum computer will make it insecure. That's where it will change everybody's life, and there're probably lots of other things.

Some of the applications for quantum technology I believe are yet to be discovered, because it's a new field and things happen that will surprise us. I don't know if you know how Bell Labs justified the investment in transistors? All amplifiers before transistors were thermionic valve amplifiers—big, power hungry, hot, full of extraordinary voltages. When Shockley and others started to think about a semiconductor that could make a transistor, they got it accepted by the Bell Labs organization. They got them to agree to invest with one application in mind, the killer app that enabled them to invest: to build a hearing aid for the deaf. Because all they wanted was a compact amplifier, and that's what you need for a hearing aid. Stanley Williams at HP Labs in the United States always says that all we need in quantum technology is the quantum hearing aid. In other words, some small development which will enable people to confidently invest and build something. Because once you've done that, millions of applications emerge from everywhere. When they built a transistor, they had no idea of the way that they were going to change the world—except for the hearing aid. So, all we need, to quote Stan Williams, is a quantum hearing aid. It will work, and then people will say, hey I can use this in all these other applications as well. Surprises happen in new emerging technology, and I haven't even thought of the big things that are bound to happen. Be prepared for surprises.

I think it's really interesting where we see this investment race going on around the world. It seems as if governments have a kind of virility test where they think, oh we've got to invest because everybody else is investing. This is called fear of missing out. I think that we have to be all really careful not to hype up quantum tech, to over promise, to say it's going to be revolutionary in every aspect. We've really tried not to hype it up, but I think we are already seeing things that are transformative, so although we try to avoid hype, we are seeing some wonderful things.

Xiaosong Ma: Exactly. Speaking of investments in the quantum technology industry, as far as I know, you are one of the leaders in setting up the quantum technology program in the UK. Can you briefly tell us about the history? Was it difficult at the beginning? Where do you see this project in the next five years?

Peter Knight: We've had a history of quality scientific research in quantum optics and atomic physics and so on in the UK which was verified by external review and so on. But we could see, by around

2010 roughly, that some of the challenges of actually understanding how to manipulate and control individual quantum systems—basically our focus then—could then be applied in terms of things that had engineering importance. Around that period, we started to think about how to move quantum science to quantum technology. It was an exciting period because in the UK we had real strengths in the area. But what we realized is that if we could bring the partners—industry, government departments, universities—together, we could do so much more if we coordinated. We had this vision of this national program where we could bring everybody together to play a part. We started to talk about the idea, and we managed to get a fair bit of support from people about how this as an experiment could succeed. At that particular time in the UK we had a science minister who I think really understood where clever people could make a difference. Although we talked about it for quite a while, suddenly it got momentum. I remember in 2012–2013, we had to write short briefing notes for politicians about what quantum physics could do. And by short I really mean short, so our Finance Minister wanted a 4-page summary; and then the Prime Minister said, could I have a 1-page summary? Then it all moved very, very fast. At the end of 2013, we got a new commitment of £270 million—a lot of money in those days—of completely new money, to build this national program. To that we then added other things, so it grew in that first period to about half a billion. We built these hubs, we worked with industry, and so on. And then I helped to write the vision piece for another five years of funding, so we we've got about a billion now to do this. And that meant that we probably started in a coordinated program quite a long time before everybody else. Other countries always had very strong quantum science programs, but the idea that you could coordinate it was relatively new. It was tremendous fun doing this, bringing in people with completely different attitudes—engineers, computer scientists, physicists, the government people who worry about the impact on policy, and so on. And it was interesting. Others began to note the way that we approach this, looking at quantum sensors, quantum communication, quantum imaging, and then quantum computing, and those four pillars have become the pillars of other people's programs around the world as well. So the European Union flagship mirrors this and so do the United States NQI programs as well, so I think we got it right, basically, but we got there a bit earlier.

Xiaosong Ma: My next question would be about your mentoring. I've noticed that many of today's leading physicists in the quantum optics field came from your group. Can you share with us your secrets, or your recipes for mentoring and advancing young scientists and students?
Peter Knight: I don't think there's a secret. I think it comes down to a number of human characteristics that I think are important. Firstly, respect for others—understanding that you may not have the secret of everything, therefore you should respect what other people are telling you. Respect, sympathy, and the ability to see that others deserve the chance that you had. I think in some areas of science, you see the big chief doing all the great stuff and getting all the credit, and a lot of people in subsidiary positions. That's one model of doing that kind of science. But in an emerging field, it may not be the best way to do it, because things come out in a surprising way. I really benefited from quite an early stage in my career from demonstrating independence. When I came back to start my own group, I think I was 27. Giving people an early opportunity to be independent is part of it, so when you've got really bright students don't regard them as a personal possession. They are not personal possessions, they are people who are changing the subject. I spent most of my life as a university teacher, and the whole point about a teacher is to foster new knowledge and to encourage the next generation to flourish—that's our job. So, getting the very best people in, giving them a chance to really excel, and also finding mechanisms by which they get early independence themselves. That's been the trick.

I'll run through some of my students, for example, and of course it will be hugely embarrassing for them to be so named, but I'm going to do it. I mentioned Artur Ekert and Artur got a fellowship immediately after his PhD and that gave him independence. Another really smart student is Stephen Barnett. Stephen Barnett was my student and again very quickly got fellowships. He's now a Royal Society research professor in Scotland. Let me continue with the students. Barry Sanders in Calgary was another student. Giving them a chance to demonstrate their individual strengths and powers is really important, because two things happen: they flourish and the field flourishes, which impacts us as well. So, I think mentoring is really important. I wish more people would play more attention to mentoring, because that's the way the field really effectively grows. Young people are not slaves. Young people change the world, and you mustn't put obstacles in front of them. Let me think of some of the other students like Vlatko Vedral, for example, now a professor in Oxford…many of them have gone on to do a really great job…Myungshik Kim, who is one of my successors at Imperial. And I can keep going on about these things. The trick on this one is respect, respect for what they can contribute, rather than their ability to follow orders from you. Because then the whole field benefits. Not only that, you'll still have good people wanting to work with you. Try not to be a tyrant, because then people get scared off.

Xiaosong Ma: Respect and giving students early independence are very important. My personal experience also benefits from that. I think this advice will be extremely helpful for young research group leaders, and all the others.
Peter Knight: You have a responsibility, therefore, when you're generating new sources of resource and funding, to make sure that funding can be used by the next generation as well, to create fellowship schemes and so on. Because that will enable this to happen. As well as pushing for the big programs on funding particular investigations, making sure that you've put resources in, in terms of skills, career development, and so on. And it works!

Xiaosong Ma: You have been in many important positions, such as deputy rector at the Imperial College, and president of the IOP, and president of the OSA, etc. I can imagine you must have a very busy schedule. How do you manage to keep research, administration, and life in balance?
Peter Knight: This is a really good question, and there is only one honest answer: you don't. You don't keep a balance. If you look at my career, when I was most productive in terms of research was when I had the least amount of external administrative responsibilities. My own personal scientific productivity really dipped when I started to take on the university leadership activity, because you can't really sensibly run a really high-level research program and run a university. If you look at my publication rate, you can see the Google Scholar graphs dip immediately after I started to do this. So, the honest answer is, you can just about keep research active as you manage these things and the key to a lot of this is finding the optimum balance, given your other responsibilities. When I was president of the OSA, that was a time when I didn't really have an enormous range of administrative responsibilities, so that was relatively straightforward, although it did mean getting on airplanes to the United States quite a lot.

Technically, I retired 10 years ago. When you work in my field, what does retirement mean? It means that they stop paying you, but you don't stop working. I live on my pension. That really means that I can strike out and try some new things that are high risk. Taking on a lot of what we're doing with the UK national program and so on

is because I'm a free agent now. I've had a really great career, so I have the time to do it. I think that's another part of being convincing: when you're trying to persuade a government to put together a billion pounds to fund a program, if the person advocating it is not advocating it for personal gain but to propel the field, you get listened to. Whereas if I were still running an enormous research group, they would say, oh, Peter's just trying to get stuff for himself. You can't have a compelling vision that's trusted in that role. So, to be honest, retirement was a really good thing for me, because it meant that I could really propel these things along. But coming back to the basics of your question, you can't run a really world-class, high-level research activity and take on a lot of research responsibilities at the same time without terrible things happening. Productivity goes up and down, and so on, so you have to work out what is most beneficial. In the 1990s onwards, research time for me was easy and so on, but once you have a voice, you can use that voice to enable others to do things as well.

Xiaosong Ma: I believe the quantum researchers in UK should thank you for your advocacy to the government to provide stable funding over long periods of time. Moreover, such a national program also inspires other countries to invest in quantum technology. Therefore, I think all of us should be very grateful for your efforts.

Peter Knight: Thank you for saying that. Of course, it's the energy, enthusiasm, and interest in the entire community that make it worthwhile. When you see the things that are going around the world, it really is exciting in so many ways. I remember when I first arrived at the University of Rochester as a postdoc, I would go to lunch with the people in the offices around me. The people in the offices around me were Emil Wolf, Leonard Mandel, Joseph Eberly, and Carlos Stroud. If we had ever thought, any of us, that there would be a quantum technology industry, we'd have been very surprised. What can we learn from that? It takes time, basically, and persistence, to do this. But being a young researcher, being exposed to people like Mandel, Wolf, Eberly, and Stroud was just hugely important for me, because it demonstrated how the intellectual life of science can be so exciting that you want to be really a part of it. It consumes your life.

Xiaosong Ma: Yes, it's very exciting. I think you just mentioned the 1970s, around 1974, as a golden age for quantum optics in Rochester. You have so many colleagues whom nowadays we, as young researchers, can only access in the textbooks—but you have lunch with them every day…That's very exciting.

Peter Knight: I know. One of the great engines in photonics, for example, in quantum photonics, is called the Hong–Ou–Mandel dip: the amplitude for two photons interfere in an interesting way. And I can remember the first I heard about that was when Leonard Mandel said, "you know this works, if you put two identical photons into a beam splitter, they will come up that way or that way, but not that way and that way." And the rest of us that the lunch table said, "really?" When you hear things that you know are going to be just amazing, it's wonderful. That's why you should do science—because it's part of the cultural experience of everybody: to get amazed by new developments. It's exciting.

Let me finish with one of my protégés, I can only claim him partly as a protégé because he wasn't my student, although he was a postdoc with me for a while, and then later became a faculty member and a professor. This is Terry Rudolph. Terry has done some of the most advanced thinking about fundamental science. He's one of the founders of a quantum computing company called PsiQuantum. PsiQuantum recently did a major series fundraising and was valued by NASDAQ just two weeks ago at $3.15 billion dollars. Who would have thought that you could do that? He's still writing wonderful fundamental scientific papers, but he as the theoretician and others as well—Jeremy O'Brien leading the experimental side with Pete Shadbolt and others—have got this way of building a quantum engine which is now valued at $3 billion dollars. Terry Rudolph, when he started on this thing, looking at fundamental physics, and then built what is basically one of the largest quantum computing companies in the world. That's an astonishing journey. But it's built on the foundations of decades of hard work from people around the world. I think this ability to work collectively together and get the very best around the world to work with us, is really intriguing. Terry is British, but of course he was brought up in Australia and Malawi, and Jeremy O'Brien is Australian. We look at this world talent that we've got, and it's been transformative. In China, you have Jianwei Pan, who is incredible in realizing large-scale quantum network and achieving quantum computation advantages. We've got leaders around the world who are changing us.

Xiaosong Ma is a professor in the School of Physics at Nanjing University. He obtained his BS degree from Nanjing University in 2003, his MS degree from Leiden University in 2005, and his PhD from University of Vienna in 2010. A subsequent postdoctoral research post in experimental quantum physics at University of Vienna, was followed by a postdoc in integrated quantum photonics at Yale University.

Peter Knight is a senior research investigator in the Physics Department at Imperial College, chair of the UK National Quantum Technology Programme Strategic Advisory Board, and chair of the National Physical Laboratory Quantum Metrology Institute. Prior to retiring in 2010 as a deputy rector (research), he was responsible for the Imperial research strategy. A former president of the Institute of Physics (2011–2013), he was a member of the Imperial College Management Board and Council, and a professor of quantum optics. He was knighted in the Queen's Birthday Honours List in 2005 for his work in optical physics. He was until 2008 principal of the Faculty of Natural Sciences at Imperial College London. He was head of the Physics Department, Imperial College London, from 2001 to 2005. A past president of the Optical Society of America, he was a director of the OSA Foundation. He is an editor of *Contemporary Physics* and serves on a number of other editorial boards. He is a Thomson-ISI "Highly Cited Author." After receiving his doctorate at Sussex University, he was a research associate in the Department of Physics and Astronomy at the University of Rochester and the Stanford University Physics Department and SLAC. He joined Imperial College in 1979 first as a lecturer, becoming a professor in 1988.

Review Article

ADVANCED PHOTONICS

Color centers in wide-bandgap semiconductors for subdiffraction imaging: a review

Stefania Castelletto[a,*] and Alberto Boretti[b]
[a]RMIT University, School of Engineering, Bundoora, Australia
[b]Prince Mohammad Bin Fahd University, Deanship of Research, Al Khobar, Saudi Arabia

Abstract. Solid-state atomic-sized color centers in wide-band-gap semiconductors, such as diamond, silicon carbide, and hexagonal boron nitride, are important platforms for quantum technologies, specifically for single-photon sources and quantum sensing. One of the emerging applications of these quantum emitters is subdiffraction imaging. This capability is provided by the specific photophysical properties of color centers, such as high dipole moments, photostability, and a variety of spectral ranges of the emitters with associated optical and microwave control of their quantum states. We review applications of color centers in traditional super-resolution microscopy and quantum imaging methods, and compare relative performance. The current state and perspectives of their applications in biomedical, chemistry, and material science imaging are outlined.

Keywords: color centers; quantum optics; single photon emitters; super-resolution imaging; transparent semiconductors.

Received May 21, 2021; revised manuscript received Jul. 13, 2021; accepted for publication Aug. 19, 2021; published online Sep. 13, 2021.

[DOI: 10.1117/1.AP.3.5.054001]

1 Introduction

The resolution of common fluorescence microscopes (wide-field or confocal microscopes) is limited by the diffraction of light, known as the Abbe limit. The attainable resolution is given by the full-width at half-maximum (FWHM) of the point spread function (PSF) of the beam at the focus of the objective. A high numerical aperture (NA = 1.4) objective with visible light ($\lambda = 532$ nm) can theoretically reach a resolution of $d \approx \lambda/(2\sqrt{2} \times \mathrm{NA}) \sim 134$ nm and $d \approx \lambda/(2 \times \mathrm{NA}) \sim 190$ nm for the confocal and wide field, respectively, whereas the experimental resolution is generally in the range of ~200 to 250 nm due to the sample optical properties and beam imperfections. Super-resolution fluorescence microscopy (SRM) permits us to beat the diffraction limit, and it obtains images with a higher resolution, from 100 nm to as low as 20 nm or, in some cases, even lower, with few nanometer localization in some cases. This is a resolution/localization possible only by electron scanning probe microscopes. SRM's impact in life science, chemical, and physical sciences has been recognized by the Nobel Prize for Chemistry in 2014,[1] and it has revolutionized many areas of cellular microscopy[2] and even virology.[3,4]

Current SRM methods have resolved many problems in imaging using high localization molecules, with the opportunity to reach a very high resolution in principle. In general, they can provide high spatial localization and resolution with, however, limited applicability in tracking real-time biological processes with the required speed. In addition, the application of the currently achieved ultimate resolution in some of the SRM methods to specific biological samples, with associated high localization and the required sensitivity, is a prerequisite that is not yet fully achieved.

The current outstanding limitations in a few SRM approaches are

- the size of the fluorescent probes and their fluorescent properties;
- the use of near-ultraviolet excitation which is responsible for DNA damage and higher imaging background, reducing applicability for extended imaging time and tracking;
- the photobleaching of the fluorescent tags, which limits the duration of observation;

*Address all correspondence to Stefania Castelletto, stefania.castelletto@rmit.edu.au

• the extended acquisition or scanning time needed to achieve the highest resolution, which limits the imaging speed and applicability for *in vivo* imaging and tracking;
• lack of achievement of in-depth imaging with the same high in-plane resolution.

Among these limitations, the type and size of the fluorescent tags are extremely important to directly access the subdiffraction biological components and features of interest, achieve the desired resolution in the cells' environment, follow internal biological mechanisms in cells, and track cellular processes at specific locations. The quest for ideal SRM tags is to have probes that introduce as few as possible artifacts in imaging and have limited interaction with the sample functionalities. They must possess photophysical properties fulfilling the requirements of the SRM principles. They should not photobleach. Furthermore, depending on the process that needs to be imaged, the fluorophores with distinct fluorescence properties are sought after first and foremost, for their brightness, fluorescence lifetime, photostability, emission wavelength, and, as in some cases, photoswitching capabilities. While these properties are essential for advancing the application of SRM to biological samples, they are also important for applications in imaging in material science, chemistry, and physics. Other emerging applications of SRM, where in particular color centers (CCs) in diamond have also been utilized, are optical data storage,[5,6] imaging of current flow at the nanoscale as an example in two-dimensional (2D) materials, such as graphene,[7] and using quantum magnetometry to study magnetic optical effects in solid state.[8] Many fluorescent nanoprobes are now available for SRM, and, more recently, solid-state probes based on nanoparticles (NPs) have been investigated for these applications[9] in virtue of their high brightness, high photostability, and unique optical-switching properties in addition to other physical and chemical functionalities. CCs in wide-bandgap semiconductors, in particular, have emerged as potential atomic size probes (which is an ultimate quest), due to their extreme photostability, lack of bleaching also in the presence of high laser power density, high dipole moment, generally long optical transition lifetime, and available long life metastable (MS) state. In addition, CCs can exist in various charge states, and photoswitching between them can be achieved using different laser excitation wavelengths. Finally, most of the CCs have a nonzero electron spin, which can be read out optically and can serve as a probe of the local magnetic and electric field, as well as of local strain. Fluorescence modulation of CCs can be achieved by nonspin preserving transitions into the MS state, inducing spin polarization of a degenerate ground state (GS). The manipulation of the spin properties using the additional microwave or radiofrequency excitations can also provide an extra-nonlinear optical response to be used in super-resolution approaches. The most notable material hosting CCs is diamond, with a large variety of emitters mostly studied in bulk diamond,[10,11] and, specifically, the most studied is the nitrogen-vacancy (NV) center.[12] Diamonds and nanodiamonds (NDs) are currently widely studied nanoprobes due to their biocompatibility and low phototoxicity in various medicine applications.[13] Diamond has been recently followed by silicon carbide (SiC)[14,15] with the carbon antisite vacancy pair (CAV),[16,17] divacancy (DV),[18,19] and interface defects.[20] SiC and its nanostructures have also been studied as biological nanosensors, nanocarriers, and biomedical applications.[21–23] Other wide-bandgap materials, such as 2D hexagonal boron nitride (hBN), which have driven the attention in photonics and single-photon (SP) emission,[24,25] have also shown applicability to conventional super-resolution methods[26] due to a variety of functionalization options and low cells toxicity,[27,28] albeit only a few studies are available today. We will briefly assess the current state of the art of these three materials' CCs for their performance in SRM. While the diamond NV center has been the first to be used for SRM for more than 10 years,[29] proving to be a robust system to push the limit of the present SRM methods accuracy, its applicability as fluorescent probes even in traditional SRM methods is still limited. This is due to the current limitation of CCs embedded in NPs, with relatively large size, which has currently limited application in traditional SRM.[9] However, some of the best resolutions achieved, biocompatibility and photostability for biological *in vitro* and living samples imaging, are associated as an example to NDs.[30] The only limitation is the lack of availability of highly performing CCs photophysical and spin properties in single-digit size NDs as their quantum dots (QDs) counterparts. Using NV centers as probes, the first traditional SRM methods have been demonstrated, such as stimulated emission depletion (STED) microscopy,[29] ground-state depletion (GSD) microscopy,[31] MS state depletion[32] microscopy, and stochastic optical reconstruction microscopy (STORM).[33] From the initial SRM demonstrated using NV in diamond, other variants of these methods were proposed and implemented,[34] and we can, after 10 years, observe a certain degree of advances in using specific photophysical properties of this CC in SRM. In addition, using the NV center in diamond, nontraditional SRM methods have been developed to achieve subdiffraction images based on their specific photophysical properties. Defect charge conversion upon different illumination energy [charge state depletion (CSD) microscopy[35]] and spin fluorescence modulation based on optical detected magnetic resonance (ODMR)[12] are examples of properties used to achieve super-resolved images of NV in diamond. This last approach based on the electron spin readout of NV, used as a sensor of other nearby electron and nuclear spins, in particular, is leading toward nano magnetic resonance imaging (MRI)[36] or nuclear magnetic resonance (NMR) spectroscopy,[37] showing at present few nuclear spins or single electron spin sensitivity (nano MRI or NMR). These methods are borrowed from MRI approaches and adjusted to operate using an atomic-scale quantum probe rather than a magnetic field coil. They are based on the implementation of electron spin-echo, Hanh-echo sequence,[38,39] or more complex dynamical spin decoupling sequences.[40,41] Here, the readout is based on the optical signal of NV centers. Recent focus on the use of NV in diamond as a magnetic sensor[42] designed for biological living systems has reached, even in DC magnetometry, the sensitivity of 100 $\mathrm{pT}/\sqrt{\mathrm{Hz}}$,[43] and, by using a lock-in-based technique to read out optically the NV spin , a sensitivity of 68 $\mathrm{nT}/\sqrt{\mathrm{Hz}}$ within the (sub)cellular scale has been achieved.[44] As such, the quantum properties of CCs can be used or combined with traditional SRM that does not rely on the quantum nature of the nanoprobes but on their nonlinear optical properties or on their nonstationary fluorescence, which makes them discernible from one to another. The combination of quantum magnetic imaging methods with super-resolution localization can lead to nanoscale magnetic sensing and imaging with subdiffraction localization. In this direction, using NV centers in diamond, a variant of traditional SRM, has been implemented using ODMR to address single or ensemble spin with super-resolved localization; namely

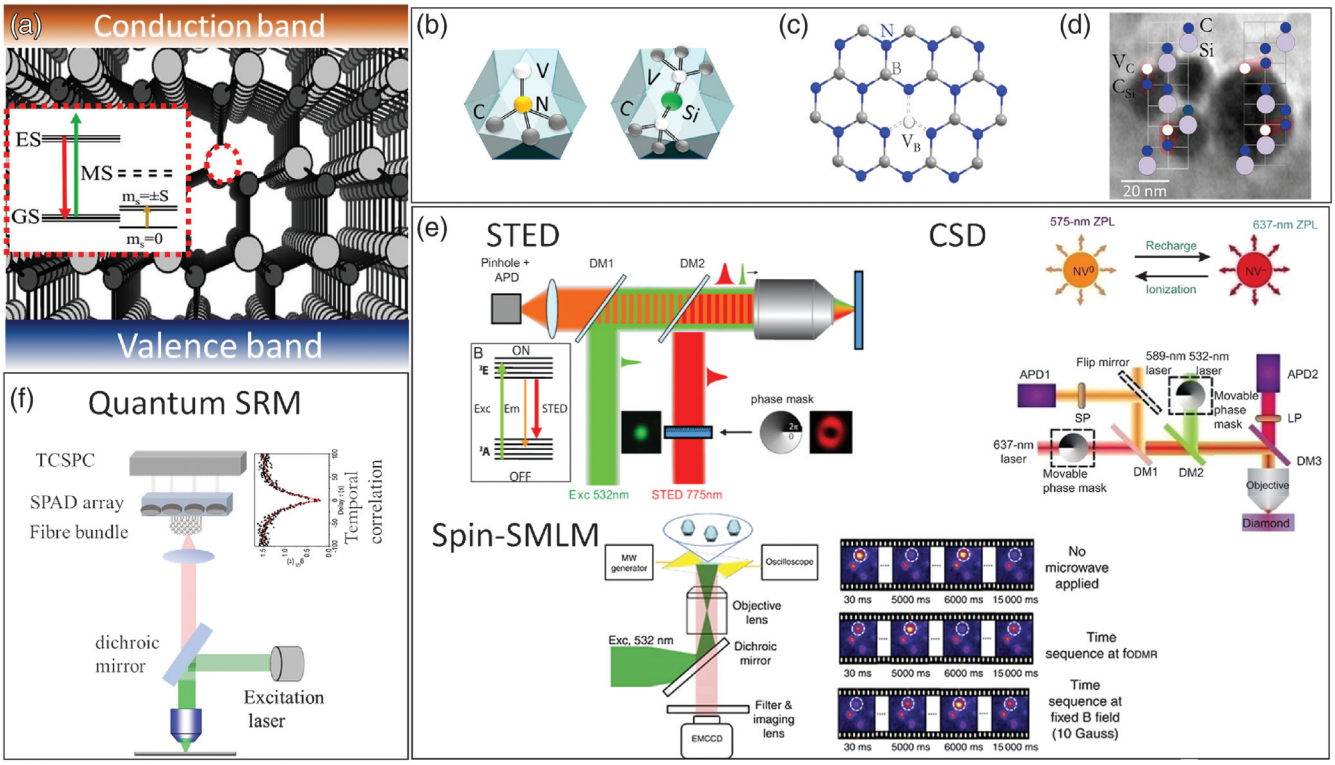

Fig. 1 CCs and traditional and quantum SRM. (a) Conceptual representation of a vacancy in a wide bandgap semiconductor, giving origin to a three or more levels system made of a ground state (GS) (with spin triplets, depending on the spin number), an excited state (ES), and a metastable state (MS) or intersystem crossing state. (b) The NV and the SiV in diamond are used for SRM methods. (c) 2D hBN showing the boron vacancy. (d) The CAV pairs that can be used for SRM due to their photoswitching properties.[59] (e) Traditional SRM methods schematics such as STED, based on depletion of ES via stimulated emission, and SMLM as fully nondeterministic methods, based on the photoswitching of the fluorophore. CSD microscopy originated from the charge conversion of NV from the negative to neutral state, using three laser probes in a more complex approach than STED. STED figure is reproduced from Ref. 60; with permission copyright (2010) John Wiley and Sons, Inc., CSD and Spin-SMLM figures are reproduced from Refs. 48 and 35, under Creative Commons Attribution-NonCommercial-NoDerivs (BY-NC-ND) 4.0 International license. A detailed description of the schematics is provided in the references. (f) Conceptual schematics of the quantum-enhanced SRM developed based on antibunching, giving rise to the mapping of localized single emitters from the spatial imaging of single emitters using a bundle of fibers and array of SPADs and time-correlated single-photon counting (TCSPC).[57]

STED-ODMR,[45] SPIN-RESOLFT,[46] and SPIN-STORM[47–49] have been extended to achieve spin localization using ODMR and other spin manipulation methods used in AC magnetometry, primarily spin-echo sequences.[50] Even some dynamical spin decoupling sequences are used in the nano-MRI to increase the sensitivity of dilute ensembles of nuclear spins or single electron spin. These methods have been developed in the NV quantum sensing approaches and led to relevant imaging capability, for example, sensing ferritin in single cells,[51] single electron spin,[52] and electron flow in graphene.[53] The combination of increased sensitivity from quantum sensing with nanometric localization and tracking is a very sought-after objective that could be achieved using the quantum properties of CCs. Alternatively, using the quantum optical properties of single CCs as SP sources, quantum imaging methods based on SP higher-order correlation have been developed to achieve subdiffraction imaging.[54,55] These quantum methods can also be used to enhance conventional SRM, such as quantum-enhanced STORM.[56,57] One of the most promising applications of NV centers in NDs is to achieve highly localized temperature sensing,[58] which could be combined with super-resolution methods. In addition to the most notable NV in diamond, other CCs in diamond, mainly silicon-vacancy (SiV), in SiC, and few layers of hBN have emerged as possible tools for SRM; alternatively, these CCs can be better studied using SRM. In Fig. 1, illustrations of examples of CCs used for traditional and quantum-based SRM with their conceptual operation are shown. In Table 1, we summarize the CCs properties in diamond, SiC, and hBN that have been tested or recognized as relevant for SRM applications, such as emission wavelength, quantum yield or quantum efficiency, excited state (ES) and MS or intersystem state lifetimes, known coexisting charge states, stimulated emission cross-section, optical spin coherence time, SP availability, and nanomaterial associated properties when available. Compared with other solid-state

Table 1 CCs in diamond, SiC, and hBN flakes with charge states, ZPL, and their optical and spin properties relevant for SRM and quantum enhanced SRM. Specifically, the negative charge state of NV and SiV in diamond, the NVN (H3) center in diamond, the positive CAV pair, the neutral DV in SiC, the negative boron vacancy V_B^- and the complex boron vacancy and carbon–nitrogen antisite $V_BC_N^-$. Properties such as quantum yield (η), fluorescence lifetime (τ_{fl}), intersystem crossing lifetime (τ_{ISC}), stimulated emission cross section (σ), and spin coherence time (T_2) are listed. NDs sized 25 to 100 g nm, SiC NPs of 3 to 50 nm. All of the below CCs have been isolated as single emitters except the V_B^-. Here, n.m. stands for not measured and n.a. for not available.

Color center	ZPL (nm)	η (%)	τ_{fl} (ns)	τ_{ISC} (ns)	$\sigma \times 10^{-17}$ (cm^2)	T_2 (μs)
$NV^{-/0}$ C-bulk	637	70[29]	11.7	150×10^9[61]	1.2[29]	2400[62]
$NV^{-/0}$ NDs	637	23 to 90	21.4 to 22.8	300[63–68]	—	0.44 to 1.27[69]
$SiV^{-/0}$ C-bulk	738	0.5[70]	1.78	22.4[71]	4[72]	0.035 (T_2^*)[73]
$SiV^{-/0}$ NDs	738	0.3 to 9.2[74]	0.23 to 1.3[75]	1200 to 9100[74]	—	n.m.
NVH NDs	503	95	27,[76] 40[77]	—	2.1	n.m.
$CAV^{+/0}$[16] 4H-SiC-bulk	648	70	1.8	40	—	n.a.
$CAV^{+/0}$ 3C-SiC-NPs[17]	645	—	2.1 to 5.3	300 to 800	—	n.a.
$DV^{0/+}$ 4H-SiC-bulk	1100	—	14	—	—	1200[18,19]
$DV^{0/+}$ 4H-SiC-NPs[78]	1100	—	—	—	—	n.m.
$N_CV_{Si}^-$ 4H-SiC-bulk[79]	1230	98	2.4 to 2.8	601 to 684	—	17.2 [80,81]
$V_BC_N^-$ hBN[82,83]	571	65 to 95[84]	3.58	167 to 833[84]	5.5 to 10[85]	n.m.
V_B^- hBN[86]	850	—	1.2	—	—	2[87]

emitters, most of the diamond CCs are in the red spectral region (except for the H3 center) and do not need to use UV excitation. For SiC, there are emitters in red as in diamond and emission toward infrared (IR), providing also reduced scattering of the excitation laser (780 or 980 nm) for depth imaging. hBN emitters are from green to red and require excitation mostly at 532 nm or below; however, two-photon excitation with a 780-nm laser can be achieved in some emitters. Details of CCs in these materials can be found in a specific recent review,[11,15,26] whereas, here, the summary is done only of the centers used in SRM. Details of which properties are relevant for the specific SRM methods are discussed in the related sections of this paper. In this paper, we review the current diamond, SiC, and hBN CCs status of their applications in SRM, and we look at their possible applicability in SRM and quantum sensing as well as in quantum super-resolution methods. We first review traditional SRM methods applied to CCs in diamond, SiC, and hBN and compare their relative properties. We consider the variant of traditional SRM methods applied to these emitters together with the spin sensing capabilities to determine state of the art spin nanoscopy and their applications. Then, we review the so-called quantum-enhanced SRM methods developed using the quantum optics properties, such as SP emission or sub-Poissonian statistics. We show their performances in comparison with conventional methods and current use of CCs in this space.

2 Traditional Super-Resolution Microscopy Methods and Their CCs Variant

SRM principles rely upon switching off the fluorescence of the samples in a subdiffraction limited area using the modulation of the photophysical properties of the fluorophores and spatial control of the excitation beam. Two major groups of far-field SRM methods are generally identified depending on the fluorescence tags' physical processes used and on the image reconstruction methods, based on the switching mechanism either deterministic or stochastic. SRM deterministic methods rely on the nonlinear optical response of the fluorophore to the excitation laser, e.g., by exciting the fluorophore from its GS to the ES and then delving into its dark state with two or more excitation beams as in STED,[88] GSD,[89] MS state depletion[90] microscopy, and reversible saturable optical fluorescence transitions (RESOLFT) microscopy.[91] In STED and GSD microscopies, the dark state is a GS, whereas, in the other methods, the dark state is a long-lived MS state or intersystem crossing state. Among deterministic methods, structural illumination microscopy (SIM) is based on excitation using the spatially structured pattern of light-generating interference patterns, whose mathematical deconvolution provides super-resolution images with a lateral resolution in 100 nm.[92] Stochastic methods rely on the chemical (such as oxidation or redox or electron tunneling) complex properties of many single nanoemitters showing photoswitching behavior at separate times, so nanometric distant fluorophores can be resolvable in time and then localized. The time localization is then converted into spatial localization using specific algorithms deconvolving each fluorophore point spread function (PSF). These methods are known as single-molecule switching or localization microscopy (SMLM) divided into photoactivation localization microscopy (PALM)[93] and STORM.[94] An additional variation of these methods depends on the used fluorophores and their photochemistry properties, and they can achieve super-resolution in 2D or 3D. As a common feature, these methods permit us to achieve spatial resolution below 100 nm, enabling the imaging of nanometric entities for the examination of their architectural details and their interactions with other systems, mostly biological samples and cell constituents. These methods permit the resolution of images better than 20 nm and achieve 10-nm localization accuracy. While high resolution can be achieved with these methods, they suffer from slow acquisition time and/or postprocessing of images, as well as in some cases of phototoxicity or photobleaching of

fluorescent tags that make volumetric time elapse imaging of living samples impractical. Recent reviews presenting the working principles of these methods and the main complementary achievements and advantages can be found in Refs. 2, 95, and 96. Here, briefly, we repeat that deterministic methods generally require higher optical power than nondeterministic methods, having the first as a major advantage in real-time imaging that is not possible with nondeterministic methods requiring postprocessing and longer acquisition time. As such, nondeterministic methods such as SMLM are less suitable for *in vivo* imaging regardless of their better resolution.

3 Stimulated Emission Depletion Microscopy

The STED microscopy conceptual framework was first proposed more than 25 years ago.[88] Details of how to build a STED microscope today are reviewed in Ref. 97. In STED, a fluorescent probe is first excited by light from the GS to an ES, and then it is either de-excited by applying a STED beam via stimulated emission or, spontaneously, via fluorescence emission. To efficiently force a fluorophore to the GS, the stimulated emission rate has to be faster than the spontaneous emission rate, i.e., the inverse of the optical lifetime, τ_{fl}, which typically occurs within a few nanoseconds after the excitation event. The fluorescent subdiffraction spots in STED are obtained by scanning the sample with a coaligned Gaussian excitation beam with a second excitation beam tuned in wavelength to achieve stimulated emission and engineered with a doughnut-shaped focal intensity distribution corresponding to a "zero"-intensity point in the center. This second beam is also known as the STED beam, and it is tuned generally in the phonon side band of the emitter.

The expected resolution is given as

$$d \approx \frac{\lambda_{\mathrm{STED}}}{2 \times \mathrm{NA} \times (1 + aI_{\mathrm{max}}/I_s)} \sim 50 \text{ nm}, \tag{1}$$

where I_{max} is the maximum STED beam intensity, I_s is the stimulated emission saturation intensity of the fluorophore, and a takes into account a nonperfect doughnut-shaped STED beam. The stimulated emission rate is given by $\sigma \times I_{\mathrm{STED}} \times \lambda_{\mathrm{STED}}/(hc) \gg 1/\tau_{\mathrm{fl}}$, where σ is the stimulated emission cross section. The advantage of STED microscopy is the real-time creation of the super-resolved image with a simple acquisition process, without the need of image postprocessing, which may induce potential postprocessing image artifacts. However, achieving high resolution and high speed comes at the expense of phototoxicity. When exposing samples with high laser intensities in the level of $\approx$GW cm^{-2}, as with the STED beam, radicals or singlet oxygen can be generated causing photobleaching and phototoxicity in living systems with subsequent cell death. However, living cell imaging with STED has been achieved[98,99] by optimizing the sample preparation protocols and using fast beam-scanning methods. Nevertheless, STED microscopy, even if it can be used for fast live cells and fixed cells studies, due to the inevitable still too high laser power required, is less suitable for a long period of live-cell imaging, while its application in imaging the molecular environment in biological systems is widespread.[100]

STED was first applied to NV in optical grade bulk diamonds exciting the spontaneous fluorescence emission occurring between 650 and 750 nm with a 532-nm laser and inducing the stimulated emission of the ES to the GS with a 775-nm laser. The unique properties of NV in diamond for STED are

- the stimulated emission decay rate is much larger than the spontaneous decay rate;
- NV long spontaneous emission lifetime ($\tau_{\mathrm{fl}} = 11.7$ ns in bulk and 23 ns in NDs[63]);
- high stimulated emission cross-section σ;
- phononic coupling of its GS enables quenching of the excited NV centers more efficiently;
- NV quantum efficiency is high (0.7);
- NV possesses extreme photostability once probed with a STED beam of $I_{\mathrm{max}} = 3.7$ GW/cm^2;
- NV broad emission allows using a quite wide spectral separation of the excitation and STED beams.

Using the STED beam with a Gaussian excitation beam, the spontaneous emission occurred only in the region where the STED beam intensity is zero, that is in the excitation beam center, identifying a subdiffraction emission area, with a resolution between 16 and 80 nm. The record emitter localization was determined to be 8 nm in bulk diamond.[29] Later, STED was extended to NDs to permit the application of these nanoprobes to biological samples imaging. NDs as small as 25 nm have been employed where each particle contained up to seven NV centers. 3D super-resolution has been achieved with 50-nm resolution.[32] This result has prompted STED applications of fluorescent nanodiamonds (FNDs) and NDs with a high concentration of NV centers, covalently conjugated with bovine serum albumin or α-lactalbumin as markers in cells [Figs. 2(a)–2(c)], achieving a resolution of $\approx$50 nm.[101] Other green fluorescent CCs in NDs due to high concentration of N-V-N (or H3) defects were used for STED imaging with 70-nm resolution in the cell environment. Here, green FNDs were used as STED biomarkers up-taken into HeLa cells[76] [Fig. 2(d)]. In conjunction with NV in FNDs, these CCs provide a way to perform two-color STED observations and to achieve STED correlation imaging, which is used for dynamic nanoscale interactions for *in-vivo* cell studies.[103] FNDs can also be used as dual-contrast for correlative imaging of high-resolution STED/confocal and transmission electron microscopy (TEM) experiments[102] [Figs. 2(e)–2(g)]. More studies of correlative electron and fluorescence microscopy (CELM) of FNDs have shown that FNDs can withstand electron beam exposure with their fluorescent properties remaining intact for light microscopy.[104] CELM has been used for subdiffraction imaging of antigens CD44 on the HeLa cell surface by FNDs encapsulated in biotinylated lipids with localization of 50 nm.[105] STED has been recently applied to H3 centers in bulk diamond[106] using 470-nm excitation and achieving a resolution of 50 nm. Using these centers in diamond, a departure of the STED resolution from the inverse square-root dependence of the stimulated emission excitation beam intensity is shown, suggesting the presence of charge traps between the ES of the centers and the conduction band.

STED has been applied to the SiV CC in diamond, which exhibits a ZPL at 738 nm; this center possesses better charge stability of the NV, with a two to four times higher stimulated emission cross-section compared to NV,[72] as shown in Table 1. The STED beam was tuned between 765 and 800 nm. However, the resolution obtained was only 89 nm, limited by the specifically used STED beam pulse energy, whereas it is expected to reach 20 nm with higher energy. As the SiV has been recently

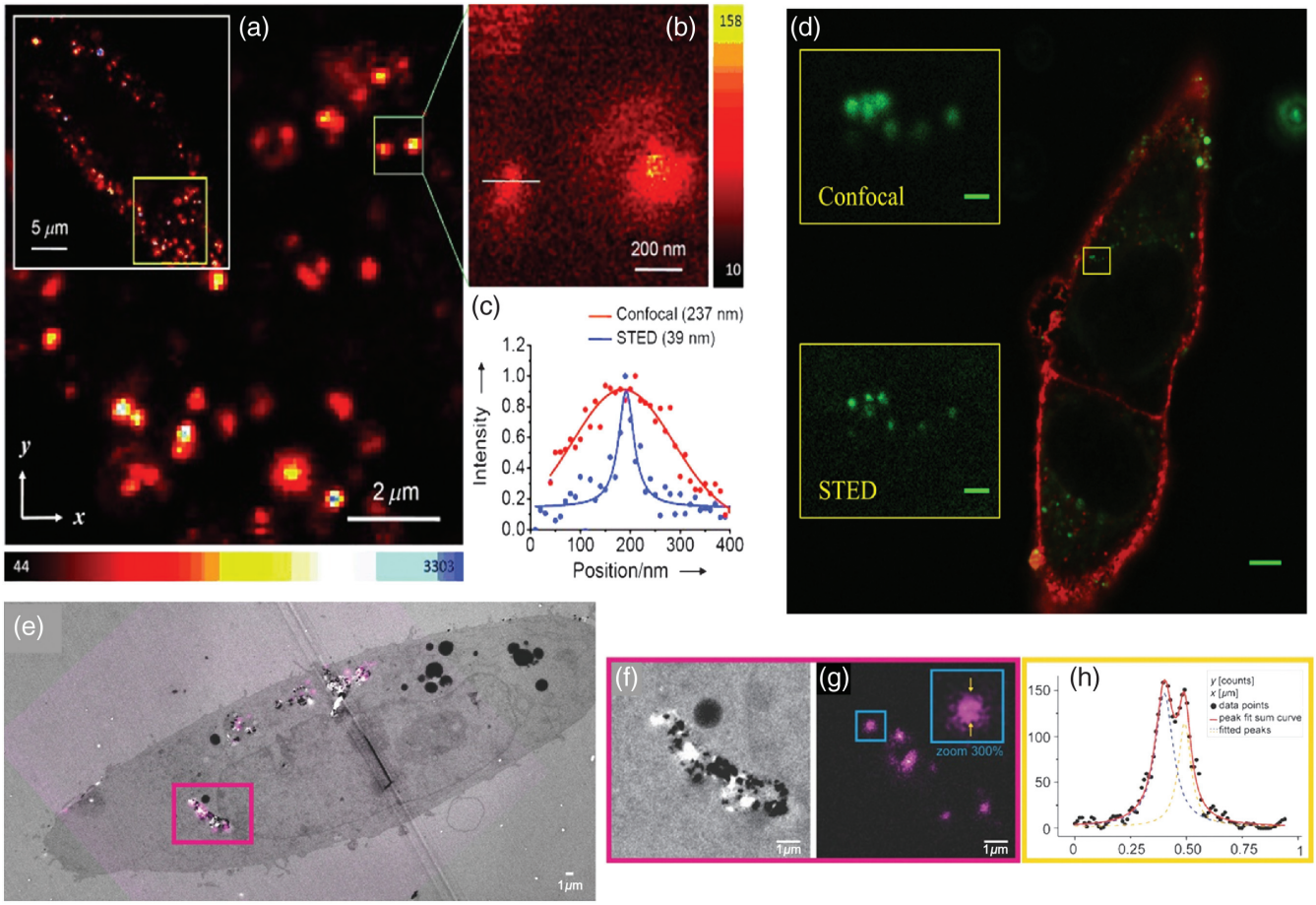

Fig. 2 STED applied to FNDs and green FNDs in cells. (a) Scanning confocal image of a BSA-conjugated NV-FND-labeled cell in the white rectangle. (b) STED image of single BSA-conjugated FND enclosed within the green rectangle in (a). (c) Confocal and STED fluorescence intensity profiles of the FND indicated in (b). Solid curves represent the best fits for Gaussian (confocal) or Lorentzian (STED) functions with the FWHM. Images reproduced with permission from Ref. 101, © 2011 John Wiley and Sons, Inc. (d) Superresolution imaging of green FNDs up-taken into an HeLa cell, which is tagged in red with an organic dye. The main image is a confocal scan. The green FNDs appear green, and the absence of fluorescence inside the cells reveals the positions of the nuclei. The two insets are magnified images of the highlighted area of the cell. Scale bars are 5 μm in the main image and 500 nm in the insets. Images reproduced from Ref. 76, © 2015 Optical Society of America (OSA). STED-TEM correlative imaging of intracellular FNDs in TEM sections. (e) A correlation result on a single cell with TEM in gray and fluorescence signal from FNDs in magenta. (f), (g) Zoomed sections of the correlation result for TEM and STED, respectively. (h) The line profile values of an FND in (g), and a two-peak Lorentzian fit of the data with peaks ≈90 nm apart. Images reproduced with permission from Ref. 102, © 2018 John Wiley and Sons, Inc.

incorporated in 10 nm NDs,[107] this could provide a multicolor STED microscope in a single nanoprobe and compete in the use of CCs-based NDs for STED in biomedical applications. However, the SiV properties in 10-nm NDs have not been studied in detail, even if high brightness was achieved from a single emitter.

STED based on FNDs with red, green, and near-infrared (NIR) emitters has shown very limited applications in biological samples so far due to the large size of NDs, which cannot allow imaging and localization of the 10 nm labeled cell's anatomy features. While the use of STED with NDs has been mostly driven by a feasibility assessment of achieving higher resolution compared with other currently used fluorophores, the applicability is limited by their size.[108]

The spin variant of STED based on NV quantum sensing as described in the next section may have more possibilities to advance their applications in biological science.

Similarly, STED in bulk diamond CCs has not been applied so far in biological samples imaging, while it is sometimes used for the study of the nanoscale photophysical properties of the quantum emitters or to assess their nanoscale fabrication.[60] For example, the stimulated emission of NV in diamond has

been used to induce lasing in NV, laying the foundation for laser magnetometry.[109] A laser magnetometer could achieve a very high contrast for the NV ODMR and prompt more practical applications of MRI using bulk diamond. STED has been applied to the study of a group of quantum emitters in 2D hBN, which presents a large variety of SP emission[110,111] from the UV to the NIR. These emitters have been recently identified as carbon related,[24] specifically a carbon–nitrogen substitution with boron vacancies. Here, STED was applied to the emitters at 2 to 2.2 eV as a spectroscopic tool for the examination of vibronic states, confirming the assigned origin.[82] In similar quantum emitters at 580 nm, a variant of STED known as time-gated CW-STED achieved a resolution of 50 nm limited by an objective with NA = 0.8.[85] The stimulated emission cross-section in these quantum emitters in hBN appears larger than in diamond CCs, showing some promises for biological samples imaging.

3.1 Spin Stimulated Emission Depletion Microscopy

By modifying a STED microscopy system, NV spin states could be imaged and localized with 6 nm accuracy,[45] later improved to 2.4 nm using a solid immersion lens fabricated directly in the bulk diamond.[112] These microlenses are used to locally reduce the depletion beam power. These results established a STED variant method for diamond NV spin nanoscopy. A STED beam was added to a typical pulsed confocal-ODMR setup,[12] constituted of a 532-nm polarization beam and a microwave pulse tuned to the NV^- GS spin transitions with an applied static magnetic field. By adding the STED beam, it was possible to distinguish and control the NV^- ODMR signal of five NV^- centers, whereas the diffraction-limited image was able to control only two NVs. It has been determined that the STED beam can preserve the NV spin state in Rabi oscillation if the STED beam does not start to populate the MS state. Rabi oscillation[113] can be performed with subdiffraction spin localization, whereas the effect of the STED beam induced a loss of information in the phase of the spin state when applying the Hahn-echo sequence, showing that quantum sensing is limited in STED high power operation. This was attributed to the different zero-field splitting of the ground and ESs; when a STED beam is applied and NV is forced to the ES, even if it is then de-excited, it experiences different coupling with external spins, as it has acquired a phase caused by the coupling of the ES, breaking the symmetry of the Hahn-echo sequence. Due to the high refractive index of diamond (2.4) and Mie-scattering resonances in NDs, a limit was believed to exist for STED to image multiple NV centers in NDs; thus, it was shown that STED can be used to distinguish multiple nanometric distant NV centers in 40- to 250-nm-sized NDs with a resolution of 10 nm.[114] In Figs. 3(a)–3(e), multiple NV centers in 100 nm NDs are shown using STED, and their image is correlated with SEM images and with their ODMR spectra. This result also proved the possibility of attributing a

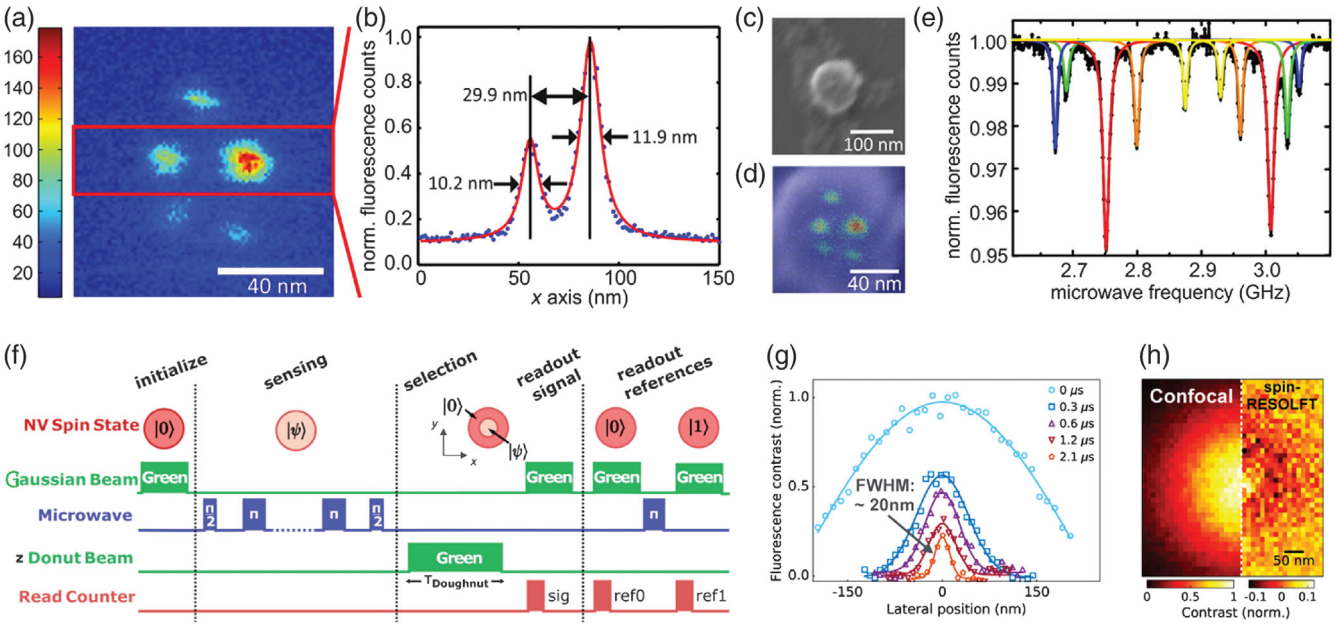

Fig. 3 Spin-STED applied to multiple isolated NV^- centers in 100 nm ND. (a) Subdiffraction image of five isolated NV centers in a single ND. (b) Vertical STED image profiles as indicated in (a). (c) SEM image of the same ND with (d) the overlay of the STED image. (e) ODMR spectrum of the same NV centers in the same ND showing distinct frequency pairs corresponding to the five NV centers. Reproduced with permission from Ref. 114, © 2013 American Chemical Society (ACS). (f) Spin-RESOLFT experimental sequence combined with AC magnetometry with the dynamical decoupling pulse sequence for quantum sensing using NV centers in diamond. (g) Spin-RESOLFT profiles for a single NV center and different doughnut beam duration with a power of 700 μW. (h) Spin-RESOLFT image of the same NV as in (g) with similar resolution of ≈35 nm but with 25 μW power and a longer duration of 50 μs. Images reproduced from Ref. 115, © 2017 OSA.

spin transition to each NV in the ND, opening the door for studies of fundamental spin-spin interaction of NV in NDs, for example, collective emission. While spin-STED has never been applied for biomedical imaging due to the high energy used, its current area of application is in NV centers fabrication with nm precision/localization. In this space, only a few examples of spin-STED use can be found. For scalable architecture, for example, in quantum technology using spin qubits, quantum photonics, and quantum sensing, the fabrication of an array of NV^- centers is required. Here, there is a need for two conditions to be simultaneously achieved, which are the accurate positioning of the NV centers and its high probability of creation. Using few keV ions energy, it is possible to achieve a positioning accuracy of NV in the nanometer range, with, however, a low yield in the few percent of conversion of nitrogen to NV centers after annealing. STED can be used to assess implantation/detection technology of single implanted atoms as an example[60] to determine the spatial accuracy of NV implantation and yield. However, so far, STED for NV fabrication has not been widely used. Nanoscale site selective magnetic sensing of 1×4 arrays of NV sites with a 60 nm diameter and 100 nm spacing was achieved using STED imaging.[116]

3.2 Spin-Reversible Saturable Optical Fluorescence Transitions

RESOLFT is a variant of STED, where fluorescence depletion occurs via an MS or intersystem crossing state. The MS state is required to have a long lifetime. In general, RESOLFT requires lower power than the STED beam, as such, it is easier to apply the process that can be affected by high laser intensity, specifically in biological samples, where phototoxicity is a major issue in live imaging.[117] Spin-RESOLFT is thus another variant of spin-STED or RESOLFT when applied to NV^- centers in diamond[46] for achieving super-resolution of the spin localization. Spin-RESOLFT is thus a deterministic superresolution method providing targeted probing of individual NV spins with nanometric resolution well suited for coherent nanoscale AC magnetometry. Due to the involvement of the long-lived MS state and the lower intensity, compared with STED, it has the potential to achieve coherent manipulation of NV spins using complex spin sequences with simultaneous superresolution imaging of the NV position, without disturbing the phase of the surrounding spins and thus achieving nano MRI with subdiffraction localization.

NV^- undergoes the transition to the nonspin selective MS state for spin numbers of ± 1, inducing fluorescence reduction. Spin-RESOLFT has been implemented by illuminating the sample with a sequence of a Gaussian 532-nm pulsed laser to polarize the NV^- spins in the $m_s = 0$ GS, whereas a microwave pulse excites the spin to the state $m_s = \pm 1$, and another doughnut-shaped green laser selectively allows us to manipulate the spin only in the central part of the beam, achieving subdiffraction spin manipulation of NV^- centers. The technique resolution is given as

$$d \approx \frac{\lambda}{2 \times \mathrm{NA} \times \sqrt{1 + \Gamma \tau_D}}, \tag{2}$$

where Γ is the rate of optical excitation of the spin, and τ_D is the duration of the doughnut beam that is only limited by the spin-state relaxation time (>100 ms) and the optical transition lifetime $\tau_{\mathrm{fl}} \approx 12$ ns (this is instead of limiting STED resolution). The advantage compared with spin-STED is the reduced power at the sub-mW level, which is four orders of magnitude lower than STED, while achieving the same resolution.[115] Due to the lower power used in this method, spin manipulation based on Rabi oscillations and spin-echo measurements could be performed with spatial selectivity locating 150 nm apart NVs centers. This enabled the study of the spin coherence times of closeby NVs to determine the content of magnetic impurities in the local nanoenvironment. Spin-RESOLFT microscopy can enable precise nanoscale mapping of magnetic field patterns with a shown resolution as low as ≈20 nm, using a lower power depletion beam. In particular, mapping of the nuclear spins exterior to the diamond was achieved and imaged with 50 nm lateral resolution. The proton NMR line-width was not degraded by the scanning laser beam,[115] showing promise for NMR signals detection of nuclear spins with high spatial localization. In Figs. 3(f)–3(h), a scheme of spin-RESOLFT combined with a quantum sensing sequence (XY8-k dynamical decoupling pulse sequence) is achieved in bulk diamond with 20 nm resolution. A spin-RESOLFT magnetic imaging sensitivity of 250 $\mathrm{nT}/\sqrt{\mathrm{Hz}}$ was achieved with a resolution of 50 nm (whereas on the confocal mode, the sensitivity is of 60 $\mathrm{nT}/\sqrt{\mathrm{Hz}}$), as the resolution is increased by longer duration of the doughnut laser beam, which in turn reduces the sensitivity. As such spin-RESOLFT based on diamond CCs may be more applicable to biology and quantum sensing than all the techniques described so far.

4 Ground-State Depletion Microscopy, Metastable-State Depletion Microscopy, and Structured Illumination Microscopy

In the GSD microscopy method, the NV GS is depleted by shelving the emitter in the ES. A high-intensity 532 nm excitation beam has a doughnut shape and is used to force the NV in its ES, whereas NV emission occurs in all of the samples except in the dark center. The location of closely packed NVs is observed as nanosized dark spots in a larger bright area. The localization below the diffraction limit corresponds to a dark point.[31] Imaging was achieved with this approach in diamond due to low photobleaching at high-intensity beams. Mathematical deconvolution postprocessing algorithms using the effective calculated PSF are used to obtain the positive image. With this method, a resolution of 8 nm with several $\mathrm{GW/cm^2}$ in a low-density NV sample of an optical grade bulk diamond has been obtained. The direct super-resolved image could be obtained using an excitation Gaussian beam modulated at 1 kHz and, at 561 nm, used to excite the fluorescence of the NVs located at the doughnut minimum that remained dark, as in the GS. With the direct GSD methods, 14 nm resolution was achieved, and NVs 17 nm apart were located in the sample. A variant of GSD has been demonstrated via shelving in the MS state,[61] as it had been initially proposed.[89] A long-lived MS state is required. A red laser at 638 nm excites the NV center and efficiently transfers it to an MS dark state, while the dark state is emptied by blue light (479 nm) back to the ES, thereby depleting its GS. A resolution of 16 nm was achieved with 5 mW power. It is understood that GSD via the dark state can be sample dependent, where high nitrogen doping is necessary to avoid conversion of the NV^- from the negative to the neutral

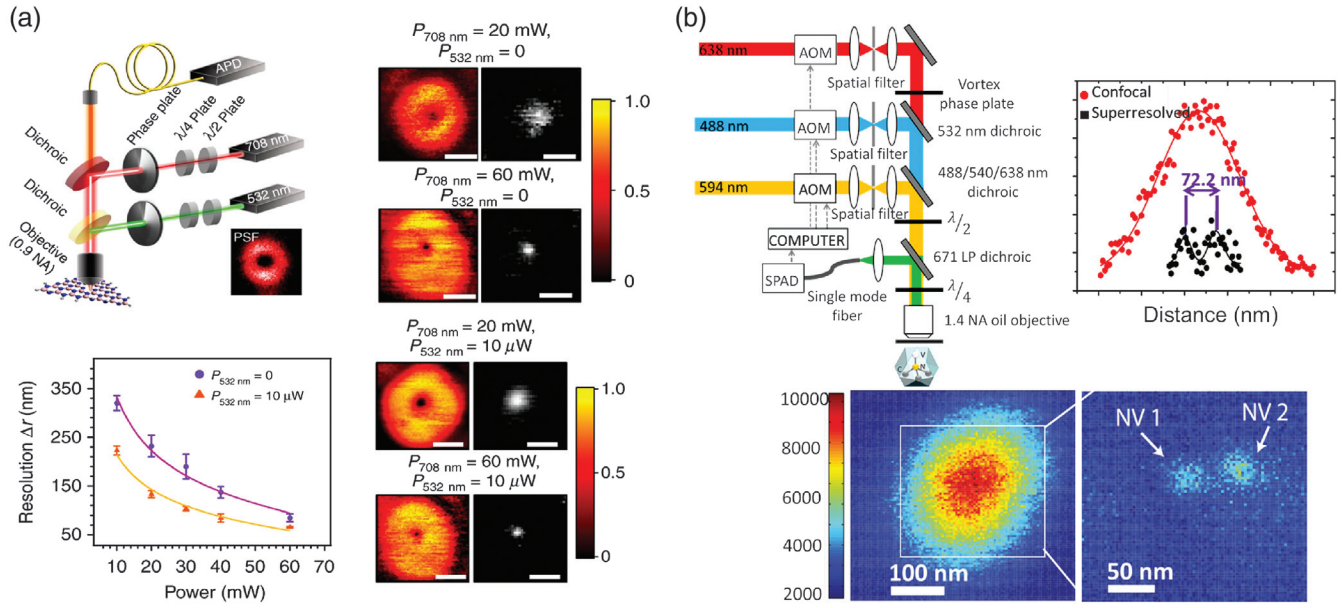

Fig. 4 (a) Schematic of the experimental conditions used to perform GSD nanoscopy applied to hBN flakes with one or two excitation lasers with doughnut-shaped intensity profiles. Here, 532 nm is used as a repumping laser. The direct images and deconvoluted ones are shown in the presence of only the 532-nm or both 532- and 708-nm lasers, together with the resolution achieved, showing an improved resolution in the presence of the two lasers. Images reproduced from Ref. 119, Creative Commons BY license. (b) Schematic representation of GSD microscopy applied to NV^- in NDs. Three lasers operating at the wavelengths of 488, 594, and 638 nm are used. The 638-nm laser has a doughnut-shaped intensity profile and switches off the center via the MS state, while the 488-nm laser is a reset beam used to repopulate the ES. Confocal and super-resolved images of 2 NV^- at 72-nm distance in the same ND. A single NV was resolved with 36 nm. Images reproduced from Ref. 118, Creative Commons BY license.

charge state. Compared with STED, as this method involves a long-lived MS state, it requires a lower power, also in comparison to the GSD via the ES. This method has never been applied in spin manipulation, and it has been referred to in recent literature to be a CSD method, involving the NV charge state conversion from a negative to a neutral state. GSD microscopy using the MS state has been applied to NDs,[118] where the charge conversion of the NV^- was not observed due to the high concentration of nitrogen in the NDs. Here, three beams were used: a probe beam at 594 nm, a depletion beam at 638 nm, and a reset beam at 488 nm. The depletion beam at 638 nm shelves the NV^- centers to the MS dark state everywhere except in the local minimum, whereas a Gaussian beam at 594 nm probes the NV^- centers, and a 488-nm reset beam is used to repopulate the ES. Super-resolution imaging of a single NV^- center with an FWHM of 36 nm is demonstrated, and two nearby NV^- centers were resolved with 72-nm separation, as shown in Fig. 4(b). GSD microscopy applied to NV^- in NDs requires a much lower optical power compared with the bulk diamond previously reported. However, this work further evidences the need to control the NDs nitrogen concentration to better tailor the NV photophysics as an example to separate the charge conversion possibility and combine GSD in NDs with spin control. So far, GSD has not been applied in spin manipulation.

A variant of GSD microscopy was applied to a class of quantum emitters with a zero phonon line (ZPL) at 778 nm in 2D hBN[119] [Fig. 4(a)]. Here, complex photophysics of a four-level system is assigned to the photon-correlation dynamics of the emitters under different laser excitation wavelengths, where it is found that 675-nm (or 708-nm) excitation induces a transition to a dark state (possibly a different charge state) through the long-lived MS state; while combining the 708-nm with a 532-nm excitation, the emitter is repumped in the ES, inhibiting the otherwise faster nonradiative decay from the intermediate to the GS. As such, by combining GSD with two excitation beams, a resolution of 62 nm was achieved with a lower power compared with a single beam GSD. This method could also be associated with a charge state conversion. No CCs GSD microscopy has been used in the cellular environment so far due to the high energy used. Structured illumination (SIM) has been compared to STED side-by-side using NV centers in 35-nm FNDs and bulk diamond material. It has been shown that STED provides more structural details, whereas SIM provides a larger field of view with a higher imaging speed. SIM has been compared also with wide-field imaging, as it is expected to have a factor of 2 resolution improvement, and, using NV centers in FNDs, the achieved resolution was ≈304 and ≈131 nm, respectively.[120] While this is not the ultimate resolution of SIM with FNDs, SIM has found many applications in biological science, where less resolution is needed, and it is not excluded that such large FNDs could find better applications in SIM rather than STED.

5 Single Molecules Location Microscopy and Spin-SMLM

SRM techniques can use statistical intensity switching due to the fluorescence intermittency of the fluorescent nanoprobes in the entire field of view of a wide-field microscope. Using single emitters localization imaging reconstruction algorithms, the precise locations of the probes surrounding sub-100 nm features of the object to image can be achieved. SMLM is the general term used to group all of the techniques based on this approach. SMLM methods are implemented on a wide-field microscope using an electron-multiplying charge-coupled device camera with sensitivity of single photons detection being possible. Sequences from 100 to 10,000 individual camera frames are taken, and each frame is imaging only a limited number of different subsets of individual isolated fluorescent nanoprobes each time, which is accidentally switched on for each subsequent camera frame. The image with sub-100 nm resolution is reconstructed by determining the spatial positions of the individual fluorescent molecules from their intensity intermittency in these many camera frames. Deconvolution of the single emitters PSF is achieved. SMLM relies upon the presence of a high density of single emitters, which can be switched on and off within a time frame of 10 to 100 ms. Different fluorophores photophysics are used to achieve their stochastic on-off switching, and this differentiates various methods. PALM employs the excitation laser wavelength-dependent fluorescence activation of the so-called "photo-activable" fluorescent labels, which are brought to an "on" state by the laser excitation; after activation, these fluorophores emissions subsequently photobleach. Specifically, PALM uses photoactivable green fluorescent proteins as labels, which are genetically engineered fluorescent proteins. Instead, STORM originally utilized stochastic fluorescence transitions of organic dye. These methods can achieve higher resolution (10 to 20 nm) than STED with much lower power and, as such, lower phototoxicity than the other deterministic methods; however, at the expense of longer acquisition time of many frames, they are thus less applicable to *in vivo* imaging. SMLM high spatial resolution (10 to 20 nm) is achieved at the expense of low time resolution, usually from a few to several seconds. It has been improved to reach 0.5 s using single excitation in 2D imaging in the cell environment[121] with a reduced spatial resolution of 25 nm; whereas, time resolution of 1 to 2 s is needed to achieve a 3D spatial resolution of 30 nm in the lateral directions and 50 nm in the axial direction. The long acquisition time can introduce drift, requiring fiducial markers and correction to avoid image artifact. More importantly, long acquisition times introduce an upper limit to the time resolution and speed when it is needed to resolve live-cell dynamics or to achieve real-time imaging of subcellular components. Various deconvolution and machine learning algorithms can accelerate PALM and STORM as an example, using deep learning methods;[122] however, these techniques are not yet commonly applied, even if they are very promising. The localization of the emitters in SMLM is given as

$$\Delta \mathrm{loc} \approx \frac{\Delta}{\sqrt{N}}, \tag{3}$$

where Δ is the FWHM of the PSF (resolution) of the single emitter, and N is the photon count. The technique is only limited by the number of photon counts associated with the single emitters. As such, bright single emitters with fast switching from the bright and dark state can provide very high localization and resolution.

Several fluorescent labels have been used for SMLM as described above: organic molecules have the smallest size, and the excellent blinking properties are, however, generally dim and undergo rapid photobleaching; photoactivable or photoswitchable fluorescent proteins suffer from poor localization precision and low photon counts. Nanomaterials, such as QDs, carbon dots, polymers dots, and silica NPs, have been used, showing promising results due to their high brightness and photostability. Nanomaterial limitations can be found in their phototoxicity or their large size compared with organic molecules.[123] Among these nanoprobes, NDs have been also used.

SMLM has been applied to NV centers in NDs[33] based on the blinking behavior of NV^- photoluminescence due to the surface defects and electron tunneling to near-surface defects, achieving a resolution of 20 nm and being able to discern two NVs in a single ND 20 nm apart. A STORM microscope enhanced by spin manipulation was achieved in bulk diamond using the photoionization of NV^- to its NV^0 for single sparse NVs, achieving a super-resolution of 27 nm with the spin manipulation and magnetic field sensitivity of 190 $\mu T/\sqrt{Hz}$.[47] SMLM based on NV in diamond and NDs can permit parallel magnetic imaging with nanoscale resolution. However, the photophysics of NV^- are due to the low nitrogen concentration bulk diamond, which also has a limited number of naturally occurring NV centers, reducing the possibility of reconstructing the image of nanometric size samples. SMLM in NDs has further been implemented to achieve spin manipulation with subnanometer resolution in NDs,[48] permitting also the improvement of the super-resolved images of collective blinking NV^- centers to 23 nm (otherwise of 50 nm). By labeling cells bound to iron oxide magnetic NPs with biotinylated 70 nm FNDs, the nanoscale magnetic field optical images with 17 nm resolution within the cells were achieved using the spin-SMLM method[49] and magnetic field sensitivity of 85 $nT/\sqrt{Hz}$, as 1000 NVs were present in a single FND rather than 1 NV. This is the first application of the spin-SRM method to the cells' environments. One limitation for *in vivo* imaging with this technique is the longer acquisition time, which could be improved using deep learning methods.[124] SMLM and its spin variant using NDs have more potential for biomedical applications if smaller NDs with bright NV centers could be available, while, at the moment, large NDs of 35 to 70 nm have been used. An improvement of the NDs material to achieve better applicability of these techniques is expected, for example, with lower nitrogen content for improved quantum sensing combined with parallel super-resolution imaging.[125–127]

Using quantum spin control, super-resolution localization of NV^- centers in diamond with localization better than 1.4 nm was achieved with subnanometric resolution. Here, a scanning confocal microscope and quantum-controlled photoswitching were used.[128] Photo-switching is realized by encoding the spin quantum phase using a pulsed magnetic field gradient. This method can find applications in addressing and controlling coupled qubits spins in diamonds.

Other CCs in solid-state nanoscale materials are emerging as probes for SMLM. SMLM has been applied to quantum emitters in a monolayer of hBN.[129] The mechanism is attributed to the CCs photoswitching after exposure to a 561-nm laser due to possible photo-induced ionization and recombination of defects, revealed by correlated TEM imaging, such as boron vacancy

(V_B), and switching between its neutral and negative charged states. Here, the super-resolved images of 46 nm were achieved with the possibility of locating quantum emitters 11 nm apart. This technique is relevant to increase the understanding of quantum emitters in 2D materials. By combining SMLM and spectroscopy, the spatial and spectral correlation of quantum emitters in chemical vapor deposition (CVD) and exfoliated flakes of 2D hBN was shown,[130] where two types and one type of defects were identified in the respective material [Fig. 5(c)]. These results align with recent findings of the origin of the

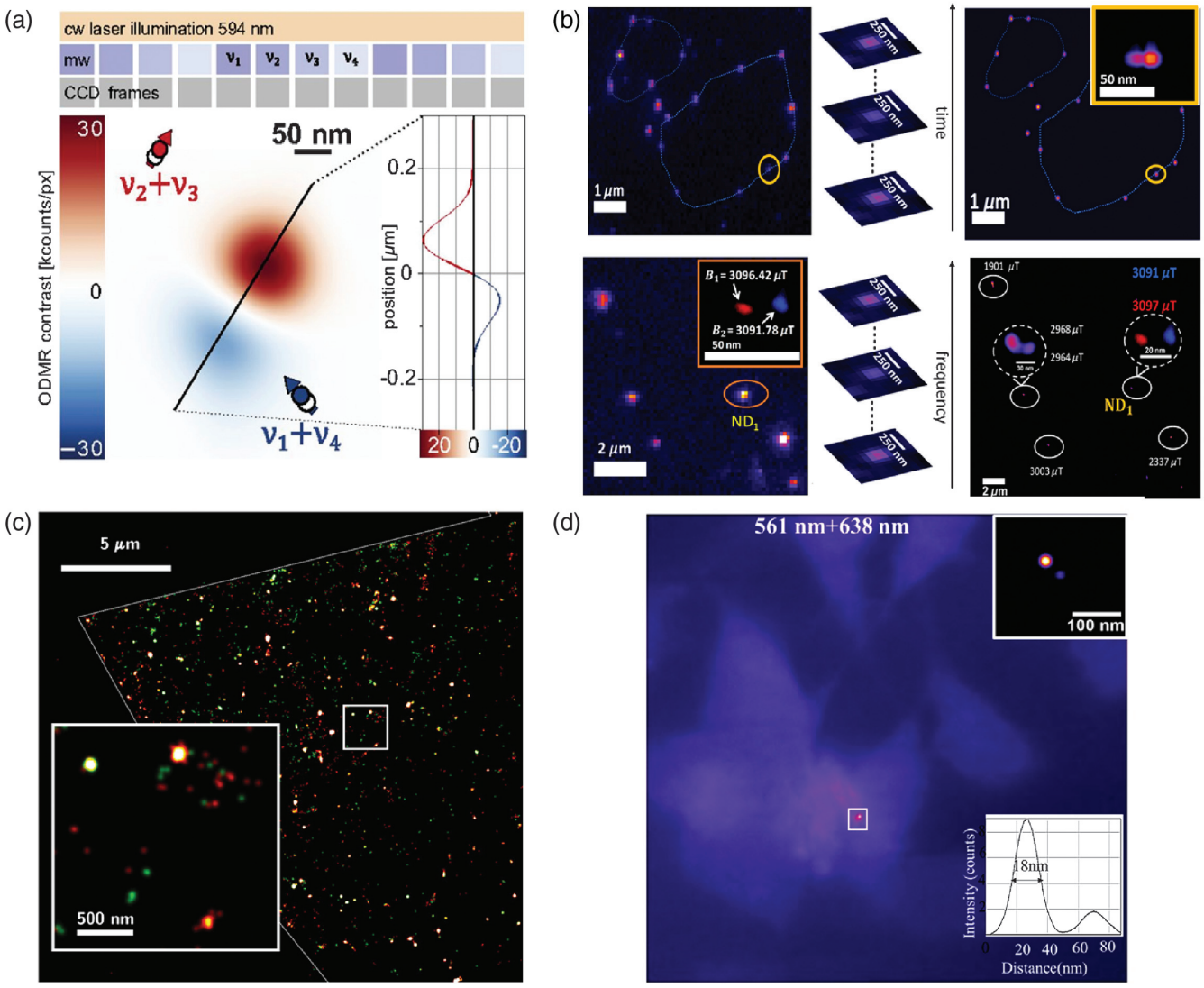

Fig. 5 (a) Spin STORM applied to NV^- center in bulk diamond. STORM-ODMR measurement sequence under a 594-nm excitation laser to induce photoionization of the center into its neutral charge state, combined with a scanning of the microwave frequency for each widefield frame. Sensing of two NV^- centers is shown with a nanometric localization and STORM-ODMR image. The zero-crossing (line scan) between both centers shows mutual distances of the centers below the STORM resolution. Image reproduced from Ref. 47. (b) Nanoscale magnetic field optical images of labeled cells bound to iron oxide magnetic NPs with biotinylated 70 nm NDs. Upper figures showing super-resolution only based on SMLM using 561 nm and lower figures showing magnetic field sensing and localization combining ODMR information achieved by a microwave frequency scan. Reproduced from Ref. 49, with permission from the Royal Society of Chemistry. (c) Super-resolved image of hBN flakes resolving the different types of emitters (green and red) based on photoswitching of the V_B charge states and other emitters in the 2 to 2.2 eV spectral region. Reprinted with permission from Ref. 130, © 2019 ACS. (d) SMLM applied to 4H-SiC NPs of 40 nm after cell incubation achieving 18 nm in the cellular environment. The SiC NPs revealed the presence of multiemitters in the same NP with SMLM using different excitation wavelengths at 561 and 638 nm. Image reproduced from Ref. 59, © 2020 American Physical Society (APS).

quantum emitters in exfoliated flakes of hBN attributed to V_BC_N concerning visible emitters and the V_B in the neutral or negative charge states. The SMLM technique was also applied to investigate the optical properties of single-digit hBN NPs (3.0± 0.7 nm) produced by cryogenic exfoliation.[131] hBN NPs/nanoflakes due to their size properties can be applied for bioimaging and sensing applications in combination with SMLM, GSD, or RESOLFT microscopy; however, so far, no applications in biological samples imaging have been shown. SMLM in hBN has been performed to achieve information about the origin of the emitters, which is often not fully understood.

While hBN emitters have recently shown the possibility of having an ODMR signal[86] concerning the negative charge state of V_B^- with a coherence time of 2 μs at room temperature, its application to spin-SMLM has not been shown yet, possibly due to its central wavelength of 850 nm when excited at 532 nm. This emitter has not yet been isolated as a single emitter. The V_B^- has been determined to be the dark state of the V_BH used in a recent demonstration of SMLM[132] of hBN samples in air and acidic solutions. The presence of water increases the conversion into the visible luminescent neutral charge state. A recent review on the potentials of hBN in SRM and the photophysics of CCs involved can be found in Ref. 26.

SMLM was used to study the blinking properties of quantum emitters in bulk SiC and NPs sized from 8 to 100 nm[15] of different SiC polytypes, showing a resolution dependent on the NPs size and excitation wavelength.[59] A resolution of 20 nm and a minimum distance between single emitters of 40 nm were observed, even with the uptake of the SiC NPs in the cellular environment of MCF10A cells [Fig. 5(d)], showing the potential of these nanoprobes as biomarkers. Using single digit (3 nm) SiC NPs with the ODMR emitters signature,[78] spin nanoscopy using dual-color excitation could also be achieved as the red (CAV) and NIR (DV) CCs are present in the same NPs. As SiC NPs can reach the size of 1 to 1.5 nm, comparable with those of pores in the cellular membrane,[23] and their biocompatibility has been demonstrated[133]; the combination of 3-nm NPs with CCs with optical spin readout may be the solution to the large FNDs applicability to spin-SRM. However, spin-SMLM has not yet been demonstrated, as the quantum emitters are in the infrared (900 and 1100 nm), where commercial systems do not operate, as well as the conventional detectors' efficiency is much lower.

6 Two-Photon Microscopy

Two-photon microscopy (2PM) is used to increase the resolution along the optical axis of the microscope, which is generally much worse compared with lateral resolution for any fluorescent microscopy method. Its main application is deep tissue imaging,[134] as by exciting with two photons at a longer wavelength (generally in the infrared) scattering and background are reduced. Combined with adaptive optics to correct the optical aberration within the sample limiting resolution, it can provide SRM in 3D.[135] 2PM has been applied first to diamond bulk material[136] using 1064 nm and showing it is possible to excite NV in the same way as using SP absorption with 532 nm, showing similar photostability with high power excitation. Application to micron-sized diamonds with NV centers has followed,[137] with FNDs for their characterization of high brightness due to many NV centers being created within the NDs,[138] then for drug delivery,[139] and in living cells.[140] 2PM, however, does not provide SRM by itself, but can be combined with SRM to achieve better resolution in the z direction. It can be used to image the localization of the production of NV centers with depth in bulk diamond.[141] 2PM has then been implemented in 5- to 100-nm NDs in combination with adaptive optics and super-resolution radial fluctuations algorithms,[142,143] achieving 43-nm resolution. This is a freely available plug-in module for ImageJ, which requires a minimum of 100 frames of confocal images. Super-resolution radial fluctuations make use of the fluctuations in the radial symmetry measured over a large number of images of the same object to extract super-resolution images, and it is a computational method.[144] 2P microscopy has also been successfully applied to ≈200-nm hBN flakes using a ps-pulsed laser at 708 nm.[145] No applications of 2PM in combination with SRM using CCs in the cellular environment have been shown.

7 Charge-State Depletion Microscopy

As previously mentioned, the NV center in diamond, like many other CCs, occurs in two fluorescent charged states: neutrally charged NV^0 and negatively charged NV^-. Their well-known studied ZPLs are at 575 and 637 nm, respectively. The presence of one or the other charge state is dependent on the nitrogen doping concentration of the starting material (the presence of substitutional nitrogen center P1) in both bulk and NDs.[146] In low nitrogen concentration of diamond with different excitation conditions, the two charged states can transform from one to the other, known as he photochromic effect.[147,148] Only the NV^- electron spin GS can be optically initialized and detected, whereas the NV^0 charge state does not exhibit such properties ($S = 1/2$). They are both very photostable once the charge state is controlled. It is understood that high nitrogen doping can stabilize the charge state of the NV^-.[149] On the other hand, a high nitrogen concentration is the main source of the reduced coherence time of the NV^-.[150] The charge state conversion process of the NV center excited by visible light has been demonstrated to be a two-photon process, increasing quadratically with the optical field intensity.[148] CSD microscopy[35] relies on using a 637-nm laser to convert the NV^- into the NV^0, and a 532-nm laser coverts it back or initializes the NV^-, achieving a resolution of 4.1 nm by optimizing the laser pulse sequences. The method is not deterministic, as the conversion rate of the charge state for NV^- is around 75%, and this is a limitation of the technique. In CSD nanoscopy, three lasers are applied in sequence: the NV centers at the focal point of a Gaussian beam are initialized to NV^- by a 532-nm laser beam, and a doughnut-shaped 637-nm laser beam is applied to convert the charge state to NV^0, except for the NV centers at exactly the center of the doughnut-shaped beam. The third laser at 589 nm is nondestructively used to read out the NV charge state, as it can efficiently pump the spontaneous emission of NV^- centers without changing its charge state. Only the NV centers at the 637-nm laser beam center will be bright in the image under 589-nm excitation. The resolution of CSD nanoscopy can be increased by increasing the power and duration of the doughnut-shaped depletion-laser beam. The electron spin-state dynamics of adjacent NV^- centers can also be controlled via the CSD. Using ODMR CSD and Rabi oscillation with CSD, two 100-nm distant NV^- spin states, with the same resonant microwave frequency, were individually controlled.[35] Here, the CSD method is not influencing nearby spins, as the method is based on charge state conversion, and, as such, when NV is in the neutral charge state, it is not influenced by the microwave. CSD and its spin variant have been applied to ultrapure diamond, with 500-ppb nitrogen

concentration, and, as such, this method also appears to be material doping dependent. CSD microscopy has been applied to an ensemble of NV centers in bulk diamond with 6.1-nm resolution.[151] Using an NIR laser (780 nm), the charge-state conversion rate was improved in CSD.[152] Using picosecond lasers and a low repetition rate, a resolution of 12 nm was achieved with 1-mW depletion power, bringing the technique among the lowest power high-resolution methods.[153] The resolution of the technique can be increased by a longer depletion beam pulse and higher power. Super-resolution multifunctional sensing has been shown using low-power CSD nanoscopy of arrays of high-density NV centers used as local electromagnetic field sensors for local density of states and electrical conduction with a resolution of ~49 nm.[154] The methods regardless of the low power have never been applied to biological samples, mainly because they have never been applied to NDs or FNDs as of yet, possibly due to the high nitrogen concentration of the NDs.

8 Quantum Methods

While the previously described methods rely on nonlinear optics effects or nonstationary emission of fluorescent markers for overcoming the diffraction barrier, which is due to stationary and linear classical optics, an alternative approach is based on resorting to quantum optics. High-order quantum interference patterns arising in quantum optics can yield spatial distribution of correlations much denser than what is classically allowed. Using nonclassical light as the source of illumination, subshot noise measurement can be achieved in virtue of quantum entanglement; the techniques are known as quantum illumination,[155] which permits us to achieve imaging in the presence of noisy low illumination conditions, while they do not provide super-resolution. Various methods to achieve high sensitivity, image contrast, and, to a certain extent, resolution enhancement via quantum optics have been based on illuminating an object with nonclassical light, such as squeezed light, SP emitters, or entangled photons.[156] Another proposal was based on using samples that emit multiphotons while being illuminated by classical light. By using coincidence measurements, the diffraction limit can be defeated.[157] However, no samples can currently emit photon pairs or multiple photons. As such, an alternative to Hell's proposal is to use higher-order correlation methods[158] in the specific SP emitters.

8.1 Single Photon Second and Higher Correlation Methods

Photon antibunching[159] is observed in most common fluorophores, such as organic dyes, QDs, and CCs, in wide-bandgap materials even at room temperature. For these emitters, the photons have sub-Poissonian statistics, which consist of the suppression of emission of two photons at the same time. Therefore, simultaneously detected pairs of photons from such fluorophores provide information of the number of emitters; if N emitters are measured, their zero delays ($\tau = 0$) second-order photon correlation is $g^{(2)}(\tau = 0) = 1 - \frac{1}{N}$. The same quantum emitters are widely used in traditional nonlinear and nonstationary SRM, as described in previous sections, via spontaneous emission. Because of photon antibunching, a scanning fluorescence microscope spatial points in the image are, in principle, based on sub-Poissonian photon statistics, where the number of simultaneous multiphoton detection events is much smaller than it is for classical light for any order. Performing an N-photon coincidence measurement is equivalent to measuring N-photon, narrowing the effective PSF by a factor of $\sqrt{N}$.[160] The PSF is, in this case, the probability of detecting a photon at the position x, $P(x)$, where the probability of detecting N photons at x is narrower, $P(x)^N$, so the FWHM reduces by $\sqrt{N}$. The first experimental demonstration was based on CdSe/CdS/ZnS colloidal QDs photon antibunching in the image plane of a wide-field fluorescence microscope, determining the spatial distribution of missing two- and three-photon coincidence events and reconstructing second- and third-order super-resolved images.[54] This method resembles super-resolution optical fluctuation imaging (SOFI),[161] as intensity correlations are detected in the image plane of a fluorescence microscope. However, in SOFI, the fluorophore brightness fluctuations provide super-Poissonian photon statistics, whereas quantum SRM antibunching of photon emission is a sub-Poissonian statistic. Super-Poissonian photon statistics are highly dependent on the specific emission fluctuations of the fluorophores, while antibunching is a universal subshot statistic. Antibunching imaging is limited by the SP detector technologies background noise and, by their point detectors nature, responsible for a small fill factor.[162] The method has been applied to NV in electronic grade bulk diamond,[55] where second- and third-order photon correlation functions, $g^{(2)}(0)$, $g^{(3)}(0)$ maps, were obtained and deconvolved to determine the PSF, $P(x)$, to reconstruct the super-resolved images [Figs. 6(a)–6(e)]. Here, a confocal setup with single-photon avalanche photodiodes (SPADs) and photon correlation electronics was used. An FWHM of 290 nm was achieved to resolve the location of 3 NV centers with 2 NVs at 270 nm apart [Fig. 6(e)]. The localization and super-resolution are limited to the third order, with a factor of $\sqrt{3} = 1.73$ improvement. The method appears very far from the current resolution and localization obtained from STED or SMLM, and it is unclear if it can be applied in a higher density of NV centers as in optical grade diamond or NDs due to the presence of high background and multiple CCs in the same ND, in addition to collective emission effects observed.[48] Further, the time acquisition to achieve a higher-order correlation function and the complexity to implement higher-order correlation using single SPADs could be a limit to improving the current resolution.

8.2 Quantum Enhanced SRM

Quantum correlation methods have shown the possibility to be improved by adopting image scanning microscopy (ISM), which makes use of a fiber bundle in place of the confocal pinhole and on a small array of faster SPADs, offering a twofold enhancement in resolution compared with a traditional wide-field or scanning confocal microscope.[165] In particular, ISM has been proposed as a method in traditional SRM that could be implemented together with the quantum correlation of single emitters, as shown by quantum image scanning microscopy (Q-ISM) [Figs. 6(f)–6(h)].[57,163] This is because in ISM each pixel in a detector array acts as a small pinhole in a confocal laser-scanning microscope,[166] which can be further improved using a recently developed array of SPADs.[162] In addition, by adopting ISM, SMLM could also be equipped with quantum correlation functionalities. First, it has been shown how the quantum correlation could be applied to SMLM implemented by a fiber bundle camera.[163] Here, the SMLM localization principle is implemented using high quantum efficiency, low noise, scalable architecture group of SPADs, where the fill factor is improved

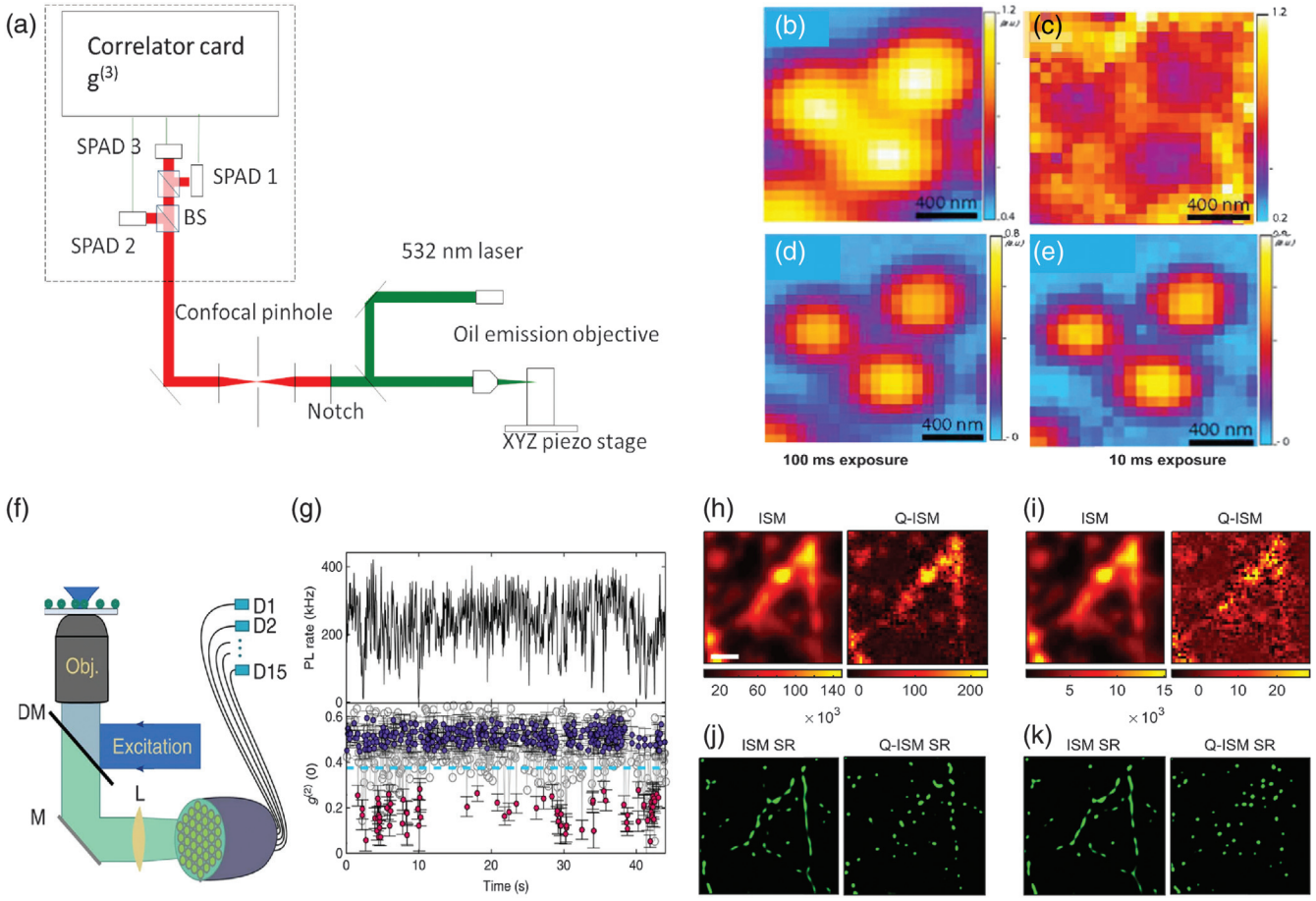

Fig. 6 (a) Schematic of a confocal laser scanning microscope equipped with SPADs and a third-order correlation electronics. (b) Diffraction-limited image from the confocal point of three NV centers in bulk diamond. (c) Map of the $g^{(2)}$ function and super-resolved images using the quantum correlation information after using a quantum reconstruction algorithm for (d) the second-order and (e) third-order. (b)–(e) Images are reproduced with permission from Ref. 55, © 2014 APS. (f) Schematic of an SP fiber bundle camera with 15 SPADs. (g) Photon count time trace (top) and quantum correlation (bottom) for two QDs. Blinking of one QD is followed by antibunching, $g^{(2)}(0) \approx 0$, in red. Blue circles correspond to the case of more than one emitter blinking, while gray circles correspond to insufficient statistics. Images (f) and (g) are reproduced from Ref. 163, Creative Commons BY license. (h), (i) Images of microtubules in a fixed 3T3 cell labeled with QDs imaged using ISM and Q-ISM and corresponding SR images (j), (k) for 100 ms and 10 ms acquisition times; the scale bar is 500 nm. Images (h)–(k) are from Ref. 164, © 2019 OSA.

using the fiber bundle. The time traces of single QDs count rates are acquired with the second-order photon correlation function $g^{(2)}(t)$ [Fig. 6(g)] and analyzed in time bins of 0.1 s. Single-emitter localization is achieved, postselecting only single emitters based on the values of $g^{(2)}(0) < 0.375$ with localization of 20 nm on a single emitter, which is comparable with SMLM in the widefield imaging mode. Tracking of single and two emitters separated by 100 nm was achieved with this method. Both localization and tracking are not currently superior to traditional SMLM due to the small field of view. This method, however, provides a solution to the current SMLM, requiring a sparse number of single emitters to avoid multiemitters in the diffraction spots (which generally require many camera frames), and, also, it relies less on the fluorophores photoswitching underlying mechanism, as it can be applied also to photostable single emitters. This method permits the rejection of multiemitters from the quantum correlation measurements or the use of multi-emitters fitting algorithms. The approach can be scaled up by SPAD arrays to achieve faster antibunching maps.[162] In addition, faster blinking emitters could be used to increase the occurrence of single-emitter events and localizations of three emitters or more. As such, scalability of this method still relies on a photoswitching mechanism. If compared with SMLM traditional methods for both localization and tracking, in quantum-enhanced SMLM, it is not clear if outstanding problems in SMLM, such as limited speed due to acquisition of many camera frames, can be surpassed, as the antibunching acquisition can slow down this method as well. Localization precision below 30 nm or better has been theoretically predicted using antibunching and photoswitching (quantum-optically enhanced

STORM) of multiple emitters, even when closely spaced (125 emitters per μm).[56] Super-resolution Q-ISM has recently proved an increase in the resolution of confocal scanning microscopy up to twofold, and it has been applied to microtubules of fixed 3T3 cells labeled with QDs.[57] Images of the microtubules with confocal scanning microscopy, ISM, and Q-ISM are compared.[57] The resolution enhancement factors compared with the wide-field image are 1.29 and 1.74 for the ISM and Q-ISM, respectively, for the image of single QD. The use of nanosecond response time SPADs permits the improvement of the signal-to-noise ratio. Using Fourier reweighted[165] Q-ISM, further resolution improvement of 2.34 was achieved. The acquisition time to achieve a high signal-to-noise ratio in a Q-ISM image is generally longer than that for an ISM image, of the order of tens of milliseconds per scan step. As such, joint reconstruction of the images of the two methods was implemented via sparse reconstruction (SR) algorithms, and images of fluorescent QDs were validated via correlative electron microscope measurements.[164] In Figs. 6(h)–6(k), images from ISM and Q-ISM and their SR of fixed 3T3 cells labeled with fluorescent QDs with different dwell times are shown, providing a relatively accurate reconstruction of the images with 10 ms exposure time.

Another quantum correlation-enhanced microscopy approach to defeat the diffraction limit has been proposed theoretically. It has been proposed to combine quantum correlation and structured illumination (SIM) to achieve higher resolution. SIM introduces a resolution improvement of factor 2 and quantum correlation alone a factor of $\sqrt{k}$, where k is the correlation order or photon-number correlation. Quantum correlation combined with SIM could lead to an improvement scaling as $k + \sqrt{k}$.[167] The use of photon antibunching of single emitters to obtain sub-diffraction localization of pairs of quantum emitters of unknown relative intensity has been proposed. Specifically, the localization can be reconstructed by three separate Hanbury Brown and Twiss measurements.[168] This problem is impossible to solve based on intensity measurements alone. Two single emitters within the diffraction limit with different intensities can provide $g^2(0) < 0.5$ in a diffraction-limited image.

9 Conclusions and Outlook

In Table 2, we summarize the main results of SRM using CCs in diamond, SiC, and hBN with the achieved resolution and when spin nanoscopy has been achieved with the related magnetic

Table 2 Super-resolution and their spin variant techniques based on CCs with achieved subdiffraction resolution and magnetic imaging localization resolution and magnetic field sensitivity.

System (CC)	Method (magnetic field sensitivity) (nT/$\sqrt{\text{Hz}}$)	Resolution (magnetic imaging) (nm)
NV C-bulk	STED	5.8 to 80[29]
NV C-bulk	Spin-STED (ODMR and Rabi)	>100[45]
NV C-bulk	SIL-STED	2.4[112]
NV NDs	STED	10 to 40[32,114]
NV NDs	Spin-STED (ODMR)	>40[114]
NVN C-bulk	STED	50[106]
NV or NVN NDs in cells	STED	50 to 70[76,101]
NV C-bulk	CSD	4.1[35]
NV C-bulk	Spin-CSD	>100[35]
NV C-bulk	Spin-RESOFLT	35 to 50[115]
	Hahn-echo and magnetic sensing (250)	20 to 150[115]
NV C-bulk	GSD	8 to 16[31,61]
NV NDs	GSD	36[118]
NV C-bulk	SMLM	27 to 29[47]
NV C-bulk	Spin-SMLM (ODMR) (190000)	50 to 100[47]
NV NDs	Super-resolution radial fluctuations and 2PM	43[142]
NV NDs	SMLM	20 to 23[33,48]
NV NDs	Spin-SMLM (ODMR) (85)	17 to 20[48]
NV C-bulk	Single photon quantum correlation	290[55]
SiV C-bulk	STED	89[72]
hBN few layers flakes $V_BC_N^-$[83]	STED	50[85]
hBN few layers flakes	GSD	62[119]
hBN monolayer V_B[83]	SMLM	46[129]
SiC 4H CAV	SMLM	50[59]
SiC CAV 4H-NPs in cells	SMLM	18[59]

imaging localization resolution and, if available, the associated sensitivity. From Table 2, the merits of the various CCs and the current gaps can be identified. Progress in using CCs in SRM techniques has been achieved mainly in bulk diamond with the best resolution and some cases with ND NV centers. The variability of resolution may be attributed mostly to the material, as photophysical properties of ND NVs can vary due to the presence of dopants, other impurities, strain, and surface defects. While the SiV and H3 centers in diamond are the only other centers that have so far been used in STED, achieving a lower resolution than NV. STED microscopy has also been applied using hBN emitters mainly to investigate the spectroscopy of the vibronic states of the emitters. Due to the higher stimulated emission cross-section of the SiV and hBN CCs (see Table 1), together with bright SiV sub-10-nm NDs, it is expected that further studies could provide better performance than NV in specific applications for biological samples with sub-50-nm features. However, the SiV in NDs may not provide the opportunity of quantum sensing as does NV. Quantum sensing using hBN flakes has not yet been demonstrated, and optical spin read-out studies in this material are in their infancy. Other CCs in diamond, such as the germanium vacancy[169] or nickel-related centers[34] available from CVD originated NDs, should be investigated for STED application, even if their properties for SRM are not yet very well-known due to the difficulty of their mass production as SP emitters and in NDs. The combination of SRM with spin control and sensing or magnetic field mapping has also progressed. Based on the above-outlined studies, it appears that deterministic methods for achieving super-resolution, such as STED, GSD, and RESOLFT, can easily enable nanoscale resolution ODMR, with GSD and RESOLFT having a better perspective due to the lower optical intensities needed. Using the GS and the MS states, issues related to loss of phase of nearby spins may be less prominent than in STED, as observed in SPIN-RESOLFT.[115] However, it is expected that using the MS dark states in RESOLFT could also affect external spin states, thus limiting the control of nearby NVs. Two NVs at 150 nm apart were imaged. On the other hand, using a dark state as the charge state, such as NV^0, it has been shown that the nuclear spin control is still possible.[170] ODMR and Rabi oscillation combined with CSD may be a better approach for spin manipulation with a subdiffraction resolution, as nuclear spin states are preserved during ionization and deionization. In CSD-ODMR, only one NV is subject to microwave control, while the other is in a different charge state, unlike in STED where all NVs are subject to microwave control. Using CSD-ODMR and Rabi oscillation, two NVs separated by 100 nm were spin manipulated.[35] The SMLM's method to switch off NV can also interfere less in terms of nearby external spin dephasing as in CSD. ODMR-SMLM was achieved for magnetic field imaging with subdiffraction resolution.[47,48] Nanoscale magnetic imaging of 27 nm was achieved using spin-SMLM,[47] and the spin of two NVs was super-resolved using spin-SMLM with 23-nm resolution.[48] However, no Rabi-oscillation or spin-echo has been performed with SMLM yet. Spin-RESOLFT has enabled up to 20-nm resolution in mapping magnetic fields and 50-nm in mapping external nuclear spins. Spin-RESOLFT has achieved a sensitivity of 250 $\mathrm{nT}/\sqrt{\mathrm{Hz}}$ by sacrificing resolution with longer doughnut laser beam duration; while it improves resolution, it reduces the spin contrast. In spin-SMLM,[48] a higher sensitivity ($85\ \mathrm{nT}/\sqrt{\mathrm{Hz}}$) is achieved with longer dwell time compared with simple subdiffraction imaging localization without spin control. In this case, sensitivity increases by increasing the number of NV centers in an ND. While improving the sensitivity to achieve nano-MRI, a dynamical decoupling sequence is applied to shallow NVs using spin-RESOLFT.[115] Other super-resolution methods could also be explored in the future using CCs, such as the recently developed iso-STED, where adaptive optics is used to achieve sub-50-nm 3D resolution of structures in tissue.[171] While the bulk diamond NV has provided the highest localization and resolution, its resolution in NDs is limited by the size of the NDs, and, as such, the applicability to biological samples is limited. Nevertheless, using SMLM, NV^- in NDs could be used for nanoscale imaging and sensing of a magnetic field in a cellular environment. Other spin quantum-controlled methods could be used in conjunction with NDs to increase the applicability of these techniques in resolving biological samples. The need for improving the quality of NDs is not only in reducing the size while maintaining the spin and optical properties required, but also to better control their nitrogen doping. Controlling the nitrogen doping in NDs is relevant for the application of NDs in MS state depletion, GSD, RESOLFT, and CSD microscopy. In particular, CSD using ND NV centers has not yet been demonstrated and could be applied with quantum sensing and a lower optical excitation power to biological samples. While FNDs are presently not suitable to super-resolve nanometric size objects due to their 25-nm sizes, other nanomaterials such as SiC NPs and hBN flakes could be better used in the super-resolution of nanometric features. However, the application of SRM in SiC NPs is still limited to only one demonstration in still large particles. In hBN, the variety of CCs of yet not fully known origin or controlled fabrication can limit its current applicability to specific biological samples investigations; however, SMLM and STED in hBN have provided an understanding of the chemical properties of the hBN defects. Both SiC and hBN have the potential to apply spin nanoscopy methods as for the NV^- in diamond. However, the current CCs used for SMLM and STED have not yet been studied from the point of view of spin optical read-out and control in nanomaterials, or they have a very small ODMR signature, which makes their use in spin nanoscopy currently difficult. As such, more fundamental studies on these materials' other CCs are required to determine their full potential in SRM.

Quantum optics methods based on SP emission and second and higher-order photons correlation measurements have been recently implemented, and only one demonstration was applied to the NV in bulk diamond. While these methods based on their current implementation in colloidal QDs show promise in speeding up and extending applicability as an example of SMLM to nonblinking emitters, so far their performances are limited at the best to a factor of 2 resolution improvement ($\approx$120 nm) compared with confocal scanning microscopy and still far from the sub-50-nm resolution of the current state-of-the-art SMLM. Nevertheless, these methods appear promising because of the fast occurring technological advances in SP detectors' time resolution and should be investigated more in the space of CCs, for example, in hBN, where the concentration of single emitters and blinking properties are favorable to quantum-enhanced-SMLM. In addition, other quantum light-based methods[172] relying on quantum correlation have improved the signal-to-noise ratio in a coherent Raman microscope revealing molecular bonds within a cell, thus providing subdiffraction resolution. Such a nonlinear microscope enhanced by quantum correlation may apply to CCs in diamond or other point defects

imaging. Finally, other CCs in diamond and SiC could be investigated for super-resolution imaging combinations with quantum sensing.

References

1. L. Möckl, D. C. Lamb, and C. Bräuchle, "Super-resolved fluorescence microscopy: Nobel Prize in Chemistry 2014 for Eric Betzig, Stefan Hell, and William E. Moerner," *Angew. Chem. Int. Ed.* **53**(51), 13972–13977 (2014).
2. L. Schermelleh et al., "Super-resolution microscopy demystified," *Nat. Cell Biol.* **21**(1), 72–84 (2019).
3. S. Banerjee, S. Maurya, and R. Roy, "Single-molecule fluorescence imaging: generating insights into molecular interactions in virology," *J. Biosci.* **43**(3), 519–540 (2018).
4. S. Castelletto and A. Boretti, "Viral particle imaging by super-resolution fluorescence microscopy," *Chem. Phys. Impact* **2**, 100013 (2021).
5. S. Dhomkar et al., "Long-term data storage in diamond," *Sci. Adv.* **2**(10), e1600911 (2016).
6. M. Gu, Q. Zhang, and S. Lamon, "Nanomaterials for optical data storage," *Nat. Rev. Mater.* **3**(12), 16070 (2016).
7. J.-P. Tetienne et al., "Quantum imaging of current flow in graphene," *Sci. Adv.* **3**(4), e1602429 (2017).
8. F. Casola, T. van der Sar, and A. Yacoby, "Probing condensed matter physics with magnetometry based on nitrogen-vacancy centres in diamond," *Nat. Rev. Mater.* **3**(1), 17088 (2018).
9. D. Jin et al., "Nanoparticles for super-resolution microscopy and single-molecule tracking," *Nat. Methods* **15**(6), 415–423 (2018).
10. I. Aharonovich et al., "Diamond-based single-photon emitters," *Rep. Prog. Phys.* **74**(7), 076501 (2011).
11. C. Bradac et al., "Quantum nanophotonics with group IV defects in diamond," *Nat. Commun.* **10**(1), 5625 (2019).
12. A. Gruber et al., "Scanning confocal optical microscopy and magnetic resonance on single defect centers," *Science* **276**(5321), 2012–2014 (1997).
13. D. Ho, C.-H. K. Wang, and E. K.-H. Chow, "Nanodiamonds: the intersection of nanotechnology, drug development, and personalized medicine," *Sci. Adv.* **3**(7), e1500439 (2015).
14. A. Lohrmann et al., "A review on single photon sources in silicon carbide," *Rep. Prog. Phys.* **80**(3), 034502 (2017).
15. S. Castelletto and A. Boretti, "Silicon carbide color centers for quantum applications," *J. Phys. Photonics* **2**(2), 022001 (2020).
16. S. Castelletto et al., "A silicon carbide room-temperature single-photon source," *Nat. Mater.* **13**(2), 151–156 (2014).
17. S. Castelletto et al., "Room temperature quantum emission from cubic silicon carbide nanoparticles," *ACS Nano* **8**(8), 7938–7947 (2014).
18. W. F. Koehl et al., "Room temperature coherent control of defect spin qubits in silicon carbide," *Nature* **479**(7371), 84–87 (2011).
19. D. J. Christle et al., "Isolated electron spins in silicon carbide with millisecond coherence times," *Nat. Mater.* **14**(2), 160–163 (2015).
20. A. Lohrmann et al., "Activation and control of visible single defects in 4h-, 6h-, and 3c-sic by oxidation," *Appl. Phys. Lett.* **108**(2), 021107 (2016).
21. A. Oliveros, A. Guiseppi-Elie, and S. E. Saddow, "Silicon carbide: a versatile material for biosensor applications," *Biomed. Microdevices* **15**(2), 353–368 (2013).
22. J. S. Ponraj et al., "Sic nanostructures toward biomedical applications and its future challenges," *Crit. Rev. Solid State Mater. Sci.* **41**(5), 430–446 (2016).
23. T. Bělinová et al., "Immunomodulatory potential of differently-terminated ultra-small silicon carbide nanoparticles," *Nanomaterials* **10**(3), 573 (2020).
24. F. Hayee et al., "Revealing multiple classes of stable quantum emitters in hexagonal boron nitride with correlated optical and electron microscopy," *Nat. Mater.* **19**(5), 534–539 (2020).
25. J. D. Caldwell et al., "Photonics with hexagonal boron nitride," *Nat. Rev. Mater.* **4**(8), 552–567 (2019).
26. C. Bradac, "High-resolution optical imaging and sensing using quantum emitters in hexagonal boron-nitride," *Front. Phys.* **9**, 117 (2021).
27. L. Horváth et al., "*In vitro* investigation of the cellular toxicity of boron nitride nanotubes," *ACS Nano* **5**(5), 3800–3810 (2011).
28. A. Salvetti et al., "*In vivo* biocompatibility of boron nitride nanotubes: effects on stem cell biology and tissue regeneration in planarians," *Nanomedicine* **10**(12), 1911–1922 (2015).
29. E. Rittweger et al., "STED microscopy reveals crystal colour centres with nanometric resolution," *Nat. Photonics* **3**(3), 144–147 (2009).
30. M. H. Alkahtani et al., "Fluorescent nanodiamonds: past, present, and future," *Nanophotonics* **7**(8), 1423–1453 (2018).
31. E. Rittweger, D. Wildanger, and S. W. Hell, "Far-field fluorescence nanoscopy of diamond color centers by ground state depletion," *Europhys. Lett.* **86**(1), 14001 (2009).
32. K. Y. Han et al., "Three-dimensional stimulated emission depletion microscopy of nitrogen-vacancy centers in diamond using continuous-wave light," *Nano Lett.* **9**(9), 3323–3329 (2009).
33. M. Gu et al., "Super-resolving single nitrogen vacancy centers within single nanodiamonds using a localization microscope," *Opt. Express* **21**(15), 17639–17646 (2013).
34. S. Castelletto et al., "Production of multiple diamond-based single-photon sources," *IEEE J. Sel. Top. Quantum Electron.* **18**(6), 1792–1798 (2012).
35. X. Chen et al., "Subdiffraction optical manipulation of the charge state of nitrogen vacancy center in diamond," *Light Sci. Appl.* **4**(1), e230 (2015).
36. K. Arai et al., "Fourier magnetic imaging with nanoscale resolution and compressed sensing speed-up using electronic spins in diamond," *Nat. Nanotechnol.* **10**(10), 859–864 (2015).
37. H. Mamin et al., "Nanoscale nuclear magnetic resonance with a nitrogen-vacancy spin sensor," *Science* **339**(6119), 557–560 (2013).
38. J. Wrachtrup and F. Jelezko, "Processing quantum information in diamond," *J. Phys. Condens. Matter* **18**(21), S807–S824 (2006).
39. L. Childress et al., "Fault-tolerant quantum communication based on solid-state photon emitters," *Phys. Rev. Lett.* **96**(7), 070504 (2006).
40. N. Bar-Gill et al., "Solid-state electronic spin coherence time approaching one second," *Nat. Commun.* **4**(1), 1743 (2013).
41. D. Farfurnik et al., "Optimizing a dynamical decoupling protocol for solid-state electronic spin ensembles in diamond," *Phys. Rev. B* **92**(6), 060301 (2015).
42. A. Boretti et al., "Nitrogen-vacancy centers in diamond for nanoscale magnetic resonance imaging applications," *Beilstein J. Nanotechnol.* **10**(1), 2128–2151 (2019).
43. J. L. Webb et al., "Optimization of a diamond nitrogen vacancy centre magnetometer for sensing of biological signals," *Front. Phys.* **8**, 430 (2020).
44. E. Bernardi et al., "A biocompatible technique for magnetic field sensing at (sub)cellular scale using nitrogen-vacancy centers," *EPJ Quantum Technol.* **7**(1), 13 (2020).
45. D. Wildanger, J. R. Maze, and S. W. Hell, "Diffraction unlimited all-optical recording of electron spin resonances," *Phys. Rev. Lett.* **107**(1), 017601 (2011).
46. P. C. Maurer et al., "Far-field optical imaging and manipulation of individual spins with nanoscale resolution," *Nat. Phys.* **6**(11), 912–918 (2010).
47. M. Pfender et al., "Single-spin stochastic optical reconstruction microscopy," *Proc. Natl. Acad. Sci. U. S. A.* **111**(41), 14669–14674 (2014).
48. M. Barbiero et al., "Spin-manipulated nanoscopy for single nitrogen-vacancy center localizations in nanodiamonds," *Light Sci. Appl.* **6**(11), e17085 (2017).

49. M. Barbiero et al., "Nanoscale magnetic imaging enabled by nitrogen vacancy centres in nanodiamonds labelled by iron-oxide nanoparticles," *Nanoscale* **12**(16), 8847–8857 (2020).
50. A. Boretti and S. Castelletto, "Nanometric resolution magnetic resonance imaging methods for mapping functional activity in neuronal networks," *MethodsX* **3**, 297–306 (2016).
51. P. Wang et al., "Nanoscale magnetic imaging of ferritins in a single cell," *Sci. Adv.* **5**(4), eaau8038 (2019).
52. M. S. Grinolds et al., "Nanoscale magnetic imaging of a single electron spin under ambient conditions," *Nat. Phys.* **9**(4), 215–219 (2013).
53. M. J. Ku et al., "Imaging viscous flow of the Dirac fluid in graphene," *Nature* **583**(7817), 537–541 (2020).
54. O. Schwartz et al., "Superresolution microscopy with quantum emitters," *Nano Lett.* **13**(12), 5832–5836 (2013).
55. D. G. Monticone et al., "Beating the Abbe diffraction limit in confocal microscopy via nonclassical photon statistics," *Phys. Rev. Lett.* **113**(14), 143602 (2014).
56. M. Aßmann, "Quantum-optically enhanced storm (QUEST) for multi-emitter localization," *Sci. Rep.* **8**(1), 7829 (2018).
57. R. Tenne et al., "Super-resolution enhancement by quantum image scanning microscopy," *Nat. Photonics* **13**(2), 116–122 (2019).
58. Y. Nishimura et al., "Wide-field fluorescent nanodiamond spin measurements toward real-time large-area intracellular thermometry," *Sci. Rep.* **11**(1), 4248 (2021).
59. S. Castelletto et al., "Imaging with nanometer resolution using optically active defects in silicon carbide," *Phys. Rev. Appl.* **14**(3), 034021 (2020).
60. S. Pezzagna et al., "Nanoscale engineering and optical addressing of single spins in diamond," *Small* **6**(19), 2117–2121 (2010).
61. K. Y. Han et al., "Metastable dark states enable ground state depletion microscopy of nitrogen vacancy centers in diamond with diffraction-unlimited resolution," *Nano Lett.* **10**(8), 3199–3203 (2010).
62. E. Herbschleb et al., "Ultra-long coherence times amongst room-temperature solid-state spins," *Nat. Commun.* **10**(1), 3766 (2019).
63. J. Storteboom et al., "Lifetime investigation of single nitrogen vacancy centres in nanodiamonds," *Opt. Express* **23**(9), 11327–11333 (2015).
64. C. Kurtsiefer et al., "Stable solid-state source of single photons," *Phys. Rev. Lett.* **85**(2), 290–293 (2000).
65. F. A. Inam et al., "Emission and nonradiative decay of nanodiamond NV centers in a low refractive index environment," *ACS Nano* **7**(5), 3833–3843 (2013).
66. A. Mohtashami and A. F. Koenderink, "Suitability of nanodiamond nitrogen–vacancy centers for spontaneous emission control experiments," *New J. Phys.* **15**(4), 043017 (2013).
67. T. Plakhotnik and H. Aman, "NV-centers in nanodiamonds: how good they are," *Diam. Relat. Mater.* **82**, 87–95 (2018).
68. P. Reineck et al., "Not all fluorescent nanodiamonds are created equal: a comparative study," *Part. Part. Syst. Char.* **36**(3), 1900009 (2019).
69. H. S. Knowles, D. M. Kara, and M. Atatüre, "Observing bulk diamond spin coherence in high-purity nanodiamonds," *Nat. Mater.* **13**(1), 21–25 (2014).
70. A. V. Turukhin et al., "Picosecond photoluminescence decay of si-doped chemical-vapor-deposited diamond films," *Phys. Rev. B* **54**(23), 16448–16451 (1996).
71. C. Wang et al., "Single photon emission from SIV centres in diamond produced by ion implantation," *J. Phys. B* **39**(1), 37–41 (2005).
72. Y. Silani, F. Hubert, and V. M. Acosta, "Stimulated emission depletion microscopy with diamond silicon vacancy centers," *ACS Photonics* **6**(10), 2577–2582 (2019).
73. L. J. Rogers et al., "All-optical initialization, readout, and coherent preparation of single silicon-vacancy spins in diamond," *Phys. Rev. Lett.* **113**(26), 263602 (2014).
74. E. Neu, M. Agio, and C. Becher, "Photophysics of single silicon vacancy centers in diamond: implications for single photon emission," *Opt. Express* **20**(18), 19956–19971 (2012).
75. E. Neu et al., "Single photon emission from silicon-vacancy colour centres in chemical vapour deposition nano-diamonds on iridium," *New J. Phys.* **13**(2), 025012 (2011).
76. G. Laporte and D. Psaltis, "Sted imaging of green fluorescent nanodiamonds containing nitrogen-vacancy-nitrogen centers," *Biomed. Opt. Express* **7**(1), 34–44 (2016).
77. J.-H. Hsu et al., "Nonblinking green emission from single H3 color centers in nanodiamonds," *Appl. Phys. Lett.* **98**(19), 193116 (2011).
78. D. Beke et al., "Room-temperature defect qubits in ultrasmall nanocrystals," *J. Phys. Chem. Lett.* **11**(5), 1675–1681 (2020).
79. J.-F. Wang et al., "Experimental optical properties of single nitrogen vacancy centers in silicon carbide at room temperature," *ACS Photonics* **7**(7), 1611–1616 (2020).
80. J.-F. Wang et al., "Coherent control of nitrogen-vacancy center spins in silicon carbide at room temperature," *Phys. Rev. Lett.* **124**(22), 223601 (2020).
81. Z. Mu et al., "Coherent manipulation with resonant excitation and single emitter creation of nitrogen vacancy centers in 4H silicon carbide," *Nano Lett.* **20**(8), 6142–6147 (2020).
82. R. N. E. Malein et al., "Stimulated emission depletion spectroscopy of color centers in hexagonal boron nitride," *ACS Photonics* **8**(4), 1007–1012 (2021).
83. N. Mendelson et al., "Identifying carbon as the source of visible single-photon emission from hexagonal boron nitride," *Nat. Mater.* **20**(3), 321–328 (2021).
84. M. K. Boll et al., "Photophysics of quantum emitters in hexagonal boron-nitride nano-flakes," *Opt. Express* **28**(5), 7475–7487 (2020).
85. P. Khatri et al., "Stimulated emission depletion microscopy with color centers in hexagonal boron nitride," *ACS Photonics* **8**(7), 2081–2087 (2021).
86. A. Gottscholl et al., "Initialization and read-out of intrinsic spin defects in a van der Waals crystal at room temperature," *Nat. Mater.* **19**(5), 540–545 (2020).
87. A. Gottscholl et al., "Room temperature coherent control of spin defects in hexagonal boron nitride," *Sci. Adv.* **7**(14), eabf3630 (2021).
88. S. W. Hell and J. Wichmann, "Breaking the diffraction resolution limit by stimulated emission: stimulated-emission-depletion fluorescence microscopy," *Opt. Lett.* **19**(11), 780–782 (1994).
89. S. W. Hell and M. Kroug, "Ground-state-depletion fluorescence microscopy: a concept for breaking the diffraction resolution limit," *Appl. Phys. B* **60**(5), 495–497 (1995).
90. S. Bretschneider, C. Eggeling, and S. W. Hell, "Breaking the diffraction barrier in fluorescence microscopy by optical shelving," *Phys. Rev. Lett.* **98**(21), 218103 (2007).
91. M. Hofmann et al., "Breaking the diffraction barrier in fluorescence microscopy at low light intensities by using reversibly photoswitchable proteins," *Proc. Natl. Acad. Sci. U. S. A.* **102**(49), 17565–17569 (2005).
92. M. G. L. Gustafsson, "Surpassing the lateral resolution limit by a factor of two using structured illumination microscopy," *J. Microsc.* **198**(2), 82–87 (2000).
93. E. Betzig et al., "Imaging intracellular fluorescent proteins at nanometer resolution," *Science* **313**(5793), 1642–1645 (2006).
94. S. Hess, T. Girirajan, and M. Mason, "Ultra-high resolution imaging by fluorescence photoactivation localization microscopy," *Biophys. J.* **91**(11), 4258–4272 (2006).
95. B. Huang, M. Bates, and X. Zhuang, "Super-resolution fluorescence microscopy," *Annu. Rev. Biochem.* **78**(1), 993–1016 (2009).
96. G. Huszka and M. A. Gijs, "Super-resolution optical imaging: a comparison," *Micro Nano Eng.* **2**, 7–28 (2019).
97. G. Vicidomini, P. Bianchini, and A. Diaspro, "STED super-resolved microscopy," *Nat. Methods* **15**(3), 173–182 (2018).

98. U. V. Nägerl et al., "Live-cell imaging of dendritic spines by STED microscopy," *Proc. Natl. Acad. Sci. U. S. A.* **105**(48), 18982–18987 (2008).
99. F. Bottanelli et al., "Two-colour live-cell nanoscale imaging of intracellular targets," *Nat. Commun.* **7**(1), 10778 (2016).
100. N. H. Revelo and S. O. Rizzoli, "Application of sted microscopy to cell biology questions," in *Advanced Fluorescence Microscopy*, P. Verveer, Ed., Vol. 1251, pp. 213–230, Humana Press, New York (2015).
101. Y.-K. Tzeng et al., "Superresolution imaging of albumin-conjugated fluorescent nanodiamonds in cells by stimulated emission depletion," *Angew. Chem. Int. Ed.* **50**(10), 2262–2265 (2011).
102. N. Prabhakar et al., "Sted-tem correlative microscopy leveraging nanodiamonds as intracellular dual-contrast markers," *Small* **14**(5), 1701807 (2018).
103. P. A. Pellett et al., "Two-color sted microscopy in living cells," *Biomed. Opt. Express* **2**(8), 2364–2371 (2011).
104. N. Prabhakar et al., "Fluorescent and electron-dense green color emitting nanodiamonds for single-cell correlative microscopy," *Molecules* **25**(24), 5897 (2020).
105. F.-J. Hsieh et al., "Correlative light-electron microscopy of lipid-encapsulated fluorescent nanodiamonds for nanometric localization of cell surface antigens," *Anal. Chem.* **90**(3), 1566–1571 (2018).
106. R. Kolesov et al., "Superresolution microscopy of single rare-earth emitters in YAG and H3 centers in diamond," *Phys. Rev. Lett.* **120**(3), 033903 (2018).
107. S. V. Bolshedvorskii et al., "Single silicon vacancy centers in 10 nm diamonds for quantum information applications," *ACS Appl. Nano Mater.* **2**(8), 4765–4772 (2019).
108. M. D. Torelli, N. A. Nunn, and O. A. Shenderova, "A perspective on fluorescent nanodiamond bioimaging," *Small* **15**(48), 1902151 (2019).
109. J. Jeske et al., "Stimulated emission from nitrogen-vacancy centres in diamond," *Nat. Commun.* **8**(1), 14000 (2017).
110. A. Sajid, M. J. Ford, and J. R. Reimers, "Single-photon emitters in hexagonal boron nitride: a review of progress," *Rep. Prog. Phys.* **83**(4), 044501 (2020).
111. S. Castelletto et al., "Hexagonal boron nitride: a review of the emerging material platform for single-photon sources and the spin–photon interface," *Beilstein J. Nanotechnol.* **11**(1), 740–769 (2020).
112. D. Wildanger et al., "Solid immersion facilitates fluorescence microscopy with nanometer resolution and sub-Ångström emitter localization," *Adv. Mater.* **24**(44), OP309–OP313 (2012).
113. F. Jelezko et al., "Observation of coherent oscillations in a single electron spin," *Phys. Rev. Lett.* **92**(7), 076401 (2004).
114. S. Arroyo-Camejo et al., "Stimulated emission depletion microscopy resolves individual nitrogen vacancy centers in diamond nanocrystals," *ACS Nano* **7**(12), 10912–10919 (2013).
115. J.-C. Jaskula et al., "Superresolution optical magnetic imaging and spectroscopy using individual electronic spins in diamond," *Opt. Express* **25**(10), 11048–11064 (2017).
116. H. Zhang et al., "Selective addressing of solid-state spins at the nanoscale via magnetic resonance frequency encoding," *npj Quantum Inf.* **3**(1), 31 (2017).
117. I. Testa et al., "Nanoscopy of living brain slices with low light levels," *Neuron* **75**(6), 992–1000 (2012).
118. J. Storterboom et al., "Ground-state depletion nanoscopy of nitrogen-vacancy centres in nanodiamonds," *Nanoscale Res. Lett.* **16**, 44 (2021).
119. M. Kianinia et al., "All-optical control and super-resolution imaging of quantum emitters in layered materials," *Nat. Commun.* **9**(1), 874 (2018).
120. X. Yang et al., "Sub-diffraction imaging of nitrogen-vacancy centers in diamond by stimulated emission depletion and structured illumination," *RSC Adv.* **4**(22), 11305–11310 (2014).
121. S. A. Jones et al., "Fast, three-dimensional super-resolution imaging of live cells," *Nat. Methods* **8**(6), 499–505 (2011).
122. R. Strack, "Deep learning advances super-resolution imaging," *Nat. Methods* **15**(6), 403 (2018).
123. F. Wang et al., "Editorial: recent advances in fluorescent probes for super-resolution microscopy," *Front. Chem.* **9**, 698531 (2021).
124. E. Nehme et al., "Deep-storm: super-resolution single-molecule microscopy by deep learning," *Optica* **5**(4), 458–464 (2018).
125. M. Alkahtani et al., "Growth of high-purity low-strain fluorescent nanodiamonds," *ACS Photonics* **6**(5), 1266–1271 (2019).
126. M. Motlag et al., "Molecular-scale nanodiamond with high-density color centers fabricated from graphite by laser shocking," *Cell Rep. Phys. Sci.* **3**(5), 100054 (2020).
127. C. Laube et al., "Controlling the fluorescence properties of nitrogen vacancy centers in nanodiamonds," *Nanoscale* **11**(4), 1770–1783 (2019).
128. Y. Huang et al., "Superresolution localization of nitrogen-vacancy centers in diamond with quantum-controlled photoswitching," *Phys. Rev. A* **102**(4), 040601 (2020).
129. J. Feng et al., "Imaging of optically active defects with nanometer resolution," *Nano Lett.* **18**(3), 1739–1744 (2018).
130. J. Comtet et al., "Wide-field spectral super-resolution mapping of optically active defects in hexagonal boron nitride," *Nano Lett.* **19**(4), 2516–2523 (2019).
131. N. M. H. Duong et al., "Facile production of hexagonal boron nitride nanoparticles by cryogenic exfoliation," *Nano Lett.* **19**(8), 5417–5422 (2019).
132. J. Comtet et al., "Direct observation of water-mediated single-proton transport between HBN surface defects," *Nat. Nanotechnol.* **15**(7), 598–604 (2020).
133. F. Chen et al., "Cellular toxicity of silicon carbide nanomaterials as a function of morphology," *Biomaterials* **179**, 60–70 (2018).
134. F. Helmchen and W. Denk, "Deep tissue two-photon microscopy," *Nat. Methods* **2**(12), 932–940 (2005).
135. T. J. Gould et al., "Adaptive optics enables 3D STED microscopy in aberrating specimens," *Opt. Express* **20**(19), 20998–21009 (2012).
136. T.-L. Wee et al., "Two-photon excited fluorescence of nitrogen-vacancy centers in proton-irradiated type ib diamond," *J. Phys. Chem. A* **111**(38), 9379–9386 (2007).
137. P. Ji et al., "Multiple-photon excitation of nitrogen vacancy centers in diamond," *Phys. Rev. B* **97**(13), 134112 (2018).
138. Y.-R. Chang et al., "Mass production and dynamic imaging of fluorescent nanodiamonds," *Nat. Nanotechnol.* **3**(5), 284–288 (2008).
139. C. M. Jimenez et al., "Nanodiamond–PMO for two-photon PDT and drug delivery," *J. Mater. Chem. B* **4**(35), 5803–5808 (2016).
140. Y. Y. Hui et al., "Two-photon fluorescence correlation spectroscopy of lipid-encapsulated fluorescent nanodiamonds in living cells," *Opt. Express* **18**, 5896–5905 (2010).
141. M. Barbiero, S. Castelletto, and M. Gu, "Multi-focal laser fabrication of nitrogen vacancy centres in a bulk diamond," *OSA Continuum* **3**(12), 3416–3423 (2020).
142. G. E. Johnstone, G. S. Cairns, and B. R. Patton, "Nanodiamonds enable adaptive-optics enhanced, super-resolution, two-photon excitation microscopy," *R. Soc. Open Sci.* **6**(7), 190589 (2019).
143. S. Culley et al., "SRRF: universal live-cell super-resolution microscopy," *Int. J. Biochem. Cell Biol.* **101**, 74–79 (2018).
144. N. Gustafsson et al., "Fast live-cell conventional fluorophore nanoscopy with imagej through super-resolution radial fluctuations," *Nat. Commun.* **7**(1), 12471 (2016).
145. A. W. Schell et al., "Non-linear excitation of quantum emitters in hexagonal boron nitride multiplayers," *APL Photonics* **3**(9), 091302 (2016).
146. M. Alkahtani and P. Hemmer, "Charge stability of nitrogen-vacancy color centers in organic nanodiamonds," *Opt. Mater. Express* **10**(5), 1224–1231 (2020).

147. N. Aslam et al., "Photo-induced ionization dynamics of the nitrogen vacancy defect in diamond investigated by single-shot charge state detection," *New J. Phys.* **15**(1), 013064 (2013).
148. P. Siyushev et al., "Optically controlled switching of the charge state of a single nitrogen-vacancy center in diamond at cryogenic temperatures," *Phys. Rev. Lett.* **110**(16), 167402 (2013).
149. Y. Doi et al., "Pure negatively charged state of the NV center in n-type diamond," *Phys. Rev. B* **93**(8), 081203 (2016).
150. E. Bauch et al., "Ultralong dephasing times in solid-state spin ensembles via quantum control," *Phys. Rev. X* **8**(3), 031025 (2018).
151. S. Li et al., "Optical far-field super-resolution microscopy using nitrogen vacancy center ensemble in bulk diamond," *Appl. Phys. Lett.* **109**(11), 111107 (2016).
152. X.-D. Chen et al., "Near-infrared-enhanced charge-state conversion for low-power optical nanoscopy with nitrogen-vacancy centers in diamond," *Phys. Rev. Appl.* **7**(1), 014008 (2017).
153. D.-F. Li et al., "Low power charge state depletion nanoscopy of the defect in diamonds with a pulsed laser excitation," *Opt. Lett.* **45**(3), 730–733 (2020).
154. X.-D. Chen et al., "Superresolution multifunctional sensing with the nitrogen-vacancy center in diamond," *Phys. Rev. Appl.* **12**(4), 044039 (2019).
155. T. Gregory et al., "Imaging through noise with quantum illumination," *Sci. Adv.* **6**(6), eaay2652 (2020).
156. P.-A. Moreau et al., "Imaging with quantum states of light," *Nat. Rev. Phys.* **3**(6), 367–380 (2019).
157. S. W. Hell, J. Soukka, and P. E. Hänninen, "Two- and multiphoton detection as an imaging mode and means of increasing the resolution in far-field light microscopy: a study based on photon-optics," *Bioimaging* **3**(2), 64–69 (1995).
158. P. Hong and G. Zhang, "A review of super-resolution imaging through optical high-order interference [invited]," *Appl. Sci.* **9**(6), 1166 (2019).
159. H. J. Kimble, M. Dagenais, and L. Mandel, "Photon antibunching in resonance fluorescence," *Phys. Rev. Lett.* **39**(11), 691–695 (1977).
160. O. Schwartz and D. Oron, "Improved resolution in fluorescence microscopy using quantum correlations," *Phys. Rev. A* **85**(3), 033812 (2012).
161. T. Dertinger et al., "Fast, background-free, 3D super-resolution optical fluctuation imaging (SOFI)," *Proc. Natl. Acad. Sci.* **106**(52), 22287–22292 (2009).
162. G. Lubin et al., "Quantum correlation measurement with single photon avalanche diode arrays," *Opt. Express* **27**(23), 32863–32882 (2019).
163. Y. Israel et al., "Quantum correlation enhanced super-resolution localization microscopy enabled by a fibre bundle camera," *Nat. Commun.* **8**(1), 14786 (2017).
164. U. Rossman et al., "Rapid quantum image scanning microscopy by joint sparse reconstruction," *Optica* **6**(10), 1290–1296 (2019).
165. C. B. Müller and J. Enderlein, "Image scanning microscopy," *Phys. Rev. Lett.* **104**(19), 198101 (2010).
166. C. J. Sheppard, S. B. Mehta, and R. Heintzmann, "Super-resolution by image scanning microscopy using pixel reassignment," *Opt. Lett.* **38**(15), 2889–2892 (2013).
167. A. Classen et al., "Superresolution via structured illumination quantum correlation microscopy," *Optica* **4**(6), 580–587 (2017).
168. J. G. Worboys, D. W. Drumm, and A. D. Greentree, "Quantum multilateration: subdiffraction emitter pair localization via three spatially separate Hanbury Brown and Twiss measurements," *Phys. Rev. A* **101**(1), 013810 (2020).
169. T. Iwasaki et al., "Germanium-vacancy single color centers in diamond," *Sci. Rep.* **5**(1), 12882 (2015).
170. G. Waldherr et al., "Dark states of single nitrogen-vacancy centers in diamond unraveled by single shot NMR," *Phys. Rev. Lett.* **106**(15), 157601 (2011).
171. X. Hao et al., "Three-dimensional adaptive optical nanoscopy for thick specimen imaging at sub-50-nm resolution," *Nat. Methods* **18**(6), 688–693 (2021).
172. C. A. Casacio et al., "Quantum-enhanced nonlinear microscopy," *Nature* **594**(7862), 201–206 (2021).

Stefania Castelletto is a professor of engineering at RMIT University. She received her degree in physics from the University of Turin in 1992 and her PhD in quantum metrology from the Polytechnic of Turin University in 1998. She is the author of more than 160 journal articles and three book chapters. Her current research interests include super-resolution in nanodiamonds and silicon carbide, color centers in diamond, and silicon carbide for quantum technologies.

Alberto Boretti completed his PhD in energy engineering in 1988. He has been a senior researcher and manager in the automotive industry in Italy for 17 years. Then, he has been a senior research fellow, and engineering associate professor, professor, and head of a department, in universities in Australia, USA, and GCC countries for 15 years. He is currently dean of research and graduates' studies. He has published so far about 370 articles in refereed journals, mostly single-author, plus book, book chapters, patents, and conference papers, in various fields of science and engineering.

Review Article

ADVANCED PHOTONICS

Quantum entanglement on photonic chips: a review

Xiaojiong Chen,[a,†] Zhaorong Fu,[a,†] Qihuang Gong,[a,b,c,d] and Jianwei Wang[a,b,c,d,*]
[a]Peking University, School of Physics, State Key Laboratory for Mesoscopic Physics, Beijing, China
[b]Peking University, Frontiers Science Center for Nano-Optoelectronics, Collaborative Innovation Center of Quantum Matter, Beijing, China
[c]Shanxi University, Collaborative Innovation Center of Extreme Optics, Taiyuan, China
[d]Peking University Yangtze Delta Institute of Optoelectronics, Nantong, China

Abstract. Entanglement is one of the most vital properties of quantum mechanical systems, and it forms the backbone of quantum information technologies. Taking advantage of nano/microfabrication and particularly complementary metal-oxide-semiconductor manufacturing technologies, photonic integrated circuits (PICs) have emerged as a versatile platform for the generation, manipulation, and measurement of entangled photonic states. We summarize the recent progress of quantum entanglement on PICs, starting from the generation of nonentangled and entangled biphoton states, to the generation of entangled states of multiple photons, multiple dimensions, and multiple degrees of freedom, as well as their applications for quantum information processing.

Keywords: quantum entanglement; integrated optics; photonic chip.

Received Aug. 21, 2021; revised manuscript received Nov. 8, 2021; accepted for publication Nov. 15, 2021; published online Dec. 7, 2021.

[DOI: 10.1117/1.AP.3.6.064002]

1 Introduction

The famous Einstein–Podolsky–Rosen (EPR) state was originally proposed[1] and later named "entangled state"[2] for the debate of the completeness of the quantum mechanical description of reality. Pioneering experiments of EPR entanglement have allowed the exclusion of the presence of local hidden variables by violating the Bell inequality[3] and allowed significant Bell tests with a closure of detection and distance loopholes.[4–6] Moreover, entanglement has also become the enabling resource for quantum information applications in the fields of quantum communication and networks,[7] quantum metrology and imaging,[8,9] and quantum computation and simulations.[10,11] In all of the above fundamental investigations and technological developments, the photon has been in the core position, owing to its low-noise nature, ease of control, room-temperature operation, and high-speed transmission.[12] For example, the loophole-free Bell tests were implemented in entangled photonic systems.[4–6] The photon is recognized as the inevitable carrier for global-scale quantum key distribution[13] and quantum internet.[14] Recently, Boson sampling with photons was used to demonstrate quantum computational advantages.[15] Universal quantum computing with photons is possible with largely entangled cluster states.[16–18] Integrated quantum photonics provides a compact, reliable, reprogrammable, and scalable platform for the study of fundamental quantum physics and for the implementation of profound quantum applications.[19] Leveraging mature complementary metal-oxide-semiconductor (CMOS) fabrication, integrated photonic quantum technology progressed significantly since its first demonstration in the controlled-NOT logic gate on silica waveguide circuits in 2008.[20] This includes the development of advanced material systems,[20–32] implementations of major quantum communication protocols,[28,32,33] and proof-of-principle demonstrations of quantum computation and quantum simulation algorithms.[34–36] We recommend other reviews of those topics in Refs. 19 and 37.

In this review, we summarize the experimental progress of on-chip generation, manipulation, and measurement of entangled photonic states on integrated silicon-photonic quantum chips. In Sec. 2, we introduce the representation of on-chip quantum states in various degrees of freedom (DoFs) of single photons. In Sec. 3, we introduce integrated parametric photon-pair sources (nonentangled photon-pairs). In Sec. 4, we then focus on various types of photonic entangled states, including entangled biphoton states and entangled states of multiple

*Address all correspondence to Jianwei Wang, jianwei.wang@pku.edu.cn
†These authors contributed equally to this work.

photons, multiple dimensions, and multiple DoFs. Finally, we briefly review possible chip-scale applications with entangled states and discuss future challenges and opportunities.

2 On-Chip Encoding Single-Photon Quantum States

A photon features a broad spectrum of different DoFs that can represent the basic units of quantum information, i.e., qubit $\alpha|0\rangle + \beta|1\rangle$, where α, β are the complex amplitudes. The available DoFs include position (path), polarization, frequency (wavelength), and spatial and temporal modes. Notably, the basic quantum information unit usually is defined in the binary format as a qubit, but it can be generally defined in the d-nary format as a qudit $\frac{1}{\sqrt{d}}\sum_{i=0}^{d-1} c_i|i\rangle$, where $|i\rangle$ is the logical state in the i'th mode.

In bulk-optics quantum experiments, the DoF of polarization has been extensively explored, e.g., in early seminal demonstrations.[38–40] Similar to the bulk-optics realization of polarized qubits by a birefringent waveplate and polarization beamsplitter (PBS) on integrated photonic chips, the polarization of photons can be manipulated by an integrated polarization rotator and PBS (i.e., birefringent waveguide or structure), which have been well developed in the silicon-photonics field.[41,42] Another commonly implemented DoF is the location or position information of photons. On integrated photonic chips, the $|0\rangle$ and $|1\rangle$ logic states can be well-defined in two modes in two separate optical waveguides that are physically phase-stabilized when manipulating the qubit states. This approach usually refers to path-encoding or dual-rail encoding in integrated quantum photonics. Path-encoded qubits can be manipulated by integrated beamsplitters and optical interferometers with high levels of fidelity, universality, dense integration, and reprogrammability, and therefore have been widely adopted in many integrated photonic quantum experiments.[24,43,44] The temporal mode of photons is also one of the available DoFs. Using fast light modulation or long optical delays, qubit states in two temporal modes or time bins can be generated. With the recent development of fast modulator and low-loss waveguides, time-bin encoded photons may provide an efficient solution for the implementation of chip-scale quantum key distributions. Moreover, optical waveguides support high-order eigenmodes, which allows the encoding of qubit or qudit states in the spatial mode DoF. The recent development of multimode silicon photonics enables mode-entanglement and its applications.[45,46] Such a mode-encoding state in optical waveguides can be reliably operated and transmitted, which is fundamentally similar to the case of optical orbital angular momentum in bulk-optics, where it is reliable.[47–50] Discrete frequency bins, usually existing in optical microresonators, can be in a coherent superposition state, thus allowing the preparation of qubits or qudits in the frequency DoF.[51] This approach recently has allowed interesting demonstrations of frequency entanglement.[52,53]

3 Integrated Waveguide Photon-Pair Sources

High-quality single-photon sources are indispensable in photonic quantum technologies. An ideal single-photon source has to produce pure photons with high efficiency, and the photons have to be identical to those from other independent sources. Parametric nonlinear-optical sources emit photons nondeterministically, and they can be integrated into large arrays, in which each owns high purity, heralding efficiency and indistinguishability. Such parametric photon sources produce a pair of photons, and the success of detecting one of them indicates the presence of the other, referring to heralding single-photon sources. The integration of parametric nonlinear-optical sources not only provides the possibility for future multiplexing high-efficiency single-photon sources[54] but also for the generation of different entangled states.

The generation of entangled photons relies on the spontaneous parametric down conversion (SPDC) process in $\chi^{(2)}$ materials or the spontaneous four-wave mixing (SFWM) process in $\chi^{(3)}$ materials. Integrated SPDC photon-pair sources and entangled sources have been demonstrated in periodically poled lithium niobate,[26,27] gallium arsenide,[30,31] and aluminum nitride[55] waveguides and structures. Here, we focus more on the discussion of third-order silicon-based material systems, such as silicon-on-insulator and silicon nitride.

The physical laws governing photon-pair generation are the conservations of momentum and energy. The former usually refers to the phase matching condition for nonlinear-optical processes. The simplest photon-pair source is the one using straight waveguides, e.g., silicon waveguides. By optimizing the waveguide geometry such as waveguide width, thickness, or etching depth to engineer group velocity dispersion, photon pairs can be generated in a wide spectrum through SFWM. This type of straight waveguide source can be easily and reliably implemented on chip, for example, an array of 16 waveguide sources.[43] However, it only reaches high spectral purity at the expense of losing brightness and heralding efficiency. To achieve both high purity and heralding efficiency, dual-pump SFWM[56,57] and intermodal SFWM[58] have been proposed. Recently, a multimode waveguides source based on a dual-mode pump-delayed excitation scheme was demonstrated in silicon, with a spectral purity of 0.9904(6), a mutual indistinguishability of 0.987(2), and >90% heralding efficiency.[59] Another type of integrated photon-pair source is based on optical microresonators, e.g., microring and microdisk. For a simple point-coupled ring resonator, the maximum photon pair generation rate can be achieved at a critical coupling point, but the heralding efficiency of photon pairs is bounded by 0.50, implying a trade-off balance.[60] At the same time, the spectral purity relies on the quantity factor, and it shows a theoretical upper limit of the purity of 0.93.[61] An experimental demonstration of an array of microresonator-based photon-pair sources was reported with purity of 0.90, heralding efficiency of 0.50, and indistinguishability of 0.90.[62] Two approaches are proposed to improve the performance. One is to adopt two delayed pulsed lights for pumping, in which the pump spectral width can be increased, and thus the upper limit of purity can be improved up to 0.999.[63] The second is to use a dual-MZI-coupled microring resonator to independently control the linewidths of the pump and signal (idler) photons working at different coupling points,[61] and a purity of 0.95 was experimentally obtained.[64] A similar scheme has also been experimentally investigated.[65]

4 Generation, Manipulation, and Measurement of Entanglement on Photonic Chips

The generation, manipulation, and measurement of large entanglement structure is at the heart of on-chip quantum information processing. For instance, one-way quantum computing requires large-scale cluster states to transmit coherent logical operators along the entanglement structure.[16,66] Quantum internet relies on

the distribution of entanglement between quantum processors at different locations.[14] In this section, we introduce how to entangle photons such as Bell states on quantum photonic chips, and, in particular, how to generate multi-DoF, multiphoton, and multidimensional entanglement states.

Integrated photonics is able to engineer multiple DoFs to encode and process quantum information. The coherent conversion between different DoFs of photons can make use of their own advantages for implementing different tasks. For example, path-to-polarization conversion allows the reliable distribution of entangled states between two separate chips, maintaining coherence and robustness both on chip and in optical fibers[62,67] [see Fig. 1(a)]. Coherent conversion of entangled states between path, polarization, and transverse mode was also reported in a silicon chip[68] [see Fig. 1(b)]. Moreover, simultaneously entangling multiple DoFs of photons, named hyperentanglement, provides an efficient way to expand the Hilbert space and enrich applications.[69,70] In bulk-optics, three different DoFs (path, polarization, and orbital angular momentum mode) of six photons have been simultaneously entangled to deliver an 18-qubit

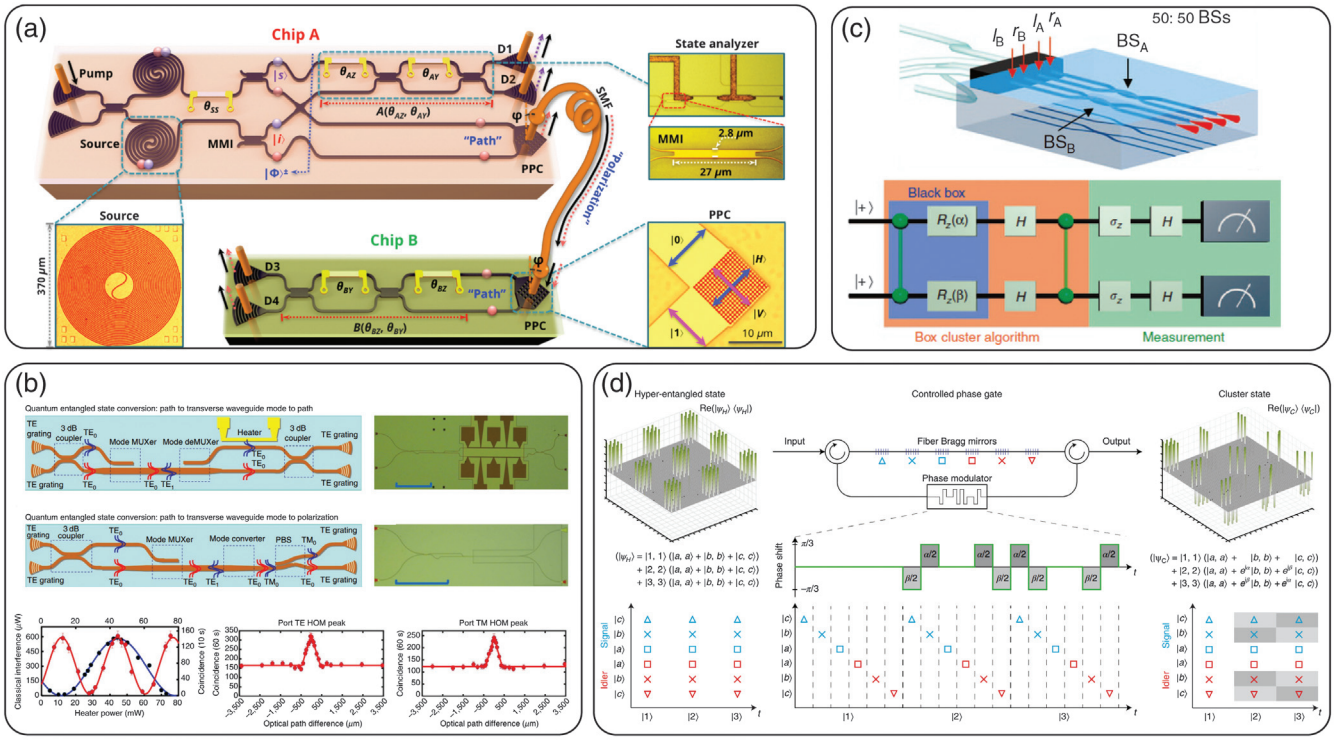

Fig. 1 On-chip conversion of multiple DoFs and multi-DoF entanglement. (a) Chip-to-chip quantum entanglement distribution by path-polarization interconversion. A pair of entangled photons, coded in path, were generated on chip A, then one photon was distributed to chip B via two-dimensional grating couplers, while the other photon remained on chip A. As a result, a two-photon entangled state $|\phi^+\rangle = \frac{1}{\sqrt{2}}(|00\rangle + |11\rangle)$ was distributed coherently between two separate chips. Bell-type violation of $S = 2.638 \pm 0.039$ showed the strong entanglement between two separate photons. (b) Quantum entangled state conversion between different DoFs of path, transverse mode, and polarization. Two photons were coupled into the silicon chip, and then NOON entangled state, $\frac{1}{\sqrt{2}}(|2\rangle_0|0\rangle_1 + |0\rangle_0|2\rangle_1)$ coded in path, was generated by an interference. With a mode multiplexer, the generated state coded in path was first converted into a transverse waveguide mode TE_0/TE_1. Then, the quantum information was converted back to the path by a mode demultiplexer or to polarization by a PBS. Two-photon interference and Hong–Ou–Mandel effect measurements show the preservation of quantum coherence during the conversion between different DoFs. (c) Four-qubit hyperentanglement cluster state by entangling the path and polarization simultaneously. Quantum state tomography and genuine multipartite entanglement witness were analyzed to ensure high fidelity of the prepared four-qubit cluster state. Based on the model of one-way quantum computing, Grover's search algorithm was performed, where the average success rate of the algorithm was 0.960 ± 0.007. (d) Two photon 4-qutrit hyperentangled cluster state. Three-level time-bin entangled state with three frequency modes $|\psi_H\rangle$ was created on a micro-ring resonator. Then, hyperentanglement of time-frequency $|\psi_C\rangle$ was realized by a controlled phase gate (composed of fiber Bragg mirrors and an electro-optical phase modulator). Basic high-dimensional one way quantum computing operators were tested. Panels reproduced from: (a) Ref. 67, Optica; (b) Ref. 68, Springer Nature; (c) Ref. 34, Springer Nature; and (d) Ref. 72, Springer Nature.

entangled state.[71] The first on-chip demonstration of hyperentanglement was implemented on silica waveguide circuits fabricated by laser writing techniques[34] [see Fig. 1(c)]. Path and polarization DoFs were adopted to prepare a four-qubit cluster state, which then was used to process the Grover's search algorithm in the one-way model. A four-qutrit cluster state with hyperentanglement of frequency and time bins was created in a micoring resonator together with fiber optics[72] [see Fig. 1(d)].

A multiphoton (three-photon) Greenberger–Horne–Zeilinger (GHZ) entangled state was proposed and experimentally demonstrated in 1997 with strong incompatibility to local realism,[73] and it then became a key resource for quantum computing[74] and communication.[75] In a bulk-optics system, to date, an up to 12-photon GHZ entangled state has been reported.[76] In photonic chips, the number of GHZ entangled photons has been limited to 4 to date,[62,77] due to a far less-optimized photon source and relatively high loss of the chip. Multiphoton quantum interference or multiphoton nonentangled states have been prepared on chip.[78–81] The first on-chip demonstrations of four-photon GHZ entanglement were reported on two silicon chips, one enabled to be reconfigured to generate both the GHZ state and graph state[77] [see Fig. 2(b)], and the other chip with microring resonant sources to create and verify genuine GHZ entanglement and teleportation[62] [see Fig. 2(a)]. Recently, four-photon eight-qubit graph entangled states were generated on a silicon photonic chip by remapping the qudit state into qubits.[82] It was reconfigured to implement the one-way quantum computing model and to implement error-corrected qubits [see Fig. 2(c)].

Going beyond the two-level qubit systems, multilevel quantum dit (qudit) systems offer unique properties and new capacities.[83] It not only leads to the expansion of Hilbert space, but brings in new physics and applications, such as stronger Bell violation,[84] noise-robustness in quantum communication,[85] and

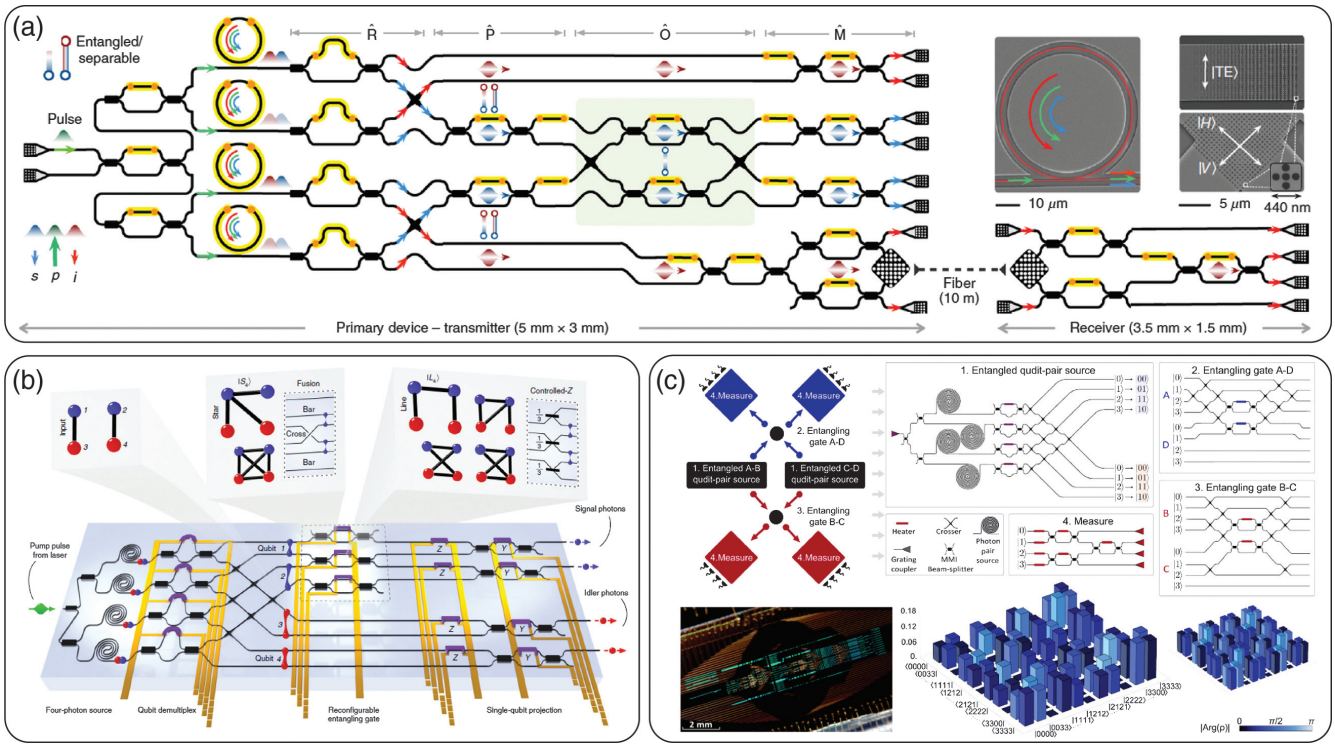

Fig. 2 On-chip generation of multiphoton entanglement. (a) Generation of four-photon four-qubit genuine GHZ entangled states on a silicon photonic chip. Two photon-pairs with high purity and indistinguishability were produced by an array of microring resonators. Then, a reconfigurable fusion entangling operator was performed on two indistinguishable photons, generating the genuine four-photon GHZ entangled state. Entanglement witness confirmed the genuine multiphoton entanglement. (b) Generation of four-photon four-qubit cluster states on a silicon photonic chip. An entangling gate could be tuned to perform either a fusion operator or controlled-*Z* operator, by which the linear- and star-cluster states were created. Thanks to the highly reconfigurable photonics chip, all types of four-photon graph states were prepared. Nonlocality of the multiphoton state was verified by the Mermin test. (c) Generation of four-photon eight-qubit graph states on a silicon photonic chip, in which each of the four-dimensional qudits was remapped into two qubits. High-dimensional entangling gates were ultilized to generate four-photon four-dimensional entanglement from two pairs of two-photon four-dimensional entangled states. Error-corrected qubits were used to implement quantum computational algorithms. When running the phase-estimation algorithm with error protection, the success rate would raise from 62.5% to 95.8%. Panels reproduced from: (a) Ref. 62, Springer Nature; (b) Ref. 77, Springer Nature; and (c) Ref. 82, Springer Nature.

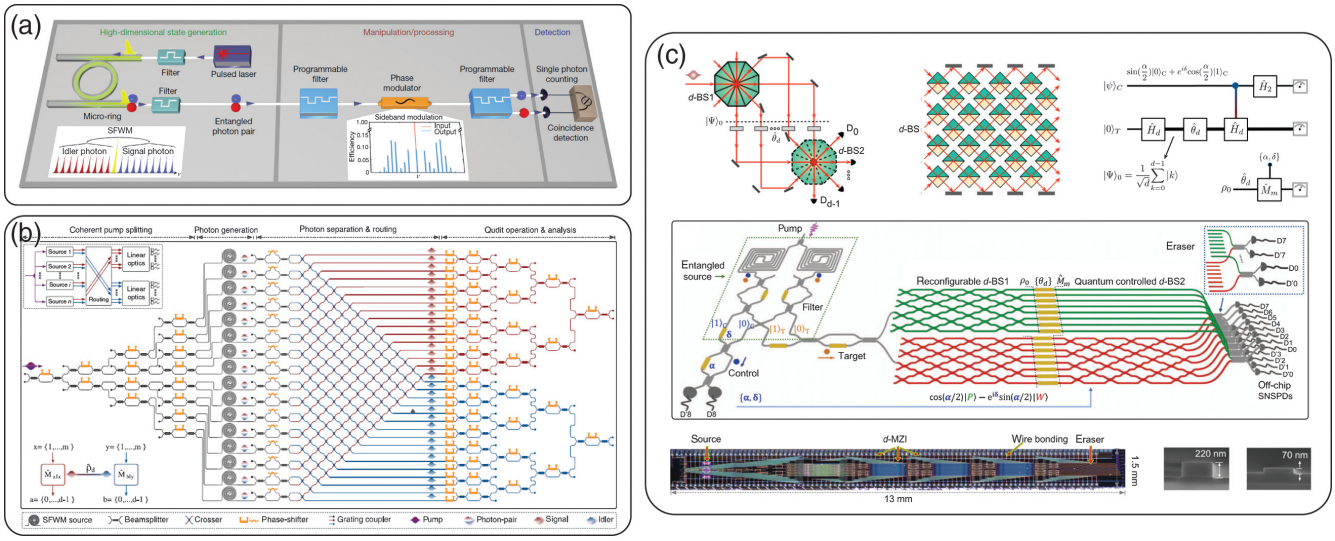

Fig. 3 On-chip generation of multidimensional entanglement. (a) Generation of frequency-bin encoded multidimensional entangled state. An integrated microring resonator was used to produce a pair of frequency-entangled photons with up to 10-dimensions. High-dimensional gate operations in the frequency domain were executed on qudits, demonstrating qudit two-photon interference and qudit tomography. (b) Generation of path-encoded multidimensional entanglement on a large-scale programmable silicon-photonic chip, where 16 identical SFWM single-photon sources and qudit operation/analyzing networks were all integrated monolithically. Each single-photon source would generate a pair of highly indistinguishable photons. By this means, this chip can create, control, and measure 15×15 entangled states. Genuine multidimensional entanglement was verified by quantum state tomography, and experimental violation of generalized Bell inequality and steering inequality. (c) Multipath wave-particle duality experiment on a large-scale silicon chip. The state-process entanglement technique was adopted to implement the quantum-controlled generalized Hadamard operations. The process (wave/particle) of the target photon going through would be coherently controlled by the state of the control photon. The generalized multipath wave-particle duality was demonstrated qualitatively and quantitatively. Panels reproduced from: (a) Ref. 51, Springer Nature; (b) Ref. 43, AAAS; and (c) Ref. 90, Springer Nature.

high efficiency in quantum computing.[86] Photonics naturally allows the preparation of multidimensional entanglement in various DoFs. Utilizing an integrated microring, multidimensional entangled states with a 10 frequency-bin have been demonstrated [see Fig. 3(a)],[51] in which arbitrary operation is performed by telecommunication fiber optical components. Qudit states encoded in multiple paths can be arbitrarily and reconfigurably manipulated by integrated quantum photonic circuits.[87,88] A 15-dimensional entangled state has been demonstrated on a large-scale silicon chip,[43] allowing the generation, manipulation, and measurement of entanglement [see Fig. 3(b)]. Genuine multidimensional entanglement was verified by quantum state tomography and experimental violation of generalized Bell inequality and steering inequality. A three-dimensional entangled state was obtained by a similar method.[89] In addition, generalized multipath wave-particle duality, multipath coherence, and multimode quantizations were confirmed on a large-scale integrated quantum chip, providing the basics for multidimensional quantum technologies [see Fig. 3(c)].[90]

5 Outlook and Conclusion

Generation and control of entanglement with integrated quantum photonics could enable profound applications in quantum communication, computing, and simulations. The first chip-to-chip entanglement distribution[67] and quantum teleportation[62] were demonstrated between two programmable photonic chips. The path-polarization conversion technique was invented to ensure the stability and coherence of the chip-to-chip system. Integrated optics may lead to low-cost, compact, fast, and portable chip-scale quantum communication chips. Integrated quantum photonics could provide a reliable, programmable, and scalable system to generate largely entangled cluster states, which is the key for the implementation of measurement-based quantum computing.[34,77] Four-photon four-qubit GHZ states[62] and cluster states[77] have been generated on silicon photonic chips. Two-photon four-qubit cluster states[34] and four-photon eight-qubit graph states[82] have been demonstrated on photonic chips. Such controllable quantum devices may find near-term applications in the simulations of complex physical and chemical systems. For example, phase estimation,[91] variational eigenvalue solver,[92] and their combined algorithm[35] were demonstrated to calculate the ground state energy of molecules. Together with machine learning techniques, integrated photonic chips could be adopted to validate the Hamiltonian model and verify the simulating device.[36]

The functionality and capability of integrated quantum photonics rely on the ability to generate, control, and analyze complex entanglement. It thus requires further and continuous

development of on-chip multi-DoF entanglement with many different DoFs, multiphoton entanglement with a large number of single photons, and multidimensional entanglement with a large number of spatial modes.

Thanks to a mature silicon-on-insulator CMOS fabrication process,[93] a large quantity of quantum photonic components can be integrated monolithically on a single silicon chip.[43,44,90,94] Meanwhile, CMOS-compatible platforms based on other material systems, like silicon nitride and high-index doped silica,[95] are also explored widely to make use of their intrinsic optical properties. The negligible two-photon absorption gives silicon nitride a huge advantage over silicon, while the intrinsic ultra-low loss makes silica a strong candidate for next generation of integrated quantum photonics platform. Lithium niobate[96] is the first choice for ultra-fast on-chip modulators. The key technical challenge is how to integrate various materials monolithically on a single chip by means of hybrid integration. An integrated chip with multiple superior performances may become the next development direction of integrated photonics quantum technology.

Acknowledgments

We would like to acknowledge the support from the National Key Research and Development (R&D) Program of China (Nos. 2019YFA0308702, 2018YFB1107205, and 2016YFA0301302), the National Natural Science Foundation of China (Nos. 61975001, 61590933, 61904196, 61675007, 11975026, and 12075159), Beijing Natural Science Foundation (No. Z190005), and the Key R&D Program of Guangdong Province (No. 2018B030329001).

References

1. A. Einstein, B. Podolsky, and N. Rosen, "Can quantum-mechanical description of physical reality be considered complete?" *Phys. Rev.* **47**(10), 777–780 (1935).
2. E. Schrödinger, "Probability relations between separated systems," *Math. Proc. Cambridge Philos. Soc.* **32**(3), 446–452 (1936).
3. J. S. Bell, "On the Einstein–Podolsky–Rosen paradox," *Phys.* **1**(3), 195–200 (1964).
4. B. Hensen et al., "Loophole-free bell inequality violation using electron spins separated by 1.3 kilometres," *Nature* **526**(7575), 682–686 (2015).
5. L. K. Shalm et al., "Strong loophole-free test of local realism," *Phys. Rev. Lett.* **115**(25), 250402 (2015).
6. M. Giustina et al., "Significant-loophole-free test of Bell's theorem with entangled photons," *Phys. Rev. Lett.* **115**(25), 250401 (2015).
7. N. Gisin et al., "Quantum cryptography," *Rev. Mod. Phys.* **74**(1), 145–195 (2002).
8. V. Giovannetti, S. Lloyd, and L. Maccone, "Quantum-enhanced measurements: beating the standard quantum limit," *Science* **306**(5700), 1330–1336 (2004).
9. G. B. Lemos et al., "Quantum imaging with undetected photons," *Nature* **512**(7515), 409–412 (2014).
10. T. D. Ladd et al., "Quantum computers," *Nature* **464**(7285), 45–53 (2010).
11. I. M. Georgescu, S. Ashhab, and F. Nori, "Quantum simulation," *Rev. Mod. Phys.* **86**(1), 153–185 (2014).
12. J.-W. Pan et al., "Multiphoton entanglement and interferometry," *Rev. Mod. Phys.* **84**(2), 777–838 (2012).
13. N. Gisin and R. Thew, "Quantum communication," *Nat. Photonics* **1**(3), 165–171 (2007).
14. H. J. Kimble, "Quantum internet," *Nature* **453**(7198), 1023–1030 (2008).
15. H.-S. Zhong et al., "Quantum computational advantage using photons," *Science* **370**(6523), 1460–1463 (2020).
16. R. Raussendorf and H. J. Briegel, "A one-way quantum computer," *Phys. Rev. Lett.* **86**(22), 5188–5191 (2001).
17. P. Kok et al., "Linear optical quantum computing with photonic qubits," *Rev. Mod. Phys.* **79**(1), 135–174 (2007).
18. J. L. O'Brien, "Optical quantum computing," *Science* **318**(5856), 1567–1570 (2007).
19. J. Wang et al., "Integrated photonic quantum technologies," *Nat. Photonics* **14**(5), 273–284 (2020).
20. A. Politi et al., "Silica-on-silicon waveguide quantum circuits," *Science* **320**(5876), 646–649 (2008).
21. J. C. F. Matthews et al., "Manipulation of multiphoton entanglement in waveguide quantum circuits," *Nat. Photonics* **3**(6), 346–350 (2009).
22. P. J. Shadbolt et al., "Generating, manipulating and measuring entanglement and mixture with a reconfigurable photonic circuit," *Nat. Photonics* **6**(1), 45–49 (2012).
23. H. Takesue et al., "Entanglement generation using silicon wire waveguide," *Appl. Phys. Lett.* **91**(20), 201108 (2007).
24. J. W. Silverstone et al., "On-chip quantum interference between silicon photon-pair sources," *Nat. Photonics* **8**(2), 104–108 (2014).
25. B. J. Smith et al., "Phase-controlled integrated photonic quantum circuits," *Opt. Express* **17**(16), 13516–13525 (2009).
26. S. Tanzilli et al., "PPLN waveguide for quantum communication," *Eur. Phys. J. D* **18**(2), 155–160 (2002).
27. H. Jin et al., "On-chip generation and manipulation of entangled photons based on reconfigurable lithium-niobate waveguide circuits," *Phys. Rev. Lett.* **113**(10), 103601 (2014).
28. X. Lu et al., "Chip-integrated visible-telecom entangled photon pair source for quantum communication," *Nat. Phys.* **15**(4), 373–381 (2019).
29. X. Zhang et al., "Integrated silicon nitride time-bin entanglement circuits," *Opt. Lett.* **43**(15), 3469–3472 (2018).
30. R. Horn et al., "Monolithic source of photon pairs," *Phys. Rev. Lett.* **108**(15), 153605 (2012).
31. J. Wang et al., "Gallium arsenide (GaAS) quantum photonic waveguide circuits," *Opt. Commun.* **327**, 49–55 (2014).
32. P. Sibson et al., "Chip-based quantum key distribution," *Nat. Commun.* **8**, 13984 (2017).
33. H. Semenenko et al., "Chip-based measurement-device-independent quantum key distribution," *Optica* **7**(3), 238–242 (2020).
34. M. A. Ciampini et al., "Path-polarization hyperentangled and cluster states of photons on a chip," *Light Sci. Appl.* **5**(4), e16064 (2016).
35. R. Santagati et al., "Witnessing eigenstates for quantum simulation of Hamiltonian spectra," *Sci. Adv.* **4**(1), eaap9646 (2018).
36. J. Wang et al., "Experimental quantum Hamiltonian learning," *Nat. Phys.* **13**(6), 551–555 (2017).
37. J. C. Adcock et al., "Advances in silicon quantum photonics," *IEEE J. Sel. Top. Quantum Electron.* **27**(2), 6700224 (2021).
38. A. Aspect, P. Grangier, and G. Roger, "Experimental realization of Einstein–Podolsky–Rosen–Bohm *Gedankenexperiment*: a new violation of Bell's inequalities," *Phys. Rev. Lett.* **49**(2), 91–94 (1982).
39. D. Bouwmeester et al., "Observation of three-photon Greenberger–Horne–Zeilinger entanglement," *Phys. Rev. Lett.* **82**(7), 1345–1349 (1999).
40. D. Bouwmeester et al., "Experimental quantum teleportation," *Nature* **390**(6660), 575–579 (1997).
41. D. Dai et al., "Polarization management for silicon photonic integrated circuits," *Laser Photonics Rev.* **7**(3), 303–328 (2013).
42. N. Matsuda et al., "A monolithically integrated polarization entangled photon pair source on a silicon chip," *Sci. Rep.* **2**(1), 817 (2012).
43. J. Wang et al., "Multidimensional quantum entanglement with large-scale integrated optics," *Science* **360**(6386), 285–291 (2018).

44. X. Qiang et al., "Large-scale silicon quantum photonics implementing arbitrary two-qubit processing," *Nat. Photonics* **12**(9), 534–539 (2018).
45. L.-T. Feng et al., "On-chip transverse-mode entangled photon pair source," *NPJ Quantum Inf.* **5**, 2 (2019).
46. A. Mohanty et al., "Quantum interference between transverse spatial waveguide modes," *Nat. Commun.* **8**, 14010 (2017).
47. A. Mair et al., "Entanglement of the orbital angular momentum states of photons," *Nature* **412**(6844), 313–316 (2001).
48. R. Fickler et al., "Quantum entanglement of high angular momenta," *Science* **338**(6107), 640–643 (2012).
49. M. Malik et al., "Multi-photon entanglement in high dimensions," *Nat. Photonics* **10**(4), 248–252 (2016).
50. A. Babazadeh et al., "High-dimensional single-photon quantum gates: concepts and experiments," *Phys. Rev. Lett.* **119**(18), 180510 (2017).
51. M. Kues et al., "On-chip generation of high-dimensional entangled quantum states and their coherent control," *Nature* **546**(7660), 622–626 (2017).
52. L. Olislager et al., "Frequency-bin entangled photons," *Phys. Rev. A* **82**(1), 013804 (2010).
53. L. Olislager et al., "Creating and manipulating entangled optical qubits in the frequency domain," *Phys. Rev. A* **89**(5), 052323 (2014).
54. F. Kaneda and P. G. Kwiat, "High-efficiency single-photon generation via large-scale active time multiplexing," *Sci. Adv.* **5**(10), eaaw8586 (2019).
55. X. Guo et al., "Parametric down-conversion photon-pair source on a nanophotonic chip," *Light Sci. Appl.* **6**(5), e16249–e16249 (2017).
56. Y. Zhang et al., "Dual-pump approach to photon-pair generation: demonstration of enhanced characterization and engineering capabilities," *Opt. Express* **27**(13), 19050–19061 (2019).
57. B. Fang et al., "State engineering of photon pairs produced through dual-pump spontaneous four-wave mixing," *Opt. Express* **21**(3), 2707–2717 (2013).
58. S. Signorini et al., "Intermodal four-wave mixing in silicon waveguides," *Photonics Res.* **6**(8), 805–814 (2018).
59. S. Paesani et al., "Near-ideal spontaneous photon sources in silicon quantum photonics," *Nat. Commun.* **11**, 2505 (2020).
60. Z. Vernon, M. Liscidini, and J. E. Sipe, "No free lunch: the trade-off between heralding rate and efficiency in microresonator-based heralded single photon sources," *Opt. Lett.* **41**(4), 788–791 (2016).
61. Z. Vernon et al., "Truly unentangled photon pairs without spectral filtering," *Opt. Lett.* **42**(18), 3638–3641 (2017).
62. D. Llewellyn et al., "Chip-to-chip quantum teleportation and multi-photon entanglement in silicon," *Nat. Phys.* **16**(2), 148–153 (2020).
63. J. B. Christensen et al., "Engineering spectrally unentangled photon pairs from nonlinear microring resonators by pump manipulation," *Opt. Lett.* **43**(4), 859–862 (2018).
64. Y. Liu et al., "High-spectral-purity photon generation from a dual-interferometer-coupled silicon microring," *Opt. Lett.* **45**(1), 73–76 (2020).
65. B. M. Burridge et al., "High spectro-temporal purity single-photons from silicon micro-racetrack resonators using a dual-pulse configuration," *Opt. Lett.* **45**(14), 4048–4051 (2020).
66. P. Walther et al., "Experimental one-way quantum computing," *Nature* **434**(7030), 169–176 (2005).
67. J. Wang et al., "Chip-to-chip quantum photonic interconnect by path-polarization interconversion," *Optica* **3**(4), 407–413 (2016).
68. L.-T. Feng et al., "On-chip coherent conversion of photonic quantum entanglement between different degrees of freedom," *Nat. Commun.* **7**, 11985 (2016).
69. J. T. Barreiro, T.-C. Wei, and P. G. Kwiat, "Beating the channel capacity limit for linear photonic superdense coding," *Nat. Phys.* **4**(4), 282–286 (2008).
70. M. Fiorentino and F. N. C. Wong, "Deterministic controlled-not gate for single-photon two-qubit quantum logic," *Phys. Rev. Lett.* **93**(7), 070502 (2004).
71. X.-L. Wang et al., "18-qubit entanglement with six photons' three degrees of freedom," *Phys. Rev. Lett.* **120**(26), 260502 (2018).
72. C. Reimer et al., "High-dimensional one-way quantum processing implemented on *d*-level cluster states," *Nat. Phys.* **15**(2), 148–153 (2019).
73. N. D. Mermin, "What's wrong with these elements of reality?" *Phys. Today* **43**(6), 9–11 (1990).
74. M. Gimeno-Segovia et al., "From three-photon Greenberger–Horne–Zeilinger states to ballistic universal quantum computation," *Phys. Rev. Lett.* **115**(2), 020502 (2015).
75. Z.-D. Li et al., "Experimental quantum repeater without quantum memory," *Nat. Photonics* **13**(9), 644–648 (2019).
76. H.-S. Zhong et al., "12-photon entanglement and scalable scattershot boson sampling with optimal entangled-photon pairs from parametric down-conversion," *Phys. Rev. Lett.* **121**(25), 250505 (2018).
77. J. C. Adcock et al., "Programmable four-photon graph states on a silicon chip," *Nat. Commun.* **10**, 3528 (2019).
78. S. Paesani et al., "Generation and sampling of quantum states of light in a silicon chip," *Nat. Phys.* **15**(9), 925–929 (2019).
79. M. Zhang et al., "Generation of multiphoton quantum states on silicon," *Light Sci. Appl.* **8**(1), 41 (2019).
80. L.-T. Feng et al., "Observation of nonlocal quantum interference between the origins of a four-photon state in a silicon chip," arXiv: 2103.14277 (2021).
81. C. Reimer et al., "Generation of multiphoton entangled quantum states by means of integrated frequency combs," *Science* **351**(6278), 1176–1180 (2016).
82. C. Vigliar et al., "Error protected qubits in a silicon photonic chip," *Nat. Phys.* **17**, 1137–1143 (2021).
83. M. Erhard, M. Krenn, and A. Zeilinger, "Advances in high-dimensional quantum entanglement," *Nat. Rev. Phys.* **2**(7), 365–381 (2020).
84. D. Collins et al., "Bell inequalities for arbitrarily high-dimensional systems," *Phys. Rev. Lett.* **88**(4), 040404 (2002).
85. N. J. Cerf et al., "Security of quantum key distribution using *d*-level systems," *Phys. Rev. Lett.* **88**(12), 127902 (2002).
86. B. P. Lanyon et al., "Simplifying quantum logic using higher-dimensional Hilbert spaces," *Nat. Phys.* **5**(2), 134–140 (2009).
87. C. Schaeff et al., "Experimental access to higher-dimensional entangled quantum systems using integrated optics," *Optica* **2**(6), 523–529 (2015).
88. W. R. Clements et al., "Optimal design for universal multiport interferometers," *Optica* **3**(12), 1460–1465 (2016).
89. L. Lu et al., "Three-dimensional entanglement on a silicon chip," *NPJ Quantum Inf.* **6**(1), 30 (2020).
90. X. Chen et al., "A generalized multipath delayed-choice experiment on a large-scale quantum nanophotonic chip," *Nat. Commun.* **12**, 2712 (2021).
91. S. Paesani et al., "Experimental Bayesian quantum phase estimation on a silicon photonic chip," *Phys. Rev. Lett.* **118**(10), 100503 (2017).
92. A. Peruzzo et al., "A variational eigenvalue solver on a photonic quantum processor," *Nat. Commun.* **5**, 4213 (2014).
93. A. H. Atabaki et al., "Integrating photonics with silicon nanoelectronics for the next generation of systems on a chip," *Nature* **556**(7701), 349–354 (2018).
94. N. C. Harris et al., "Quantum transport simulations in a programmable nanophotonic processor," *Nat. Photonics* **11**(7), 447–452 (2017).
95. D. J. Moss et al., "New CMOS-compatible platforms based on silicon nitride and hydex for nonlinear optics," *Nat. Photonics* **7**(8), 597–607 (2013).
96. C. Wang et al., "Integrated lithium niobate electro-optic modulators operating at CMOS-compatible voltages," *Nature* **562**(7725), 101–104 (2018).

Xiaojiong Chen received his bachelor's degree in physics from Zhejiang University, Hangzhou, China, in 2018. He is currently a PhD student at

the School of Physics of Peking University. His current research focuses on the integrated silicon photonic platform for quantum information, especially in multidimensional quantum technology for fundamental sciences and applications.

Zhaorong Fu is a senior undergraduate student majoring in physics at Peking University. He joined the PKU Q-chip Lab in 2019. His research focuses on integrated photonics and quantum information.

Qihuang Gong is currently the Boya Chair Professor and Cheung Kong Professor of Physics at Peking University, Beijing, China. His current research interests include ultrafast optics and spectroscopy, nonlinear and quantum photonics, and mesoscopic optical devices for applications in optical information processing and communication. He is an academician of the Chinese Academy of Sciences, a member of the World Academy of Sciences, president of the Chinese Optical Society, and vice president of the Chinese Physical Society. He is a standing committee member of China Association for Science and Technology, vice president for International Commission for Optics, and vice chair for IUPAP C17.

Jianwei Wang received his bachelor's and master's degrees from Zhejiang University, Hangzhou, China, in 2008 and 2011, respectively, and his PhD in physics from the University of Bristol, Bristol, UK, in 2016. He is currently an assistant professor at the School of Physics, Peking University, Beijing, China. He was a postdoc at the University of Bristol. His current research focuses on quantum information science and technologies with photons, in both fundamental physics and advanced applications.

Letter

ADVANCED PHOTONICS

Enhanced generation of nondegenerate photon pairs in nonlinear metasurfaces

Matthew Parry,[a,b,*] Andrea Mazzanti,[a,c] Alexander Poddubny,[a,d,e] Giuseppe Della Valle,[c,f] Dragomir N. Neshev,[a,b] and Andrey A. Sukhorukov[a,b,*]

[a]Australia National University, Research School of Physics, Canberra, Australia
[b]ARC Centre of Excellence for Transformative Meta-Optical Systems, Canberra, Australia
[c]Politecnico di Milano, Dipartimento di Fisica, Milan, Italy
[d]ITMO University, Department of Physics, Saint Petersburg, Russia
[e]Ioffe Institute, Saint Petersburg, Russia
[f]Consiglio Nazionale delle Ricerche, Istituto di Fotonica e Nanotecnologie, Milan, Italy

Abstract. We predict theoretically a regime of photon-pair generation driven by the interplay of multiple bound states in the continuum resonances in nonlinear metasurfaces. This nondegenerate photon-pair generation is derived from the hyperbolic topology of the transverse phase matching and can enable orders-of-magnitude enhancement of the photon rate and spectral brightness, as compared to the degenerate regime. We show through comprehensive simulations that the entanglement of the photon pairs can be tuned by varying the pump polarization, which can underpin future advances and applications of ultracompact quantum light sources.

Keywords: optics; photonics; light; metasurface; spontaneous parametric down-conversion; entanglement.

Received Jun. 25, 2021; revised manuscript received Jul. 20, 2021; accepted for publication Aug. 9, 2021; published online Sep. 1, 2021.

[DOI: 10.1117/1.AP.3.5.055001]

1 Introduction

Metasurfaces (MSs) offer an ultracompact and versatile platform for enhancing nonlinear optical processes, including harmonic generation and frequency mixing.[1,2] To realize such nonlinear interactions in bulk crystals and waveguides, one requires extended propagation distances, but in MSs a strong enhancement of light–matter interactions can be achieved with subwavelength thicknesses through the excitation of high-quality factor optical resonances. Notably, this can be facilitated by designing Bound State in the Continuum (BIC) resonances,[3–7] which support a high confinement of the optical field within the nonlinear material.[8–10]

In addition to classical frequency mixing, nonlinear MSs can also, through Spontaneous Parametric Down-Conversion (SPDC), generate entangled photons with a strong degree of spatial coherence.[11] SPDC in carefully engineered MSs has the potential to drive fundamental advances in the field of ultracompact multi-photon sources[12] that operate at room temperature, which are suitable for integration in end-user devices with applications that include quantum imaging[13] and free-space communications.[14] Traditionally, SPDC is performed in bulk nonlinear crystals with dimensions up to centimeters in length, while integrated waveguides have enabled a reduction of the footprint to millimeter[15] and down to 100 μm length scales.[16] At the subwavelength scale, generation of photon pairs was reported experimentally from a single AlGaAs nanoresonator[17] and lithium niobate MSs,[18] and studies were also conducted on monolayers of MoS_2,[19] carbon nanotubes,[20] and directional emission from nanoresonators.[21]

Importantly, SPDC in ultrathin nonlinear layers[22–24] can give rise to strong spatial correlations and allow quantum state engineering without the constraints of longitudinal phase matching. It has been proposed that a so-called "accidental" BIC at the pump frequency can increase the photon rate at a single nanoresonator,[25] while a photonic crystal slab with a BIC resonance can enhance SPDC in a monolayer of WS_2,[26] although the theoretically estimated rate was still much lower than with conventional sources. There is now strong interest in new concepts and

*Address all correspondence to Matthew Parry, Matthew.Parry@anu.edu.au; Andrey A. Sukhorukov, Andrey.Sukhorukov@anu.edu.au

practical approaches for even stronger enhancement of the brightness of SPDC photon-pair generation in subwavelength scale structures.

In this theoretical paper, we present a general approach for orders-of-magnitude enhancement of the photon-pair generation rate and spectral brightness in nonlinear MSs. We reveal, for the first time, to the best of our knowledge, that nondegenerate SPDC efficiency can be dramatically increased when the signal and idler photons are supported by BIC resonances at different frequencies. We demonstrate how these features can be realized in practice by engineering the symmetry of the MS to deliver a projected spectral brightness five orders of magnitude higher than for an unpatterned film. Our results are fundamentally different from the recently demonstrated SPDC generation using linear MS-lenses that engineer the quantum state by focusing the pump at multiple spots in a bulk crystal.[27]

2 Principles and Methods

We demonstrate that a MS with reduced global rotational symmetry allows much greater flexibility in tailoring the dispersion from several BICs, in which the signal and idler photons are generated. Consequently, we can control the form of the transverse phase matching for SPDC according to the energy and momentum conservation, as illustrated in Fig. 1(a):

$$\mathbf{k}_{p,\perp} = \mathbf{k}_{s,\perp} + \mathbf{k}_{i,\perp}, \tag{1}$$

$$\omega_p(\mathbf{k}_{p,\perp}) = \omega_s(\mathbf{k}_{s,\perp}) + \omega_i(\mathbf{k}_{i,\perp}), \tag{2}$$

where the indices refer to pump (p), signal (s), and idler (i) photons with the corresponding frequencies ω. The wave-vectors $\mathbf{k}$ define the propagation directions in free space, and $\perp$ indicates the transverse components in the plane of the MS. We note that the photon polarization weakly affects phase matching (see Sec. S6 in the Supplementary Material).

We focus on a MS with D_{2h} symmetry and outline other possibilities in Sec. S2 in the Supplementary Material. According to our concept, we designed a MS composed of a square array of cylinders with two holes, or ghost oligomers, inserted to remove the 90-deg rotational symmetry [Fig. 1(b)]. This structure supports multiple extended photonic-crystal-like BICs,[3] where the field localization arises from a mismatch between the symmetry of the collective modes and the available radiation channels.

We consider resonators made of $Al_{0.18}Ga_{0.82}As$, which possess strong quadratic nonlinearity and can be manufactured with established procedures. We chose a (111) crystal orientation, as it provides the best off-BIC conversion efficiency in the normal propagation direction (see Sec. S3 in the Supplementary Material) and hence gives a better measure of the enhancement due to the BIC. In our modeling, we have omitted a substrate to focus on the generic features (see Sec. S1 in the Supplementary Material for details on the simulation methods). Adding a substrate will convert the BICs to quasi-BICs, due to the up/down asymmetry introduced. But as we discuss in the following, the photon generation is associated with quasi-BICs formed by off-normal angles, thus confirming that the ideal BICs with formally infinite quality factors are not required.

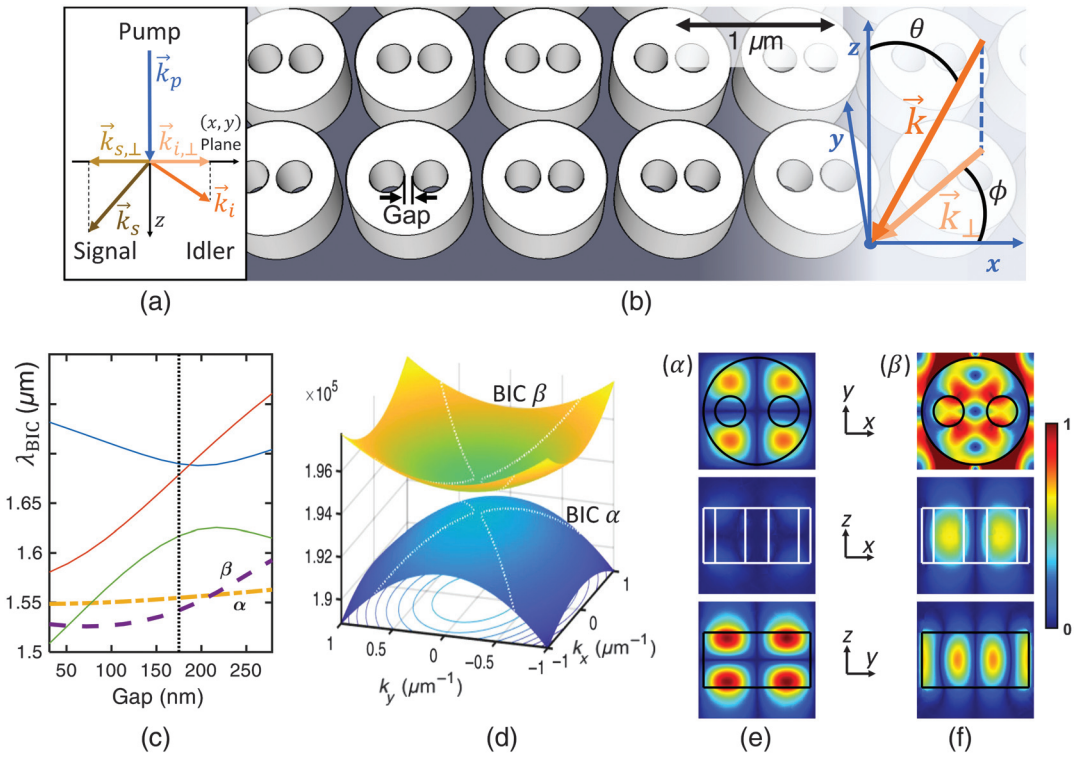

Fig. 1 The MS and its modes. (a) Diagram of transverse phase matching. (b) MS design and the coordinate axes: θ is the polar and ϕ the azimuthal angle. (c) BIC wavelengths versus the gap between the two holes. (d) The dispersion for two quasi-BICs: (α) lower and (β) upper surfaces. Dotted white lines: two-BIC phase matching for $\lambda_p = 774.22$ nm. (e), (f) Fields $|\mathbf{E}|$ of the two BICs.

We therefore conclude that a strong enhancement will still be achieved when a substrate is present. Our general approach can also be applied to MSs made of different nonlinear materials, including lithium niobate, where efficient classical frequency conversion has been demonstrated.[28–30]

An important feature of BICs is that changes in the dimensions of the meta-atoms will not destroy a photonic-crystal like BIC so long as the relevant symmetry is maintained. This enables simultaneous tuning of the resonant frequencies for several BICs by adjusting the design parameters, such as the separation between the hole pairs, as shown in Fig. 1(c). By shifting the position of the holes, the proportion of the electric field within these two low refractive index regions changes, which in turn changes the energy of the modes. The way in which each mode is affected depends on the profile of the mode over the region through which the holes move. Similar configurability is found with the other dimensions of the meta-atoms. This tunability offers an important advantage with SPDC generation when compared to using so-called accidental BICs[31] in individual nanoresonators, which only appear at very specific resonator dimensions.

The dispersion of the two BICs studied in this paper is shown in Fig. 1(d), which, importantly, have opposite dispersion. Their mode profiles are shown in Figs. 1(e) and 1(f), where the fields are normalized to the peak value inside the resonator for each BIC. They are also marked α and β in Fig. 1(c), where the dotted line shows the value of the gap used in the two-BIC study. The single BIC study uses BIC α [Fig. 1(e)] with a gap of 52 nm, which gives a good separation from the other BICs.

3 Results

3.1 Single BIC

As a first study, we present an analysis of SPDC with the signal and idler photons being generated at a single BIC. We calculated the SPDC generation rate via the quantum-classical correspondence between SPDC and sum frequency generation (SFG),[11,17,32,33] which is exact in the absence of other nonlinear effects. We performed full SFG numerical simulations and used these results to predict the efficiency of quantum photon-pair generation through SPDC:

$$\Xi_{\mathrm{SPDC}} = \frac{1}{(2\pi)^3}\frac{\lambda_p^2}{\lambda_s^{\mathrm{BIC}}\lambda_i^{\mathrm{BIC}}}\frac{\Phi_{\mathrm{SFG}}}{\Phi_s\Phi_i}, \tag{3}$$

where Φ_{SFG} is the zeroth order far-field SFG intensity, and Φ_s and Φ_i are the incident signal and idler intensities. For SPDC calculations, we take the small angle approximation, where in the far-field the z component is zero, so the $|H\rangle$ and $|V\rangle$ notations indicate the polarization primarily along the x and y axes, respectively. The solid line in Fig. 2(a) shows the results of such modeling.

We then confirmed that the SPDC generation is approximately proportional to the product of the maximum intensity of the signal and idler electric fields inside the resonator. We present a typical dependence of this quantity near a BIC resonance, obtained from linear simulations, with the dashed line in Fig. 2(a), where there is a slightly off-normal signal and idler ($\theta_s = 0.2$ deg), and the pump wavelength is $\lambda_p = 775$ nm. We can see that the shapes of solid and dashed lines match closely. This is a physically important observation, as it means

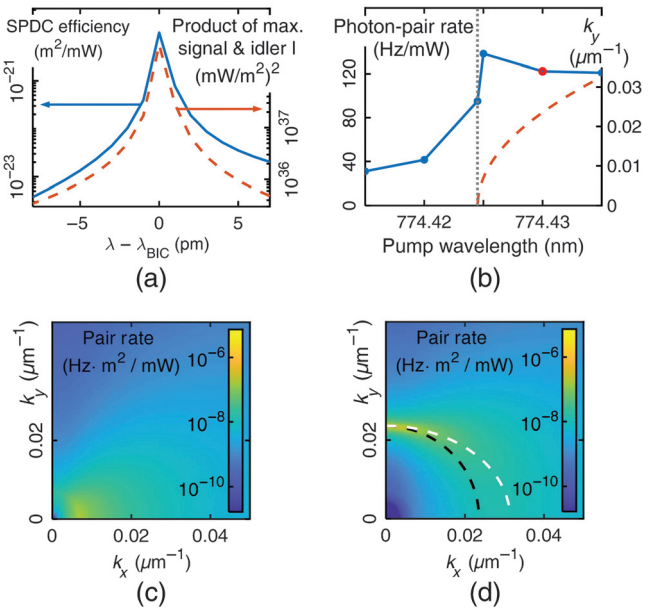

Fig. 2 SPDC at a single BIC. (a) Solid line: the generation rate for a horizontally polarized, normally incident pump, $|HH\rangle$ signal and idler state, $\phi = 79$ deg and $\theta_s = 0.2$ deg for the signal, opposite angle for the idler. Dashed line: the product of the maximum intensity inside the resonator of the signal and idler fields. (b) Solid line: generation rate versus the pump wavelength. The red dot marks the wavelength used in (d) and Fig. 4. Dashed: k_y at phase matching when $k_x = 0$. (c), (d) Generation rate in k-space for (c) phase matching at the Γ point and (d) for $\lambda_p = 774.43$ nm. White dashed line: phase matching condition; black dashed line: the path of constant θ_s in Fig. 4(a).

that the designed MS optimally translates the BIC enhancement of the signal and idler to a corresponding increase of SPDC.

We conducted studies of the intensity enhancement for different angles of θ_s and ϕ_s. The simulated intensities are fitted to a Lorentzian function $L(\omega, \mathbf{k})$ (see Sec. S5 in the Supplementary Material), and, from this fitted function, we calculate

$$\Xi_{\mathrm{SPDC}} = \frac{1}{(2\pi)^3}\frac{\lambda_p^2}{\lambda_s^{\mathrm{BIC}}\lambda_i^{\mathrm{BIC}}}\sum_{\substack{|HH\rangle,|HV\rangle,\\|VH\rangle,|VV\rangle}}\Xi_0 L(\omega_s, \mathbf{k_s})L(\omega_p - \omega_s, \mathbf{k}_p - \mathbf{k_s}), \tag{4}$$

where Ξ_0 is the ratio of the SFG zeroth diffraction order far-field intensity to the product of the maximum signal and idler intensities inside the resonator (see Sec. S4 in the Supplementary Material). The sum is taken over all polarization combinations of horizontal ($|H\rangle$) and vertical ($|V\rangle$) for the signal and idler, which forms the polarization basis for our wavefunction. The total photon pair generation rate across all angles and wavelengths can then be calculated via

$$\frac{1}{A_{\mathrm{tot}}\Phi_p}\frac{\mathrm{d}N_{\mathrm{pair}}}{\mathrm{d}t} = \iiint \Xi_{\mathrm{SPDC}}\mathrm{d}\omega_s\,\mathrm{d}k_{s,x}\,\mathrm{d}k_{s,y}, \tag{5}$$

where A_{tot} is the total sample area, and Φ_p is the incident pump intensity.

If we only integrate Eq. (5) over frequency, then we will obtain the pair-rate as a function of the signal wavevector, as seen in Figs. 2(c) and 2(d). Figure 2(c) has a pump wavelength at which the transverse phase matching condition occurs at the Γ point, and Fig. 2(d) has $\lambda_p = 774.43$ nm, which was chosen for illustrative purposes. Note that the pair-rate falls off near the Γ point, as symmetry protected BICs have singularities at the Γ point. We therefore only see enhancement in the off-Γ, quasi-BIC regime. In Fig. 2(d), the dashed white line shows the angle in k-space at which the transverse phase matching condition occurs, which matches the peak in generation as expected.

By then integrating over k-space, we obtain the total photon-pair generation rate as a function of the pump wavelength, as shown with a solid line in Fig. 2(b). Notably, the peak does not occur at the Γ point but just beyond it, as can be seen by comparing this plot with the dashed line showing the value of k_y at the transverse phase matching condition when $k_x = 0$. This, again, is due to the singularity at the Γ point. We calculate the theoretical peak brightness of this quasi-BIC to be $110\ \mathrm{Hz} \cdot \mathrm{mW}^{-1} \cdot \mathrm{nm}^{-1}$ over a 1.3-nm bandwidth, which is 2×10^3 that of simulations of an unpatterned nonlinear film.

3.2 Two BICs

Next, we studied the case where the signal and idler are generated at two different BICs. The most distinguishing feature here is the occurrence of hyperbolic transverse phase matching, as shown in Fig. 3(a), calculated according to the right-hand side of Eq. (2) for the normally incident pump with $\mathbf{k}_{p,\perp} = 0$. The condition for the pump wavelength of $\lambda_p = 774.22$ nm is shown by the dotted white line in Figs. 1(d), 3(a), and 3(d).

For the two-BIC case, in Fig. 3(c), we show the angular dependence in k-space of the photon-pair generation when transverse phase matching occurs at the Γ point, and, in Fig. 3(d), the case in which $\lambda_p = 774.22$ nm. As before, there is a peak in generation at the transverse phase matching condition (dashed white line). In Fig. 3(b), we see that the photon-pair generation rate is almost two orders of magnitude higher than for the single BIC case in Fig. 2(b). A factor of 6 of the enhancement can be attributed to different mode profiles and their overlap (see Sec. S4 in the Supplementary Material). Importantly, an order-of-magnitude increase is due to hyperbolic phase matching, whereby SPDC enhancement occurs for a much broader range of transverse photon wavevectors, in contrast to the single BIC case with elliptical phase matching only allowing a small range of wavevectors close to the Γ point. We calculated the theoretical peak brightness to be $4900\ \mathrm{Hz} \cdot \mathrm{mW}^{-1} \cdot \mathrm{nm}^{-1}$ over a 1.2-nm bandwidth, which is 10^5 that of simulations for an unpatterned nonlinear film. Such predicted brightness enhancement is also much stronger than for MSs based on Mie-like resonances.[18]

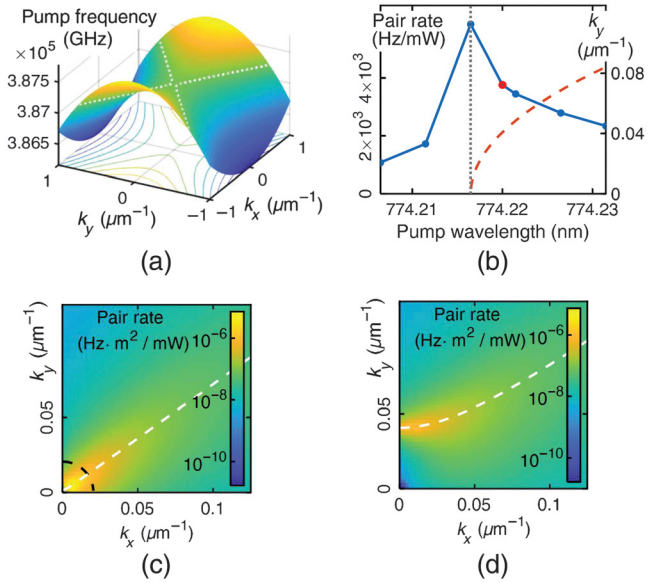

Fig. 3 Nondegenerate signal and idler at different BICs. (a) Transverse phase matching condition according to Eq. (2). The dotted white line corresponds to $\lambda_p = 774.22$ nm. (b) Solid line: generation rate versus the pump wavelength. The red circle is the integration of (d). Dashed line: k_y at transverse phase matching when $k_x = 0$. (c), (d) Generation rate in k-space at (c) phase matching at the Γ point ($\lambda_p = 774.2165$ nm) and (d) $\lambda_p = 774.22$ nm. White dashed line: phase matching condition; black dashed line: the path of constant θ_s in Fig. 4(c).

3.3 Entanglement

We determined the polarization entanglement of the generated signal and idler by performing a Schmidt decomposition (see Sec. S7 in the Supplementary Material), where the Schmidt number $K = 1$ indicates no entanglement and $K = 2$ maximum entanglement. In Fig. 4(a), we show that for the single BIC case the entanglement peaks at $K = 2$ when the azimuthal angle of the signal-photon emission is $\phi_s = 77$ deg, and the pump is horizontally polarized. The maximally entangled signal and

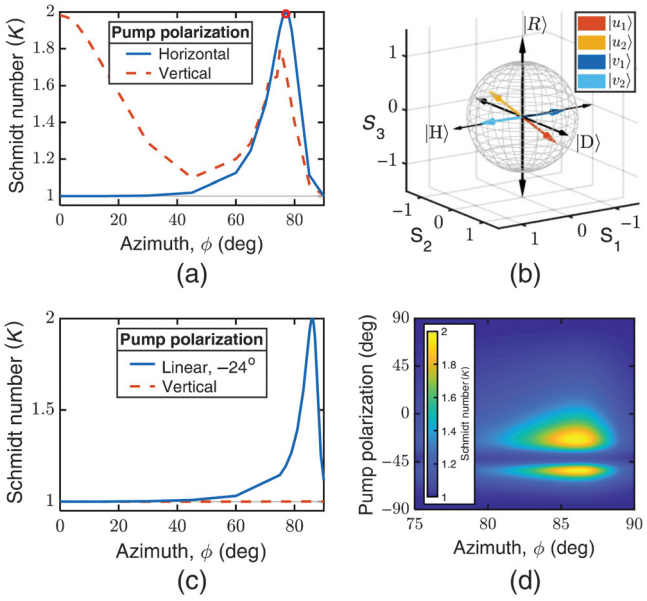

Fig. 4 Entanglement of the signal and idler photons generated from: (a), (b) a single BIC with $\lambda_p = 774.43$ nm; (c), (d) two different BICs with $\lambda_p = 774.2165$ nm. (a), (c) Schmidt number versus the photon angle. (b) Schmidt decomposition of the wavefunction plotted on the Poincaré sphere for the red dot in (a). (d) Schmidt number versus the pump polarization and photon angle.

idler pair states $\{|u_1\rangle, |v_1\rangle\}$ or $\{|u_2\rangle, |v_2\rangle\}$ are visualized in Fig. 4(b). For the two-BIC case, we can switch from full to no entanglement by changing the linear polarization of the pump [see Figs. 4(c) and 4(d)].

4 Discussion

The two elliptic paraboloids in Fig. 1(d) can only sum to a hyperbolic paraboloid because the MS lacks $\pi/2$ in-plane rotational symmetry. The D_{2h} symmetry of the MS means that the BICs must have an elliptic paraboloid dispersion near the ω point, as that matches the rotation and mirror symmetries of the MS. In our case, k_x and k_y are the major and minor axes, but a set of axes can always be chosen such that the dispersion is of the form

$$\omega(\mathbf{k}_\perp) = \zeta\left(\frac{k_x^2}{a^2} + \frac{k_y^2}{b^2}\right) + \omega_0, \tag{6}$$

where $\zeta = \pm 1$. The transverse phase matching condition, for a pump with normal incidence, is thus given by

$$\begin{aligned}\omega_p(\mathbf{k}_{p,\perp} = 0) &= \omega_s(\mathbf{k}_{s,\perp}) + \omega_i(\mathbf{k}_{i,\perp} = -\mathbf{k}_{s,\perp}) \\ &= k_{s,x}^2\left(\frac{\zeta_s}{a_s^2} + \frac{\zeta_i}{a_i^2}\right) + k_{s,y}^2\left(\frac{\zeta_s}{b_s^2} + \frac{\zeta_i}{b_i^2}\right) + \omega_{s,0} + \omega_{i,0} \\ &= \zeta_x \frac{k_{s,x}^2}{a_p^2} + \zeta_y \frac{k_{s,y}^2}{b_p^2} + \omega_{p,0},\end{aligned} \tag{7}$$

which can be either an elliptic or hyperbolic paraboloid, with the latter enabling enhanced photon-pair generation, as discussed above. In contrast, for an MS with D_{4h} symmetry (such as a slab with a square array of single holes), $\zeta_x \equiv \zeta_y$ and $a_p \equiv b_p$, which excludes a hyperbolic type of transverse phase matching.

We note that the symmetry properties enabling hyperbolic transverse phase matching will also hold when taking into account a MS substrate, as the presence of a substrate will convert the BICs at the Γ point into quasi-BICs, and the dominant emission of the photon pairs occurs in the off Γ (off-normal) direction in the quasi-BIC regime in any case, as shown in Figs. 2 and 3. These results suggest that strong SPDC enhancement will still persist in the presence of a substrate.

The influence of experimental imperfections on the other hand depends on their type. If the dimensions of the nanostructures, for example, the hole sizes, are varied equally in the whole MS, then the BIC states will remain, and the SPDC enhancement will be preserved, usually at slightly shifted wavelengths similar to the dependencies shown in Fig. 1(c). On the other hand, the random deviations in individual unit cells that effectively break the periodicity could lead to significant deterioration of the quality-factors, since the extended BIC states are based on resonances across multiple nanoresonators. Accordingly, for the best SPDC enhancement, it would be most important to maintain consistent periodic nanopatterning over the whole spatial extent of the MS. Additionally, the MS dimensions should be sufficiently large, with tens or hundreds of periods in each spatial direction, to avoid limitations on the resonance Q factor.[6,34] These conditions can be achieved with the state-of-the-art nanofabrication facilities. For example, ultrahigh Q factors of over 10,000 in dielectric MSs were reported for extended BICs.[6]

5 Conclusion

We have developed a method of enhanced photon-pair generation via symmetry protected BICs in nonlinear MSs, which are designed to realize a hyperbolic transverse phase matching condition. In terms of the brightness of the photon pair-generation, our nanoscale platform provides five orders of magnitude improvement over unpatterned films. Additional benefits are the tunability of the photon wavelengths and the degree of polarization entanglement. We anticipate that these predictions can stimulate significant experimental advances in miniaturized quantum light sources based on ultrathin nonlinear MSs for fundamental research and applications.

Acknowledgments

The authors would like to thank Jihua Zhang for the useful discussions and comments. We would like to acknowledge the support by the Australian Research Council (Nos. DP190101559, CE200100010, and FT170100331). A. M. and G. D. V. would like to acknowledge the support of the European Union Horizon 2020 Research and Innovation Programme through the METAFAST project (Grant No. 899673). The authors declare no conflicts of interest.

Code, Data, and Materials Availability

The COMSOL simulations were run using a specially developed code, which is made available at https://github.com/mettw/COMSOLd.

References

1. G. Li, S. Zhang, and T. Zentgraf, "Nonlinear photonic metasurfaces," *Nat. Rev. Mater.* **2**(5), 17010 (2017).
2. C. De Angelis, G. Leo, and D. N. Neshev, *Nonlinear Meta-Optics*, CRC Press, London (2020).
3. C. W. Hsu et al., "Bound states in the continuum," *Nat. Rev. Mater.* **1**(9), 16048 (2016).
4. M. V. Rybin et al., "High-Q supercavity modes in subwavelength dielectric resonators," *Phys. Rev. Lett.* **119**(24), 243901 (2017).
5. K. Koshelev et al., "Asymmetric metasurfaces with high-Q resonances governed by bound states in the continuum," *Phys. Rev. Lett.* **121**(19), 193903 (2018).
6. Z. J. Liu et al., "High-Q quasibound states in the continuum for nonlinear metasurfaces," *Phys. Rev. Lett.* **123**(25), 253901 (2019).
7. K. Koshelev et al., "Subwavelength dielectric resonators for nonlinear nanophotonics," *Science* **367**(6475), 288–292 (2020).
8. P. P. Vabishchevich et al., "Enhanced second-harmonic generation using broken symmetry III-V semiconductor Fano metasurfaces," *ACS Photonics* **5**(5), 1685–1690 (2018).
9. L. Carletti et al., "Second harmonic generation in monolithic lithium niobate metasurfaces," *Opt. Express* **27**(23), 33391–33398 (2019).
10. Z. Huang et al., "Highly efficient second harmonic generation of thin film lithium niobate nanograting near bound states in the continuum," *Nanotechnology* **32**(32), 325207 (2021).
11. A. N. Poddubny, D. N. Neshev, and A. A. Sukhorukov, "Quantum nonlinear metasurfaces," in *Nonlinear Meta-Optics*, C. De Angelis, G. Leo, and D. N. Neshev, Eds., pp. 147–180, CRC Press, London (2020).
12. A. S. Solntsev, G. S. Agarwal, and Y. S. Kivshar, "Metasurfaces for quantum photonics," *Nat. Photonics* **15**(5), 327–336 (2021).
13. M. G. Basset et al., "Perspectives for applications of quantum imaging," *Laser Photonics Rev.* **13**(10), 1900097 (2019).

14. F. Steinlechner et al., "Distribution of high-dimensional entanglement via an intra-city free-space link," *Nat. Commun.* **8**(1), 15971 (2017).
15. A. Orieux et al., "Direct Bell states generation on a III-V semiconductor chip at room temperature," *Phys. Rev. Lett.* **110**(16), 160502 (2013).
16. M. J. Collins et al., "Integrated spatial multiplexing of heralded single-photon sources," *Nat. Commun.* **4**(1), 2582 (2013).
17. G. Marino et al., "Spontaneous photon-pair generation from a dielectric nanoantenna," *Optica* **6**(11), 1416–1422 (2019).
18. T. Santiago-Cruz et al., "Photon pairs from resonant metasurfaces," *Nano Lett.* **21**(10), 4423–4429 (2021).
19. H. D. Saleh et al., "Towards spontaneous parametric down conversion from monolayer MoS_2," *Sci. Rep.* **8**(1), 3862 (2018).
20. K. F. Lee et al., "Photon-pair generation with a 100 nm thick carbon nanotube film," *Adv. Mater.* **29**(24), 1605978 (2017).
21. A. Nikolaeva et al., "Directional emission of down-converted photons from a dielectric nanoresonator," *Phys. Rev. A* **103**(4), 043703 (2021).
22. C. Okoth et al., "Microscale generation of entangled photons without momentum conservation," *Phys. Rev. Lett.* **123**(26), 263602 (2019).
23. C. Okoth et al., "Idealized Einstein–Podolsky–Rosen states from non-phase-matched parametric down-conversion," *Phys. Rev. A* **101**(1), 011801(R) (2020).
24. T. Santiago-Cruz et al., "Entangled photons from subwavelength nonlinear films," *Opt. Lett.* **46**(3), 653–656 (2021).
25. A. N. Poddubny and D. A. Smirnova, "Nonlinear generation of quantum-entangled photons from high-Q states in dielectric nanoparticles," arXiv:1808.04811 (2018).
26. T. C. Wang et al., "Improved generation of correlated photon pairs from monolayer WS_2 based on bound states in the continuum," *Photonics Res.* **7**(3), 341–350 (2019).
27. L. Li et al., "Metalens-array-based high-dimensional and multiphoton quantum source," *Science* **368**(6498), 1487–1490 (2020).
28. J. Ma et al., "Resonantly tunable second harmonic generation from lithium niobate metasurfaces," arXiv:2002.06594 (2020).
29. Z. J. Huang et al., "Fano resonance on nanostructured lithium niobate for highly efficient and tunable second harmonic generation," *Nanomaterials (Basel)* **9**(1), 69 (2019).
30. A. Fedotova et al., "Second-harmonic generation in resonant nonlinear metasurfaces based on lithium niobate," *Nano Lett.* **20**(12), 8608–8614 (2020).
31. L. Carletti et al., "Giant nonlinear response at the nanoscale driven by bound states in the continuum," *Phys. Rev. Lett.* **121**(3), 033903 (2018).
32. A. N. Poddubny et al., "Generation of photon-plasmon quantum states in nonlinear hyperbolic metamaterials," *Phys. Rev. Lett.* **117**(12), 123901 (2016).
33. F. Lenzini et al., "Direct characterization of a nonlinear photonic circuit's wave function with laser light," *Light Sci. Appl.* **7**(1), 17143 (2018).
34. M. S. Bin-Alam et al., "Ultra-high-Q resonances in plasmonic metasurfaces," *Nat. Commun.* **12**(1), 974 (2021).
35. L. Carletti et al., "Controlling second-harmonic generation at the nanoscale with monolithic AlGaAs-on-AlOx antennas," *Nanotechnology* **28**(11), 114005 (2017).
36. D. Schattschneider, "Plane symmetry groups—their recognition and notation," *Am. Math. Monthly* **85**(6), 439–450 (1978).
37. J. D. Sautter et al., "Tailoring second-harmonic emission from (111)-GaAs nanoantennas," *Nano Lett.* **19**(6), 3905–3911 (2019).
38. S. Buckley et al., "Second-harmonic generation in GaAs photonic crystal cavities in (111)B and (001) crystal orientations," *ACS Photonics* **1**(6), 516–523 (2014).
39. Y. J. Lu and Z. Y. Ou, "Optical parametric oscillator far below threshold: experiment versus theory," *Phys. Rev. A* **62**(3), 033804 (2000).
40. M. V. Fedorov and N. I. Miklin, "Schmidt modes and entanglement," *Contemp. Phys.* **55**(2), 94–109 (2014).
41. I. Lankham, B. Nachtergaele, and A. Schilling, *Linear Algebra as an Introduction to Abstract Mathematics*, World Scientific, Singapore (2016).
42. P. Kaye, R. Laflamme, and M. Mosca, *An Introduction to Quantum Computing*, Oxford University Press, Oxford (2007).

Matthew Parry received his bachelor's degree from the University of New South Wales, Sydney, Australia. He is a PhD student at the Australian National University (ANU). His research interests are in metasurfaces, especially with respect to quantum applications. He is a member of SPIE.

Andrea Mazzanti received his MSc degree in engineering physics from Politecnico di Milano, Milan, Italy, in 2017 and his PhD in 2021. His research interests include the design and modeling of optical metastructures for a variety of nanophotonic applications, such as nonlinear frequency generation, plasmonic nanoheater aggregates assisted drug delivery, and all-optically controllable dielectric metasurfaces.

Alexander Poddubny received his PhD from Ioffe Institute, St. Petersburg, Russia, in 2008 and became a professor of the Russian Academy of Sciences in 2018. He is an Australian future fellow at the ANU and a senior researcher at the Ioffe Institute. His current research interests include quantum optics, many-body physics, and optomechanics.

Giuseppe Della Valle is a professor in the Physics Department of the Politecnico di Milano, where he teaches courses of general physics, nano-optics, and plasmonics. His research activity is devoted to both theoretical and experimental research in physics and optics, with particular interest to the development of innovative photonic structures at the micro- and nanoscale for the generation and coherent control of light.

Dragomir N. Neshev is a professor in physics at the ANU and the director of the Australian Research Council Centre of Excellence for Transformative Meta-Optical Systems (TMOS). He has worked in the field of optics at several research centers and joined the ANU in 2002. His activities span over several branches of optics, including periodic photonic structures, singular optics, plasmonics, and optical metasurfaces.

Andrey A. Sukhorukov is a professor at the Research School of Physics of the ANU. He leads a research group on nonlinear and quantum photonics, targeting the fundamental aspects of miniaturization of optical elements down to micro- and nanoscale. In 2015, he was elected a fellow of The Optical Society for contributions to nonlinear and quantum integrated photonics, including frequency conversion and broadband light manipulation in waveguide circuits and metamaterials.

Letter

ADVANCED PHOTONICS

Heterogeneously integrated, superconducting silicon-photonic platform for measurement-device-independent quantum key distribution

Xiaodong Zheng,[a,†] Peiyu Zhang,[a,†] Renyou Ge,[b,†] Liangliang Lu,[a,†] Guanglong He,[a,†] Qi Chen,[a,†] Fangchao Qu,[a] Labao Zhang,[a,*] Xinlun Cai,[b,*] Yanqing Lu,[a] Shining Zhu,[a] Peiheng Wu,[a] and Xiao-Song Ma[a,*]

[a]Nanjing University, National Laboratory of Solid-state Microstructures, School of Physics, Research Institute of Superconducting Electronics, School of Electronic Science and Engineering, College of Engineering and Applied Sciences, Collaborative Innovation Center of Advanced Microstructures, Nanjing, China

[b]Sun Yat-sen University, State Key Laboratory of Optoelectronic Materials and Technologies, School of Electronics and Information Technology, Guangzhou, China

Abstract. Integrated photonics provides a route to both miniaturization of quantum key distribution (QKD) devices and enhancing their performance. A key element for achieving discrete-variable QKD is a single-photon detector. It is highly desirable to integrate detectors onto a photonic chip to enable the realization of practical and scalable quantum networks. We realize a heterogeneously integrated, superconducting silicon-photonic chip. Harnessing the unique high-speed feature of our optical waveguide-integrated superconducting detector, we perform the first optimal Bell-state measurement (BSM) of time-bin encoded qubits generated from two independent lasers. The optimal BSM enables an increased key rate of measurement-device-independent QKD (MDI-QKD), which is immune to all attacks against the detection system and hence provides the basis for a QKD network with untrusted relays. Together with the time-multiplexed technique, we have enhanced the sifted key rate by almost one order of magnitude. With a 125-MHz clock rate, we obtain a secure key rate of 6.166 kbps over 24.0 dB loss, which is comparable to the state-of-the-art MDI-QKD experimental results with a GHz clock rate. Combined with integrated QKD transmitters, a scalable, chip-based, and cost-effective QKD network should become realizable in the near future.

Keywords: quantum key distribution; hybrid photonics; single-photon detector; Bell-state measurement; time-multiplexing.

Received Jun. 17, 2021; revised manuscript received Sep. 27, 2021; accepted for publication Sep. 29, 2021; published online Oct. 30, 2021.

[DOI: 10.1117/1.AP.3.5.055002]

1 Introduction

Quantum key distribution (QKD) employs the laws of quantum physics to provide information-theoretical security for key exchange.[1–5] Despite the substantial progress in the past 35 years, practical implementations of QKD still deviate from ideal descriptions in security proofs, mainly due to potential side-channel attacks. For instance, a series of loopholes have been identified due to the imperfections of measurement devices.[6–9] Inspired by the time-reversed entanglement-based QKD, measurement-device-independent QKD (MDI-QKD), which removes all detector side attacks, has been proposed.[10,11] Instead of relying on the trusted nodes of traditional QKD protocols, MDI-QKD requires only a central node (Charlie) to perform a Bell-state measurement (BSM). The correlations between the two senders (Alice and Bob) can be obtained from the BSM results. Importantly, even if Charlie is not trusted, one can still guarantee the security of the MDI-QKD as long as Charlie can project his two photons onto Bell states. The outstanding features of MDI-QKD invite global experimental efforts, which

*Address all correspondence to Labao Zhang, lzhang@nju.edu.cn; Xinlun Cai, caixlun5@mail.sysu.edu.cn; Xiao-Song Ma, xiaosong.ma@nju.edu.cn

†These authors contributed equally to this work.

are mainly based on bulk/fiber components.[12–20] Despite the additional BSM by Charlie, the key rate[17] and the communication distance[18] of MDI-QKD can be comparable with those of traditional QKD. Furthermore, the star-like topology of the MDI-QKD quantum network is naturally suited for the metropolitan network with multiple users.[21–23] Recently, the generalization of the MDI protocol to multipartite schemes has been investigated.[24–26] It has been shown that the performance of the multipartite schemes can be advantageous to iterative use of independent bipartite protocols.[26]

From the perspectives of hardware, recent developments involve particular integrated photonic devices for QKD, including on-chip encoders based on silicon modulators,[27–31] on-chip transmitters including lasers, photodiodes, modulators based on indium phosphide,[32,33] and decoders based on silicon oxynitride[34] and silicon dioxide,[35] as well as integrated silicon-photonic chips for continuous-variable (CV) QKD.[36,37] The notion of MDI has also been extended to CV protocols[38] and can be applied for multipartite metropolitan networks with a considerable rate.[39] Most of the components used in QKD, including lasers, modulators, and passive components [such as beam splitters (BSs) and attenuators] are widely used in classical optical communication systems and are not specifically designed for QKD. In addition, single-photon detectors are indispensable for discrete-variable QKD systems, because the senders' pulses have to have a mean photon number of <1 to guarantee communication security. So far, a single-photon detector integrated chip platform has not been employed in an MDI-QKD system. In this work, we report the realization of a heterogeneously integrated, superconducting silicon-photonic chip, and its application for MDI-QKD.

2 Schematic of a Time-Multiplexed MDI-QKD

We use time-bin qubits to encode bit information, which are well suited for fiber-based quantum communication due to their immunity to random polarization rotations in fibers. The conceptual scheme of our experiment is shown in Fig. 1(a). Alice and Bob encode keys with time-bin qubits using modulated weak coherent pulse sets. In Pauli Z-basis, the time-bins are encoded as the early $|e\rangle$ and the late $|l\rangle$ for bit values of 0 and 1, respectively. The temporal separation between $|e\rangle$ and $|l\rangle$ is Δt. In Pauli X-basis, the keys are encoded as the coherent superposition states between $|e\rangle$ and $|l\rangle$: $|+\rangle = (|e\rangle + |l\rangle)/\sqrt{2}$ and $|-\rangle = (|e\rangle - |l\rangle)/\sqrt{2}$, representing bit values of 0 and 1, respectively. The Z-basis code is used for key exchange, and the X-basis code is for error detection. These encoded time-bin qubits are then sent to Charlie, who performs the BSM on the incoming time-bin qubits using a BS and two single-photon detectors (D_1 and D_2).[10,11] Using linear optical elements, the success probability of BSM is bounded by 50%.[40] For projective measurements, optimal BSM corresponds to distinguish two out of four Bell states. Although time-bin qubits are well suited for fiber-based quantum communication, optimal BSM for time-bin qubits has yet to be realized. The bottleneck so far has been the lack of high-speed single-photon detectors.[33,41,42] The BSM scheme for time-bin qubits is shown in the inset of Fig. 1(a). The coincidence counts between two different detectors at different time bins correspond to coincidence counts between $|e\rangle_{D_1}$ (D_1 detects a photon at an early bin, red) and $|l\rangle_{D_2}$ (D_2 detects a photon at a late bin, red), or coincidence counts between $|l\rangle_{D_1}$ and $|e\rangle_{D_2}$. Such coincidence detection projects two photons onto $|\Psi^-\rangle = (|el\rangle - |le\rangle)/\sqrt{2}$, which is the common scenario realized in most of the time-bin BSM schemes.[14,33,42] In order to achieve optimal BSM, we also need to detect $|\Psi^+\rangle = (|el\rangle + |le\rangle)/\sqrt{2}$ by measuring the coincidence counts of one detector at different time bins, corresponding to the coincidence detection between $|e\rangle_{D_1}$ and $|l\rangle_{D_1}$, or $|e\rangle_{D_2}$ and $|l\rangle_{D_2}$. This particular BSM requires high-speed single-photon detection, able to detect consecutive photons separated by Δt. The unique design of the waveguide-integrated superconducting nanowire single-photon detector (SNSPD) provides a short recovery time (<10 ns) for single-photon detection, enabling us to perform time-bin-encoded optimal BSM between two independent lasers for the first time. Note that if we only use one set of time-bin qubits, the system repetition rate will be limited to $1/(2\Delta t)$.

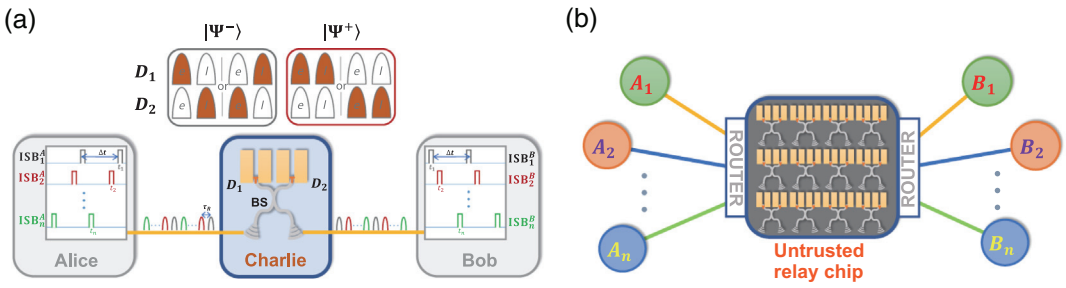

Fig. 1 Schematic of a time-multiplexed MDI-QKD and a star-like MDI-QKD network. (a) Schematic of a time-multiplexed MDI-QKD with optimal BSM. Alice and Bob send time-bin encoded qubits to Charlie for exchanging keys. By detecting the coincidence (red) between the early (e) and late (l) pulses with two detectors (D_1 and D_2), or with one detector (D_1 or D_2), Charlie projects two incoming photons onto $|\Psi^-\rangle$ or $|\Psi^+\rangle$ to facilitate the key exchanges between Alice and Bob. The full-recovery time of the single-photon detector sets the lower limit of the temporal separation (Δt) between e and l pulses for realizing optimal BSM. We insert ISBs between e and l for realizing time-multiplexing and hence increase the key rate by reducing the bin separation from Δt to τ_R. (b) A star-like MDI-QKD network with the untrusted relay server. A series of Alice ($A_1, A_2, \ldots, A_n$) and Bob ($B_1, B_2, \ldots, B_n$) prepare modulated weak coherent pulses and send to the routers. Two routers select a pair of Alice and Bob and send their pulses to an untrusted relay server controlled by Charlie.

In order to maximize the channel efficiency, we use time-multiplexed encoding to insert independent sets of bins ($\mathrm{ISB}_2^A, \ldots, \mathrm{ISB}_n^A$ and $\mathrm{ISB}_2^B, \ldots, \mathrm{ISB}_n^B$) between the $|e\rangle$ and $|l\rangle$ bins of ISB_1^A and ISB_1^B. Therefore, the system repetition rate will be greatly increased to $1/(2\tau_R)$, where τ_R is the time difference between t_1 and t_2. By harnessing the optimal BSM and time-multiplexing, the key rate generation is enhanced by an order of magnitude compared to the system without using these two techniques. Consequently, our key rate is comparable to the state-of-the-art MDI-QKD experimental results with a GHz clock rate, as detailed later.

3 Integrated Relay Server for MDI-QKD Based on Superconducting Silicon Photonics

Our heterogeneously integrated, superconducting silicon-photonic platform provides a server architecture for realizing a multiple-user trust-node-free quantum network with a fully connected bipartite-graph topology. As shown in Fig. 1(b), modulated weak coherent pulses are prepared by Alices $(A_1, A_2, \ldots, A_n)$ and Bobs $(B_1, B_2, \ldots, B_n)$ and are sent to the routers. Two routers select the pair of the communicating Alice and Bob and send their pulses to an untrusted relay server controlled by Charlie. At Charlie's station, a chip with multiple low-dead-time,[43] low-timing-jitter,[44] and high-efficiency detectors in conjunction with low-loss silicon photonics[45] is used to realize the BSM. This configuration allows any user at Alice's side to communicate with any user at Bob's side and hence to realize a fully connected bipartite quantum network.

The schematic of our experimental setup is shown in Fig. 2(a). Alice (Bob) chops the CW laser operated at about 1536.47 nm into the desired pulse sequences. The pulse is about 370 ps wide and separated by 12 ns at a rate of 41.7 MHz rate (1/24 ns). Z-basis (X-basis) states are generated by chopping the laser into $|e\rangle$ or (and) $|l\rangle$ states with intensity modulators (IMs). The average photon numbers per pulse in the two bases are about the same. The resulting pulses are sent into a phase modulator (PM) with (without) π-phase shift for the generation of $|-\rangle$ ($|+\rangle$) states. The electrical signals applied to the modulators are generated by an arbitrary waveform generator [not shown in Fig. 2(a)]. An additional 50:50 BS combined with a power sensor (PS) is employed to monitor the long-term stability of laser power in each encoder.

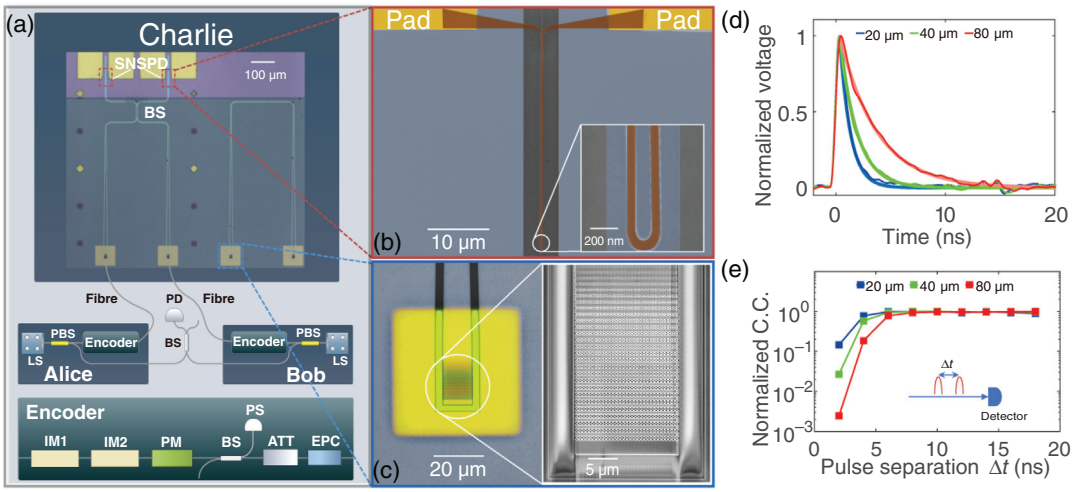

Fig. 2 Experimental device and setup. (a) Schematic of the experiment setup. Alice (Bob) employs a CW laser as the LS and encodes the keys into optical pulses with an encoder module. In this module, one intensity modulator (IM1) chops out early ($|e\rangle$) and late ($|l\rangle$) temporal modes to generate time-bin qubits with a 370 ps duration and separated by 12 ns with a 41.7 MHz repetition rate. IM2 implements intensity modulation for the decoy-state protocol. A PM applies a π-phase to the late temporal modes for $|-\rangle$ and 0-phase for $|+\rangle$ in X-basis. This PM also implements the phase randomization required for MDI-QKD. A variable attenuator prepares weak coherent pulses and simulates the propagation loss in fibers. An EPC adjusts the polarization of the input pulses. The pulses travel through fibers and are coupled into the integrated chip of the relay server (Charlie) for BSM. On the chip, we use a multi-mode interferometer acting as a 50:50 BS and two SNSPDs. (b) False-color scanning electron micrograph (SEM) of the SNSPD. A 80-nm-wide, 80-μm-long U-shaped NbN nanowire is integrated on a 500-nm-wide silicon optical waveguide and connected with two gold pads for electrical readout. The inset shows the zoomed part of the nanowire. (c) Optical and SEM graphs of the high-efficiency photonic-crystal grating coupler with a back-reflected mirror. (d) The averaged amplified response pulses of the 80-nm-wide SNSPD with different lengths. The 1/e-decay time of different SNSPDs is obtained by fitting: 20 μm to 0.96 ns; 40 μm to 1.56 ns; 80 μm to 3.39 ns. (e) Normalized coincidence counts of one detector consecutively detecting both early and late time bins as a function of time separation Δt between them. PBS, polarization beam splitter; PD, photodiode; PS, power sensor; and EPC, electrical polarization controller.

One of the most important requirements of MDI-QKD is to obtain high-quality two-photon Hong–Ou–Mandel (HOM) interference on the integrated relay server. To achieve that, it is necessary for Alice and Bob to generate indistinguishable weak-coherent pulses. The interfering pulses have to be indistinguishable in all degrees of freedom (DOFs), including spectrum, time, and polarization. For the spectrum DOF, Alice's and Bob's unmodulated pulses pass through polarization beam splitters (PBSs), with one of the outputs connected with a 50:50 BS for frequency beating. From the beating signal, we feedback onto one of the lasers and regulate the frequency difference of these two lasers to be within 10 MHz (see Supplementary Material for details). For the polarization DOF, two electrical polarization controllers (EPCs) are used to optimize the polarization of both pulses before they are coupled into Charlie's chip. For the temporal DOF, we adjust the relative electrical delay between Alice's and Bob's IMs to ensure that their pulses arrive at the chip simultaneously. Attenuators are used to adjust the average photon number per pulse and simulate the loss of the communication channels.

These pulses are then sent to Charlie's relay server chip, which is mounted on a nanopositioner in a closed-cycle cryostat with a base temperature of 2.1 K. We show the U-shape waveguide-integrated SNSPD in Fig. 2(b) in which the superconducting nanowire (80-nm-wide, 80-μm-long) is highlighted in red and the silicon optical waveguide (500 nm-wide) is shown in blue. Figure 2(c) shows the scanning electron microscope image of the photonic-crystal grating coupler,[46,47] which couples light from the fiber array to the chip. We obtain coupling loss from the reference device, which is at the right side of the main device.[48] The grating coupler with a back-reflected mirror offers a coupling loss of ~2.24 dB at a wavelength of 1536 nm. The main device has two identical grating couplers, coupling Alice's and Bob's pulses from fiber to chip. Silicon optical waveguides guide the pulses to a multi-mode interference (MMI) coupler, which acts as a 50:50 BS. At the output of the MMI, two waveguide-integrated SNSPDs work simultaneously for detecting photons. Both SNSPDs are biased with constant voltage sources and connected with electronic readout circuitries. In Fig. 2(d), we show the electrical signals of waveguide-integrated SNSPDs with different nanowire lengths. The decay time of SNSPD is directly proportional to the kinetic inductance of the nanowire. Shorter detectors exhibit lower kinetic inductance and therefore have shorter decay times, resulting in faster detector recovery.[49] However, for traditional normal-incidence SNSPDs, the shorter nanowire length leads to lower detection efficiency, because it is necessary to fabricate large-area meander nanowire to match the optical modes from fibers to obtain high detection efficiency. Therefore, it is hard to simultaneously obtain low dead time and high detection efficiency with the traditional design. In our work, we use the evanescent coupling between the optical waveguide and superconducting nanowire to circumvent this trade-off. Therefore, we are able to obtain low dead time as well as high on-chip detection efficiency. To further quantitatively characterize the efficiency of our SNSPDs for projecting two photons onto $|\Psi^+\rangle$, we measure the normalized coincidence counts of one detector consecutively detecting both early and late time bins as a function of the time separation Δt between them. The experimental results are shown in Fig. 2(e). The detection probability is significantly decreased when the time separation is smaller than the dead time and is fully recovered for separation larger than 12 ns. Based on these results, the dead time of the SNSPD we use in our QKD system is about 3.4 ns for the 1/e-delay time, and we set the time separation between $|e\rangle$ and $|l\rangle$ to be 12 ns. This short time separation not only allows high-speed detection but also greatly simplifies frequency stabilization of the light source (LS). For a traditional normal-incidence SNSPD that limits 75 ns time-bin separation,[50] a 185-kHz frequency difference between two lasers can result in a 5-deg phase error, which is technologically challenging and not practical. By contrast, for our waveguide-integrated SNSPD, the frequency-stabilization requirement is only 1.2 MHz for achieving the same phase error, which is significantly more feasible in practice.

4 Optimal Bell-State Measurement for Time-Bin Qubits

In Figs. 3(a) and 3(b), we show the two-photon coincidence counts with optimal BSM as a function of the relative electronic delays between Alice's and Bob's pulse sequence in which Charlie projects the two photons sent by Alice and Bob onto $|\Psi^-\rangle$ and $|\Psi^+\rangle$, respectively. The dependence of the coincidence counts on the delay is a result of BSM, showing the coherent two-photon superposition. Due to the symmetry of $|\Psi^-\rangle$ and $|\Psi^+\rangle$, when Alice and Bob send the same states in X-basis, $|++\rangle$ or $|--\rangle$, we obtain the destructive/constructive interference patterns for the BSM results of $|\Psi^-\rangle/|\Psi^+\rangle$, as shown by the blue dots in Figs. 3(a) and 3(b). When Alice and Bob send the orthogonal states in X-basis, $|+-\rangle$ or $|-+\rangle$, we obtain the inverse results, as shown by the red dots in Figs. 3(a) and 3(b). [The logic of coincidence detection for $|\Psi^-\rangle$ and $|\Psi^+\rangle$ is shown in the inset of Fig. 1(a).]

We obtain secure keys from the Z-basis measurements and verify the reliability of the QKD system in X-basis.[18] To quantify the performance of the system, we analyze the quantum bit error rate (QBER). For instance, Alice and Bob exchange their keys conditionally on Charlie obtaining $|\Psi^-\rangle/|\Psi^+\rangle$ from his BSM, when Alice and Bob send the same/orthogonal states. For X-basis, the probability of Charlie obtaining a coincidence at two subsequent time bins with time separation Δt is $P_X^-(t,t+\Delta t)/P_X^+(t,t+\Delta t)$. We then obtain the QBER in X-basis ($\mathrm{QBER}_X^{|\Psi^-\rangle}/\mathrm{QBER}_X^{|\Psi^+\rangle}$) based on[51]

$$\mathrm{QBER}_X^{|\Psi^-\rangle}=\frac{P_X^-(t,t+\Delta t)}{P_X^+(t,t+\Delta t)+P_X^-(t,t+\Delta t)}, \tag{1}$$

$$\mathrm{QBER}_X^{|\Psi^+\rangle}=\frac{P_X^+(t,t+\Delta t)}{P_X^+(t,t+\Delta t)+P_X^-(t,t+\Delta t)}, \tag{2}$$

$$\mathrm{QBER}_Z^{|\Psi^\pm\rangle}=\frac{P_Z^-(t,t+\Delta t)}{P_Z^+(t,t+\Delta t)+P_Z^-(t,t+\Delta t)}. \tag{3}$$

In addition, the phase difference of two subsequent time bins induced by frequency difference is

$$\theta=2\pi\Delta\omega\Delta t=2\pi(\omega_a-\omega_b)\Delta t=2\pi c\Delta t\frac{|\lambda_a-\lambda_b|}{\lambda_a\lambda_b}, \tag{4}$$

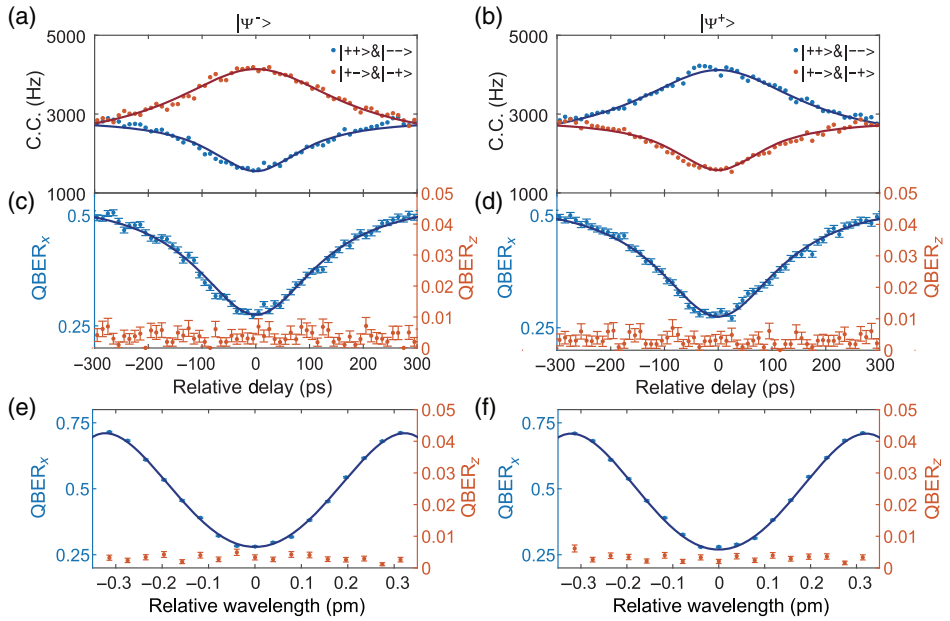

Fig. 3 Experimental results of optimal BSM and QBER. (a) BSM results of $|\Psi^-\rangle$. When Alice and Bob send the same states ($|++\rangle/|--\rangle$, blue dots), or different states ($|+-\rangle/|-+\rangle$, red dots), we obtain destructive and constructive interference in coincidence counts as functions of relative temporal delay, respectively. (b) BSM results of $|\Psi^+\rangle$. Note that the correlations between Alice and Bob are inverted comparing to $|\Psi^-\rangle$. (c), (d) The QBER in X-basis (blue) and Z-basis (red) for $|\Psi^-\rangle$ and $|\Psi^+\rangle$, respectively. (e), (f) The measured QBER in X-basis and Z-basis as a function of the wavelength detuning between two lasers for two different Bell states.

where c is the speed of light and ω_a (ω_b) and λ_a (λ_b) are the laser's frequency and wavelength of Alice (Bob), respectively.

$P_X^-(t, t+\Delta t)/P_X^+(t, t+\Delta t)$ can be written as

$$P_X^{\pm}(t, t+\Delta t) = 1 \pm V \exp\left[-\tau^2\left(c\frac{|\lambda_a - \lambda_b|}{\lambda_a\lambda_b}\right)^2\right]\cos\theta, \qquad (5)$$

where V is the visibility and τ is the coincidence window.

As for Z-basis, QBER_Z always have the same formula for $|\Psi^-\rangle/|\Psi^+\rangle$. In Figs. 3(c) and 3(d), we show the measured $\mathrm{QBER}_X^{|\Psi^-\rangle}$ and $\mathrm{QBER}_X^{|\Psi^+\rangle}$ (blue) as functions of time delays between Alice and Bob, which show the minimum close to 0.25 at the zero time delay. For Z-basis, the measured $\mathrm{QBER}_Z^{|\Psi^\pm\rangle}$ (red) are close to zero, showing the high quality of our system. In Figs. 3(e) and 3(f), we vary the relative central wavelength between Alice's and Bob's lasers. Also, we show the results for $\mathrm{QBER}_X^{|\Psi^-\rangle}$ and $\mathrm{QBER}_X^{|\Psi^+\rangle}$ as functions of the relative wavelength, respectively. The experimental data (blue dots) agree well with the theoretical prediction (blue curves).

5 Enhancing Key Rate with Time-Multiplexing

Although the full-recovery time of the detector determines the time-bin separation to be 12 ns, we can harness the time-multiplexed technique by inserting more pairs of time-bin pulses to enhance the key rate. This is particularly useful in high-loss communication applications. As shown in the insets of Fig. 4(a), we insert up to five bins within 12 ns with an equal temporal separation of 2 ns. By combining this

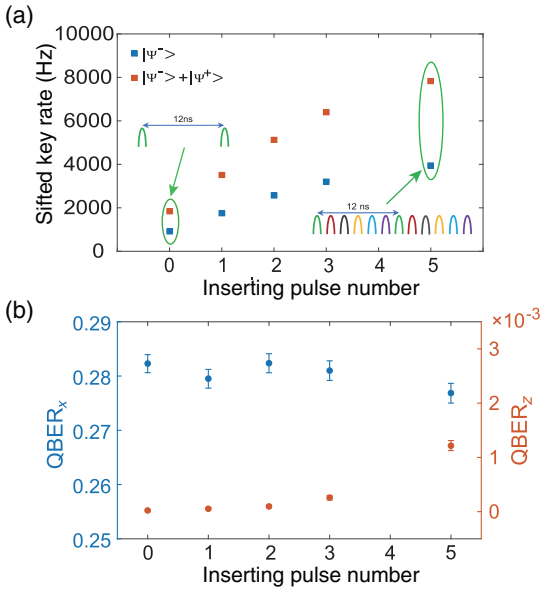

Fig. 4 Enhanced key rate by time-multiplexing. (a) The sifted key rate as a function of the inserted pulse number within the full-recovery time of SNSPD (12 ns). Red squares are the results of optimal BSM and blue squares are the results of $|\Psi^-\rangle$ only measurement. To compare fairly, in all the results presented here, Alice and Bob send the weak coherent pulses with the average photon number of 0.66 per pulse, and the total loss is 35.0 dB (including chip insertion loss ~4.5 dB). (b) QBER_X and QBER_Z versus inserting pulse number, indicating that time-multiplexing has little influence on error rate.

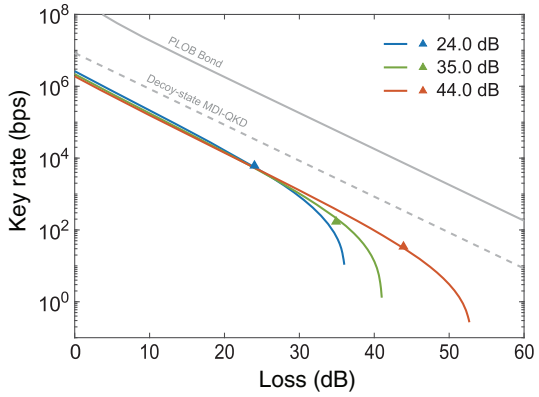

Fig. 5 The key rate at different losses including chip insertion loss. The solid lines show theoretical simulations and the triangle symbols show experimental results with a loss of 24.0, 35.0, and 44.0 dB, respectively. For different losses, the parameters (the intensities, s, μ, ν, and the probabilities of intensities, P_s, P_μ, P_ν) are different (see Supplementary Material for detailed parameters of theoretical simulations). The gray solid line: PLOB bond[55] and the gray dotted line: decoy-state MDI-QKD are numerical simulations (see Supplementary Material for details).

time-multiplexed technique and optimal BSM, we enhance the sifted key rate by almost an order of magnitude. At the same time, these two techniques have little impact on QBER_X and QBER_Z, as shown in Fig. 4(b).

We demonstrate a complete MDI-QKD system including decoy states and phase randomization for guaranteeing the security[13–20,52,53] with our heterogeneously integrated, superconducting silicon-photonic platform. We use a four-intensity encoding protocol[52] with three intensities (μ, ν, o) in the X-basis for decoy-state analysis and one intensity (s) in the Z-basis for key generation. Finite-key effects are considered in the secure-key-rate analysis with a failure probability of 10^{-10}.[54] For statistical fluctuations, we use the joint constraints where the same observables are combined and treated together[52] (see Supplementary Material for details).

In this part of the experiment, we evenly insert two more pairs of time-bin qubits within 12 ns separation. Therefore, the effective clock rate of our system is tripled to 125 MHz (1/8 ns). The secure key rates for different losses are shown in Fig. 5. With the 125 MHz clock rate, we obtain the key rate of 6.166 kbps at the loss of 24.0 dB. This loss includes chip insertion loss ~4.5 dB. The actual transmission loss is about 19.5 dB, which corresponds to 98 km standard fiber. To the best of our knowledge, this is the highest secure key rate obtained experimentally with ~20 dB transmission loss in MDI-QKD, which is highly relevant in the context of a metropolitan quantum network without detector vulnerabilities. Furthermore, we obtain the secure key rates of 170 and 34 bps with total losses of about 35.0 and 44.0 dB. We emphasize that our secure key rates with the 125 MHz clocked system are very close to the best MDI-QKD experiments with a GHz clock rate.[31,56] In contrast with the GHz clock rate MDI-QKD experiments, our system does not require the complicated injection locking technique, which significantly reduces the complexity of the transmitter (see Table S1 in the Supplementary Material for detailed comparison).

6 Conclusion

We have demonstrated the first integrated relay server for MDI-QKD with a heterogeneous superconducting silicon-photonic chip. The excellent optical and electronic performance of this chip not only facilitates the experimental high-visibility HOM interference and low QBER, but also allows us to perform optimal BSM for time-bin qubits for the first time. Our work shows that integrated quantum-photonic chips provide not only a route to miniaturization but also significantly enhance the system performance more than traditional platforms. Our chip-based relay server can also be employed in twin-field QKD (TF-QKD),[57] which can overcome the rate-distance limit of QKD without quantum repeaters. TF-QKD is indispensable in long-distance intercity communication links. Moreover, the chip-based relay server with the MDI-QKD protocol presented in this work could be an ideal solution for a scalable trust-node-free metropolitan quantum network. Using more advanced waveguide-integrated SNSPDs,[45] one can further improve the integrated server with a high detection efficiency, low timing jitter, and high repetition rate. Combined with photonic-chip transmitters,[31,33] a fully chip-based, scalable, and high-key-rate MDI-QKD metropolitan quantum network should be realized in the near future.

Acknowledgments

We would like to thank R. Chen and A. Miller for helpful discussions. This research was supported by the National Key Research and Development Program of China (Nos. 2017YFA0303704, 2019YFA0308700, and 2017YFA0304002), the National Natural Science Foundation of China (Nos. 11690032, 11321063, and 12033002), the NSFC-BRICS (No. 61961146001), the Leading-Edge Technology Program of Jiangsu Natural Science Foundation (No. BK20192001), and the Fundamental Research Funds for the Central Universities.

References

1. H.-K. Lo and H. F. Chau, "Unconditional security of quantum key distribution over arbitrarily long distances," *Science* **283**(5410), 2050–2056 (1999).
2. N. Gisin et al., "Quantum cryptography," *Rev. Mod. Phys.* **74**(1), 145–195 (2002).
3. V. Scarani et al., "The security of practical quantum key distribution," *Rev. Mod. Phys.* **81**(3), 1301–1350 (2009).
4. F. Xu et al., "Secure quantum key distribution with realistic devices," *Rev. Mod. Phys.* **92**(2), 025002 (2020).
5. S. Pirandola et al., "Advances in quantum cryptography," *Adv. Opt. Photonics* **12**(4), 1012–1236 (2020).
6. V. Makarov, A. Anisimov, and J. Skaar, "Effects of detector efficiency mismatch on security of quantum cryptosystems," *Phys. Rev. A* **74**(2), 022313 (2006).
7. Y. Zhao et al., "Quantum hacking: experimental demonstration of time-shift attack against practical quantum-key-distribution systems," *Phys. Rev. A* **78**(4), 042333 (2008).
8. L. Lydersen et al., "Hacking commercial quantum cryptography systems by tailored bright illumination," *Nat. Photonics* **4**(10), 686–689 (2010).
9. M. Elezov et al., "Countermeasure against bright-light attack on superconducting nanowire single-photon detector in quantum key distribution," *Opt. Express* **27**(21), 30979–30988 (2019).
10. S. L. Braunstein and S. Pirandola, "Side-channel-free quantum key distribution," *Phys. Rev. Lett.* **108**(13), 130502 (2012).

11. H.-K. Lo, M. Curty, and B. Qi, "Measurement-device-independent quantum key distribution," *Phys. Rev. Lett.* **108**(13), 130503 (2012).
12. A. Rubenok et al., "Real-world two-photon interference and proof-of-principle quantum key distribution immune to detector attacks," *Phys. Rev. Lett.* **111**(13), 130501 (2013).
13. Y. Liu et al., "Experimental measurement-device-independent quantum key distribution," *Phys. Rev. Lett.* **111**(13), 130502 (2013).
14. Y.-L. Tang et al., "Measurement-device-independent quantum key distribution over 200 km," *Phys. Rev. Lett.* **113**(19), 190501 (2014).
15. Z. Tang et al., "Experimental demonstration of polarization encoding measurement-device-independent quantum key distribution," *Phys. Rev. Lett.* **112**(19), 190503 (2014).
16. C. Wang et al., "Phase-reference-free experiment of measurement-device-independent quantum key distribution," *Phys. Rev. Lett.* **115**(16), 160502 (2015).
17. L. Comandar et al., "Quantum key distribution without detector vulnerabilities using optically seeded lasers," *Nat. Photonics* **10**(5), 312–315 (2016).
18. H.-L. Yin et al., "Measurement-device-independent quantum key distribution over a 404 km optical fiber," *Phys. Rev. Lett.* **117**(19), 190501 (2016).
19. C. Wang et al., "Measurement-device-independent quantum key distribution robust against environmental disturbances," *Optica* **4**(9), 1016–1023 (2017).
20. H. Liu et al., "Experimental demonstration of high-rate measurement-device-independent quantum key distribution over asymmetric channels," *Phys. Rev. Lett.* **122**(16), 160501 (2019).
21. B. Fröhlich et al., "A quantum access network," *Nature* **501**(7465), 69–72 (2013).
22. R. J. Hughes et al., "Network-centric quantum communications with application to critical infrastructure protection," arXiv:1305.0305 (2013).
23. Y.-L. Tang et al., "Measurement-device-independent quantum key distribution over untrustful metropolitan network," *Phys. Rev. X* **6**(1), 011024 (2016).
24. Y. Fu et al., "Long-distance measurement-device-independent multiparty quantum communication," *Phys. Rev. Lett.* **114**(9), 090501 (2015).
25. C. Zhu, F. Xu, and C. Pei, "W-state analyzer and multi-party measurement-device-independent quantum key distribution," *Sci. Rep.* **5**(1), 17449 (2015).
26. F. Grasselli, H. Kampermann, and D. Bruß, "Conference key agreement with single-photon interference," *New J. Phys.* **21**(12), 123002 (2019).
27. Y. Ding et al., "High-dimensional quantum key distribution based on multicore fiber using silicon photonic integrated circuits," *npj Quantum Inf.* **3**(1), 25 (2017).
28. D. Bunandar et al., "Metropolitan quantum key distribution with silicon photonics," *Phys. Rev. X* **8**(2), 021009 (2018).
29. C. Ma et al., "Silicon photonic transmitter for polarization-encoded quantum key distribution," *Optica* **3**(11), 1274–1278 (2016).
30. P. Sibson et al., "Integrated silicon photonics for high-speed quantum key distribution," *Optica* **4**(2), 172–177 (2017).
31. K. Wei et al., "High-speed measurement-device-independent quantum key distribution with integrated silicon photonics," *Phys. Rev. X* **10**(3), 031030 (2020).
32. C. Agnesi et al., "Hong–Ou–Mandel interference between independent III–V on silicon waveguide integrated lasers," *Opt. Lett.* **44**(2), 271–274 (2019).
33. H. Semenenko et al., "Chip-based measurement-device-independent quantum key distribution," *Optica* **7**(3), 238–242 (2020).
34. P. Sibson et al., "Chip-based quantum key distribution," *Nat. Commun.* **8**(1), 13984 (2017).
35. C.-Y. Wang et al., "Integrated measurement server for measurement-device-independent quantum key distribution network," *Opt. Express* **27**(5), 5982–5989 (2019).
36. G. Zhang et al., "An integrated silicon photonic chip platform for continuous-variable quantum key distribution," *Nat. Photonics* **13**(12), 839–842 (2019).
37. J. F. Tasker et al., "Silicon photonics interfaced with integrated electronics for 9 GHz measurement of squeezed light," *Nat. Photonics* **15**(1), 11–15 (2021).
38. S. Pirandola et al., "High-rate measurement-device-independent quantum cryptography," *Nat. Photonics* **9**(6), 397–402 (2015).
39. C. Ottaviani et al., "Modular network for high-rate quantum conferencing," *Commun. Phys.* **2**(1), 118 (2019).
40. J. Calsamiglia and N. Lütkenhaus, "Maximum efficiency of a linear-optical Bell-state analyzer," *Appl. Phys. B* **72**(1), 67–71 (2001).
41. J. A. W. van Houwelingen et al., "Quantum teleportation with a three-Bell-state analyzer," *Phys. Rev. Lett.* **96**(13), 130502 (2006).
42. F. Samara et al., "Entanglement swapping between independent and asynchronous integrated photon-pair sources," *Quantum Sci. Technol.* **6**, 045024 (2021)
43. W. H. Pernice et al., "High-speed and high-efficiency travelling wave single-photon detectors embedded in nanophotonic circuits," *Nat. Commun.* **3**(1), 1325 (2012).
44. B. Korzh et al., "Demonstration of sub-3 ps temporal resolution with a superconducting nanowire single-photon detector," *Nat. Photonics* **14**(4), 250–255 (2020).
45. S. Ferrari, C. Schuck, and W. Pernice, "Waveguide-integrated superconducting nanowire single-photon detectors," *Nanophotonics* **7**(11), 1725–1758 (2018).
46. Y. Ding et al., "Fully etched apodized grating coupler on the SOI platform with −0.58 dB coupling efficiency," *Opt. Lett.* **39**(18), 5348–5350 (2014).
47. Y. Luo et al., "Low-loss two-dimensional silicon photonic grating coupler with a backside metal mirror," *Opt. Lett.* **43**(3), 474–477 (2018).
48. A. Gaggero et al., "Amplitude-multiplexed readout of single photon detectors based on superconducting nanowires," *Optica* **6**(6), 823–828 (2019).
49. A. J. Kerman et al., "Kinetic-inductance-limited reset time of superconducting nanowire photon counters," *Appl. Phys. Lett.* **88**(11), 111116 (2006).
50. R. Valivarthi et al., "Efficient Bell state analyzer for time-bin qubits with fast-recovery WSi superconducting single photon detectors," *Opt. Express* **22**(20), 24497–24506 (2014).
51. J. Jin et al., "Two-photon interference of weak coherent laser pulses recalled from separate solid-state quantum memories," *Nat. Commun.* **4**(1), 2386 (2013).
52. Y.-H. Zhou, Z.-W. Yu, and X.-B. Wang, "Making the decoy-state measurement-device-independent quantum key distribution practically useful," *Phys. Rev. A* **93**(4), 042324 (2016).
53. Z. Zhang et al., "Improved key-rate bounds for practical decoy-state quantum-key-distribution systems," *Phys. Rev. A* **95**(1), 012333 (2017).
54. M. Curty et al., "Finite-key analysis for measurement-device-independent quantum key distribution," *Nat. Commun.* **5**(1), 3732 (2014).
55. S. Pirandola et al., "Fundamental limits of repeaterless quantum communications," *Nat. Commun.* **8**(1), 15043 (2017).
56. R. I. Woodward et al., "Gigahertz measurement-device-independent quantum key distribution using directly modulated lasers," *npj Quantum Inf.* **7**(1), 58 (2021).
57. M. Lucamarini et al., "Overcoming the rate–distance limit of quantum key distribution without quantum repeaters," *Nature* **557**(7705), 400–403 (2018).

Xiaodong Zheng is a PhD student working under the supervision of Xiao-Song Ma at the School of Physics of Nanjing University (NJU). Currently, he is working on superconducting nanowire single-photon detection and quantum key distribution.

Peiyu Zhang received her MS degree from NJU in 2020. Currently, she is working on optical communication.

Renyou Ge received his PhD from Sun Yat-sen University in 2021. Currently, he is working on integrated optical devices.

Liangliang Lu received his BS degree from Guangzhou University in 2009 and his PhD from NJU in 2015. He worked as a researcher at the School of Physics of NJU from 2017 to 2020 and joined the School of Physical Science and Technology at Nanjing Normal University in November 2020. His research area is integrated photonic quantum information processing, including quantum simulation, quantum key distribution, and nonlinear optics.

Guanglong He is a PhD student working under the supervision of Labao Zhang at the School of Electronic Science and Engineering of NJU. Currently, he is working on superconducting nanowire single-photon detectors.

Qi Chen is a PhD student working under the supervision of Labao Zhang at the School of Electronic Science and Engineering of NJU. Currently, he is working on superconducting nanowire single-photon detectors.

Fangchao Qu received his MS degree from NJU in 2020. Currently, he is working on integrated circuits.

Labao Zhang received his PhD from NJU, Nanjing, China, in 2010. He is currently a professor at NJU. His current research interests include the phenomena and the physics of nanostructured superconductors.

Xinlun Cai received his PhD in electrical and electronics engineering from the University of Bristol, Bristol, UK, in 2012. He is currently a professor at the School of Electronics and Information Technology, Sun Yat-sen University, Guangzhou, China. His research is mainly focused on optical communication and photonic integrated devices.

Yanqing Lu received his BS and PhD degrees from NJU, Nanjing, China, in 1991 and 1996, respectively. He has 5 years of experience in the U.S. and China telecom industries. He designed and developed a serial of liquid-crystal-based fiber-optic devices with his colleagues, which include variable optical attenuators, variable Mux/Demux, and DWDM wavelength blockers. He is currently a Changjiang distinguished professor at NJU. His research interests include liquid crystal photonics, nonlinear optics, and quantum optics.

Shining Zhu is a professor at the School of Physics and a principal investigator at the National Laboratory of Solid State Microstructures, NJU, Nanjing, China. He is an academician of the Chinese Academy of Sciences (CAS) and a fellow of Optical Society of America, Chinese Optical Society, and American Physical Society, respectively. His research interests include microstructured functional materials, nonlinear optics, laser physics, quantum communication, and integrated quantum optics.

Peiheng Wu received his PhD in physics from NJU, Nanjing, China, in 1961. He has been a professor at NJU, since 1985 and an academician at the CAS, Beijing, China, since 2005. From January 2001 to July 2001, he was a professor with RIEC, Tohoku University, Sendai, Japan. His research interests include superconducting electronics, high-frequency techniques, and their applications.

Xiao-Song Ma received his BS degree from NJU in 2003 and his PhD from the University of Vienna in 2010. He worked as a postdoc fellow at the University of Vienna and Yale University from 2010 to 2015. He joined the School of Physics at NJU as a professor in 2015. His research interests include quantum communication, quantum network, quantum simulation and computation, solid-state quantum memory, and integrated photonic quantum technologies.

Letter

ADVANCED PHOTONICS

Entanglement-based quantum key distribution with a blinking-free quantum dot operated at a temperature up to 20 K

Christian Schimpf,*,† Santanu Manna,*,† Saimon F. Covre da Silva, Maximilian Aigner, and Armando Rastelli
Johannes Kepler University Linz, Institute of Semiconductor and Solid State Physics, Linz, Austria

Abstract. Entanglement-based quantum key distribution (QKD) promises enhanced robustness against eavesdropping and compatibility with future quantum networks. Among other sources, semiconductor quantum dots (QDs) can generate polarization-entangled photon pairs with near-unity entanglement fidelity and a multiphoton emission probability close to zero even at maximum brightness. These properties have been demonstrated under resonant two-photon excitation (TPE) and at operation temperatures below 10 K. However, source blinking is often reported under TPE conditions, limiting the maximum achievable photon rate. In addition, operation temperatures reachable with compact cryocoolers could facilitate the widespread deployment of QDs, e.g., in satellite-based quantum communication. We demonstrate blinking-free emission of highly entangled photon pairs from GaAs QDs embedded in a p-i-n diode. High fidelity entanglement persists at temperatures of at least 20 K, which we use to implement fiber-based QKD between two buildings with an average raw key rate of 55 bits/s and a qubit error rate of 8.4%. We are confident that by combining electrical control with already demonstrated photonic and strain engineering, QDs will keep approaching the ideal source of entangled photons for real world applications.

Keywords: quantum optics; quantum dots; nanophotonics; quantum cryptography.

Received Aug. 31, 2021; revised manuscript received Nov. 25, 2021; accepted for publication Nov. 26, 2021; published online Dec. 17, 2021.

[DOI: 10.1117/1.AP.3.6.065001]

1 Introduction

Quantum key distribution (QKD) relying on single photons is regarded as one of the most mature quantum technologies.[1,2] However, the impossibility of amplifying single photons sets restrictions on the transmission distance. Entanglement-based QKD schemes are able to overcome these range limitations when embedded in quantum networks,[3,4] while also exhibiting a lower vulnerability to eavesdropping attacks.[1,5–8] For both fiber-based[9] and satellite-based[10] quantum cryptography, the most prominent sources of entangled photon pairs to date are based on the spontaneous parametric downconversion (SPDC) process. These sources are commercially available and can be operated in a large temperature range.[11] As a drawback, SPDC sources exhibit approximately Poissonian photon pair emission characteristics,[12] which severely limits their brightness when a high degree of entanglement—and thus a low qubit error rate (QBER)—is demanded. The biexciton–exciton (XX-X) spontaneous decay cascade in epitaxially grown semiconductor quantum dots (QDs) has been demonstrated to be a viable alternative to SPDC sources due to the sub-Poissonian entangled photon pair emission statistics.[13] In particular, GaAs QDs obtained by the Al droplet etching technique[14] are capable of emitting polarization-entangled photon pairs with a fidelity to the $|\phi^+\rangle$ Bell state beyond 0.98,[15,16] owing to an intrinsically low exciton fine structure splitting (FSS),[17] a low exciton lifetime of about 230 ps, and a near-zero multiphoton emission probability even at maximum brightness.[18] This allowed the demonstration of entanglement-based QKD with a QBER as low as 1.9%.[16,19]

Independent of the QD materials used, the best performances in terms of entanglement fidelity and biexciton state-preparation efficiency have been obtained by operating the QD sources at

*Address all correspondence to Christian Schimpf, christian.schimpf@jku.at; Santanu Manna, santanu.manna@jku.at
†These authors contributed equally.

temperatures below 10 K and using the resonant two-photon-excitation (TPE) condition.[20,21] One of the drawbacks of the very low working temperatures is that they are difficult to achieve in satellites, where strong payload restrictions have to be met. Starting from about 30 K, cryocoolers for lower temperatures become exceedingly bulkier than higher temperature models.[22] Regarding TPE and, in general, resonant excitation schemes, their main limitation is represented by random charge capture in the QD, normally resulting in a significant drop of the time fraction β, in which the QD is optically active (also known as blinking).[23,24] For the generation of single photons via strictly resonant excitation, blinking has been successfully suppressed by embedding QDs into charge-tunable devices,[25] which allows the charge state of a QD to be deterministically controlled.[26,27] The question whether blinking can be suppressed under TPE is not trivial, since—different from single photon resonant excitation—TPE requires excitation powers about 50 times larger, which can produce free carriers in the continuum via two-photon absorption in the barrier material. Although two-photon absorption by a QD in a diode structure has been observed via photocurrent measurements,[28] the usefulness of charge-tunable devices in the context of entangled-photon-pair generation with the TPE method has not been tested.

Here, we investigate the optical properties of GaAs QDs embedded in a p-i-n tunnel diode at a temperature of at least 20 K, demonstrate blinking-free emission of entangled photon pairs under TPE, and use these photons to successfully implement the BBM92 QKD protocol[6] under these conditions. The key generation happens between two buildings, connected by a 350-m long single-mode fiber inside the campus of the Johannes Kepler University.

Varying the voltage applied to the diode within a certain window allows for fine-tuning of the emission wavelength in a range of about 0.2 nm, while keeping the blinking-free emission intact. These structures can therefore be vital for applications in quantum networks,[3] where a precise matching of the wavelengths of multiple emitters becomes important,[29,30] and the transmission rate scales with β^2.[24]

2 GaAs Quantum Dots in a Diode Structure at a Temperature of 20 K

The GaAs QDs in a p-i-n diode structure, as shown in Fig. 1(a), were grown by molecular beam epitaxy. The first functional element is a distributed Bragg reflector, consisting of six pairs of $Al_{0.95}Ga_{0.05}As$ and $Al_{0.20}Ga_{0.80}As$ layers with 65.2 and 56.6 nm thicknesses, respectively. The n-doped region is formed by a 95-nm-thick $Al_{0.15}Ga_{0.85}As$ layer with a Si concentration of 10^{18} cm^{-3}. A combination of layers (15 nm $Al_{0.15}Ga_{0.85}As$ plus 8 nm $Al_{0.33}Ga_{0.67}As$) acts as tunnel barrier between the n-layer and the QDs, which are obtained via the local Al droplet etching technique[14] and covered by the 268-nm-thick $Al_{0.33}Ga_{0.67}As$ intrinsic region. A 65-nm thick layer of $Al_{0.15}Ga_{0.85}As$ doped with 5×10^{18} cm^{-3} carbon atoms forms the p-region. Layers of 5-nm $Al_{0.15}Ga_{0.85}As$ and 10-nm GaAs, each doped with 10^{19} cm^{-3} carbon, cap the structure to form a conductive surface and to protect the active region from oxidation. A DC voltage V_P is applied to the p-contact with respect to the grounded n-contact (see the Supplementary Material for details about the electrical contacts). A solid immersion lens on top of the structure enhances the overall extraction efficiency to about 3%.

The sample containing the GaAs QDs is fixed with silver glue on the cold-finger of a He flow cryostat and cooled to a temperature of 20 K. The temperature is measured with a calibrated silicon diode placed under the cold-finger, so we estimate that the actual sample temperature could be up to 5 K higher. One individual QD is optically excited by a focused pulsed laser with a repetition rate of 80 MHz and the laser energy E_P tuned to half of the biexciton (XX) energy, as depicted in the inset of Fig. 1(a). This resonant TPE scheme is the same as used in previous experiments.[15,16,18] Figure 1(b) shows the microphotoluminescence spectra of a QD when adjusting E_P at the working point $V_{P,0} = 0.3$ V, used for the further measurements, and then sweeping V_P from 0 to 1.5 V. The inset shows the corresponding diode current. In the voltage range of about 0.15 to 0.35 V, the QD is in its charge neutral configuration, and only the biexciton (XX) and the exciton (X) transition lines are visible. For higher voltages, a single electron tunnels into the QD so the negative trion (X^-) is addressed via phonon-assisted excitation. Figure 1(b) shows the spectrum at $V_{P,0}$, with the XX excited at the π-pulse. At this voltage, the autocorrelation function $g^{(2)}$ for a time span of 100 μs and a time-bin of 1 μs was recorded, depicted as the red data points in Fig. 1(d). In this case, the time-bin is much larger than the excitation period of 12.5 ns, so the antibunching from the single-photon emission becomes invisible. The $g^{(2)}$ is one for all time delays, which indicates the complete absence of blinking, i.e., an on-time fraction of $\beta = 1/g^{(2)}(0) = 1.00(2)$.[23] The black dashed line indicates the $g^{(2)}$ typically measured for previously used GaAs QDs without diodes, resulting in $\beta \approx 0.3$.

It is interesting to note that the diode provides a window for V_P of about 0.1 V, in which the QDs can be operated without blinking. This offers a tuning range for the central emission wavelengths of about 0.2 nm, as depicted for a different, but representative, QD in Fig. 1(e). The blue-dashed line indicates the case of $\beta = 1$, corresponding to no blinking. The same tuning range was also observed for temperatures well below 20 K.

3 Characterization of the Entangled Photon Pairs

The QDs of the diode sample used here exhibit an average FSS of about 6 μeV. Average values below 4 μeV are regularly achieved for nanoholes created at a substrate temperature of 600°C,[17,31] while a slightly higher temperature (about 610°C) was used here to possibly improve the crystal quality. Instead of resorting to strain tuning to bring the FSS of one individual QD to zero,[15] the stochastic distribution of the FSS among all QDs on the sample can be used to find a QD with a suitably low FSS for the given use case. To estimate the FSS required for a serviceable QBER in a BBM92 QKD arrangement, we first model the 2-qubit density matrix in polarization space[32] as

$$\rho_M(S, T_{1,X}, k) = \frac{k}{2}\begin{pmatrix} 1 & 0 & 0 & z^* \\ 0 & 0 & 0 & 0 \\ 0 & 0 & 0 & 0 \\ z & 0 & 0 & 1 \end{pmatrix} + \frac{1-k}{4} I^{(4)},$$
$$z = \frac{1+ix}{1+x^2}, \quad x = \frac{ST_{1,X}}{\hbar}, \tag{1}$$

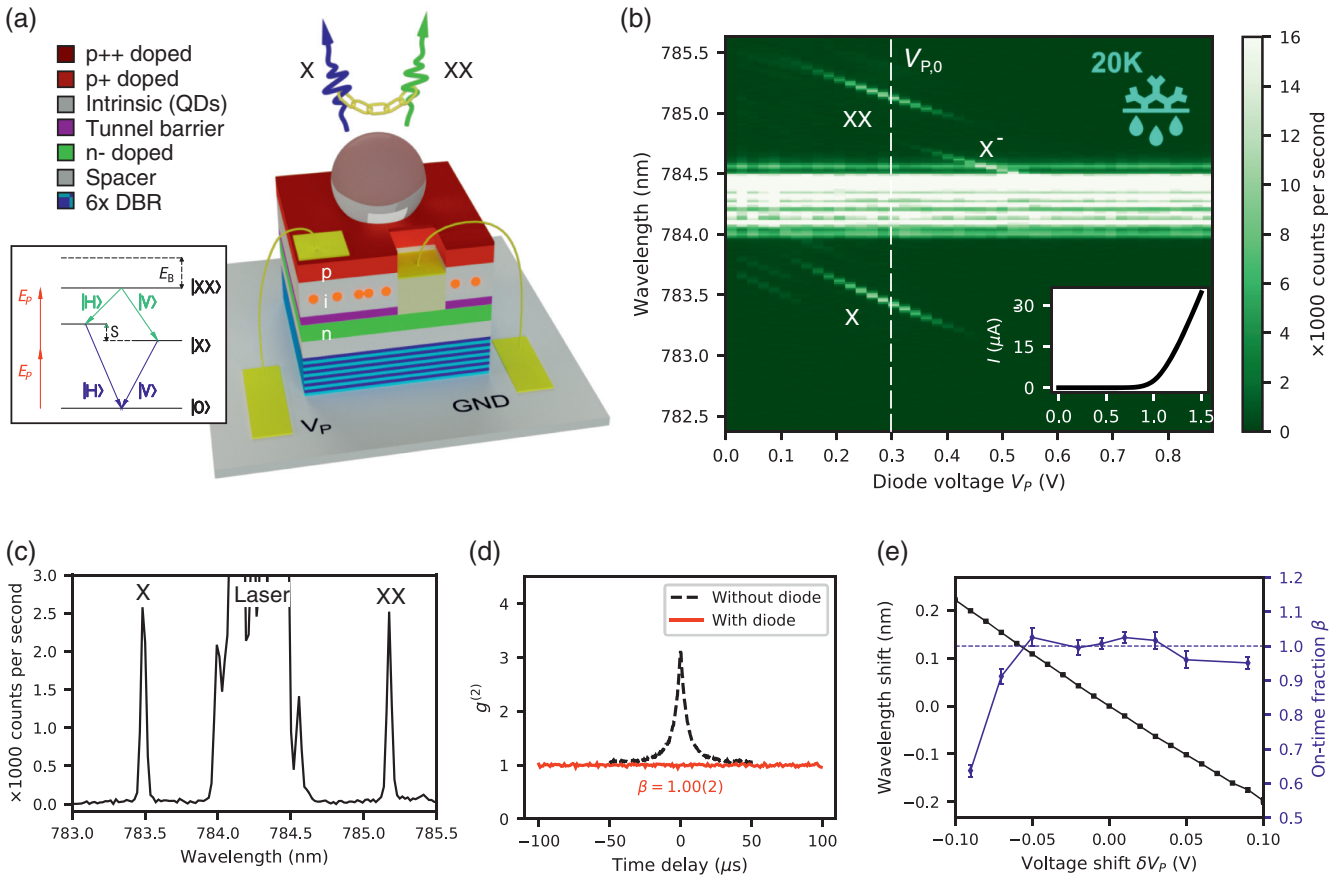

Fig. 1 Photoluminescence properties of GaAs QDs in a p-i-n diode structure at a temperature of 20 K, excited by resonant TPE. (a) p-i-n diode structure with a tunnel barrier between the n-doped and the intrinsic regions. The inset shows the principle of TPE, with E_P the laser energy, E_B the biexciton (XX) binding energy, and S the exciton (X) FSS. (b) Emission spectra at TPE conditions when sweeping the diode voltage V_P in forward bias. The inset shows the diode current I over V_P. The white-dashed line indicates $V_{P,0} = 0.3$ V, at which the diode is operated during the QKD experiment. (c) Emission at $V_P = V_{P,0}$. (d) Second-order correlation function $g^{(2)}$ of the X signal with a time-bin of 1 μs at $V_P = V_{P,0}$. The $g^{(2)}$ is shown for the QD in the diode structure (red), indicating an on-time fraction of $\beta = 1.00(2)$ and a QD without diode (black, dashed) with a typical value of $\beta \approx 0.3$. (e) Wavelength shift and β for different deviations $\delta V_P = V_P - V_{P,0}$. The blue-dashed line indicates a value of β corresponding to no blinking.

where S is the magnitude of the FSS, $T_{1,X}$ is the X lifetime, k is the purity parameter, and $I^{(4)}$ is the 4×4 identity matrix. For the estimation of the required S, we set $T_{1,X}$ to the typically observed value of 230 ps and $k = 1$. In this model, possible dephasing mechanisms other than state rotation induced by the FSS are neglected. From ρ_M, we calculate the expected QBER via

$$q(\rho_M) = \frac{1}{2}\sum_{i=1}^{4} \langle O_i|\rho_M|O_i|\rangle, \tag{2}$$

where $O_i \in \{H_A V_B, V_A H_B, D_A A_B, A_A D_B\}$ are the 2-qubit measurement bases between Alice (A) and Bob (B), in which a measured coincidence corresponds to a false key bit. After a brief scanning, we chose a QD with an FSS of $S = 0.96(9)$ μeV, for which we calculate a minimum QBER of 2.7%. In practice, a slightly higher QBER is to be expected due to additional dephasing processes.[15,32]

The XX and the X photons generated by TPE are filtered out individually and coupled into single mode fibers. Figure 2(a) shows the spectra of the XX and X emission lines merged at a 50:50 fiber beam splitter, of which one output is sent to the spectrometer. (The slightly lower XX signal intensity stems from the higher distance from the objective to the fiber collimator compared to the X signal, resulting in a lower coupling efficiency.)

Before performing the QKD experiment, a characterization of the single-photon emission characteristics and the polarization entanglement between the XX and the X photons is performed, as those properties primarily determine the QBER during the key generation process. The most important quantities are summarized in Table 1 and compared to the values for a different QD (in the same diode structure), measured at 5 K. Figure 2(b) shows a coincidence histogram of an autocorrelation measurement for both the XX and the X signals. Using a time-bin of 2 ns, the results are $g^{(2)}_{XX}(0) = 0.034(4)$

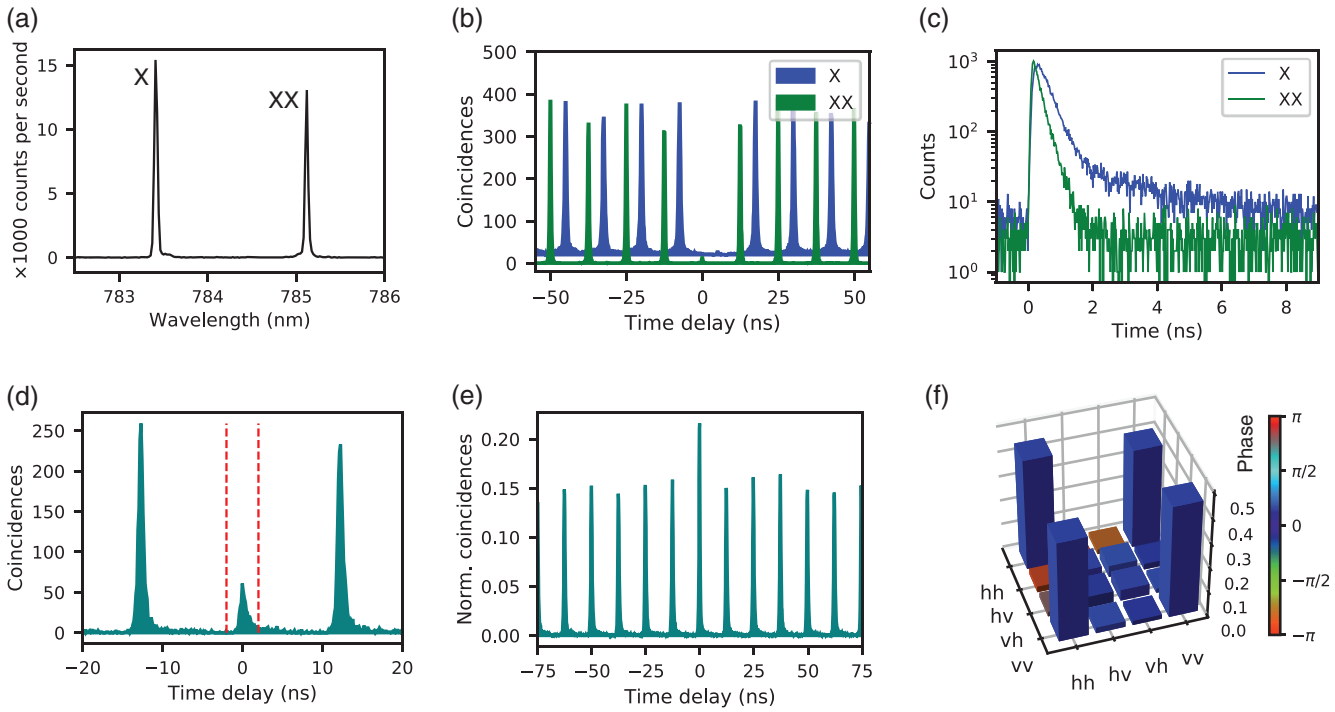

Fig. 2 Emission properties relevant for the polarization entanglement, measured at a temperature of 20 K. (a) Spectra of the individually filtered XX and X emission lines combined at a 50:50 fiber beam splitter. (b) Single-photon emission characteristics of the XX and X signals observed by detecting coincidences in a Hanbury–Brown–Twiss arrangement. The histogram for the X emission is shifted horizontally and vertically to facilitate reading. (c) Decay dynamics of the XX and X signals. The X signal exhibits a slow secondary decay channel, which is not present at temperatures lower than 10 K. (d) Examples among the 36 recorded coincidence histograms between the XX and X detections, corresponding to a measurement in the HV basis. The red-dashed lines indicate the time-bin of 2 ns, in which the coincidences are summed up to calculate the peak areas. (e) Unpolarized coincidence measurement between the XX and X photons. The excess coincidences at zero time delay stem from a nonunity photon-pair generation probability. (f) Density matrix of the two-photon polarization entangled state of the XX and X photons, recorded by full state tomography.

Table 1 Summarized emitter performance for two representative QDs in a diode structure excited by TPE, measured at temperatures of 5 K and 20 K, respectively.

	5 K		20 K	
Temperature	X	XX	X	XX
$g^{(2)}(0)$	0.017(4)	0.011(3)	0.020(3)	0.034(4)
Lifetime (ps)	238(3)	116(2)	252(9)	72(3)
Pair generation efficiency	0.91(2)		0.87(2)	
FSS (μeV)	1.13(7)		0.96(9)	
Calculated concurrence[a]	0.905		0.900	
Measured concurrence	0.904(3)		0.713(8)	
Calculated fidelity to $\|\phi^+\rangle$[a]	0.959		0.960	
Measured fidelity to $\|\phi^+\rangle$	0.975(1)		0.925(2)	

[a]Only considering expectation values of measured $g^{(2)}$, X lifetime, and FSS.[32]

and $g_X^{(2)}(0) = 0.020(3)$, which are comparable to previously measured values using the same optical arrangement at a temperature of 5 K (see Table 1), but with a slightly higher value for the XX signal. Compared to data acquired at 5 K, one can observe a broadening of the peaks belonging to the X signal. Inspecting the lifetime traces, which are shown for both the XX and X in Fig. 1(c), it becomes evident that this broadening stems from a slow decay channel of the X, which overlays with the monoexponential decay from the bright X to the ground state usually observed at 5 K (see the Supplementary Material for lifetime- and cross-correlation measurements at 5 K). A convoluted fit results in an X lifetime of $T_{1,X} = 252(9)$ ps, with the caveat that this value is slightly overestimated due to the presence of the slow decay channel. The XX lifetime is measured as $T_{1,XX} = 72(3)$ ps, which is significantly lower than the 120 ps typically observed at 5 K.

A full state tomography[33] is performed to determine the degree of entanglement between the XX and X photons. Figure 2(d) shows an example among the 36 recorded XX/X coincidence histograms, corresponding to a measurement in

the HV basis. The red-dashed lines indicate the time-bin of 2 ns, in which the coincidences are summed up and compared with the average side peak area. The coincidences originating from the slow X decay channel (the "tail" on the right side of the peaks), which are partially excluded by this time-bin, account for about 9% of the total coincidences per excitation cycle. Figure 2(e) shows the weighted sum of the histograms corresponding to the measurement bases HH, VV, HV, and VH (where H is the horizontal, and V is the vertical polarization), normalized by their respective average side peak areas. From this histogram, a photon pair generation probability per excitation pulse of $\epsilon = 0.87(2)$ is calculated (see the Supplementary Material for details), which is marginally lower than the value of 0.91(2) observed at 5 K.

From the 36 correlation histograms, the 2-qubit density matrix in polarization space is calculated and depicted in Fig. 2(f). The maximum likelihood estimator used during this process is adapted for the dynamics of the QD light emission (see the Supplementary Material). The derived concurrence is 0.713(8), and the maximum fidelity to a Bell state is 0.925(5), which show a significant drop compared to the values obtained at 5 K. (We use the fidelity definition for mixed states[34] throughout this work.) We find that ρ at a temperature of 20 K can be approximated via Eq. (1) as $\rho = \rho_{\mathrm{M}}(S, T_{1,\mathrm{X}}, 1-\overline{g}-\zeta)$, with $\overline{g} = [g^{(2)}_{\mathrm{XX}}(0) + g^{(2)}_{\mathrm{X}}(0)]/2$ the average $g^{(2)}(0)$ and $\zeta \approx 0.1$. The physical origin of the entanglement degrading effects, their temperature dependency, and their connection to the slow X decay channel appearing in the lifetime traces shown in Fig. 1(c) are subject of further investigation, as they could shed light on the changing dynamics of quasiparticles in GaAs QDs at higher temperatures.

The expected QBER of 7.45% calculated from ρ by Eq. (2) is still below the theoretical upper limit of 11% holding for the BBM92 protocol[6,8] and therefore suitable for performing QKD, as long as a sufficient amount of key bits are collected to mitigate finite key effects.[35]

4 Quantum Key Distribution with Entangled Photons

The XX and X photons in their individual single mode fibers are distributed to Alice and Bob, as shown in Fig. 3(a). The infrastructure is identical to the one used in a previous QKD experiment.[16] After an initial synchronization and polarization correction routine, the key generation is performed overnight for a total duration of about 8 h. The observed QBER, shown in Fig. 3(b), was evaluated periodically for 10% of the key bits (which were then discarded) and has an average value of 8.42%. The red-dashed line indicates the theoretical upper limit for the BBM92 protocol,[8] after which no finite key can be extracted from the raw key anymore.

The QBER shows a minimum of 6.15%, which is even lower than the 7.45% estimated from ρ, shown in Fig. 2(f). This discrepancy probably arises from the way in which the time-synchronization between Alice and Bob is maintained.

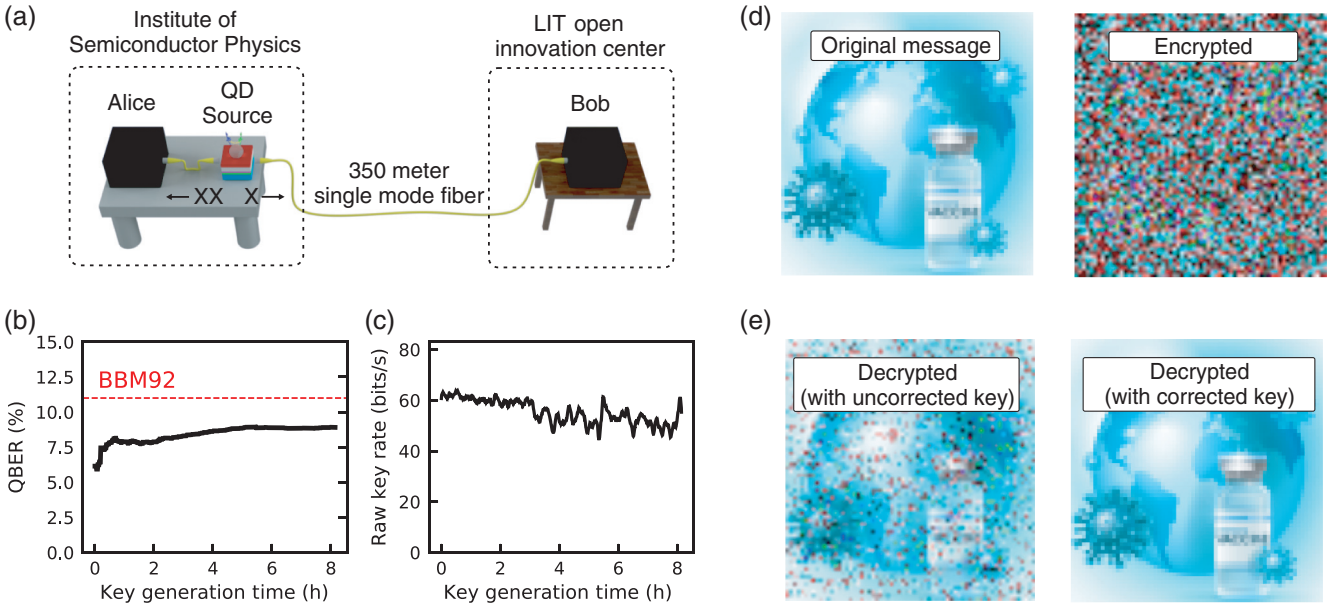

Fig. 3 Key generation in the BBM92 protocol over a time span of about 8 h and entanglement-based QKD. (a) QKD arrangement. Alice and the photon source are situated on an optical table, and Bob is placed in a movable box on a table in another building and connected with the source via a 350-m long single mode fiber. (b) QBER during the key generation with an average of 8.42%. The red-dashed line marks the maximum allowed QBER for BBM92 in the infinite key regime. (c) Raw key rate (after key sifting) with an average of 54.8 bits/s. (d) Encryption of a bitmap with the dimensions of 67×70 pixels and a color-depth of 4 bits, resulting in a total size of about 2.4 kilobytes. The encryption with Alice's key yields a scrambled message ready to be sent over a public channel. (e) Decryption at Bob's site when using an uncorrected key (left) and a corrected key (right).

To dynamically adjust the relative time delay between the arrival times of the XX and X photons at Alice and Bob, respectively, a peak in the continuously measured cross-correlation function is tracked. All photons around the peak maximum in a time window of 2 ns are used for key generation. We found that a shift of the center of this time-bin by 0.5 ns (about the time-resolution of our single photon detectors) can already change the QBER by around 2%, because a higher contribution of photons stemming from the slow X decay channel, shown in Fig. 2(c), decreases the entanglement (see the Supplementary Material for details). The time window during the key generation was therefore probably shifted with respect to the one used for calculating ρ. These findings are not only interesting for a better understanding of the underlying mechanisms degrading the entanglement at higher temperatures, but also indicate that with careful choice of the time window (within the limits of the detector resolution and clock synchronization among the communicating parties) a compromise between QBER and efficiency during the key generation process can be made.

We attribute the changing QBER over the course of the measurement to the following factors. The FSS changed from the initial 0.96(9) to 1.35(11) μeV over the course of the QKD measurements, which can add about 2% to the QBER due to an accelerated phase rotation process leading to a decreased fidelity to the ideal Bell state on average.[32] A changing FSS was never noticed before in these kinds of samples. A possible origin could be a changing strain state in the silver glue used to stick the sample on the chip carrier. The second contribution to a rising QBER could be a varying ambient temperature that affects the polarization rotation exerted by the fibers, which then leads to a larger deviation from the $|\phi^+\rangle$ Bell state, for which our QKD setup is designed. After the initial polarization correction, no active correction was performed during the 8 h of key generation.

Figure 3(c) shows the raw key generation rate after key sifting. A change in raw key rate over time occurs due to a slight drift of the cryostat relative to the objective, leading to a decreasing excitation and collection efficiency. We counter this effect by an automatized movement of the X/Y position of the cryostat via linear stages to optimize the average detector count rates, should they fall below a certain threshold. The average raw key rate over the full time span is found to be 54.8 bits/s. A total of 807,348 raw key bits were generated, corresponding to a duty cycle of about 50%. For the remaining 50% of time, the QKD system was blocked by the steps of compensating the drifts of the optics, key sifting, and QBER estimation, which were all performed sequentially to facilitate software and hardware error diagnosis. By parallelization of those steps, the duty cycle can be brought to 100%, as long as the data processing can keep up with the photon detection rate.

As the system presented here operates with an average QBER of 8.42% and therefore relatively close to the theoretical upper limit, the error correction and subsequent privacy amplification steps have to be chosen carefully to maximize the efficiency while leaking a minimum of information to a potential eavesdropper on the public channel. For this purpose, we adopt the security analysis recently employed for the Micius satellite QKD system,[10,35] where the setting is basically identical to our QKD system. This analysis addresses the effects of the estimated QBER in combination with a finite key length and adjusts the required key compression accordingly (see the Supplementary Material for details), leaving us with a total of 20,649 secure key bits after error correction.

The generated key is used to encrypt a bitmap with a size of 18,760 bits (about 2.4 kilobytes) [see Fig. 3(d)], using a one-time-pad procedure. The decryption is depicted in Fig. 3(e) for the cases when the raw/corrected key pair was used (left/right).

5 Discussion and Conclusion

In this work, we have demonstrated a blinking-free source of polarization-entangled photon pairs based on a GaAs QD operated at a temperature of at least 20 K. The intrinsically low FSS, owing to the local Al droplet etching technique,[14] together with the employed p-i-n diode allows us to generate an uninterrupted stream of photon pairs with a fidelity to the $|\phi^+\rangle$ Bell state of 0.925(2) when using the pulsed two-photon-excitation scheme.[20,21] The device also allows the fine-tuning of the emission wavelength within a range of 0.2 nm while keeping the blinking-free operation intact, which is favorable for interconnecting multiple sources to quantum networks.[3,4,24,30]

The source was used to demonstrate QKD via the BBM92 protocol[6] between two parties in two different buildings of the Johannes Kepler University, connected via a 350-m long underground single mode fiber. The average QBER was 8.42%. From the initial 807,348 key bits, a total of 20,649 error-free and privacy-amplified key bits could be distilled, using a state-of-the-art security analysis in the finite key regime.[35]

Comparing the decay dynamics of the biexciton and exciton states at temperatures of 20 K and 5 K allows us to identify a secondary slow decay channel of the exciton as the major entanglement degrading mechanism. While the physical origin of this observation and the elaboration of possible solutions will require further investigations, we find that the QBER during QKD can be optimized by a mild time filtering (see the Supplementary Material). This work makes us optimistic that combining electrical control with advanced photonic processing[36,37] and strain-tuning platforms[15,38] will lead to nearly ideal sources of entangled photon pairs that can be operated in demanding environments.

Acknowledgments

Christian Schimpf is a recipient of a DOC fellowship of the Austrian Academy of Sciences at the Institute of Semiconductor Physics at Johannes Kepler University, Linz, Austria. We thank C. Diskus for providing the Rb clocks used for QKD, M. Reindl and L. Costadedoi for their assistance in the optics laboratory, and K. Schweighofer for his contribution to the numerical optimization. Further, we thank P. Walther, M. Vyvlecka, and M. Bozzio for the continuous and fruitful discussion. This work was financially supported by the Austrian Science Fund (FWF) via the Research Group FG5, P 29603, P 30459, I 4320, I 4380, I 3762, the European Union's Horizon 2020 research and innovation program under Grant Agreements No. 899814 (Qurope) and No. 871130 (Ascent+), the Linz Institute of Technology (LIT), and the LIT Secure and Correct Systems Lab, supported by the State of Upper Austria. The authors declare no conflict of interest.

References

1. S. Pirandola et al., "Advances in quantum cryptography," *Adv. Opt. Photonics* **12**(4), 1012–1236 (2020).
2. X. Ma and J.-W. Pan, "Security of quantum key distribution with realistic devices," *Rev. Mod. Phys.* **92**(2), 025002 (2020).

3. N. Gisin and R. Thew, "Quantum communication," *Nat. Photonics* **1**(3), 165–171 (2007).
4. H. J. Kimble, "The quantum internet," *Nature* **453**(7198), 1023–1030 (2008).
5. A. K. Ekert, "Quantum cryptography based on Bell's theorem," *Phys. Rev. Lett.* **67**(6), 661–663 (1991).
6. C. H. Bennett, G. Brassard, and N. D. Mermin, "Quantum cryptography without Bell's theorem," *Phys. Rev. Lett.* **68**(5), 557–559 (1992).
7. A. Acín et al., "Device-independent security of quantum cryptography against collective attacks," *Phys. Rev. Lett.* **98**(23), 230501 (2007).
8. N. Gisin et al., "Quantum cryptography," *Rev. Mod. Phys.* **74**(1), 145–195 (2002).
9. S. Wengerowsky et al., "Passively stable distribution of polarisation entanglement over 192 km of deployed optical fibre," *NPJ Quantum Inf.* **6**(1), 5 (2020).
10. J. Yin et al., "Entanglement-based secure quantum cryptography over 1,120 kilometres," *Nature* **582**(7813), 501–505 (2020).
11. X.-Y. Pan et al., "Temperature insensitive type II quasi-phase-matched spontaneous parametric downconversion," *Appl. Phys. Lett.* **119**(2), 021107 (2021).
12. J. Schneeloch et al., "Introduction to the absolute brightness and number statistics in spontaneous parametric down-conversion," *J. Opt.* **21**(4), 043501 (2019).
13. O. Benson et al., "Regulated and entangled photons from a single quantum dot," *Phys. Rev. Lett.* **84**(11), 2513–2516 (2000).
14. M. Gurioli et al., "Droplet epitaxy of semiconductor nanostructures for quantum photonic devices," *Nat. Mater.* **18**(8), 799–810 (2019).
15. D. Huber et al., "Strain-tunable GaAs quantum dot: a nearly dephasing-free source of entangled photon pairs on demand," *Phys. Rev. Lett.* **121**(3), 033902 (2018).
16. C. Schimpf et al., "Quantum cryptography with highly entangled photons from semiconductor quantum dots," *Sci. Adv.* **7**(16), aebe8905 (2021).
17. Y. H. Huo, A. Rastelli, and O. G. Schmidt, "Ultra-small excitonic fine structure splitting in highly symmetric quantum dots on GaAs (001) substrate," *Appl. Phys. Lett.* **102**(15), 152105 (2013).
18. L. Schweickert et al., "On-demand generation of background-free single photons from a solid-state source," *Appl. Phys. Lett.* **112**(9), 093106 (2018).
19. F. Basso Basset et al., "Quantum key distribution with entangled photons generated on demand by a quantum dot," *Sci. Adv.* **7**(12), eabe6379 (2021).
20. R. Hafenbrak et al., "Triggered polarization-entangled photon pairs from a single quantum dot up to 30 K," *New J. Phys.* **9**(9), 315 (2007).
21. M. Müller et al., "On-demand generation of indistinguishable polarization-entangled photon pairs," *Nat. Photonics* **8**(3), 224–228 (2014).
22. K. D. Timmerhaus and R. Reed, *Cryogenic Engineering*, Springer (2007).
23. J. P. Jahn et al., "An artificial Rb atom in a semiconductor with lifetime-limited linewidth," *Phys. Rev. B* **92**(24), 245439 (2015).
24. K. D. Jöns et al., "Two-photon interference from two blinking quantum emitters," *Phys. Rev. B* **96**(7), 075430 (2017).
25. R. J. Warburton et al., "Optical emission from a charge-tunable quantum ring," *Nature* **405**(6789), 926–929 (2000).
26. L. Zhai et al., "Low-noise GaAs quantum dots for quantum photonics," *Nat. Commun.* **11**(1), 4745 (2020).
27. N. Somaschi et al., "Near-optimal single-photon sources in the solid state," *Nat. Photonics* **10**(5), 340–345 (2016).
28. S. Stufler et al., "Two-photon Rabi oscillations in a single $In_xGa_{1-x}As$ GaAs quantum dot," *Phys. Rev. B* **73**(12), 125304 (2006).
29. V. Giesz et al., "Cavity-enhanced two-photon interference using remote quantum dot sources," *Phys. Rev. B* **92**(16), 161302 (2015).
30. M. Reindl et al., "Phonon-assisted two-photon interference from remote quantum emitters," *Nano Lett.* **17**(7), 4090–4095 (2017).
31. R. Keil et al., "Solid-state ensemble of highly entangled photon sources at rubidium atomic transitions," *Nat. Commun.* **8**(1), 15501 (2017).
32. A. J. Hudson et al., "Coherence of an entangled exciton-photon state," *Phys. Rev. Lett.* **99**(26), 266802 (2007).
33. D. F. V. James et al., "Measurement of qubits," *Phys. Rev. A* **64**(5), 052312 (2001).
34. R. Jozsa, "Fidelity for mixed quantum states," *J. Mod. Opt.* **41**(12), 2315–2323 (1994).
35. C. C. W. Lim et al., "Security analysis of quantum key distribution with small block length and its application to quantum space communications," *Phys. Rev. Lett.* **126**(10), 100501 (2021).
36. J. Liu et al., "A solid-state source of strongly entangled photon pairs with high brightness and indistinguishability," *Nat. Nanotechnol.* **14**(6), 586–593 (2019).
37. H. Wang et al., "On-demand semiconductor source of entangled photons which simultaneously has high fidelity, efficiency, and indistinguishability," *Phys. Rev. Lett.* **122**(11), 113602 (2019).
38. R. Trotta et al., "Energy-tunable sources of entangled photons: a viable concept for solid-state-based quantum relays," *Phys. Rev. Lett.* **114**(15), 150502 (2015).
39. J. Martinez-Mateo et al., "Demystifying the information reconciliation protocol cascade," *Quantum Inf. Comput.* **15**(5–6), 453–477 (2015).
40. Z. Yuan et al., "10-Mb/s quantum key distribution," *J. Lightwave Technol.* **36**(16), 3427–3433 (2018).

Christian Schimpf's academic career started in 2012 with the beginning of his physics studies at the Johannes Kepler University Linz, Austria, where he is currently in the later stage of his PhD studies. His research focus lies on semiconductor quantum dots, with emphasis on the generation of non-classical light for quantum optics and applications in the context of quantum communication.

Santanu Manna received his PhD in physics from Indian Institute of Technology Kharagpur, India, in 2014. He is currently a university assistant in the Institute of Semiconductor and Solid State Physics, Johannes Kepler University Linz, Austria. His research interest lies in the epitaxial growth by molecular beam epitaxy, device fabrication and measurements on III–V semiconductor based quantum devices like single/entangled photon emitters, quantum cascade laser based frequency comb and THz emitters.

Saimon F. Covre da Silva: Biography is not available.

Maximilian Aigner is a master student in the Department of Semiconductor and Solid State Physics at the Johannes Kepler University Linz, Austria. His research is focused on quantum dot based quantum optics, especially on entanglement related experiments.

Armando Rastelli is professor of semiconductor physics since 2012 and corresponding member of the Austrian Academy of Sciences since 2019. His main current focus is on the optimization of GaAs quantum dots as quantum light sources and their post-growth control via microstructured piezoelectric actuators for applications in photonic quantum science and technologies. He is coauthor of more than 230 peer-reviewed papers and has given 100 invited talks on the research activities of his group.

Research Article

ADVANCED PHOTONICS

Direct characterization of coherence of quantum detectors by sequential measurements

Liang Xu,[a,b,c,d,e,†] Huichao Xu,[a,b,c,d,f,†] Jie Xie,[a,b,c,d] Hui Li,[a,b,c,d] Lin Zhou,[a,b,c,d] Feixiang Xu,[a,b,c,d] and Lijian Zhang[a,b,c,d,*]

[a]Nanjing University, College of Engineering and Applied Sciences, Nanjing, China
[b]Nanjing University, Collaborative Innovation Center of Advanced Microstructures, Nanjing, China
[c]Nanjing University, National Laboratory of Solid State Microstructures, Nanjing, China
[d]Nanjing University, Key Laboratory of Intelligent Optical Sensing and Manipulation, Nanjing, China
[e]Research Center for Quantum Sensing, Zhejiang Laboratory, Hangzhou, China
[f]Purple Mountain Laboratories, Nanjing, China

Abstract. The quantum properties of quantum measurements are indispensable resources in quantum information processing and have drawn extensive research interest. The conventional approach to revealing quantum properties relies on the reconstruction of entire measurement operators by quantum detector tomography. However, many specific properties can be determined by a part of the matrix components of the measurement operators, which makes it possible to simplify the characterization process. We propose a general framework to directly obtain individual matrix elements of the measurement operators by sequentially measuring two noncompatible observables. This method allows us to circumvent the complete tomography of the quantum measurement and extract the required information. We experimentally implement this scheme to monitor the coherent evolution of a general quantum measurement by determining the off-diagonal matrix elements. The investigation of the measurement precision indicates the good feasibility of our protocol for arbitrary quantum measurements. Our results pave the way for revealing the quantum properties of quantum measurements by selectively determining the matrix components of the measurement operators.

Keywords: direct tomography; quantum measurement; weak measurement; sequential measurement; coherence.

Received Sep. 3, 2021; revised manuscript received Oct. 28, 2021; accepted for publication Nov. 4, 2021; published online Nov. 29, 2021.

[DOI: 10.1117/1.AP.3.6.066001]

1 Introduction

The quantum properties of quantum measurements have been widely regarded as an essential resource for the preparation of quantum states,[1–3] achieving the advantages of quantum technologies,[4–7] as well as the study of fundamental quantum theories.[8–15] The time-reversal approach allows for the investigation of the properties of quantum measurements qualitatively from the perspective of quantum states.[16–18] In addition, the quantum resource theories for quantification of quantum properties of quantum measurements have been developed very recently[19–22] and have been applied to investigate coherence of quantum-optical detectors.[23] Thus developing efficient approaches to characterize the quantum properties of quantum measurements is important for both the fundamental investigations and practical applications.

A general quantum measurement and all its properties can be completely determined by the positive operator-valued measure (POVM) $\{\hat{\Pi}_l\}$, in which the element $\hat{\Pi}_l$ denotes the measurement operator corresponding to the outcome l. Several approaches have been developed to determine the unknown POVM,[24–27] of which the most representative is quantum detector tomography (QDT).[24] In QDT, a set of probe states $\{\rho^{(m)}\}$ are prepared to input the unknown measurement apparatus, and the probability of obtaining the outcome l is given by $p_l^{(m)} = \mathrm{Tr}(\rho^{(m)}\hat{\Pi}_l)$. Provided that the input states are informationally complete for the tomography, the POVM $\{\hat{\Pi}_l\}$ can be reconstructed by minimizing the gap between the theoretical calculation and the experimental results. To date, QDT has achieved great success in characterizing a variety of quantum detectors, including

*Address all correspondence to Lijian Zhang, lijian.zhang@nju.edu.cn
†These authors contributed equally to this work.

avalanche photodiodes,[28] time-multiplexed photon-number-resolving detectors,[24,29,30] transition edge sensors,[31] and superconducting nanowire detectors.[32] As the quantum detectors become increasingly complicated, the standard QDT is confronted with the experimental and computational challenges, which prompts the exploration of some helpful shortcuts. For example, the determination of a few key parameters that describe the quantum detectors makes it possible to largely reduce the characterization complexity.[33] The quantum detectors can also be self-tested with certain quantum states in the absence of prior knowledge of the apparatus.[34–37] The emerging data-pattern approach realizes the operational tomography of quantum states through fitting the detector response, which is robust to imperfections of the experimental setup.[38,39]

Though QDT is a generic protocol to acquire entire measurement operators, it does not have the direct access to the single-matrix components of the measurement operator. The complexity of the reconstruction algorithm in QDT increases dramatically with the increase of the dimensions of the quantum system (QS). Typically, tomography of full measurement operator is considered as the prerequisite for characterizing the properties of quantum measurements.[23] However, in some situations, the complete determination of the measurement operator is not necessary to fulfil specific tasks, which makes it possible to simplify the characterization process. For example, if the input state is known to lie in the subspace of the QS, it only requires the corresponding matrix components of the measurement operators to predict the probability of outcomes.[29,40,41] In particular, the coherence of a quantum measurement is largely determined by the off-diagonal matrix components of its measurement operators in certain bases.[23]

Recently, Lundeen et al.[42] proposed a method to directly measure the probability amplitudes of the wavefunction using the formalism of the weak measurement and weak values. This method, known as direct quantum state tomography, opens up a new avenue for quantum tomography technique. The direct tomography (DT) protocol has been extensively studied and the scope of its application is expanded to high-dimensional states,[43–51] mixed states[52–56] and entangled states,[57,58] quantum processes,[59] and quantum measurements.[60] The development of the DT theory from the original weak-coupling approximation to the rigorous validation with the arbitrary coupling strength ensures the accuracy and simultaneously improves the precision.[61–68] Moreover, direct state tomography allows the direct measurement of any single-matrix entry of the density matrix, which has provided an exponential reduction of measurement complexity compared to standard quantum state tomography in determining a sparse multiparticle state.[53–56,69] Recent work has extended the idea to realize the direct characterization of full measurement operators, based on weak values, showing the potential advantages over QDT in operational and computational complexity.[60] In view of the unique advantages of the DT, it is expected that the generalization of the DT scheme for directly characterizing the matrix components of measurement operators allows for the extraction of the properties of the quantum measurement in a more efficient way.

In this paper, we propose a framework to directly characterize the individual matrix components of the measurement operators by sequentially measuring two noncompatible observables with two independent meter states (MSs). In the following, the unknown quantum detector performs measurement on the QS. The specific matrix entry of the measurement operator can be extracted from the collective measurements on the MSs when the corresponding outcomes of the quantum detector are obtained. Our procedure is rigorously valid with the arbitrary non-zero coupling strength. The investigations of the measurement precision indicate the good feasibility of our scheme to characterize arbitrary quantum measurement. We experimentally demonstrate our protocol to monitor the evolution of coherence of the quantum measurement in two different situations, the dephasing and the phase rotation, by characterizing the associated off-diagonal matrix components. Our results show the great potential of the DT for capturing the quantum properties of the quantum measurement through partial determination of the measurement operators.

2 Theoretical Framework

2.1 Directly Determining the Matrix Components of the Measurement Operators

The schematic diagram for direct characterization of the matrix components of the POVM is shown in Fig. 1. We represent the POVM $\{\hat{\Pi}_l\}$ acting on the d-dimensional QS with the orthogonal basis $\{|a_j\rangle\}$ ($\mathcal{A}$), and the matrix entry of the measurement operator $\hat{\Pi}_l$ is given by $E^{(l)}_{a_j a_k} = \langle a_j|\hat{\Pi}_l|a_k\rangle$. If $j = k$, $E^{(l)}_{a_j a_k}$ corresponds to the diagonal matrix entry, which can be easily determined by inputting a preselected QS state $\rho_s^{(j)} = |a_j\rangle\langle a_j|$ to the quantum detector and collecting the probability $p_l = \langle a_j|\hat{\Pi}_l|a_j\rangle$ of obtaining the outcome l. By contrast, the off-diagonal matrix entry $E^{(l)}_{a_j a_k}$ ($j \neq k$), generally a complex number, is related to the coherence of the operator and usually indirectly reconstructed in the conventional QDT. In order to directly measure $E^{(l)}_{a_j a_k}$ ($j \neq k$), we perform the sequential measurement of the observables $\hat{O}_B = \hat{I} - 2|b_0\rangle\langle b_0|$ (note that $|b_0\rangle$

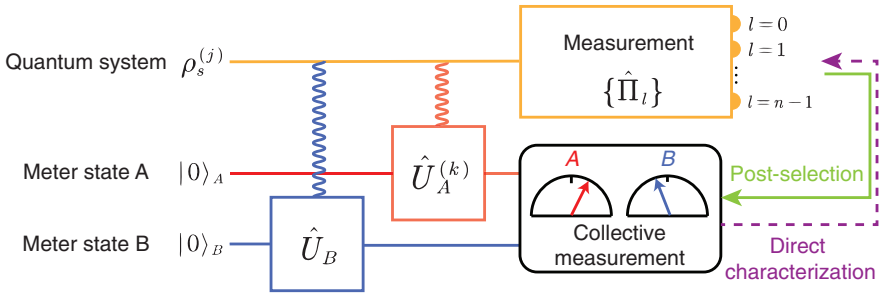

Fig. 1 The schematic diagram for direct characterization of the matrix components of the POVM $\{\hat{\Pi}_l\}$.

is a state vector which is a superposition of all the base states in basis $\mathcal{A}$ with the equal probability amplitudes, i.e., $|b_0\rangle \propto \sum_j |a_j\rangle$) and $\hat{O}_A^{(k)} = \hat{I} - 2|a_k\rangle\langle a_k|$ on the initial state $\rho_s^{(j)}$ with two independent two-dimensional MSs initialized as $|0\rangle_B$ and $|0\rangle_A$, respectively. The measurement of the observable $\hat{O}$ (generally referring to the observable $\hat{O}_B$ or $\hat{O}_A^{(k)}$) is implemented by coupling the QS with the MS under the Hamiltonian $\hat{H} = g\delta(t-t_0)\hat{O} \otimes \hat{\sigma}_y$, in which g is the coupling strength and $\hat{\sigma}_y = i(|1\rangle\langle 0| - |0\rangle\langle 1|)$ is the observable of the MS. Since the observables $\hat{O}_B$ and $\hat{O}_A^{(k)}$ do not commute, the measurement has to be performed in a particular order.

The sequential measurement process can be described by the unitary evolution of the system-MS $\rho_{sm} = \rho_s^{(j)} \otimes \rho_{m,B} \otimes \rho_{m,A}$ with the first transformation,

$$\hat{U}_B = \exp(-ig_B \hat{O}_B \otimes \hat{\sigma}_{y,B} \otimes \hat{I}_A), \tag{1}$$

and the second transformation,

$$\hat{U}_A^{(k)} = \exp(-ig_A \hat{O}_A^{(k)} \otimes \hat{I}_B \otimes \hat{\sigma}_{y,A}), \tag{2}$$

leading to the joint state,

$$\rho_J = \hat{U}_A^{(k)} \hat{U}_B \rho_{sm} \hat{U}_B^\dagger \hat{U}_A^{(k)\dagger}. \tag{3}$$

Then the unknown quantum detector to be characterized performs the postselection measurement $\{\hat{\Pi}_l\}$ on the QS. Depending on the measurement outcome l, the surviving final MS is given by $\rho'_{m,A,B} = \mathrm{Tr}_s(\hat{\Pi}_l \otimes \hat{I}_B \otimes \hat{I}_A \rho_J)/p_f$, in which $\mathrm{Tr}_s(\cdot)$ denotes the partial trace operation on the QS, and $p_f = \mathrm{Tr}(\hat{\Pi}_l \otimes \hat{I}_B \otimes \hat{I}_A \rho_J)$ is the probability for getting the outcome l.

The matrix entry $E_{a_j a_k}^{(l)}$ is related to the average value of the observables $\hat{O}_B$ and $\hat{O}_A^{(k)}$ by

$$E_{a_j a_k}^{(l)} = \frac{d}{4}\mathrm{Tr}\left[\hat{\Pi}_l(\hat{I} - \hat{O}_A^{(k)})(\hat{I} - \hat{O}_B)\rho_s^{(j)}\right]. \tag{4}$$

Both of the observables $\hat{O}_B$ and $\hat{O}_A^{(k)}$ are designed to satisfy $\hat{O}^2 = \hat{I}$ so that the unitary is exactly expanded as $\hat{U} = \exp(-ig\hat{O} \otimes \hat{\sigma}_y) = \cos g\hat{I} \otimes \hat{I} - i \sin g\hat{O} \otimes \hat{\sigma}_y$. The right side of Eq. (4) can be extracted by the joint measurement of postselected MS $\rho'_{m,A,B}$ with the observables

$$\hat{P} = \sqrt{d}\left(\frac{\hat{I} + \hat{\sigma}_z}{4\cos^2 g} - \frac{\hat{\sigma}_x}{4 \sin g \cos g}\right),$$
$$\hat{Q} = -\frac{\sqrt{d}\hat{\sigma}_y}{4 \sin g \cos g}, \tag{5}$$

each in the subsystems A and B. By defining the joint observables of MSs A and B as $\hat{R}_{B,A} = \hat{P}_B\hat{P}_A - \hat{Q}_B\hat{Q}_A$ and $\hat{T}_{B,A} = \hat{P}_B\hat{Q}_A + \hat{Q}_B\hat{P}_A$, we obtain the real and the imaginary parts of $E_{a_j a_k}^{(l)}$:

$$\mathrm{Re}[E_{a_j a_k}^{(l)}] = \mathrm{Tr}(\hat{\Pi}_l \otimes \hat{R}_{B,A}\rho_J),$$
$$\mathrm{Im}[E_{a_j a_k}^{(l)}] = \mathrm{Tr}(\hat{\Pi}_l \otimes \hat{T}_{B,A}\rho_J). \tag{6}$$

Here, the subscripts of the coupling strength g and the Pauli operators coincide with those of the operators $\hat{P}$ and $\hat{Q}$. For the sake of convenience, $g_A = g_B = g$ in the rest of this article.

2.2 Precision Analysis on Directly Characterizing the Matrix Components of the Measurement Operators

The accuracy and the precision are two essential indicators to evaluate a measurement scheme. There are no systematic errors in our protocol, since the derivation is rigorous for the arbitrary coupling strength g. According to previous studies, the precision of the DT applied to the quantum states is sensitive to both the coupling strength and the unknown states.[70] The increase of the coupling strength is beneficial to improving the precision.[62–68] When the unknown state approaches being orthogonal to the postselected state, the DT protocol is prone to large statistical errors and is therefore highly inefficient.[70,71] Here, we theoretically investigate the precision of the DT protocol applied to the quantum measurement to verify the feasibility of our protocol.

Given that the real and the imaginary parts of the matrix components are independently measured, we quantify the measurement precision with the total variance $\Delta^2 E_{a_k a_j}^{(l)} = \Delta^2 \mathrm{Re}[E_{a_k a_j}^{(l)}] + \Delta^2 \mathrm{Im}[E_{a_k a_j}^{(l)}]$. According to Eq. (6), the variance can be derived by

$$\Delta^2 E_{a_k a_j}^{(l)} = \langle \Delta^2 \hat{R}_{B,A} \rangle_f + \langle \Delta^2 \hat{T}_{B,A} \rangle_f, \tag{7}$$

where $\langle \Delta^2 \hat{M} \rangle_f = \mathrm{Tr}(\hat{\Pi}_l \hat{M}^2 \rho_J) - [\mathrm{Tr}(\hat{\Pi}_l \hat{M} \rho_J)]^2$. Since the operators $\hat{R}_{B,A}$ and $\hat{T}_{B,A}$ are usually hard to experimentally construct, an alternative is to infer the expected values of $\hat{R}_{B,A}$ and $\hat{T}_{B,A}$ as well as their squares, from the complete measurement results of the MSs B and A, each projected to the mutually unbiased bases, i.e., $\{|0\rangle, |1\rangle\}, \{|+\rangle, |-\rangle\}, \{|\circlearrowright\rangle, |\circlearrowleft\rangle\}$ with $|\pm\rangle = (|0\rangle \pm |1\rangle)/\sqrt{2}$ and $|\circlearrowright\rangle, |\circlearrowleft\rangle = (|0\rangle \pm i|1\rangle)/\sqrt{2}$. The obtained probability distribution is represented by $\{W_{mn}\}$, where m and n label the projective states $|m_B\rangle$ and $|m_A\rangle$ of the MSs B and A, respectively. The experimental variance can be obtained from $\{W_{mn}\}$ with the error transfer formula

$$\Delta^2 E_{a_k a_j}^{(l)} = \sum_{m,n} \left|\frac{\partial E_{a_k a_j}^{(l)}}{\partial Pr_{mn}}\right|^2 \delta^2 W_{mn}. \tag{8}$$

Consider that N particles are used for one measurement of W_{mn}. The variance of the probability is approximated as $\delta^2 W_{mn} \approx W_{mn}/N$ in the large N limit due to the Poissonian statistic.

As a demonstration, we theoretically derive the precision of directly measuring the off-diagonal matrix entry $E_{1,0}(\theta)$ of a general measurement operator for a two-dimensional QS as follows:

$$\hat{\Pi}(\theta) = \eta \begin{pmatrix} \cos^2\theta & E_{0,1}(\theta) \\ E_{1,0}(\theta) & \sin^2\theta \end{pmatrix}, \tag{9}$$

with different coupling strength g. According to Eq. (8), the variance of the off-diagonal matrix entry $E_{1,0}(\theta)$ is given by

$$\Delta^2 E_{1,0}(\theta) = \frac{(\sin^2\theta + \sin^2 g)(1 + 2\sin^2 g)}{\eta N \sin^4(2g)}. \tag{10}$$

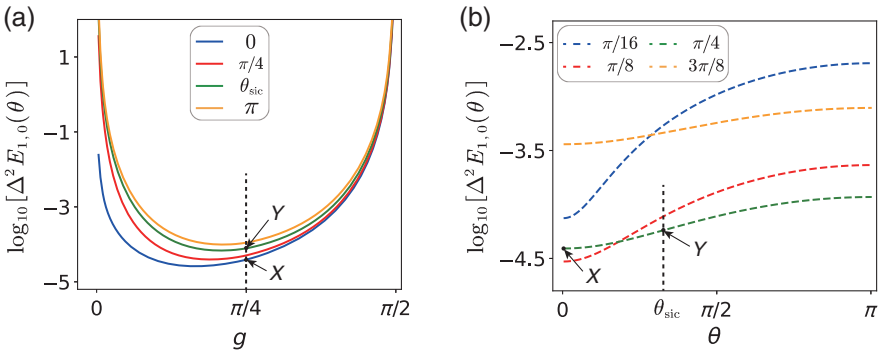

Fig. 2 The measurement precision of the off-diagonal matrix element $E_{1,0}(\theta)$ of the measurement operator $\hat{\Pi}(\theta)$ in a two-dimensional QS. (a) The variance of $E_{1,0}(\theta)$ is plotted with different g for four values of $\theta = 0, \pi/4, \theta_{\text{sic}}, \pi$ with $\theta_{\text{sic}} = \text{acos}(1/\sqrt{3})$. (b) The variance of $E_{1,0}(\theta)$ changes with different parameters θ for the coupling strength $g = \pi/16, \pi/8, \pi/4, 3\pi/8$. Here, we take $\eta = 1/2$ and $N = 12,790$ to coincide with our experimental conditions. The points X and Y refer to the precision of directly measuring the off-diagonal matrix entry of the two-dimensional symmetric informationally complete positive operator-valued measure (SIC POVM) with the coupling strength $g = \pi/4$.

In Fig. 2(a), we show how the variance of $E_{1,0}(\theta)$ changes with different g for four values of θ. We find that the statistical errors $\Delta^2 E_{1,0}(\theta)$ become large with a small coupling strength ($g \to 0$ or $g \to \pi/2$), whereas the strong coupling strength ($g \to \pi/4$) significantly decreases the variance to $\Delta^2 E_{1,0}(\theta)_{|g=\pi/4} = (1 + 2\sin^2\theta)/(\eta N)$. We also compare the characterization precision of $E_{1,0}(\theta)$ associated with different POVM parameters θ in Fig. 2(b). The statistical errors $\Delta^2 E_{1,0}(\theta)$ remain finite over all θ indicating that our protocol is applicable to characterize the arbitrary POVM of a two-dimensional QS. In addition, the variance $\Delta^2 E_{1,0}(\theta)$ is related to the parameter θ but does not depend on the value of $E_{1,0}(\theta)$. This implies that the change of the off-diagonal matrix components of the measurement operator, such as the dephasing and the phase rotation process, will not affect the characterization precision. We note that the choice of the sequential observables $\hat{O}_B$ and $\hat{O}_A^{(k)}$ is indeed not unique. How to choose the optimal observables of the QS to achieve the best characterization precision remains an open question in the field of DT. If the sequential observables of the QS are changed, the collective observables $\hat{R}_{B,A}$ and $\hat{T}_{B,A}$ of the MSs should also be changed correspondingly, and the method to reveal the matrix components $E^{(l)}_{a_j a_k}$ may be more involved.

It has been shown that the completeness condition of the POVM $\{\hat{\Pi}_l\}$, i.e., $\sum_l \hat{\Pi}_l = \hat{I}$, can be used to improve the precision of direct QDT.[60] In the following, we prove that the same condition is also helpful to improve the precision in the direct characterization of $E^{(l)}_{a_j a_k}(j \neq k)$. Since the real part of the components $E^{(l)}_{a_j a_k}$ satisfies $\sum_l \text{Re}[E^{(l)}_{a_j a_k}] = 0$, the value of $\text{Re}[E^{(l)}_{a_j a_k}]$ can be not only obtained by the direct measurement but also inferred from the components of other POVM elements $\text{Re}[E^{(u)}_{a_j a_k}]$ $(u \neq l)$ by $\text{Re}[E^{(l)^\circ}_{a_j a_k}] = -\sum_{u \neq l} \text{Re}[E^{(u)}_{a_j a_k}]$. The extra information obtained by $\text{Re}[E^{(l)^\circ}_{a_j a_k}]$ can be used to improve the measurement precision. To acquire the best precision, we adopt the weighted average of $\text{Re}[E^{(l)}_{a_j a_k}]$ and $\text{Re}[E^{(l)^\circ}_{a_j a_k}]$ with the weighting factors w and w°, respectively. The optimal weighting factors satisfy the condition

$$
\begin{aligned}
&w + w^\circ = 1,\\
&w \propto \frac{1}{\Delta^2 \text{Re}[E^{(l)}_{a_j a_k}]},\\
&w^\circ \propto \frac{1}{\sum_{u \neq l} \Delta^2 \text{Re}[E^{(u)}_{a_j a_k}]},
\end{aligned}
\tag{11}
$$

leading to the optimal precision $\Delta^2 \text{Re}[E^{(l)'}_{a_j a_k}] = w w^\circ / \sum_u \Delta^2 \text{Re}[E^{(l)}_{a_j a_k}] < \Delta^2 \text{Re}[E^{(l)}_{a_j a_k}]$.

3 Experiment

In the experiment, we apply the DT protocol to characterize the SIC POVM in the polarization degree of freedom (DOF) of photons. Since the coherence between two polarization base states only changes the off-diagonal components of the measurement operators, we demonstrate that the dephasing and the phase rotation of the SIC POVM can be monitored by only characterizing the corresponding matrix components.

The experimental setup is shown in Fig. 3. We refer to the polarization DOF of photons as the QS with the eigenstates $|H\rangle$ and $|V\rangle$. Single photons generated by the spontaneous parametric downconversion pass through the polarizing beam splitter (PBS) and a half-wave plate (HWP) at 45 deg to preselect the QS to $|V\rangle$. The "measurement 1" and "measurement 2" modules implement the measurement of the observables $\hat{O}_B = |D\rangle\langle D| - |A\rangle\langle A|$ and $\hat{O}_A = |H\rangle\langle H| - |V\rangle\langle V|$, where $|D\rangle = (|H\rangle + |V\rangle)/\sqrt{2}$ and $|A\rangle = (|H\rangle - |V\rangle)/\sqrt{2}$.

Here, we take measurement 1 as an example to describe the working principle of the coupling scenario. The HWP at 22.5 deg before the polarizing beam displacer (PBD) transforms the measurement basis $\{|D\rangle, |A\rangle\}$ into $\{|H\rangle, |V\rangle\}$, and the observable $\hat{\sigma}_z = |H\rangle\langle H| - |V\rangle\langle V|$ is measured between the two PBDs. The first PBD converts the DOF of the QS into the optical path, with $|H\rangle \to |0\rangle$ and $|V\rangle \to |1\rangle$. The polarization of photons in each path initialized to $|H\rangle$ is used as the MS. Two HWPs are arranged in parallel, each on different paths, and are rotated, respectively, to $g/2$ and $-g/2$, to realize the

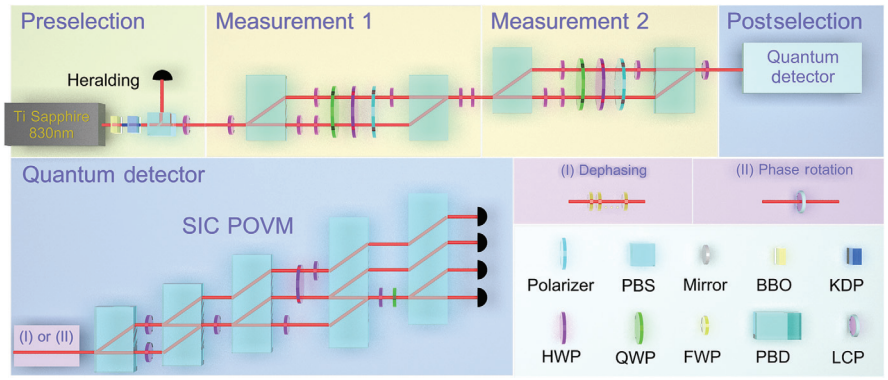

Fig. 3 The experimental setup for characterization of the evolution of the quantum measurement. The pulse laser at 830 nm enters a BBO crystal for the upconversion. The generated photons at 415 nm get through a KDP crystal for the spontaneous parametric downconversion, which simultaneously produces a pair of photons. The single photon is heralded by detecting the other one of the pair. The measurement 1 and measurement 2 modules successively implement the unitary transformation $\hat{U}_B$ and $\hat{U}_A^{(k)}$ as well as the joint measurement on the MSs. In the following, the unknown quantum detector performs the postselection measurement on the polarization DOF of photons. The quantum detector is composed of the operation of polarization evolution, i.e., "(I) dephasing" and "(II) phase rotation" and the SIC POVM realized by the quantum walk. The abbreviations of the equipment are as follows: PBS, polarizing beam splitter; BBO, β-barium borate crystal; KDP, potassium dihydrogen phosphate; HWP, half-wave plate; QWP, quarter-wave plate; PBD, polarizing beam displacer; FWP, full-wave plate; and LCP, liquid-crystal plate.

coupling between the QS and the MS. Afterward, we measure the polarization of photons to extract the information of the MS by a quarter-wave plate (QWP), an HWP, and a polarizer. The photons in two paths that pass through the polarizer recombine at the second PBD and the subsequent two HWPs at 45 deg and 22.5 deg recover the measurement basis to $\{|H\rangle, |V\rangle\}$. A similar setup of measurement 2 performs the measurement of the operator $\hat{O}_A$. Finally, the photons input the unknown detector for the postselection. By collecting the photons that arrive at the outputs, we obtain the measurement results.

We construct the SIC POVM $\{\hat{\Pi}_l\}$ with $\hat{\Pi}_l = \frac{1}{2}|\psi_l\rangle\langle\psi_l|$ $(l = 1, 2, 3, 4)$ and

$$
\begin{aligned}
|\psi_1\rangle &= |H\rangle, \\
|\psi_2\rangle &= \left(|H\rangle - \sqrt{2}|V\rangle\right)\Big/\sqrt{3}, \\
|\psi_3\rangle &= \left(|H\rangle + \sqrt{2}e^{-i2\pi/3}|V\rangle\right)\Big/\sqrt{3}, \\
|\psi_4\rangle &= \left(|H\rangle + \sqrt{2}e^{i2\pi/3}|V\rangle\right)\Big/\sqrt{3},
\end{aligned} \tag{12}
$$

through the quantum walk to perform the postselection measurement of the QS.[72] The dephasing of the POVM is realized by several full-wave plates (FWPs), which separate the wave packets in polarization states $|H\rangle$ and $|V\rangle$, i.e., $|\varphi(t_H)\rangle$ and $|\varphi(t_V)\rangle$ in the temporal DOF. This separation causes the dephasing of the POVM and the off-diagonal entries $E_{VH}^{(l)}$ are transformed to $E_{VH}^{(l),D} = E_{VH}^{(l)}\xi$ with the coefficient $\xi = \langle\varphi(t_H)|\varphi(t_V)\rangle$. The derivation of the dephasing process and the calibration of the coefficient ξ are provided in the Appendix. The phase rotation is implemented by the liquid crystal plate (LCP), which imposes a relative phase ϕ_{lc} between $|H\rangle$ and $|V\rangle$. The operation is equivalent to the unitary evolution $\hat{U}_{lc} = \exp(i\frac{\phi_{lc}}{2}\hat{C})$ of the input state, with $\hat{C} = |H\rangle\langle H| - |V\rangle\langle V|$. When the evolution is inversely performed on the SIC POVM, the non-diagonal elements $E_{VH}^{(l)}$ are transformed to $E_{VH}^{(l),R} = E_{VH}^{(l)}\exp(-i\phi_{lc})$. The calibration results of the ϕ_{lc} are shown in the Appendix, Sec. 6.2.

4 Results

In Fig. 4, we compare the experimental results of DT with those of the conventional tomography (CT) as well as the ideal SIC POVM during the dephasing and phase rotation process. The detailed information of characterizing the experimental SIC POVM by CT is provided in the Supplementary Material. The results of CT, shown in Fig. 4, are inferred from the experimental SIC POVM and the calibrated coefficient ξ (during the dephasing process) or the phase ϕ_{lc} (during the phase rotation process). As shown in Fig. 4(a), the points in each connecting solid line along the direction of arrows correspond to the relative time delay $\epsilon = 0\lambda, 20\lambda, 40\lambda, 60\lambda, 80\lambda, 120\lambda, 160\lambda, 200\lambda, 240\lambda$. The increase of the relative time delay ϵ between the separated wave packets reduces the overlap of the temporal wavefunction $\xi = \langle\varphi(t_H)|\varphi(t_V)\rangle$, which leads to the dephasing of the quantum measurement. The relation between the relative time delay ϵ and the coefficient ξ is calibrated in Fig. 5(b) of the Appendix, Sec. 6.2. Correspondingly, the modulus of $E_{VH}^{(l),D}$ gradually approaches 0, implying that the quantum measurement becomes incoherent, i.e., loses the ability of detecting the coherence information of a quantum state.

In Fig. 4(b), we plot $E_{VH}^{(l),R}$ during the phase-rotation process. The imposed voltage on the LCP is adjusted to obtain $\phi_{lc} = 2\pi/5$ and $4\pi/5$. A HWP at 0 deg is placed before the LCP to obtain $\phi_{lc} = -3\pi/5$ and $-\pi/5$. The rotated points

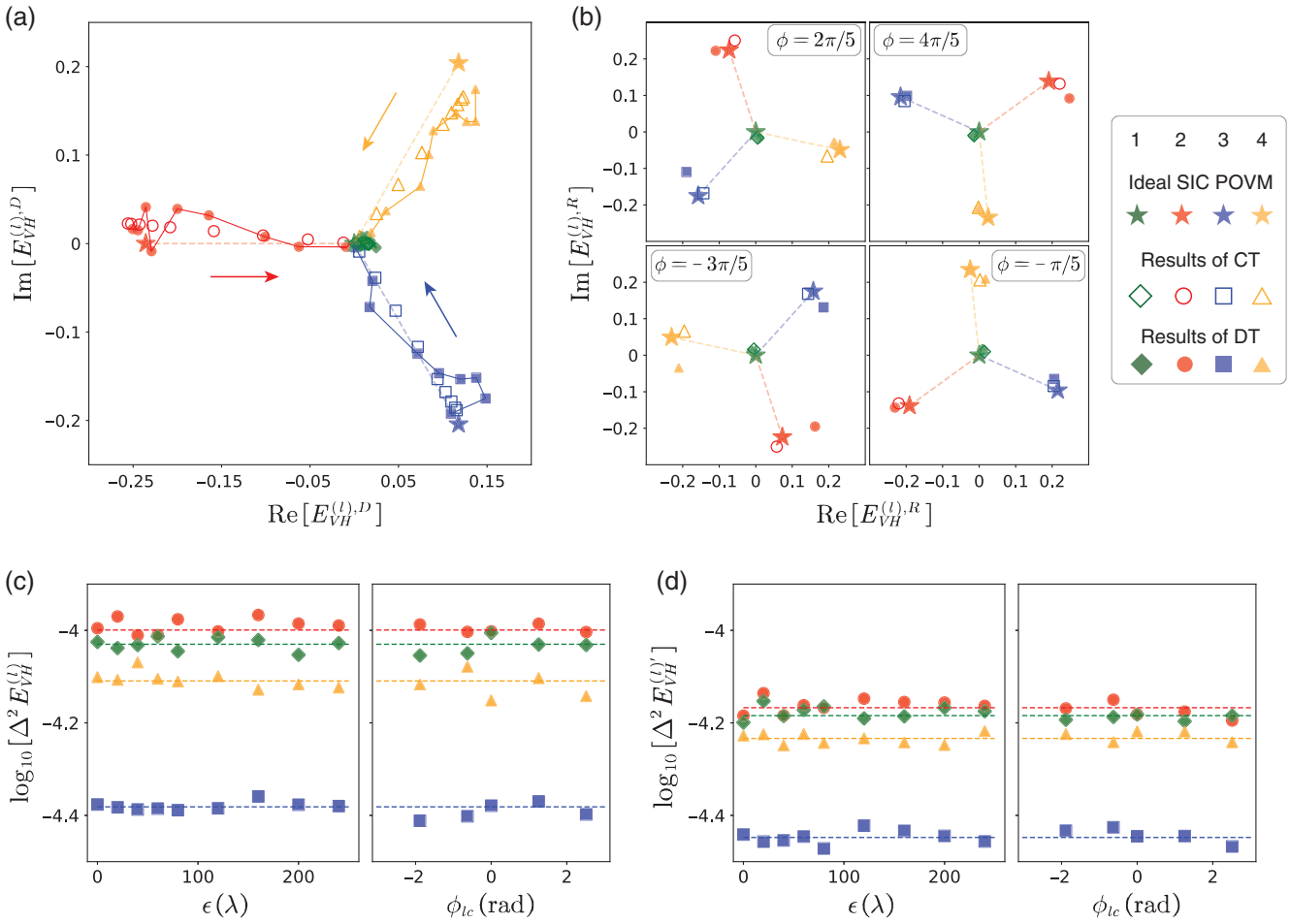

Fig. 4 (a), (b) The real and the imaginary parts of the matrix components $E_{VH}^{(l)}$ are plotted during the dephasing ($E_{VH}^{(l),D}$) and the phase rotation ($E_{VH}^{(l),R}$) of the polarization, respectively. The results of the ideal SIC POVM, the CT, and the DT are represented by the pentagrams, hollow markers, and solid markers, respectively. In panels (a) and (b), we connect each pentagram with the point (0, 0), indicating the evolution path of the ideal SIC POVM during the dephasing process as well as changes of the azimuth angles during the phase rotation process. (c) The statistical errors of the matrix components $E_{VH}^{(l)}$ are provided for both the dephasing and the phase rotation process. (d) The precision of $E_{VH}^{(l)'}$ after using the completeness condition of the POVM. The theoretical precision, represented by the dashed lines in panels (c) and (d), is inferred from the experimental results of CT. The average photon number per unit time for one collective measurement of the MSs is about $N = 12{,}790$.

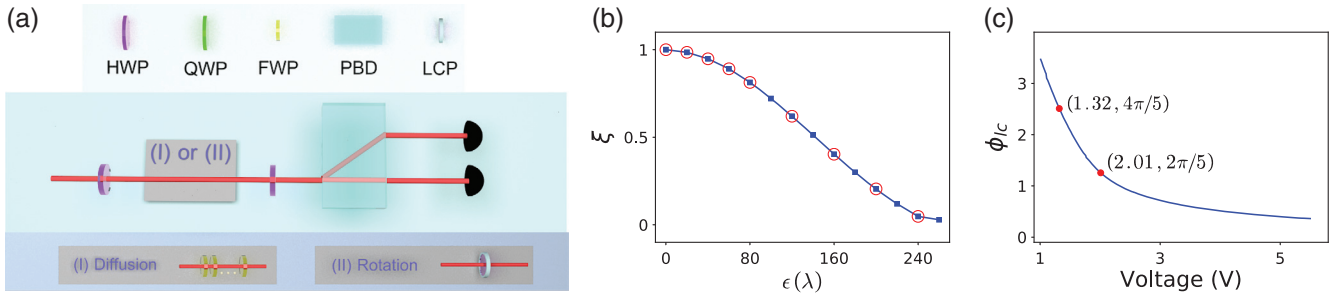

Fig. 5 The calibration of the equipment in the dephasing and the phase rotation process. (a) The calibration setup. (b) The coefficient ξ changes with the time delay ϵ between the wave packets in states $|H\rangle$ and $|V\rangle$. (c) The relative phase ϕ_{lc} between the states $|H\rangle$ and $|V\rangle$ changes with imposed voltage.

representing $E_{VH}^{(l),R}$ in the coordinates of its real and imaginary parts indicate the phase rotation of the quantum measurement. During the phase rotation process, the modulus of $E_{VH}^{(l),R}$ remains unchanged, which indicates that the coherence of the quantum measurement is maintained.

The total noise in the experiment contains the statistical noise and the technical noise. The statistical noise originates from the fluctuations of the input photon numbers per unit time due to the probabilistic generation of single photons, the loss in the channel, and the finite trials of the experiment. The technical noise is caused by the experimental imperfections, e.g., the equipment vibration or the air turbulence. As shown in Figs. 4(a) and 4(b), the experimental results fluctuate around the theoretical predictions due to both the statistical noise and the technical noise. The technical noise can be reduced by isolating the noise source or adopting appropriate signal modulation. The statistical noise determines the ultimate precision that can be achieved for a specific amount of input resources, which is an important metric to evaluate whether a measurement protocol is efficient or not.

The statistical errors of the experimental results are shown in Fig. 4(c). The theoretical precision, represented by dashed lines in Figs. 4(c) and 4(d), is inferred by assuming that the matrix components $E_{VH}^{(l)}$ of the experimental SIC POVM obtained by the CT are directly characterized. As a comparison, we can refer to Fig. 2 for the theoretical precision of the ideal SIC POVM, represented by the points X $(\theta = 0, g = \pi/4)$ and Y $(\theta = \text{acos}(1/\sqrt{3}), g = \pi/4)$. Since the experimental SIC POVM deviates from the ideal SIC POVM, the precisions of $l = 2, 3, 4$ do not equate with each other. The experimental precision is obtained from the Monte Carlo simulation based on the experimental probability distribution and the practical photon statistics to eliminate the effect of the technical noise. Our results closely follow the theoretical predictions indicating that the precision of measuring the off-diagonal matrix components of the POVM is immune to the dephasing and phase rotation of the quantum measurement. We can also find that the characterization precision after using the completeness condition in Fig. 4(d) is significantly improved compared to the original precision in Fig. 4(c).

5 Discussion and Conclusion

We have proposed a protocol to directly characterize the individual matrix components of the general POVM, extending the scope of the DT scheme. Our expression is rigorous for the arbitrary coupling strength, which allows us to change the coupling strength to improve the precision and simultaneously maintain the accuracy. The statistical errors are finite over all the choices of the POVM parameter, demonstrating the feasibility of our protocol for the arbitrary POVM. In particuliar, if the completeness condition of the POVM is appropriately used, the measurement precision can be further improved. Our results indicate that the characterization precision is not affected by the dephasing and phase rotation that only change the off-diagonal matrix components of the measurement operators. Another typical noise is the phase diffusion, meaning that the phase of the quantum measurements randomly jitters. According to the derivations in the paper,[73] the phase diffusion decreases the modulus of the off-diagonal matrix components in a similar way to the dephasing in our work. Therefore, it is expected that the precision of our protocol is immune to incoherent noise, such as phase diffusion.

Since some properties of quantum measurements may depend on a part of matrix components of the measurement operators, this protocol allows us to reveal these properties without the full tomography. We experimentally demonstrate that the evolution of the coherence of a quantum measurement can be monitored through determining the off-diagonal matrix components of the measurement operators. Our scheme makes no assumptions about the basis to represent the measurement operators. The choice of the basis depends on the specific conditions or can be optimized according to the purpose of the characterization. Sometimes, the choice of the basis is natural. For example, the photon number basis is typically employed to represent the measurement operators of photodetectors.[24,28–30,40] In some cases, we aim to acquire the response of the quantum measurements to specific properties of quantum states in which the basis is specified by that used to define the property. Additionally, the basis can be optimized to seek the best entanglement witness.[74] In this work, we choose the typical polarization basis $\{|H\rangle, |V\rangle\}$ to investigate the coherence evolution of the quantum measurements, which is basis dependent. Our protocol also provides the flexibility to characterize the matrix components of the measurement operators in any basis of interest by adjusting the initial quantum state $\rho_s^{(j)}$ as well as the observables $\hat{O}_B$ and $\hat{O}_A^{(k)}$ while other parts of the theoretical framework remain unchanged.

Our protocol can be extended to a high-dimensional QS in which the coherence information of the quantum measurement among specified base states is of interest. The conventional QDT typically requires d^2 informationally complete probe states chosen from at least $d + 1$ basis to globally reconstruct the POVM in a d-dimensional QS. Thus as the dimension d increases, the preparation of the probe states becomes an experimental challenge, and the computational complexity of the reconstruction algorithm is significantly increased. Both factors complicate the task of QDT for high-dimensional QSs. In our scheme, the preparation of the initial states and the sequentially measured observables $\hat{O}_B$ and $\hat{O}_A^{(k)}$ are simply involved in two bases, i.e., the representation basis $\{|a_j\rangle\}$ and its Fourier conjugate $\{|b\rangle\}$. The matrix components of the POVM can be directly inferred from the measurement results of the final MSs without resort to the reconstruction algorithm. When the matrix components are sparse in the measurement operators, our scheme can further simplify the characterization process. Therefore, the direct protocol also shows potential advantages over the conventional QDT in completely determining the POVM due to its better generalization to high-dimensional QSs. In conclusion, by proposing a framework to directly and precisely measure the arbitrary single-matrix entry of the measurement operators, our results pave the way for both fully characterizing the quantum measurement and investigating the quantum properties of it.

6 Appendix: Dephasing and Phase Rotation of Quantum Measurements

6.1 Theoretical Derivation

A general POVM can be implemented through quantum walk with the unitary evolution $\hat{U}$ of the QS at the position $x = 0$. After the quantum walk, the position $x = l$ corresponds to the POVM element

$$\hat{\Pi}_l = \mathrm{Tr}_W[(|0\rangle\langle 0| \otimes \hat{I})\hat{U}^\dagger(|l\rangle\langle l| \otimes \hat{I})\hat{U}], \tag{13}$$

where $\mathrm{Tr}_W[\cdot]$ denotes the partial trace in the walker position DOF. We implement the dephasing of the POVM $\{\hat{\Pi}_l\}$ by coupling the QS to the environment state ρ_E under the Hamiltonian $\hat{H}_{SE} = \frac{\epsilon}{2}\delta(t-t_0)\hat{C}\,\hat{\Omega}$ in which $\hat{C} = |a_j\rangle\langle a_j| - |a_k\rangle\langle a_k|$ and $\hat{\Omega}$ are the observables of the QS and the environment, respectively. By reducing the environment DOF, the measurement operator $\hat{\Pi}_l$ is transformed to $\hat{\Pi}_l^D = \mathrm{Tr}_E[\hat{U}_{SE}^\dagger \hat{\Pi}_l \otimes \rho_E \hat{U}_{SE}]$. We can infer that the dephasing process only changes the related matrix components $E^{(l)}_{a_j a_k}$ to $E^{(l),D}_{a_j a_k} = E^{(l)}_{a_j a_k}\xi$ with the coefficient $\xi = \mathrm{Tr}[\exp(-i\frac{\epsilon}{2}\hat{\Omega})\rho_E \exp(-i\frac{\epsilon}{2}\hat{\Omega})]$.

6.2 Experimental Calibration

To calibrate the relation between the coefficient ξ and the relative time delay $\epsilon = |t_H - t_V|$, we construct the setup shown in Fig. 5(a) in which both the HWPs are set to 22.5 deg. The photons in $|H\rangle$ enter the calibration setup resulting in the final state after the second HWP:

$$\rho^D = \frac{1+\xi}{2}|H\rangle\langle H| + \frac{1-\xi}{2}|V\rangle\langle V|. \tag{14}$$

Then ρ^D is projected to the basis $\{|H\rangle, |V\rangle\}$ with a PBD, obtaining the probabilities P_H and P_V. The parameter ξ is given by $\xi = P_H - P_V$. The relation between ξ and the relative time delay ϵ is shown in Fig. 5(b) in which we take ϵ from 0 to 260 times the wavelength ($\lambda = 830$ nm) and the red circled points are adopted for the experiment.

The liquid crystal imposes a relative phase ϕ_{lc} between $|H\rangle$ and $|V\rangle$ controlled by the voltage. Through the calibration setup in Fig. 5(a), the phase can be obtained by $\phi_{lc} = \arccos[2(P_H - P_V)]$. The calibration results of the relation between the phase ϕ_{lc} and the applied voltage are shown in Fig. 5(c). Here we adjust the voltages to 1.32 and 2.01 V, and the relative phases are $\sim 4\pi/5$ and $2\pi/5$.

Acknowledgments

This work was supported by the National Key Research and Development Program of China (Grant Nos. 2018YFA0306202 and 2017YFA0303703), National Natural Science Foundation of China (Grant Nos. 91836303, 61975077, 61490711, and 11690032), and Fundamental Research Funds for the Central Universities (Grant No. 020214380068). The authors declare no conflicts of interest.

Code, Data, and Materials Availability

The computer software code and data are available by connecting to the corresponding authors.

References

1. A. Ourjoumtsev et al., "Generation of optical 'Schrödinger cats' from photon number states," *Nature* **448**(7155), 784–786 (2007).
2. E. Bimbard et al., "Quantum-optical state engineering up to the two-photon level," *Nat. Photonics* **4**(4), 243–247 (2010).
3. A. E. Ulanov et al., "Loss-tolerant state engineering for quantum-enhanced metrology via the reverse Hong–Ou–Mandel effect," *Nat. Commun.* **7**(1), 11925 (2016).
4. B. L. Higgins et al., "Entanglement-free Heisenberg-limited phase estimation," *Nature* **450**(7168), 393–396 (2007).
5. E. Knill, R. Laflamme, and G. J. Milburn, "A scheme for efficient quantum computation with linear optics," *Nature* **409**(6816), 46–52 (2001).
6. K. J. Resch et al., "Time-reversal and super-resolving phase measurements," *Phys. Rev. Lett.* **98**(22), 223601 (2007).
7. P. Kok et al., "Linear optical quantum computing with photonic qubits," *Rev. Mod. Phys.* **79**(1), 135–174 (2007).
8. A. Zhang et al., "Experimental test of contextuality in quantum and classical systems," *Phys. Rev. Lett.* **122**(8), 080401 (2019).
9. T. Li et al., "Experimental contextuality in classical light," *Sci. Rep.* **7**(1), 44467 (2017).
10. D. Frustaglia et al., "Classical physics and the bounds of quantum correlations," *Phys. Rev. Lett.* **116**(25), 250404 (2016).
11. M. Markiewicz et al., "From contextuality of a single photon to realism of an electromagnetic wave," *NPJ Quantum Inf.* **5**(1), 5 (2019).
12. S. Berg-Johansen et al., "Classically entangled optical beams for high-speed kinematic sensing," *Optica* **2**(10), 864–868 (2015).
13. D. Guzman-Silva et al., "Demonstration of local teleportation using classical entanglement," *Laser Photonics Rev.* **10**(2), 317–321 (2016).
14. B. Ndagano et al., "Characterizing quantum channels with non-separable states of classical light," *Nat. Phys.* **13**(4), 397–402 (2017).
15. A. Z. Goldberg et al., "Extremal quantum states," *AVS Quantum Sci.* **2**(4), 044701 (2020).
16. S. M. Barnett et al., "Retrodiction for quantum optical communications," *Phys. Rev. A* **62**(2), 022313 (2000).
17. D. T. Pegg, S. M. Barnett, and J. Jeffers, "Quantum retrodiction in open systems," *Phys. Rev. A* **66**(2), 022106 (2002).
18. T. Amri, J. Laurat, and C. Fabre, "Characterizing quantum properties of a measurement apparatus: insights from the retrodictive approach," *Phys. Rev. Lett.* **106**(2), 020502 (2011).
19. T. Theurer et al., "Quantifying operations with an application to coherence," *Phys. Rev. Lett.* **122**(19), 190405 (2019).
20. V. Cimini et al., "Measuring coherence of quantum measurements," *Phys. Rev. Res.* **1**(3), 033020 (2019).
21. F. Bischof, H. Kampermann, and D. Bruß, "Resource theory of coherence based on positive-operator-valued measures," *Phys. Rev. Lett.* **123**(11), 110402 (2019).
22. T. Guff et al., "A resource theory of quantum measurements," *J. Phys. A: Math. Theor.* **54**(22), 225301 (2021).
23. H. Xu et al., "Experimental quantification of coherence of a tunable quantum detector," *Phys. Rev. Lett.* **125**(6), 060404 (2020).
24. J. Lundeen et al., "Tomography of quantum detectors," *Nat. Phys.* **5**(1), 27–30 (2009).
25. G. M. D'Ariano, L. Maccone, and P. L. Presti, "Quantum calibration of measurement instrumentation," *Phys. Rev. Lett.* **93**(25), 250407 (2004).
26. A. Luis and L. L. Sánchez-Soto, "Complete characterization of arbitrary quantum measurement processes," *Phys. Rev. Lett.* **83**(18), 3573–3576 (1999).
27. J. Fiurášek, "Maximum-likelihood estimation of quantum measurement," *Phys. Rev. A* **64**(2), 024102 (2001).
28. V. d'Auria et al., "Quantum decoherence of single-photon counters," *Phys. Rev. Lett.* **107**(5), 050504 (2011).
29. A. Feito et al., "Measuring measurement: theory and practice," *New J. Phys.* **11**(9), 093038 (2009).
30. H. B. Coldenstrodt-Ronge et al., "A proposed testbed for detector tomography," *J. Mod. Opt.* **56**(2–3), 432–441 (2009).
31. G. Brida et al., "Quantum characterization of superconducting photon counters," *New J. Phys.* **14**(8), 085001 (2012).
32. M. K. Akhlaghi, A. H. Majedi, and J. S. Lundeen, "Nonlinearity in single photon detection: modeling and quantum tomography," *Opt. Express* **19**(22), 21305–21312 (2011).

33. A. Worsley et al., "Absolute efficiency estimation of photon-number-resolving detectors using twin beams," *Opt. Express* **17**(6), 4397–4412 (2009).
34. D. Mayers and A. Yao, "Quantum cryptography with imperfect apparatus," in *Proc. 39th Annu. Symp. Found. Comput. Sci.*, IEEE, pp. 503–509 (1998).
35. E. S. Gómez et al., "Device-independent certification of a non-projective qubit measurement," *Phys. Rev. Lett.* **117**(26), 260401 (2016).
36. W.-H. Zhang et al., "Experimentally robust self-testing for bipartite and tripartite entangled states," *Phys. Rev. Lett.* **121**(24), 240402 (2018).
37. A. Tavakoli et al., "Self-testing quantum states and measurements in the prepare-and-measure scenario," *Phys. Rev. A* **98**(6), 062307 (2018).
38. J. Řeháček, D. Mogilevtsev, and Z. Hradil, "Operational tomography: fitting of data patterns," *Phys. Rev. Lett.* **105**(1), 010402 (2010).
39. D. Mogilevtsev et al., "Data pattern tomography: reconstruction with an unknown apparatus," *New J. Phys.* **15**(2), 025038 (2013).
40. L. Zhang et al., "Mapping coherence in measurement via full quantum tomography of a hybrid optical detector," *Nat. Photonics* **6**(6), 364–368 (2012).
41. J. Renema et al., "Experimental test of theories of the detection mechanism in a nanowire superconducting single photon detector," *Phys. Rev. Lett.* **112**(11), 117604 (2014).
42. J. S. Lundeen et al., "Direct measurement of the quantum wavefunction," *Nature* **474**(7350), 188–191 (2011).
43. M. Malik et al., "Direct measurement of a 27-dimensional orbital-angular-momentum state vector," *Nat. Commun.* **5**(1), 3115 (2014).
44. G. A. Howland, D. J. Lum, and J. C. Howell, "Compressive wavefront sensing with weak values," *Opt. Express* **22**(16), 18870–18880 (2014).
45. M. Mirhosseini et al., "Compressive direct measurement of the quantum wave function," *Phys. Rev. Lett.* **113**(9), 090402 (2014).
46. S. H. Knarr et al., "Compressive direct imaging of a billion-dimensional optical phase space," *Phys. Rev. A* **98**(2), 023854 (2018).
47. Z. Shi et al., "Scan-free direct measurement of an extremely high-dimensional photonic state," *Optica* **2**(4), 388–392 (2015).
48. K. Ogawa et al., "A framework for measuring weak values without weak interactions and its diagrammatic representation," *New J. Phys.* **21**(4), 043013 (2019).
49. K. Ogawa et al., "Direct measurement of ultrafast temporal wavefunctions," *Opt. Express* **29**(13), 19403–19416 (2021).
50. Y. Zhou et al., "Direct tomography of high-dimensional density matrices for general quantum states of photons," *Phys. Rev. Lett.* **127**(4), 040402 (2021).
51. M. Yang et al., "Zonal reconstruction of photonic wavefunction via momentum weak measurement," *Laser Photonics Rev.* **14**(5), 1900251 (2020).
52. J. Z. Salvail et al., "Full characterization of polarization states of light via direct measurement," *Nat. Photonics* **7**(4), 316–321 (2013).
53. C. Bamber and J. S. Lundeen, "Observing Dirac's classical phase space analog to the quantum state," *Phys. Rev. Lett.* **112**(7), 070405 (2014).
54. J. S. Lundeen and C. Bamber, "Procedure for direct measurement of general quantum states using weak measurement," *Phys. Rev. Lett.* **108**(7), 070402 (2012).
55. G. S. Thekkadath et al., "Direct measurement of the density matrix of a quantum system," *Phys. Rev. Lett.* **117**(12), 120401 (2016).
56. S. Wu, "State tomography via weak measurements," *Sci. Rep.* **3**(1), 1193 (2013).
57. C. Ren, Y. Wang, and J. Du, "Efficient direct measurement of arbitrary quantum systems via weak measurement," *Phys. Rev. Appl.* **12**(1), 014045 (2019).
58. W.-W. Pan et al., "Direct measurement of a nonlocal entangled quantum state," *Phys. Rev. Lett.* **123**(15), 150402 (2019).
59. Y. Kim et al., "Direct quantum process tomography via measuring sequential weak values of incompatible observables," *Nat. Commun.* **9**(1), 192 (2018).
60. L. Xu et al., "Direct characterization of quantum measurements using weak values," *Phys. Rev. Lett.* **127**(18), 180401 (2021).
61. P. Zou, Z.-M. Zhang, and W. Song, "Direct measurement of general quantum states using strong measurement," *Phys. Rev. A* **91**(5), 052109 (2015).
62. G. Vallone and D. Dequal, "Strong measurements give a better direct measurement of the quantum wave function," *Phys. Rev Lett.* **116**(4), 040502 (2016).
63. Y.-X. Zhang, S. Wu, and Z.-B. Chen, "Coupling-deformed pointer observables and weak values," *Phys. Rev. A* **93**(3), 032128 (2016).
64. X. Zhu, Y.-X. Zhang, and S. Wu, "Direct state reconstruction with coupling-deformed pointer observables," *Phys. Rev. A* **93**(6), 062304 (2016).
65. T. Denkmayr et al., "Experimental demonstration of direct path state characterization by strongly measuring weak values in a matter-wave interferometer," *Phys. Rev. Lett* **118**(1), 010402 (2017).
66. L. Calderaro et al., "Direct reconstruction of the quantum density matrix by strong measurements," *Phys. Rev. Lett.* **121**(23), 230501 (2018).
67. X. Zhu et al., "Hybrid direct state tomography by weak value," https://arxiv.org/abs/1909.02461 (2019).
68. C.-R. Zhang et al., "Direct measurement of the two-dimensional spatial quantum wave function via strong measurements," *Phys. Rev. A* **101**(1), 012119 (2020).
69. M.-C. Chen et al., "Directly measuring a multiparticle quantum wave function via quantum teleportation," *Phys. Rev. Lett.* **127**(3), 030402 (2021).
70. J. A. Gross et al., "Novelty, efficacy, and significance of weak measurements for quantum tomography," *Phys. Rev. A* **92**(6), 062133 (2015).
71. E. Haapasalo, P. Lahti, and J. Schultz, "Weak versus approximate values in quantum state determination," *Phys. Rev. A* **84**(5), 052107 (2011).
72. Z. Bian et al., "Realization of single-qubit positive-operator-valued measurement via a one-dimensional photonic quantum walk," *Phys. Rev. Lett.* **114**(20), 203602 (2015).
73. D. Brivio et al., "Experimental estimation of one-parameter qubit gates in the presence of phase diffusion," *Phys. Rev. A* **81**(1), 012305 (2010).
74. R. Horodecki et al., "Quantum entanglement," *Rev. Mod. Phys.* **81**(2), 865–942 (2009).

Liang Xu received his BS degree in physics of materials and his PhD in optics engineering from Nanjing University in 2014 and 2020, respectively. He is a postdoc fellow at Zhejiang Laboratory. His current research interests include weak measurement, quantum metrology, and quantum tomography.

Huichao Xu received his BS and MS degrees in telecommunication from the University of Jiamusi and University of Liverpool in 2009 and 2011, respectively, and his PhD in quantun optics from Nanjing University in 2020. He is an assistant researcher at Nanjing University. His current research interests include quantum state generation and quantum detectors.

Jie Xie received his BS degree in applied physics from Southwest Jiaotong University. He is a PhD student at the School of Physics of Nanjing University. His current research interests include quantum simulation in linear photonics.

Hui Li received his BE degree in optoelectronic information science and engineering from China University of Petroleum. He is a PhD student at the College of Engineering and Applied Sciences of Nanjing University.

His current research interests include quantum walk and quantum fluctuation.

Lin Zhou received his BS degree in physics of materials in 2020. He is a graduate student at Nanjing University. His current research interests include quantum metrology, quantum tomography and light manipulation.

Feixiang Xu received his BS degree in physics from Nanchang University in 2016, and his PhD in optics engineering from Nanjing University in 2021. He is now an assistant researcher at Nanjing University. His current research interests include the resource theory of quantum coherence, quantum imaging and quantum tomography.

Lijian Zhang received his BS and MS degrees in electrical engineering from Peking University in 2000 and 2003, respectively, and his PhD in physics from the University of Oxford in 2009. He is a professor at the College of Engineering and Applied Sciences of Nanjing University. He is the author of more than 50 journal papers and two book chapters. His current research interests include quantum optics and quantum information processing.

Research Article

ADVANCED PHOTONICS

Dynamical learning of a photonics quantum-state engineering process

Alessia Suprano,[a,†] Danilo Zia,[a,†] Emanuele Polino,[a] Taira Giordani,[a] Luca Innocenti,[b,c,d] Alessandro Ferraro,[c] Mauro Paternostro,[c] Nicolò Spagnolo,[a] and Fabio Sciarrino[a,*]

[a]Sapienza Università di Roma, Dipartimento di Fisica, Roma, Italy
[b]Palacký University, Department of Optics, Olomouc, Czech Republic
[c]Queen's University Belfast, School of Mathematics and Physics, Centre for Theoretical Atomic, Molecular, and Optical Physics, Belfast, United Kingdom
[d]Università degli Studi di Palermo, Dipartimento di Fisica e Chimica-Emilio Segrè, Palermo, Italy

Abstract. Experimental engineering of high-dimensional quantum states is a crucial task for several quantum information protocols. However, a high degree of precision in the characterization of the noisy experimental apparatus is required to apply existing quantum-state engineering protocols. This is often lacking in practical scenarios, affecting the quality of the engineered states. We implement, experimentally, an automated adaptive optimization protocol to engineer photonic orbital angular momentum (OAM) states. The protocol, given a target output state, performs an online estimation of the quality of the currently produced states, relying on output measurement statistics, and determines how to tune the experimental parameters to optimize the state generation. To achieve this, the algorithm does not need to be imbued with a description of the generation apparatus itself. Rather, it operates in a fully black-box scenario, making the scheme applicable in a wide variety of circumstances. The handles controlled by the algorithm are the rotation angles of a series of waveplates and can be used to probabilistically generate arbitrary four-dimensional OAM states. We showcase our scheme on different target states both in classical and quantum regimes and prove its robustness to external perturbations on the control parameters. This approach represents a powerful tool for automated optimizations of noisy experimental tasks for quantum information protocols and technologies.

Keywords: orbital angular momentum; state engineering; black-box optimization; algorithm; quantum walk.

Received Sep. 1, 2021; revised manuscript received Nov. 14, 2021; accepted for publication Nov. 18, 2021; published online Dec. 13, 2021.

[DOI: 10.1117/1.AP.3.6.066002]

1 Introduction

Quantum-state engineering of high-dimensional states is a pivotal task in quantum information science.[1–4] However, many existing protocols are platform-dependent and lack universality.[5–10] Conversely, a scheme to engineer arbitrary quantum states, relying on quantum walk (QW) dynamics, was showcased in Ref. 11. QWs are a particularly simple class of quantum dynamics that can be considered to generalize classical random walks.[12] QWs have been implemented in experimental platforms ranging from trapped ions[13,14] and atoms[15] to photonics circuits.[16–23] In particular, engineering of arbitrary qudit states has been experimentally demonstrated with QWs in orbital angular momentum (OAM) and polarization degrees of freedom of light.[11,24,25]

In the paraxial approximation, the angular momentum of light can be decomposed in spin angular momentum, also referred to as polarization in this context, and OAM, which is related to the spatial transverse structure of the electromagnetic field.[26–28] In the classical regime, OAM finds application in particle trapping,[29] microscopy,[30,31] metrology,[32] imaging,[33–35] and communication.[36–40] On the other hand, in the quantum regime, OAM provides a high-dimensional degree of freedom, useful, for example, to encode large amounts of information in single-photon states. Applications include quantum communication,[41–45] computing,[3,4,46] simulation,[47,48] and cryptography.[49,50]

*Address all correspondence to Fabio Sciarrino, fabio.sciarrino@uniroma1.it
†These authors equally contributed to this work.

Optimization algorithms have been proven to be useful tools in tasks such as detection of qudit states[51] and quantum state engineering.[52,53] Machine learning and genetic algorithms have also found many uses in photonics,[54,55] including the use of generative models,[56] quantum state reconstruction,[57,58] automated design of experimental platforms,[59–61] quantum-state and gate engineering,[52,53,62–65] and the study of Bell nonlocality.[66–68] Moreover, genetic algorithms have been employed to design adaptive spatial mode sorters using random scattering processes.[69] Between these types of algorithms, those based on a black box approach have the advantage that they do not rely on specific knowledge of the underlying experimental apparatus. These algorithms are built to tune a set of control parameters based on the information acquired from their environment, without having a notion of what the parameters represent in the experimental platform. This makes such approaches flexible and easier to apply in several scenarios.

In this paper, we showcase the use of RBFOpt,[70,71] a gradient-free global optimization algorithm based on radial basis functions (RBFs),[72–74] to learn how to engineer specific quantum states by efficiently tuning the parameters of a given experimental apparatus. The algorithm seeks to optimize cost function $C(\Theta)$, with Θ a set of real parameters determining the state produced by the apparatus. With cost function $C(\Theta)$, we use the quantum state fidelity between the target and current states, as estimated from a given finite number of measurement samples. This makes the cost function inherently stochastic and thus its optimization potentially more complex. As shown in Refs. 70 and 71, RBFOpt is particularly suited to optimize problems with few parameters, with a focus on operating regimes where only a small number of function evaluations are allowed. This is fully appropriate for our scenario, where functions evaluations involve the generation and measurement of photonic states and are thus relatively costly.

We apply the proposed protocol to an experimental apparatus implementing discrete-time one-dimensional QWs in the OAM and polarization degrees of freedom of light, using a platform based on polarization-controlling waveplates and q-plates (QPs):[75] devices able to couple polarization and OAM degrees of freedom. This platform was shown to be able to engineer arbitrary target quantum states.[11,24] Such an approach, however, requires full knowledge of the inner workings of the underlying experimental apparatus. This feature makes it harder to flexibly adapt a protocol to the perturbations arising in realistic noisy conditions. On the other hand, an adaptive algorithm operating in a black-box scenario, capable of finding the ideal control parameters independently of the physical substratum it operates in, is intrinsically more resilient to varying environmental and experimental circumstances. To ensure that the performance of our protocol is mostly independent of the specific task to which we apply it here, we avoided fine-tuning of the associated hyperparameters, using the default values presented in Refs. 76 and 77. To further verify the resilience of the learning process, we also performed numerical simulations introducing some noise.

In Sec. 2, we introduce the general optimization framework and the QW model underlying our experimental architecture and showcase the performance of the RBFOpt algorithm in numerical simulations with noise that mimics the experimental conditions. In Sec. 3, we describe the experimental platform and report how our optimization pipeline fares when operating directly on the experimental data. In Sec. 4, we analyze the performance of the protocol when applied to recover the optimal control parameters following sudden changes due to possible external perturbations in order to probe its flexibility under different scenarios. Finally, in Sec. 5, we summarize the results and relate our conclusions.

2 Quantum-State Engineering Process as a Black-Box and Simulated Optimization

In order to study the effects of noise on the RBFOpt algorithm and its feasibility to engineer target quantum states, we apply it to numerically simulated data, reproducing the most likely sources of noise in our experimental apparatus. We study, in particular, the effects of binomial and Poissonian fluctuations on the cost function used by the algorithm.

Generating arbitrary qudit states is a pivotal and ubiquitous task in quantum information science and quantum technologies, with applications ranging from quantum communications[1,78–82] to quantum computation.[3,4,46,83] The general quantum state engineering scenario we consider can be modeled with a parameterized unitary operation $\mathcal{U}(\Theta)$ for some set of real parameters $\Theta \in \mathbb{R}^N$. Given a pair of initial and target states $|\phi_{\text{in}}\rangle$ and $|\phi_{\text{target}}\rangle$, the state engineering task consists of finding values $\Theta^\star \in \mathbb{R}^N$ such that $\mathcal{U}(\Theta^\star)|\phi_{\text{in}}\rangle = |\phi_{\text{target}}\rangle$.

To achieve this, we employ a numerical optimization algorithm to minimize the cost function $C(\Theta) \equiv 1 - F(\Theta)$, where $F(\Theta) \equiv |\langle\phi_{\text{target}}|\mathcal{U}(\Theta)|\phi_{\text{in}}\rangle|^2$ is the fidelity between current and target states. The optimization is performed in a fully black-box scenario, meaning we want the optimization procedure to be independent of the specifics of the particular optimization task. In particular, the optimization algorithm can control and optimize only the generation parameters Θ, even if it has no knowledge about both generation of the output state $\mathcal{U}(\Theta)|\phi_{\text{in}}\rangle$ and computation of the cost function $C(\Theta)$. More specifically, we use RBFOpt,[70,71] which works by building an approximated model of the objective function—referred to as a surrogate model in this context—using a set of RBFs. RBFs are real-valued functions $\phi_{\mathbf{p}}$ that depend only on the distance from some fixed point: $\phi_{\mathbf{p}}(\mathbf{x}) = \phi(\|\mathbf{x} - \mathbf{p}\|)$ for some ϕ. The goal of the surrogate model used in RBFOpt is to optimally exploit the information collected on the objective function from a limited number of function evaluations. Based on the current estimation of the surrogate model, the algorithm selects new values of the control parameters to improve its current estimation of the model (see Appendix A for further details). This algorithm is an extension of RBF algorithms[72–74,84,85] whose performances are enhanced by providing an improved procedure to find an optimal surrogate model. A comparison of its performances with basic gradient-free algorithms is proposed in Appendix C.

In our case, $\mathcal{U}(\Theta)$ is the evolution corresponding to a one-dimensional discrete-time QW with time-dependent coin operations. In this model, one considers states in a bipartite space $\mathcal{H}_W \otimes \mathcal{H}_C$, where $\mathcal{H}_W$ is a high-dimensional Hilbert space encoding the possible states of the walker degree of freedom, and $\mathcal{H}_C$ is a two-dimensional space accommodating the coin degree of freedom. The dynamics are defined as a sequence of iterations, where each iteration is composed of a coin operation $\hat{C}(\boldsymbol{\theta})$ followed by a controlled-shift operation $\hat{S}$. To simulate the experimental conditions, the operators are defined as

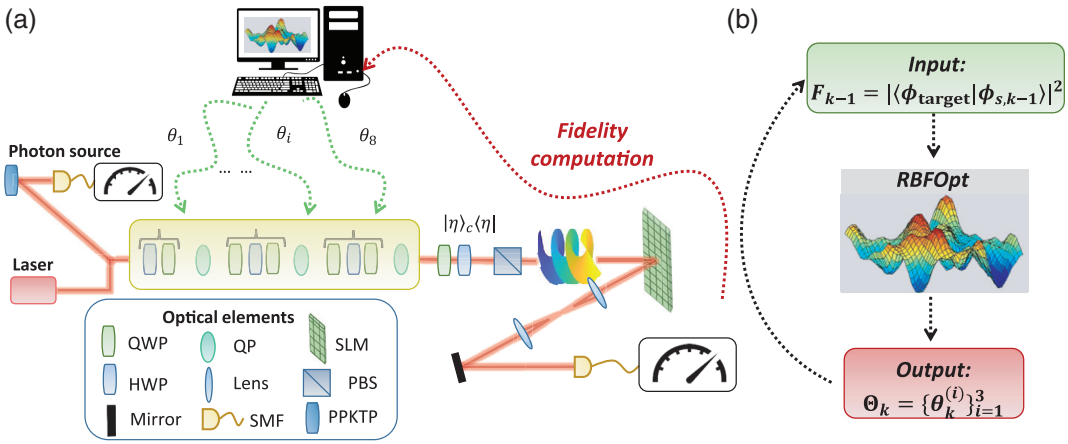

Fig. 1 Experimental apparatus. (a) The engineering protocol has been tested experimentally in a three-step discrete-time QW encoded in the OAM of light with both single-photon inputs and classical continuous wave laser light (CNI laser PSU-III-FDA) with a wavelength of 808 nm. The single-photon states are generated through a type-II spontaneous parametric down-conversion process in a periodically poled KTP crystal. The input state is characterized by a horizontal polarization and OAM eigenvalue $m = 0$. Each step of the QW is made by a coin operator, implemented through a set of waveplates (QWP–HWP–QWP), and the shift operator, realized by a QP. To obtain the desired state in the OAM space, a suitable projection in the polarization space is performed through a quarter-waveplate, a half-waveplate, and a polarizing beam-splitter. The measurement station of the OAM-state is composed by an SLM followed by a single-mode fiber, and the coupled signal is measured through a power meter, in the classical regime, or an avalanche-photodiode detector, in the quantum one. In particular, in quantum optimizations, pairs of photons are generated, and heralded detection is performed, computing the two-fold coincidences between the detectors clicks from the QW evolved photon and the trigger one. The RBFOpt ignores the features of the experimental implementation that is seen as a black box. The algorithm has access only to the Θ parameters of the coin operators and to the computed fidelity. (b) During the iterations of the algorithm, the RBFOpt samples the black-box function to construct a surrogate model that is employed in the optimization. In the k'th iteration, the algorithm receives as input the fidelity computed in the previous iteration and uses it to improve the surrogate modeling. Moreover, the new parameters Θ_k are computed based on the optimization process. This procedure is repeated for each iteration of the algorithm.

$$\hat{C}(\boldsymbol{\theta}) = \begin{pmatrix} e^{-i\beta}\cos\eta & (\cos\mu + i\sin\mu)\sin\eta \\ (-\cos\mu + i\sin\mu)\sin\eta & e^{i\beta}\cos\eta \end{pmatrix},$$
$$\hat{S} = \sum_k |k-1\rangle\langle k|_w \otimes |\downarrow\rangle\langle\uparrow|_c + |k+1\rangle\langle k|_w \otimes |\uparrow\rangle\langle\downarrow|_c, \quad (1)$$

where $\beta \equiv \theta_1 - \theta_3$, $\eta \equiv \theta_1 - 2\theta_2 + \theta_3$, $\mu \equiv \theta_1 + \theta_3$, and $\boldsymbol{\theta} \equiv (\theta_1, \theta_2, \theta_3)$ are the control parameters tuned by the algorithm. This parameterization arises from the sequence of three polarization waveplates used to implement each coin operation. The case in which there are only two waveplates, as in the first step (Fig. 1), is simply obtained from having $\theta_1 = 0$ and optimizing the values of θ_2 and θ_3. Denoting with $\boldsymbol{\theta}^{(i)} \equiv (\theta_1^{(i)}, \theta_2^{(i)}, \theta_3^{(i)})$ the free parameters characterizing the coin operation at the i'th step, the full set of parameters characterizing an n-step QW dynamics is then $\Theta = (\boldsymbol{\theta}^{(1)}, \ldots, \boldsymbol{\theta}^{(n)}) \in \mathbb{R}^{3n}$. The overall evolution operator corresponding to n steps is then $\mathcal{U}(\Theta) \equiv \prod_{i=1}^{n} \hat{S}\,\hat{C}(\boldsymbol{\theta}^{(i)})$. Following the engineering protocol presented in Refs. 11 and 24, we project the coin degree of freedom at the end of the evolution so that our target state is $|\phi_{\text{target}}\rangle \in \mathcal{H}_W$.

We apply RBFOpt to optimize a three-step QW, where in the first iteration only two free parameters are used. This corresponds to a total of eight control parameters: $\Theta = (\boldsymbol{\theta}^{(i)})_{i=1}^3$ with $\boldsymbol{\theta}^{(1)} \equiv (0, \theta_2^{(1)}, \theta_3^{(1)})$. Importantly, the algorithm does not use the information of the correct model $\mathcal{U}(\Theta)$ of the evolution. This feature permits us to use the present approach in conditions where a model of the experimental setup and noise processes is lacking.

In order to simulate the experimental calculation of the fidelity of a given target state, an orthonormal basis $\{|\psi_j\rangle\}_{j=1}^d$, where d is the dimension of the target state and $|\psi_1\rangle = |\phi_{\text{target}}\rangle$, is built through the Gram–Schmidt algorithm. This approach to estimate the cost function is used to simulate the experimental statistics collection process. Furthermore, we consider both Poissonian $[\mathcal{P}(\lambda)]$ and binomial $[\mathcal{B}(N, p)]$ fluctuations. Poissonian fluctuations are introduced to take into account laser oscillations, whereas binomial fluctuations reflect the probabilistic nature of the measurement setup.

The number of events of the binomial distribution N is extracted from a Poissonian distribution with a parameter $\lambda = 10^4$, while the probability p is equal to the fidelity between the state proposed by the algorithm in the k'th iteration and the specific element of the basis. Therefore, for each element of the orthonormal basis, the number of detected events is extracted from

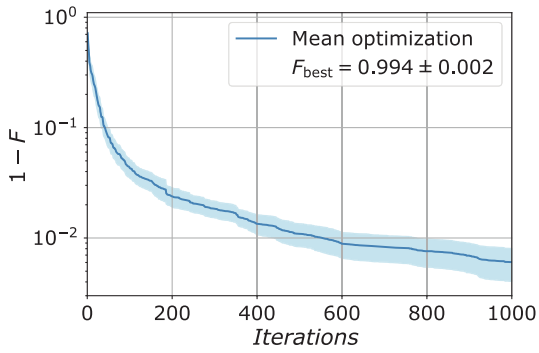

Fig. 2 Simulated optimization: infidelity $1 - F$ obtained at different stages of the optimization. We test the algorithm on 10 random target states, repeating the optimization 10 times for each. The reported results are obtained as the mean over the average behavior for each of the 10 states. The highest average fidelity obtained is 0.994 ± 0.002. The shaded area represents the standard deviation of the mean.

the binomial distribution. The noisy fidelity between the proposed state and the target state is then calculated as the ratio between the counts for the element $|\psi_1\rangle$ and the total number of counts.

We apply the optimization protocol to 10 random four-dimensional target states, repeating the optimization 10 times for each state. In Fig. 2, we show the value of the cost function—i.e., the infidelity between current and target states—obtained at different stages of the algorithm, up to the fixed maximum number of 1000 iterations. For each iteration number, we report the infidelity obtained as the mean over the average behavior of each of the 10 states. The obtained trend demonstrates that, also in noisy conditions, the algorithm manages to minimize the function, and promising results are obtained. Moreover, we also investigate the scalability of the proposed approach when the number of parameters increases. In particular, we simulated QWs of up to 17 steps (50 parameters) and observed in the investigated regime a linear increase in the mean number of iterations needed to achieve a fidelity value of at least 98%. Further details are reported in Appendix B.

3 Experimental Dynamical Learning

The capability of manipulating the OAM of light enabled effective experimental implementations of high-dimensional discrete-time QWs. Therefore, to test experimentally the optimization procedure, we exploit a setup based on the scheme proposed in Ref. 11. In particular, we implemented three steps of a discrete-time QW encoding the coin state in the photon polarization and the walker in the OAM degree of freedom. At each iteration, the coin operation is implemented as a set of polarization waveplates, while the controlled-shift occurs via a QP, a device that acts on the OAM conditionally on the polarization state of light:[75]

$$\hat{Q} = \sum_m |m-1\rangle\langle m| \otimes |L\rangle\langle R| + |m+1\rangle\langle m| \otimes |R\rangle\langle L|, \qquad (2)$$

where m is the OAM value, and R and L are the right and left circular polarizations, respectively. We implement arbitrary coin operations using two quarter-waveplates (QWPs) interspaced with a half-waveplate (HWP). The output OAM state is then obtained performing a suitable projection on the polarization. This is implemented with a set of waveplates followed by a polarizing beam-splitter [cf., Fig. 1(a)].

To measure the fidelity of the output states, we use a measurement apparatus composed of a spatial light modulator (SLM)[86,87] and a single-mode fiber. Since the SLM modulates the beam shape through computer-generated holograms, the operation of this measurement station is equivalent to a projective measurement on the state encoded in the employed hologram. To characterize an incident beam, we thus display on the SLM the hologram corresponding to each element of an orthonormal basis, obtaining the corresponding fidelities. The optimization speed is mainly limited by the measurement process, since significant statistics have to be collected for each projected hologram. Therefore, the use of algorithms able to limit the objective function evaluations, such as those based on the building of a surrogate model, is preferable.

The computed fidelities are then fed to the RBFOpt algorithm to tune the waveplate parameters Θ. To achieve this, the algorithm does not require knowledge on the final target state or on the generation and measurement functioning, as shown in Fig. 1(b). However, since the algorithm has no control over the measurement station, the parameters of the latter have been fine-tuned *a priori*, and we are confident of the correctness of this step. Therefore, through a dynamic control of the waveplates' orientation, the algorithm is able to optimize the fidelity value in real time.

To showcase the efficiency of the protocol on our experimental platform, we applied it to engineer different kinds of target states in both the classical and quantum regimes. In Fig. 3, we show the results of running the optimization algorithm on nine different classical states. In particular, we focus our analysis on the elements of the computational basis $|m\rangle$ with $m \in \{-1,1,-3,3\}$ and on the balanced superposition of two OAM values. We considered both real $\mathrm{SR}_{m_1}^{m_2} = \frac{|m_1\rangle - |m_2\rangle}{\sqrt{2}}$ and complex superpositions $\mathrm{SC}_{m_1}^{m_2} = \frac{|m_1\rangle - i|m_2\rangle}{\sqrt{2}}$, where $m_1, m_2 \in \{-1,1,-3,3\}$ with $|m_1| = |m_2|$. Moreover, to verify the efficiency of the protocol, we optimize the engineering of a randomly extracted state (R) in the four-dimensional Hilbert space with no zero coefficients corresponding to each basis element. As shown in Fig. 3(a), optimal average values are obtained in 600 algorithm iterations. In particular, the reported infidelity $1 - F$ is computed, averaging over all the experimentally engineered states, and the minimization is compatible with the numerical results reported in Fig. 2. In Fig. 3(b), we report, for each engineered state, the ratio between the fidelities found by the RBFOpt algorithm and those found using the method presented in Ref. 24 to find the optimal values of the parameters. Indeed, as demonstrated in Ref. 24, it is possible to find coin parameters resulting in an arbitrary target state—albeit possibly with different projection probabilities—regardless of the experimental conditions. We find the fidelities reached by RBFOpt to always be higher than the ones computed using the direct method presented in Ref. 24. This is due to the dynamical learning algorithm we employ, which shows higher performances in compensating experimental imperfections. This showcases the advantages of real-time optimization algorithms for quantum state engineering in realistic scenarios. Notably, we extended the experimental demonstration of the protocol, also in the quantum regime of single photon states. We showcased the engineering of

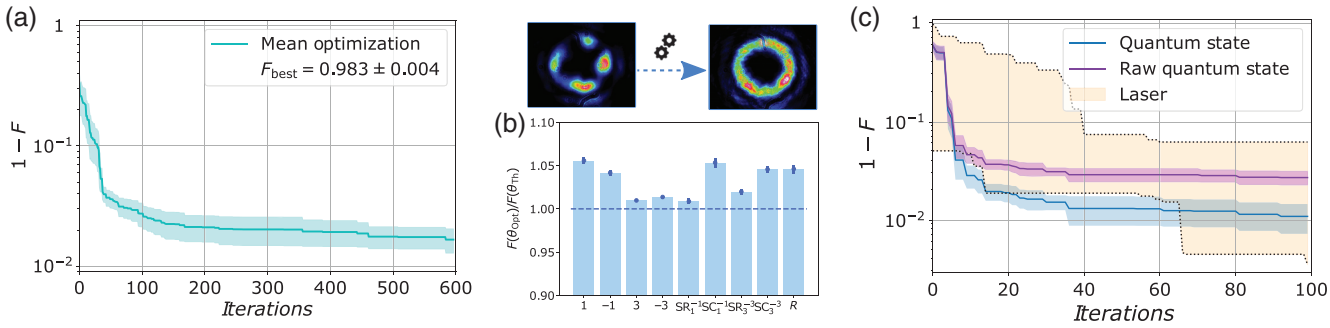

Fig. 3 Experimental results: (a) minimization of the quantity $1 - F$ averaged over the algorithm performances for different experimental states. The mean maximum value reached is 0.983 ± 0.004. (b) Ratio between the maximum experimental values of the fidelities resulted after the optimization $F(\Theta_{opt})$ and the fidelities measured with the theoretical parameters $F(\Theta_{Th})$. For each engineered state, the ratio is higher or compatible with the value 1 highlighted by the dashed line. This confirms that the adopted algorithm can reach performances compatible or even superior with respect to the one obtained with the direct method presented in Ref. 24 that considers ideal experimental platforms. In this sense, the algorithm can take into account and compensate for the experimental imperfections. All of the error bars reported are due to laser fluctuations affecting each measurement and are estimated through a Monte Carlo approach. (c) Comparison between the performances reached in 100 iterations using classical or single-photon input states. In yellow is reported the area between the best and worst optimization performed in the classical case. The blue and violet curves are associated with the minimization of the quantity $1 - F$ averaged over five different optimizations for the state SR_1^{-1} engineered in the quantum domain. In particular, the raw data are shown in violet, whereas the data after accidental counts subtraction are in blue.

the superposition state SR_1^{-1}, and we repeated the optimization 5 times, considering only 100 iterations. No differences are expected between the employment of the laser and single-photon states. In Fig. 3(c), we compared the two performances and observed a good agreement between the approaches. In particular, we reported the optimization curves obtained in the quantum regime plotting the raw data, corresponding to ~4000 Hz coincidences, and by subtracting the accidental counts. This allows us to distinguish the contribution to the cost function given by either the engineering or the measurement system. The corresponding maximum mean fidelities are $F = 0.972 \pm 0.003$ and $F = 0.989 \pm 0.003$, respectively. In conclusion, since very high fidelities are reached in only 100 steps, the proposed approach can be efficiently applied to quantum situations.

4 Dynamical Learning Protocol with External Perturbations

In realistic conditions, noise is unavoidable, which makes the capability of an algorithm to adapt to real-world perturbations pivotal. To test the robustness of RBFOpt, we have thus added external perturbations to the experimental setup. In particular, we consider a scenario where a sudden perturbation on the parameters is introduced. The algorithm is then tasked with finding again the optimal parameters required to engineer the target state. We assess the performances of the algorithm throughout the optimization, to determine whether a perturbation occurred, and thus the control parameters need to be reoptimized. More specifically:

1. Every 10 iterations, we used the optimal parameters found by the algorithm up to that time Θ_{best} to obtain a new estimate of the cost function $C_{new}(\Theta_{best})$.

2. To spot if a perturbation occurred, we compared the new value with the one obtained during the algorithm evolution $C_{sampled}(\Theta_{best})$. So choosing a threshold t, we proceed as follows.

(a) If $C_{new}(\Theta_{best}) \leq C_{sampled}(\Theta_{best}) + t$, the optimization is continued.

(b) If $C_{new}(\Theta_{best}) > C_{sampled}(\Theta_{best}) + t$, the algorithm is restarted.

Therefore, within this approach, the surrogate model is discarded and rebuilt from scratch every time the quantity of interest deteriorates. We performed this check every 10 algorithm iterations in order to have a quick response to perturbations without excessively increasing the optimization time. Indeed, each function evaluation consists of a time-consuming projective measurement with the SLM. For each engineered state, the value of the threshold was fixed by analyzing the fluctuations in the value of the measured fidelity F, and these values are reported in Table 1.

The considered perturbations act on the HWP of the second step and on the first QWP of the third step. This disturbance consists of a permanent offset in the waveplates rotation of a quantity δ. In particular, at each iteration and with probability q, the orientation of the waveplates optical axis is changed by the addition of an angle sampled from a normal distribution with mean $\mu = -30$ deg and standard deviation $\sigma = 5$ deg $[\mathcal{N}(-30 \text{ deg}, 5 \text{ deg})]$. We investigated the algorithm response using elements of the computational basis, balanced superpositions of such elements, and a random state. In these cases, several values for the parameter q are used. The engineered states and the probability q used for them are reported in Table 1.

An example of the dynamics under perturbations is reported in Fig. 4(a); here, the iteration in which a disturbance is introduced is highlighted by a vertical red or green line, respectively,

Table 1 The parameters used in the study of the optimization under perturbations for the engineered states. In the second column, we report the values of the perturbation occurrence probability q, whereas in the third column, we report the threshold values t used for deciding the algorithm restart.

Target state	Perturbation probability	Restart threshold
$\|1\rangle$	0.0015	0.02
$\|3\rangle$	0.0015	0.02
$\frac{1}{\sqrt{2}}(\|-1\rangle + \|1\rangle)$	0.008	0.02
$\frac{1}{\sqrt{2}}(\|-1\rangle + i\|1\rangle)$	0.004	0.02
$\frac{1}{\sqrt{2}}(\|-3\rangle + \|3\rangle)$	0.0015	0.05
Random	0.0015	0.02

for a shift on the HWP or on the QWP. Instead, the restart of the algorithm is indicated with a vertical orange line. As shown, after the perturbation, the minimum found by the algorithm is no longer the optimal solution, thus triggering a restart. The latter allows the algorithm to reach a new optimal solution in a different environmental condition. Moreover, in Fig. 4(b), the mean ratio between the best fidelity found before and after perturbation is reported for each analyzed state. Knowing that for each state more than one perturbation could be performed, the mean ratio is computed, averaging over all of them. Here, values close to or greater than 1 point out how, thanks to the restart, the algorithm is able to readapt its optimal solution and eventually improve the previously obtained fidelity.

5 Conclusions

The black-box optimization paradigm we discussed is highly flexible, thus promising to be a powerful tool with the potential to be applicable to problems ranging from optimizations of quantum information platforms to the study of nonclassicality.

We have showcased how the RBFOpt global optimization algorithm allows us to dynamically learn the quantum state generation process. In particular, such an approach enables the optimization of target states engineering without having to devise *ad hoc* platform-dependent protocols. First of all, we dynamically tune the QW parameters in order to optimize the engineering of nine different experimental states in the classical domain. The obtained results turned out to be comparable to the preliminary ones achieved in our numerical simulations. Moreover, the RBFOpt results in higher fidelities than those computed using the direct method of Ref. 24. Therefore, the real-time optimization allows us to take into account and compensate for experimental imperfections. Moreover, we optimized an experimental state using a single-photon source as input to prove the equivalence between the performances reached in the classical and quantum regimes and extend the proposed approach. In order to carry out a complete analysis, and as the adaptation capability of an algorithm is pivotal in realistic conditions, we simulated the effect of real-world perturbations. We have thus applied the optimization algorithm to different states while adding permanent offsets to the orientation of two waveplates in a probabilistic manner. The algorithm manages to adapt itself so as to reach fidelities comparable to those obtained before the perturbation. Our results prove the advantages of adopting real-time optimization algorithms for experimental quantum state engineering protocols. Therefore, practical experimental quantum information experiments can benefit from our work, increasing the engineering performances and employing a real-time fine-tuning of the parameters. The proposed approach can be extended to many different tasks; for example, by suitably modifying the cost function, it is possible to optimize not only the fidelity but also the success probability to generate a target state after the coin projection (see Refs. 11 and 24). Moreover, since the algorithm does not require information on the function to be optimized and on the employed experimental platform, our scheme can find applications in different engineering protocols and quantum information tasks that make use of controllable devices parameters employing, in principle, arbitrary degrees

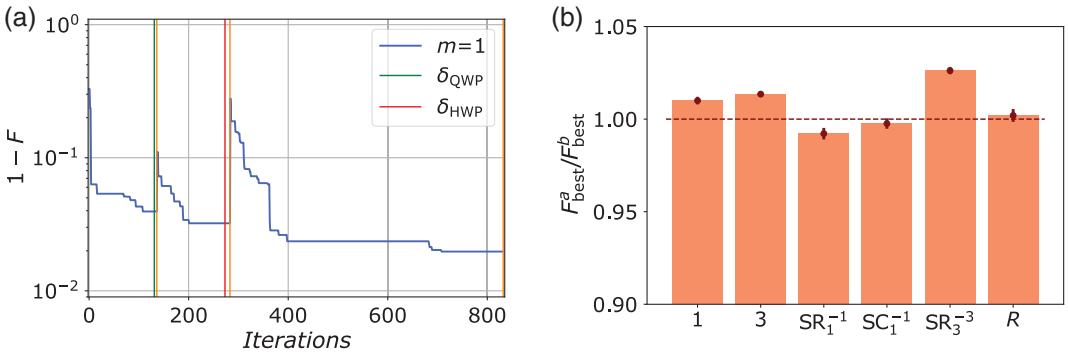

Fig. 4 Experimental perturbation results. (a) Optimization under external perturbation of the quantity $1-F$ for the state $|1\rangle$. The iterations in which a perturbation δ occurs are highlighted by a vertical red line (second step HWP) or by a vertical green line (third step QWP), and a vertical orange line highlights the iteration in which the algorithm is restarted. (b) Mean ratio between the best value obtained for the fidelity after (F^a_{best}) and before (F^b_{best}) the perturbation for the different engineered states. The ratio is close to or higher than 1 for all of them, which showcases that the algorithm is able to reobtain and eventually improve the best value sampled before the perturbation. All of the error bars reported are due to laser fluctuations affecting each measurement and are estimated through a Monte Carlo approach.

of freedom. Furthermore, going beyond the fully black-box paradigm, in principle, the approach can be exploited also for different protocols. For instance in the theoretical design of experiments, it could be used to optimize the number of quantum gates needed for a specific desired task. Moreover, it could also be used in the calibration of complex optical circuits that find applications in tasks like boson sampling[88–91] and in the engineering of multiphoton quantum states.[92] In this case, it would be crucial to tailor a suitable cost function.

6 Appendix A: Description of the RBFOpt Algorithm

The RBFOpt optimization algorithm is based on the exploitation of a radial basis interpolant, called a surrogate model.[70,71,84,85] Given k distinct parameter points $\Theta_1, \ldots, \Theta_k \in \Omega$, where Ω is a compact subset of $\mathbb{R}^N$, with corresponding cost function values $C(\Theta_1), \ldots, C(\Theta_k)$, the associated surrogate model $s_k(\Theta)$ is defined as

$$s_k(\Theta) = \sum_{i=1}^{k} \lambda_i \phi(\|\Theta - \Theta_i\|) + p(\Theta), \tag{3}$$

where $\phi(\cdot)$ is an RBF, $\lambda_1, \ldots, \lambda_k \in \mathbb{R}$, and $p(\cdot)$ is a polynomial of degree d. This degree is selected based on the type of the RBF function used in the surrogate model. The possible RBF function choices and the degree of their associated polynomial are reported in Table 2. The hyperparameter γ present in the expression of the RBFs is set to 0.1 by default.[76,77] Moreover, the RBFOpt algorithm automatically selects the RBF that appears to be the most accurate in the description of the problem. This selection is made using a cross-validation procedure, in which the performance of a surrogate model constructed with points $(\Theta_i, C(\Theta_i))$ for $i = 1, \ldots, k$ is tested at $(\Theta_j, C(\Theta_j))$ with $j \neq i$.[70,71]

The value of the parameters λ_i with $i = 1, \ldots, k$ and the coefficients of the polynomial can be determined solving the following linear system:[70,71,84,85]

$$\begin{cases} s_k(\Theta_i) = C(\Theta_i), & i = 1, \ldots, k \\ \sum_{i=1}^{k} \lambda_i \hat{p}_j(\Theta_i) = 0, & j = 1, \ldots, \tilde{d} \end{cases}, \tag{4}$$

where Π_d is the space of polynomials of degree less than or equal to d, $\tilde{d}$ is the dimension of Π_d, and $\hat{p}_1, \ldots, \hat{p}_{\tilde{d}}$ are a basis of the space.

Table 2 The RBFs exploited by the RBF algorithm and the degree of the polynomial used in the construction of the surrogate model.[70,71,84,85] When $d = -1$, the polynomial is removed from Eq. (3).

RBF $\phi(x)$	Polynomial degree d
x	0
x^3	1
$\sqrt{x^2 + \gamma^2}$	0
$x^2 \log x$	1
$e^{-\gamma x^2}$	−1

At the beginning of the optimization procedure, the surrogate model is constructed from a set of parameter points tunable in number and sampled using a Latin hypercube design.[76,77] After that, the interpolant is used to choose the next point, in which the cost function is computed. So, the evolution of the RBFOpt algorithm is composed by the repetition of following steps (say k'th step).

1. Compute the surrogate model $s_k(\Theta)$ from the data points $(\Theta_i, C(\Theta_i))$, with $i = 1, \ldots, k$, solving the linear system of Eq. (4).
2. Use the surrogate model to choose the next point Θ_{k+1}. In particular, the metric stochastic response surface method is applied.[70,71,85] Within this framework, the algorithm does a number of global steps controlled by the hyperparameter num_global_searches (default value 5[76,77]) and a local step. The latter gives as the next point the one that minimizes the surrogate model.
3. Evaluate the cost function at Θ_{k+1} and add $(\Theta_{k+1}, C(\Theta_{k+1}))$ to the data points.
4. Decide whether to restart the model for lack of improvement. Specifically, if the algorithm does not find a new optimal solution after a number of evaluations defined by the hyperparameter max_stalled_iterations (default value 100[76,77]), the actual surrogate model is discarded, and the optimization procedure is restarted from scratch.

Moreover, during the optimization, the algorithm executes a refinement step, the purpose of which is to improve the optimal solution doing a local search around it through variation of a trust region method.[70,71] The refinement step is triggered at the end of point (3) with a frequency controlled by the hyperparameter refinement frequency, with default value equal to 3.[76,77]

Furthermore, in the study concerning the evolution under external perturbation, we add, as explained in Sec. 4, a new condition for triggering a restart. Beyond the default one, we analyzed the deterioration of the optimal value founded for the cost function and decided whether to restart the optimization. This further check was done every 10 iterations in order to have a faster response to perturbations without increasing excessively the number of function evaluations that experimentally are expensive in time.

7 Appendix B: Scalability of the Optimization Approach

In this section, we study the RBFOpt behavior as the number of parameters of the objective function increases. In particular, we simulated different experimental configurations with QW steps ranging from 3 to 17 and thus considered up to 50 parameters. In fact, with N_{steps} as the number of steps and considering only two waveplates in the first coin, the number of parameters N_{par} follows the relation:

$$N_{\text{par}} = 3N_{\text{steps}} - 1. \tag{5}$$

For each case, we generated at random 50 target states and investigated the optimization procedure stopping the process when a fidelity of at least 98% was reached. In all of the evolutions, we added the same Poissonian and binomial noises described in the main text to the fidelity between the target state and the one proposed by the algorithm.

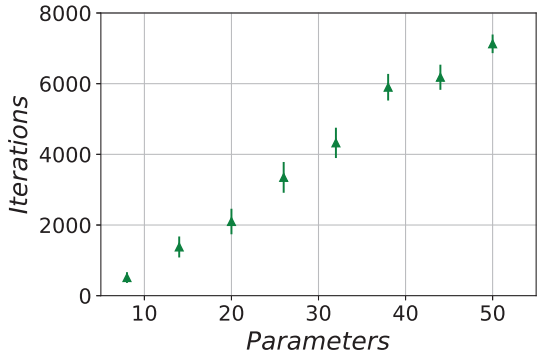

Fig. 5 Scalability: the plot shows the mean number of RBFOpt algorithm iterations as a function of the black-box problem parameters. Here, the optimization process is interrupted when a value of the fidelity between the target state and the one proposed by the algorithm of at least 98% is reached. For each configuration, the iteration values are obtained by averaging more than 50 random target states and simulating experimental noise using binomial and Poissonian distributions. The uncertainty associated with each point is provided by the standard deviation of the mean.

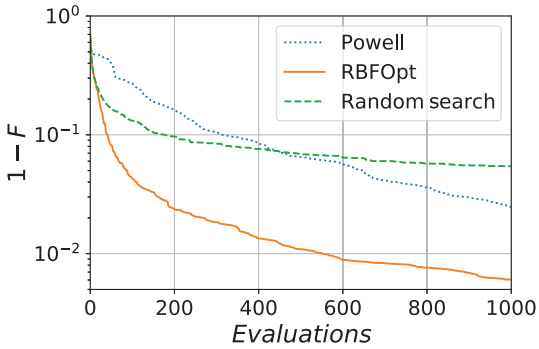

Fig. 6 Comparison between different optimization algorithms: the plot reports the simulated performances of three different algorithms averaged over the optimization of 10 different states, each of which is repeated 10 times. Dotted blue, dashed green, and continuous orange lines report the trends corresponding to Powell, random search, and RBFOpt, respectively. RBFOpt is found to perform significantly better than the alternatives in most cases. All curves are generated simulating experimental noise with both Poissonian ($\lambda = 10^4$) and binomial fluctuations.

The computational cost of performing a black-box optimization in high-dimensional spaces can be extracted analyzing how the mean number of iterations changes in relation to the number of parameters. The values obtained averaging over the 50 states considered in our study are reported in Fig. 5 for each simulated configuration. As can be seen from the plot, the RBFOpt algorithm appears to have linear scaling over the parameters number when applied to our implementation. This theoretically showcases the effectiveness of the proposed approach for the engineering of higher dimensional OAM states, and similar behaviors are expected experimentally taking into account the devices response time and adapting properly the related implementation. Finally, while similar behaviors are expected in the regime of a few parameters for higher orders of magnitude, the time needed to perform an iteration step increases drastically. In such regimes, a more refined version of the algorithm might be useful to improve its efficiency.

8 Appendix C: Comparison Between RBFOpt and Basic Algorithms

In this section, we perform simulations to compare the RBFOpt algorithm with two basic gradient-free methods suitable to multi-parameter black-box optimization. In particular, we consider both nonadaptive and adaptive approaches.

Regarding the first class, among the simplest is the random search method. As suggested by the name, in each iteration of the optimization processes, the parameters are randomly extracted with a uniform distribution in the parameter space and independently from values assumed in previous steps. The second comparative algorithm is based upon the simplest gradient-free adaptive method known as the Powell method.[93] It attempts to find the local minimum nearest to the starting point. Initially, a set of directions is defined, and the algorithm moves along one of them until a minimum is reached. This minimum becomes the uploaded starting point for the following minimization performed on the second direction. After repeating this procedure for each direction, a new direction is defined, and the algorithm proceeds to upload the set of directions.

Figure 6, shows the reported trends corresponding to each compared algorithm obtained from averaging the optimizations of 10 distinct states, each of which is repeated 10 times. The experimental conditions are simulated adding both Poissonian ($\lambda = 10^4$) and binomial fluctuations. As expected, both of the adaptive approaches results are advantageous with respect to the random approach for a considerable number of function evaluations. Moreover, since the RBFOpt spans the whole parameter space through the global steps, its performances are substantially better.

Acknowledgments

We would like to acknowledge the support from the European Union's Horizon 2020 Research and Innovation Program (Future and Emerging Technologies) through project TEQ (Grant No. 766900), QU-BOSS-ERC Advanced Grant (Grant No. 884676), the QUSHIP PRIN 2017 (Grant No. 2017SRNBRK), the DfE-SFI Investigator Program (Grant No. 15/IA/2864), COST Action CA15220, the Royal Society Wolfson Research Fellowship (No. RSWF\R3\183013), the Leverhulme Trust Research Project Grant (Grant No. RGP-2018-266), and the UK EPSRC (Grant No. EP/T028106/1).

References

1. H. Bechmann-Pasquinucci and A. Peres, "Quantum cryptography with 3-state systems," *Phys. Rev. Lett.* **85**(15), 3313–3316 (2000).
2. T. Vértesi, S. Pironio, and N. Brunner, "Closing the detection loophole in Bell experiments using qudits," *Phys. Rev. Lett.* **104**(6), 060401 (2010).
3. B. P. Lanyon et al., "Simplifying quantum logic using higher-dimensional Hilbert spaces," *Nat. Phys.* **5**(2), 134–140 (2009).
4. T. C. Ralph, K. J. Resch, and A. Gilchrist, "Efficient Toffoli gates using qudits," *Phys. Rev. A* **75**(2), 022313 (2007).
5. B. Anderson et al., "Accurate and robust unitary transformations of a high-dimensional quantum system," *Phys. Rev. Lett.* **114**(24), 240401 (2015).

6. A. Rossi et al., "Multipath entanglement of two photons," *Phys. Rev. Lett.* **102**(15), 153902 (2009).
7. M. Hofheinz et al., "Synthesizing arbitrary quantum states in a superconducting resonator," *Nature* **459**(7246), 546–549 (2009).
8. A. C. Dada et al., "Experimental high-dimensional two-photon entanglement and violations of generalized Bell inequalities," *Nat. Phys.* **7**(9), 677–680 (2011).
9. S. Rosenblum et al., "A CNOT gate between multiphoton qubits encoded in two cavities," *Nat. Commun.* **9**(1), 652 (2018).
10. R. W. Heeres et al., "Implementing a universal gate set on a logical qubit encoded in an oscillator," *Nat. Commun.* **8**(1), 94 (2017).
11. T. Giordani et al., "Experimental engineering of arbitrary qudit states with discrete-time quantum walks," *Phys. Rev. Lett.* **122**(2), 020503 (2019).
12. S. E. Venegas-Andraca, "Quantum walks: a comprehensive review," *Quantum Inf. Process.* **11**(5), 1015–1106 (2012).
13. H. Schmitz et al., "Quantum walk of a trapped ion in phase space," *Phys. Rev. Lett.* **103**(9), 090504 (2009).
14. F. Zähringer et al., "Realization of a quantum walk with one and two trapped ions," *Phys. Rev. Lett.* **104**(10), 100503 (2010).
15. M. Karski et al., "Quantum walk in position space with single optically trapped atoms," *Science* **325**(5937), 174–177 (2009).
16. L. Sansoni et al., "Two-particle bosonic-fermionic quantum walk via integrated photonics," *Phys. Rev. Lett.* **108**(1), 010502 (2012).
17. A. Crespi et al., "Anderson localization of entangled photons in an integrated quantum walk," *Nat. Photonics* **7**(4), 322–328 (2013).
18. F. Cardano et al., "Quantum walks and wavepacket dynamics on a lattice with twisted photons," *Sci. Adv.* **1**(2), e1500087 (2015).
19. F. Caruso et al., "Fast escape of a quantum walker from an integrated photonic maze," *Nat. Commun.* **7**(1), 11682 (2016).
20. T. Kitagawa et al., "Observation of topologically protected bound states in photonic quantum walks," *Nat. Commun.* **3**(1), 882 (2012).
21. X. Qiang et al., "Efficient quantum walk on a quantum processor," *Nat. Commun.* **7**(1), 11511 (2016).
22. J. O. Owens et al., "Two-photon quantum walks in an elliptical direct-write waveguide array," *New J. Phys.* **13**(7), 075003 (2011).
23. J. Boutari et al., "Large scale quantum walks by means of optical fiber cavities," *J. Opt.* **18**(9), 094007 (2016).
24. L. Innocenti et al., "Quantum state engineering using one-dimensional discrete-time quantum walks," *Phys. Rev. A* **96**(6), 062326 (2017).
25. A. Suprano et al., "Enhanced detection techniques of orbital angular momentum states in the classical and quantum regimes," *New J. Phys.* **23**(7), 073014 (2021).
26. L. Allen et al., "Orbital angular momentum of light and the transformation of Laguerre-Gaussian laser modes," *Phys. Rev. A* **45**(11), 8185–8189 (1992).
27. A. M. Yao and M. J. Padgett, "Orbital angular momentum: origins, behavior and applications," *Adv. Opt. Photonics* **3**(2), 161–204 (2011).
28. B. Piccirillo et al., "The orbital angular momentum of light: genesis and evolution of the concept and of the associated photonic technology," *Riv. Nuovo Cimento* **36**(11), 501–555 (2013).
29. Q. Zhan, "Trapping metallic Rayleigh particles with radial polarization," *Opt. Express* **12**(15), 3377–3382 (2004).
30. S. Fürhapter et al., "Spiral phase contrast imaging in microscopy," *Opt. Express* **13**(3), 689–694 (2005).
31. F. Tamburini et al., "Overcoming the Rayleigh criterion limit with optical vortices," *Phys. Rev. Lett.* **97**(16), 163903 (2006).
32. M. P. Lavery et al., "Detection of a spinning object using light's orbital angular momentum," *Science* **341**(6145), 537–540 (2013).
33. L. Torner, J. P. Torres, and S. Carrasco, "Digital spiral imaging," *Opt. Express* **13**(3), 873–881 (2005).
34. D. S. Simon and A. V. Sergienko, "Two-photon spiral imaging with correlated orbital angular momentum states," *Phys. Rev. A* **85**(4), 043825 (2012).
35. N. Uribe-Patarroyo et al., "Object identification using correlated orbital angular momentum states," *Phys. Rev. Lett.* **110**(4), 043601 (2013).
36. A. E. Willner et al., "Optical communications using orbital angular momentum beams," *Adv. Opt. Photonics* **7**(1), 66–106 (2015).
37. N. Bozinovic et al., "Terabit-scale orbital angular momentum mode division multiplexing in fibers," *Science* **340**(6140), 1545–1548 (2013).
38. M. Malik et al., "Influence of atmospheric turbulence on optical communications using orbital angular momentum for encoding," *Opt. Express* **20**(12), 13195–13200 (2012).
39. J. Baghdady et al., "Multi-gigabit/s underwater optical communication link using orbital angular momentum multiplexing," *Opt. Express* **24**(9), 9794–9805 (2016).
40. J. Wang, "Advances in communications using optical vortices," *Photonics Res.* **4**(5), B14–B28 (2016).
41. D. Cozzolino et al., "High-dimensional quantum communication: benefits, progress, and future challenges," *Adv. Quantum Technol.* **2**(12), 1900038 (2019).
42. X.-L. Wang et al., "Quantum teleportation of multiple degrees of freedom of a single photon," *Nature* **518**(7540), 516–519 (2015).
43. M. Krenn et al., "Twisted photon entanglement through turbulent air across Vienna," *Proc. Natl. Acad. Sci. U. S. A* **112**(46), 14197–14201 (2015).
44. M. Malik et al., "Multi-photon entanglement in high dimensions," *Nat. Photonics* **10**(4), 248–252 (2016).
45. A. Sit et al., "High-dimensional intracity quantum cryptography with structured photons," *Optica* **4**(9), 1006–1010 (2017).
46. S. D. Bartlett, H. deGuise, and B. C. Sanders, "Quantum encodings in spin systems and harmonic oscillators," *Phys. Rev. A* **65**(5), 052316 (2002).
47. F. Cardano et al., "Statistical moments of quantum-walk dynamics reveal topological quantum transitions," *Nat. Commun.* **7**(1), 11439 (2016).
48. I. Buluta and F. Nori, "Quantum simulators," *Science* **326**(5949), 108–111 (2009).
49. M. Mirhosseini et al., "High-dimensional quantum cryptography with twisted light," *New J. Phys.* **17**(3), 033033 (2015).
50. F. Bouchard et al., "Quantum cryptography with twisted photons through an outdoor underwater channel," *Opt. Express* **26**(17), 22563–22573 (2018).
51. J. Li, M. Zhang, and D. Wang, "Adaptive demodulator using machine learning for orbital angular momentum shift keying," *IEEE Photonics Technol. Lett.* **29**(17), 1455–1458 (2017).
52. J. M. Arrazola et al., "Machine learning method for state preparation and gate synthesis on photonic quantum computers," *Quantum Sci. Technol.* **4**(2), 024004 (2019).
53. J. Mackeprang, D. B. R. Dasari, and J. Wrachtrup, "A reinforcement learning approach for quantum state engineering," *Quantum Mach. Intell.* **2**(1), 5 (2020).
54. W. Ma et al., "Deep learning for the design of photonic structures," *Nat. Photonics* **15**(2), 77–90 (2021).
55. P. R. Wiecha et al., "Deep learning in nano-photonics: inverse design and beyond," *Photonics Res.* **9**(5), B182–B200 (2021).
56. M. Benedetti et al., "A generative modeling approach for benchmarking and training shallow quantum circuits," *npj Quantum Inf.* **5**(1), 45 (2019).
57. S. Yu et al., "Reconstruction of a photonic qubit state with reinforcement learning," *Adv. Quantum Technol.* **2**(7–8), 1800074 (2019).
58. T. Giordani et al., "Machine learning-based classification of vector vortex beams," *Phys. Rev. Lett.* **124**(16), 160401 (2020).
59. A. A. Melnikov et al., "Active learning machine learns to create new quantum experiments," *Proc. Natl. Acad. Sci. U. S. A.* **115**(6), 1221–1226 (2018).
60. Y. Ren et al., "Genetic-algorithm-based deep neural networks for highly efficient photonic device design," *Photonics Res.* **9**(6), B247–B252 (2021).

61. L. O'Driscoll, R. Nichols, and P. Knott, "A hybrid machine learning algorithm for designing quantum experiments," *Quantum Mach. Intell.* **1**(1), 5–15 (2019).
62. A. Lumino et al., "Experimental phase estimation enhanced by machine learning," *Phys. Rev. Appl.* **10**(4), 044033 (2018).
63. R. Santagati et al., "Witnessing eigenstates for quantum simulation of Hamiltonian spectra," *Sci. Adv.* **4**(1), eaap9646 (2018).
64. J. Wang et al., "Experimental quantum Hamiltonian learning," *Nat. Phys.* **13**(6), 551–555 (2017).
65. K. Rambhatla et al., "Adaptive phase estimation through a genetic algorithm," *Phys. Rev. Res.* **2**(3), 033078 (2020).
66. A. A. Melnikov, P. Sekatski, and N. Sangouard, "Setting up experimental bell tests with reinforcement learning," *Phys. Rev. Lett.* **125**(16), 160401 (2020).
67. D. Poderini et al., "Ab-initio experimental violation of bell inequalities," arXiv:2108.00574 (2021).
68. K. Bharti et al., "Machine learning meets quantum foundations: a brief survey," *AVS Quantum Sci.* **2**(3), 034101 (2020).
69. R. Fickler, M. Ginoya, and R. W. Boyd, "Custom-tailored spatial mode sorting by controlled random scattering," *Phys. Rev. B* **95**(16), 161108 (2017).
70. A. Costa and G. Nannicini, "RBFOpt: an open-source library for black-box optimization with costly function evaluations," *Math. Programming Comput.* **10**(4), 597–629 (2018).
71. G. Nannicini, "On the implementation of a global optimization method for mixed-variable problems," arXiv:2009.02183 (2021).
72. M. J. D. Powell, "The theory of radial basis function approximation in 1990," in *Advances in Numerical Analysis, Vol. II: Wavelets, Subdivision Algorithms and Radial Functions*, W. Light, Ed., pp. 105–210, Oxford University Press, Oxford (1992).
73. M. J. D. Powell, "Recent research at Cambridge on radial basis functions," in *New Developments in Approximation Theory*, M. W. Müller et al., Eds., pp. 215–232, Birkhäuser, Basel (1999).
74. M. D. Buhmann, *Radial Basis Functions: Theory and Implementations, Cambridge Monographs on Applied and Computational Mathematics*, Cambridge University Press, Cambridge (2003).
75. L. Marrucci, C. Manzo, and D. Paparo, "Optical spin-to-orbital angular momentum conversion in inhomogeneous anisotropic media," *Phys. Rev. Lett.* **96**(16), 163905 (2006).
76. "The source code of the RBFOpt algorithm," https://github.com/coin-or/rbfopt.
77. "RBFOpt documentation," https://rbfopt.readthedocs.io/_/downloads/en/latest/pdf/.
78. M. Fitzi, N. Gisin, and U. Maurer, "Quantum solution to the byzantine agreement problem," *Phys. Rev. Lett.* **87**(21), 217901 (2001).
79. N. J. Cerf et al., "Security of quantum key distribution using *d*-level systems," *Phys. Rev. Lett.* **88**(12), 127902 (2002).
80. D. Bruß and C. Macchiavello, "Optimal eavesdropping in cryptography with three-dimensional quantum states," *Phys. Rev. Lett.* **88**(12), 127901 (2002).
81. A. Acin, N. Gisin, and V. Scarani, "Security bounds in quantum cryptography using *d*-level systems," arXiv:quant-ph/0303009 (2003).
82. N. K. Langford et al., "Measuring entangled qutrits and their use for quantum bit commitment," *Phys. Rev. Lett.* **93**(5), 053601 (2004).
83. E. T. Campbell, H. Anwar, and D. E. Browne, "Magic-state distillation in all prime dimensions using quantum Reed–Muller codes," *Phys. Rev. X* **2**(4), 041021 (2012).
84. H.-M. Gutmann, "A radial basis function method for global optimization," *J. Global Optim.* **19**(3), 201–227 (2001).
85. R. Regis and C. Shoemaker, "A stochastic radial basis function method for the global optimization of expensive functions," *INFORMS J. Comput.* **19**(4), 497–509 (2007).
86. E. Bolduc et al., "Exact solution to simultaneous intensity and phase encryption with a single phase-only hologram," *Opt. Lett.* **38**(18), 3546–3549 (2013).
87. A. Forbes, A. Dudley, and M. McLaren, "Creation and detection of optical modes with spatial light modulators," *Adv. Opt. Photonics* **8**(2), 200–227 (2016).
88. H. Zhong et al., "Quantum computational advantage using photons," *Science* **370**(6523), 1460–1463 (2020).
89. V. Cimini et al., "Calibration of multiparameter sensors via machine learning at the single-photon level," *Phys. Rev. Appl.* **15**(4), 044003 (2021).
90. F. Hoch et al., "Boson sampling in a reconfigurable continuously-coupled 3D photonic circuit," arXiv:2106.08260 (2021).
91. D. Brod et al., "Photonic implementation of boson sampling: a review," *Adv. Photonics* **1**(3), 034001 (2019).
92. J. Pan et al., "Multiphoton entanglement and interferometry," *Rev. Mod. Phys.* **84**(2), 777–838 (2012).
93. M. J. D. Powell, "An efficient method for finding the minimum of a function of several variables without calculating derivatives," *Comput. J.* **7**(2), 155–162 (1964).

Alessia Suprano is a PhD student in the Quantum Information Laboratory of Professor Fabio Sciarrino. Her current interests are focused on quantum optics for the implementation and exploitation of quantum walks in the orbital angular momentum degree of freedom of photons and for the study of nonlocality in networks. She graduated in October 2018 from the Sapienza Università di Roma.

Danilo Zia is a PhD student in the Quantum Information Laboratory of Professor Fabio Sciarrino. Currently, he is investigating the applications of quantum walk dynamics in the orbital angular momentum degree of freedom of the photons using machine learning techniques. He graduated in October 2020 from Sapienza Università di Roma.

Emanuele Polino graduated in November 2016 from the Sapienza Università di Roma and obtained his PhD in February 2020. Currently, he is working on photonic technologies for quantum foundations studies and quantum information tasks. In particular, he worked on fundamental tests on wave-particle duality of photons, study of nonlocality in different quantum networks, quantum metrology protocols, generation, transmission, and measurement of quantum states of light carrying orbital angular momentum, and realization of entangled photons sources.

Taira Giordani received her PhD in physics in 2020. She is currently a postdoc in the Physics Department of Sapienza University. Her research focuses on the experimental implementation of quantum walks in integrated photonic devices and the angular momentum of light. In this context, her efforts aim to develop machine learning and optimization methods for the certification and engineering of photonic quantum walk platforms.

Luca Innocenti received his PhD in physics in 2020 from Queen's University Belfast, with a thesis on applications of machine learning to quantum information science. He is currently a researcher in the Department of Physics at the University of Palermo. His research interests focus on devising ways to apply machine learning to quantum physics, with a focus on quantum optics and photonics.

Alessandro Ferraro received his PhD in physics from the University of Milan in 2005. Afterwards, he held fellowship and research positions at ICFO and UAB (Barcelona), UCL (London), and US (Sussex). He is now a senior lecturer and head of CTAMOP research Centre at QUB (Belfast), where he was appointed in 2013. His research focuses on the theory of quantum information with continuous variables and quantum optics, including quantum correlations and machine learning, thermodynamics, and many-body systems.

Mauro Paternostro received his PhD from Queen's University Belfast before securing fellowships from Leverhulme Trust and EPSRC. He was appointed as a lecturer at Queen's in 2008, reader in 2010, and

professor in 2013. He is the head of the School of Maths and Physics and coleads the Quantum Technology group, where he works on quantum foundations and quantum technologies. His honors include a Royal Society Wolfson Fellowship. He has published more than 200 papers and attracted £20M+ in funding.

Nicolò Spagnolo received his PhD in 2012 in physical science of matter, with a thesis on experimental multiphoton quantum optical states. He is an assistant professor in the Department of Physics of Sapienza Università di Roma. His research interests have been focused on quantum computation, simulation, communication and metrology by employing different photonic platforms, such as orbital angular momentum and integrated photonics.

Fabio Sciarrino received his PhD in 2004 with a thesis in experimental quantum optics. He is a full professor and head of the Quantum Information Lab in the Department of Physics of Sapienza Università di Roma. Since 2013, he has been a fellow of the Sapienza School for Advanced Studies. His main field of research is quantum information and quantum optics, with works on quantum teleportation, optimal quantum machines, fundamental tests, quantum communication, and orbital angular momentum.

CHINESE LASER PRESS 中国激光杂志社 | SPIE.

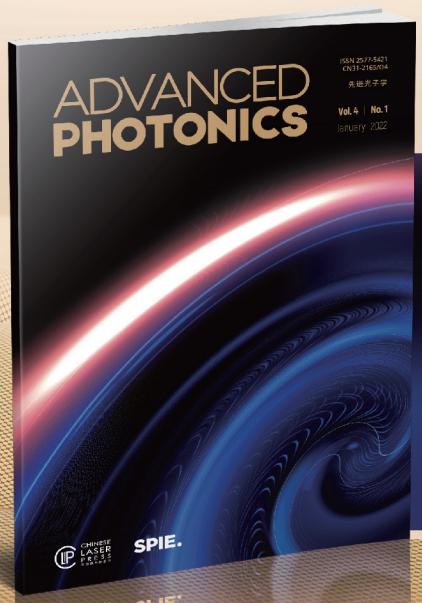

ADVANCED PHOTONICS

2021 Impact Factor **13.582**

Read cutting-edge papers

from leaders in optics and photonics

Submit your best work

to *Advanced Photonics*

ADVANCED PHOTONICS NEXUS

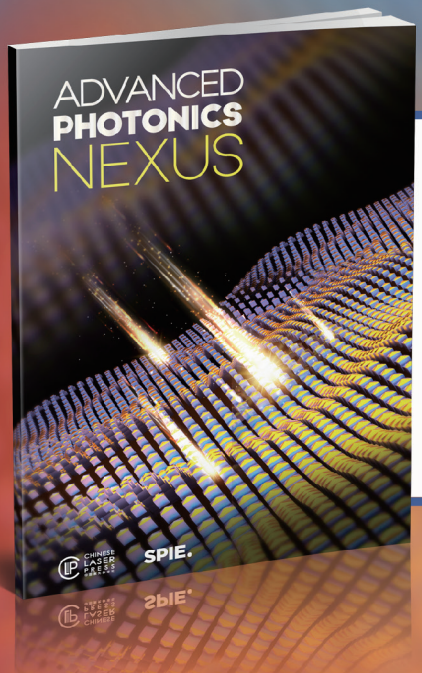

Sister journal to *Advanced Photonics*

Open for submission and fast transfer

Gold Open Access (APC waived through 2022)

ADVANCED PHOTONICS

Theme Issue on

Quantum Technologies

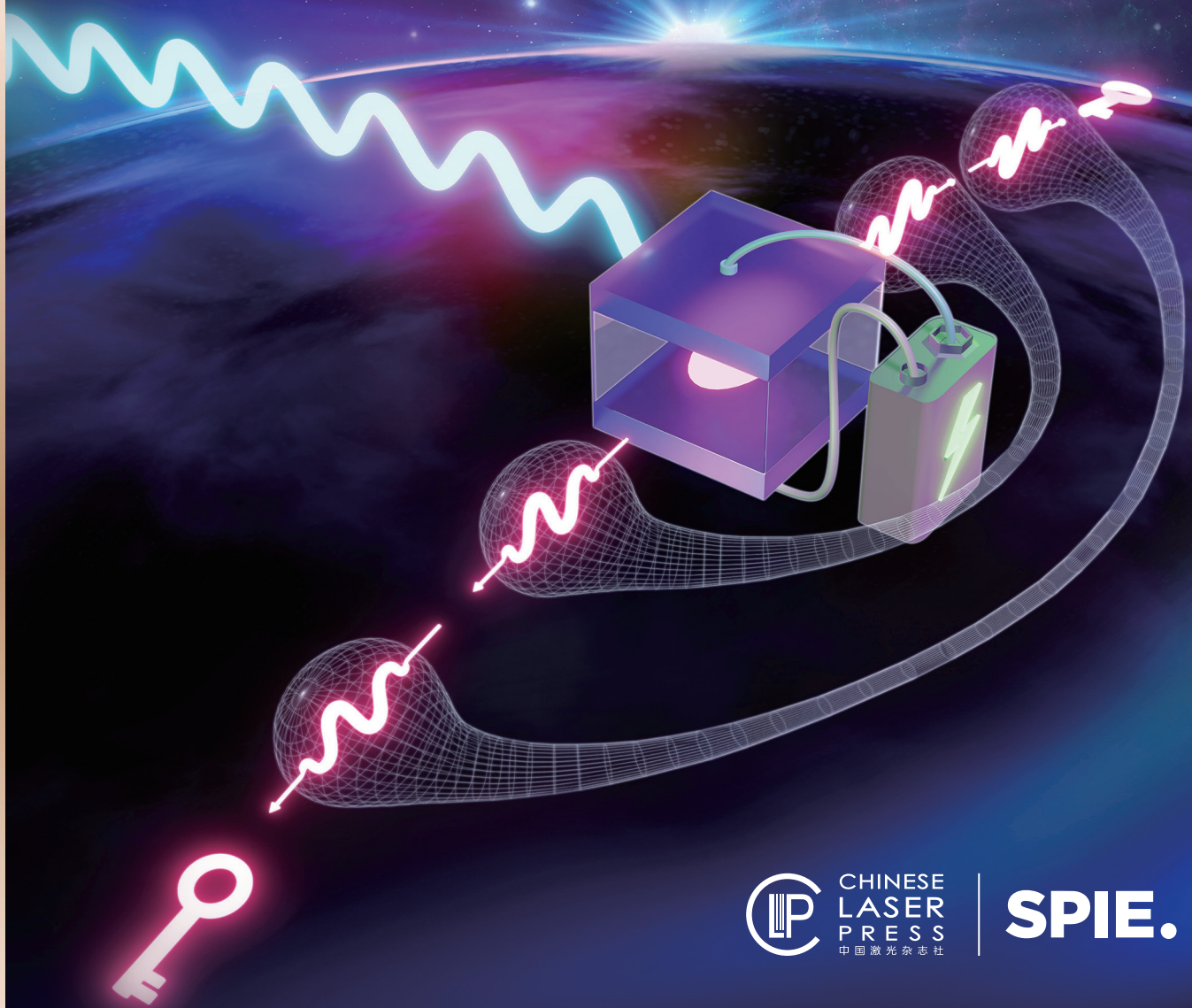

CHINESE LASER PRESS 中国激光杂志社 | SPIE.